Activation de petites molécules par des complexes bio-inspirés à liaison métal-thiol

Deborah Brazzolotto

Communauté
UNIVERSITÉ Grenoble Alpes

THÈSE

Pour obtenir le grade de

DOCTEUR DE LA COMMUNAUTE UNIVERSITE GRENOBLE ALPES

Spécialité : **Chimie Inorganique et Bioinorganique**

Arrêté ministériel : 7 août 2006

Présentée par

Deborah BRAZZOLOTTO

Thèse dirigée par **Carole DUBOC** et
Co-encadrée par **Marcello GENNARI**

préparée au sein du **Département de Chimie Moléculaire (DCM)**
dans **l'École Doctorale Chimie et Science du Vivant (EDCSV)**

Activation des petites molécules par des complexes bio-inspirés à liaison métal-thiol.

Thèse soutenue publiquement le **« 5 Octobre 2016 »**,
devant le jury composé de :

Mme. Elodie ANXOLABEHERE-MALLART
Directrice de Recherche CNRS, Université Paris 7- Diderot, Rapporteur
M. Bruno GUIGLIARELLI
Professeur, Aix-Marseille Université, Rapporteur
M. Dominique LUNEAU
Professeur, Université Claude Bernard Lyon 1, Président
M. Franc MEYER
Professeur, Institut für Anorganische Chemie, Germany, Membre
M. Vincent ARTERO
Chercheur CEA, CEA Grenoble, Membre
M. Marcello GENNARI
Chargé de Recherche CNRS, Université Grenoble Alpes, Membre
Mme. Carole DUBOC
Directrice de Recherche CNRS, Université Grenoble Alpes, Membre

Remerciements

Je terminerai la rédaction de ce manuscrit par les remerciements que j'écris non sans émotion.

Tout d'abord, je souhaite remercier les membres du jury qui ont examiné mes travaux de thèse : le Prof. Dominique Luneau qui l'a présidée, le Dr. Elodie Anxolabéhère-Mallart et le Prof. Bruno Guigliarelli, rapporteurs de ce manuscrit de thèse ainsi que le Prof. Franc Meyer en tant qu'examinateur.

Je remercie le DCM et notamment le Dr. Serge Cosnier, les Directeurs de l'équipe Cire, le Prof.Eric St-Aman et le Prof. Fabrice Thomas .Fabrice, je te remercie d'avoir mis Carole sur mon chemin ! Je Remercie également le LCBM et notamment le Dr. Stéphane Menage pour m'avoir accueillie dans son laboratoire.

Carole, comment te dire à quel point je te remercie pour tout ce que tu as fait pour moi !!! Merci, pour ses trois années d'encadrement où tu as cru en moi et m'as toujours portée vers le haut. Je n'aurais pas pu rêver de meilleure thèse. Merci aussi pour tous ces échanges, ces conseils aussi bien professionnels que privés et ta bienveillance à mon égard.

Marcello, on en aura vécu des moments ensemble, des joies, des peines ! Merci pour tout ce que tu m'as appris au cours de ces années, la rigueur, le gout du travail bien fait, et bien sur toutes ces connaissances !!!! Une réelle amitié s'est créée au fil de ses années et je pense que je vais te manquer ! Merci pour tous les moments qu'on a partagé !

Vincent, je pense qu'il était écrit dans mes gènes que je travaille avec toi un jour ! Après tout, tous les Brazzolotto « scientifiques » sont passés par ton labo ! Merci pour tout ce que tu m'as apporté, pour ces échanges toujours très constructifs.

Je voudrais aussi remercier mes labos d'accueil. Tout d'abord le DCM et plus particulièrement Eric St-Aman. Merci de m'avoir laissé la liberté d'organiser les repas de labo et merci pour les encouragements tout au long de ces trois années. Je remercie également Stéphane Ménage pour m'avoir accueillie au LCBM et de m'y être fait sentir comme chez moi.

Je remercie aussi chaleureusement Caroline, Nathalie et Gwendoline pour leur aide administrative, leur gentillesse et leur disponibilité. Merci tout particulièrement à Caro pour toute son aide et pour avoir fait au plus vite pour régler mes oublis de paiement et tous mes petits soucis administratifs. J'ai pu compter sur toi et je t'en suis très reconnaissante.

Je remercie Stéphane Ménage et Pascale Maldivi pour les comités de suivi de thèse. Merci d'avoir été une oreille attentive et de bons conseils.

Cette thèse n'aurait pas été la même sans les collaborations. Je remercie Maylis Orio pour tous les calculs theoriques, Franc Meyer pour m'avoir accueillie à Gottingen pour les mesures de Mossbauer, Serena DeBeer et Kallol Ray pour les mesures de XAS.

Je remercie également le personnel technique sans qui mes molécules n'auraient pas pu être caractérisées comme il se doit. Jacques, Christian, Nicolas, Solange, Martine, Rodolphe et Laure ainsi que Béatrice.

Bien évidemment je remercie toute l'équipe Cire. Je remercie Catherine et Aurore pour avoir toujours été de bons conseils et de m'avoir aidée à la préparation de la soutenance. Je remercie en particulier Aurore pour avoir été présente dans les moments les plus difficiles de la rédaction. Merci de m'avoir bien fait rigoler.

Je remercie Sélim pour toute son aide au cours de ces trois dernières années. Il a été indispensable à la bonne réussite de cette thèse. J'ai toujours pu compter sur toi ! Une autre personne indispensable : Florian Molton. Dieu sait que j'ai pu te solliciter pour tous les appareils de spectro et d'électroch. Flo c'est en quelque sorte un magicien. Quand je l'appelle pour un appareil qui ne marche pas et bien dès qu'il arrive, ça remarche comme par miracle. En tout cas merci à tous les deux d'avoir été patients avec moi.

Je remercie Fred Loiseau d'avoir été ma tutrice d'enseignement. Merci d'avoir toujours été de bons conseils et merci d'avoir partagé les repas de midi avec moi. Et merci d'avoir donné une bonne image de la Sicile, le pays de ma mère !!

C'est non sans émotion que je remercie Jérome Chauvin. Merci d'avoir été mon ami. Merci pour tes tenues vestimentaires toujours plus chic les unes que les autres ! Merci pour tous ces fous rires. Je vais te regretter Chauvin !

Ensuite, je remercie mon deuxième labo d'accueil, le LCBM et plus particulièrement Solhycat. Merci d'avoir fait de moi un membre à part entière au sein de cette équipe. Je voudrais particulièrement remercier Jennifer et Murielle pour leur aide, leur gentillesse et leur disponibilité. Murielle, tu nous bichonnes tous, sans toi cette équipe ne serait pas la même.

Enfin arrive le moment de remercier tous mes copains thésards !! La liste est longue mais je voudrais remercier d'abord ceux qui ont été présents dès le début de cette aventure. Mon amie Rajaa, qui me manque beaucoup, Bertrand pour tous ses conseils et nos nombreuses discussions, mon British préféré Matt, qui a aussi été mon confident. J'oublierai jamais notre bureau à 4, nos discussions et nos déco de Noël. Je remercie aussi ma super copine Solène avec qui j'ai partagé de super moments et je te souhaite une super 3ème année de thèse. Je remercie également les Nico (Nico K et Nico Q) du CEA. Les garçons, vous avez contribué à ce que j'aime venir au LCBM. Je remercie tous les autres thésards qui ont marqué d'une façon ou d'une autre ces 3 ans : Robin, Laurent, Long, Daniela, James, Caro, Nathounet, Doti, Jules, Vianney, Lianke, Margot, Assil, Wathiq et Jordan.

Je remercie également ma supère stagiaire, Shirley. Tu es une fille incroyable. Tu as été ma première « vraie stagiaire » et la meilleure de loin. Mais tu n'as pas été qu'une étudiante, tu es devenue aussi mon amie. Je ne t'oublierai pas !

Je pense aussi à tous les stagiaires qui sont passés par notre labo, Ryan, Ashlie, Lucy, Matthew… Vous faites partis, comme on dit, des belles rencontres de ce labo.

Je remercie également les post-docs que j'ai rencontrés au cours de cette thèse. Je pense à mon espagnole préférée Ester, à Eric, à Youssef : merci de m'avoir fait découvrir plein de chose, les voyages, les restos !! Merci à Adina et Julien pour leur bonne humeur et les rigolades! Merci à Trevor pour tout ce qu'il m'a appris les premières semaines de thèse.

Je remercie ma meilleure amie Vaness. Cela fait 16 ans qu'on se connait et qu'on ne se quitte pas. On va même en post-doc sur le même continent. Si ce n'est pas dingue ça. Je sais que l'on peut compter l'une sur l'autre et c'est ça qui définit une vraie amitié.

Enfin, Je dédie cette thèse aux personnes plus importantes de ma vie : mes parents, mon frère Pierre, ma sœur Rebecca et mes deux taties ! Jamais je n'aurais pu accomplir tout « ça » sans eux. Vous m'avez supportée, soutenue, encouragée. Vous avez toujours cru en moi et je vous dois tout. Merci à toute ma famille en or.

Table of contents

Introduction **1**
Résumé **4**
1.1. Introduction. 10
1.2. Electronic properties of complexes with metal-thiolate bonds 11
1.3. Metal-thiolate complexes for efficient electron transfer. 15
1.3.1. Copper-thiolate centers. 15
1.3.2. [Fe-S] clusters. 17
1.4. Reactivity of thiolates in metal-thiolate complexes. 21
1.4.1. S-reactions. 21
1.4.2. Activation of O_2 and derivatives. 22
1.4.3. NO activation. 24
1.4.4. S-alkylation. 24
1.4.5. Metal-based disulphide formation. 25
1.5. Metal-thiolate/sulphide centers for the activation of small molecules. 26
1.5.1. N_2O and N_2 reduction 26
1.5.2. CO_2 and CO activation 28
1.5.3. H_2 and H^+ activation. 29
Plan of the thesis **30**
References **32**

Chapitre I: Nickel centered proton reduction catalysis in a model of [NiFe] Hydrogenase……..35
Résumé **38**
Introduction **42**
Results and Discussion **47**
1.1. Synthesis. 47
1.1.1. Synthesis of the bypiridine-bis-thiolate ligand. 47
1.1.2. Synthesis of the Ni^{II} unit 49
1.1.3. Synthesis of the Fe^{II} units 49
1.1.4. Synthesis of the $Ni^{II}Fe^{II}Cp$ and $Ni^{II}Fe^{II}Cp^*$complexes 50
1.2. Structural characterization of the heterodinuclear $Ni^{II}Fe^{II}$ complexes 50
1.2.1. Structural characterization of the $Ni^{II}Fe^{II}Cp$ complex 50

1.2.2. Structural characterization of the $Ni^{II}Fe^{II}Cp^*$ complex. 52
1.2.3. Mössbauer characterization of the $Ni^{II}Fe^{II}Cp$ and $Ni^{II}Fe^{II}Cp^*$ complexes. 53
1.2.4. Optimized structures of $Ni^{II}Fe^{II}Cp$ and $Ni^{II}Fe^{II}Cp^*$. 54
1.3. Solution properties of $Ni^{II}Fe^{II}Cp$ and $Ni^{II}Fe^{II}Cp^*$. 54
1.3.1. Redox properties of $Ni^{II}Fe^{II}Cp$ and $Ni^{II}Fe^{II}Cp^*$. 55
1.4. Electrocatalytic activity of $Ni^{II}Fe^{II}Cp$ and $Ni^{II}Fe^{II}Cp^*$ for H_2 production 57
1.5. Investigation of the catalytic mechanism of $Ni^{II}Fe^{II}Cp$ and comparison with the [NiFe] hydrogenase 61
1.5.1. Characterization of $Ni^{I}Fe^{II}Cp$, an active Ni-L model 61
1.5.2. Characterization of $Ni^{II}Fe^{II}Cp(H)$, an active Ni-R model 65
1.5.3. Towards $Ni^{III}Fe^{II}Cp(H)$, a Ni-C model 66
1.5.4. Identification of the two-electron reduced species of $Ni^{II}Fe^{II}Cp$. 67
1.6. Effect of CO on H_2 production. 67
1.6.1. Electrocatalytic activity in the presence of CO. 67
1.6.2. EPR spectroscopy of $Ni^{II}Fe^{II}Cp^*$ in the presence of CO. 69
1.7. Discussion 70
Conclusion 75
References 76

Chapitre II: Dioxygen Activation and Catalytic Reduction to Hydrogen Peroxide by a Thiolate-Bridged Dimanganese(II) Complex with a Pendant Thiol 79

Résumé 82
Introduction 86
Results and Discussion 90
2.1. Synthesis and structural properties of Mn^{II}_2SH and Mn^{III}_2OH. 90
2.2.1. Synthesis of Mn^{II}_2SH and Mn^{III}_2OH. 90
2.1.2. Structural characterization of Mn^{II}_2SH. 90
2.1.3. Structural characterization of Mn^{III}_2OH 92
2.2. Mn and S K-Edge XAS absorption of Mn^{II}_2SH and Mn^{III}_2OH 93
2.3. Magnetic properties of Mn^{II}_2SH and Mn^{III}_2OH 95
2.4. Solution properties. 96
2.4.1. Redox properties of Mn^{II}_2SH. 96
2.4.2. Redox properties of Mn^{III}_2OH. 98

2.5. Reactivity of Mn^{II}_2SH with dioxygen.....99
2.5.1. Reactivity of Mn^{II}_2SH with dioxygen in stoichiometric conditions.....99
2.5.2. Reactivity of Mn^{II}_2SH with dioxygen in catalytic conditions.....101
2.5.3. Characterization of the products of catalysis. 102
2.6. Reactivity of Mn^{II}_2S with dioxygen 103
2.6.1. Synthesis of Mn^{II}_2S. 103
2.6.2. Synthesis and structural properties of $Mn^{IV}_2(O)_2$ and $Mn^{IV}_2(O)(OH)$. 104
2.7.1. ESI-mass spectrometry.....108
2.7.2. Acid/base properties.....108
2.7.3. Mn K-Edge XAS absorption of $Mn^{IV}_2(O)_2$. 109
2.9. Mechanistic investigation of O_2 activation by Mn^{II}_2S 110
2.10. Proposed mechanism for O_2 activation and reduction.....111
2.10.1. Mn^{II}_2SH: An unusual metal-thiol system. 111
2.10.2. Proposed O_2 reduction pathways with Mn^{II}_2SH under stoichiometric and catalytic conditions.....111
Conclusion 115
References.....116

Résumé 122
Introduction.....127
Results and Discussion.....130
3.1. Synthesis and characterization of Mn and Co complexes. 130
3.1.1. Synthesis of **Co^{II}_2SS** and **$Co^{III}I$**. 130
3.1.2 Synthesis of **Mn^{II}_2SS** and **$Mn^{III}I$**.....131
3.1.3. X-Ray characterization of **Co^{II}_2SS** and **$Co^{III}X$**. 132
3.1.4 X-Ray characterization of **Mn^{II}_2SS** and **$Mn^{III}I$**.....134
3.2. UV-Vis spectroscopic properties. 136
3.2.1. UV-Vis spectroscopy of **Co^{II}_2SS** and **$Co^{III}X$** complexes. 136
3.2.2. UV-Vis spectroscopy of **Mn^{II}_2SS** and **$Mn^{III}I$** complexes.....137
3.3. Magnetic properties.....138
3.2.1. **Mn^{II}_2SS** magnetic properties. 138

3.4. Reactivity with Iodide: disulphide/thiolate interconversion. 139
3.5. Electrochemical properties 141
3.6. Theoretical calculations. 143
Conclusion 146
References 147

Chapitre IV: An Experimental and Theoretical Investigation on Penta-coordinated Cobalt (III) complexes with an Intermediate spin state S = 1, respectively: How Halide Ligands Affect theirMagneticAnisotropy……..…….149

Résumé 152
Introduction 156
Results 159
4.1. Synthesis, structures and characterizations. 159
4.2. Magnetic properties of **$M^{III}X$ (M=Mn** or **Co**, **X= Cl, Br, I)**. 159
4.2.1. Magnetic properties of **$Mn^{III}I$**. 159
4.2.2. Magnetic properties of **$Co^{III}X$** (X=Cl, Br, I). 160
4.3. Quantum chemical calculations. 162
4.3.1. Optimized structure of **$Co^{III}X$** (X = Cl, Br, I). 162
4.3.2. Prediction of the spin state of $Co^{III}X$ (X = Cl, Br, I). 162
4.3.3. Electronic structure of **$Co^{III}X$** (X = Cl, Br, I).....163
4.3.2. Prediction of the *zfs* of **$Co^{III}X$** (X = Cl, Br, I). 165
Discussion and conclusion 167
References 169

Conclusion……..171
Experimental section…….....179
Appendix……..…..…..205
Abstract……..…..…..…..213

Introduction

Table of content

Résumé 4

1.1. Introduction. 10

1.2. Electronic properties of complexes with metal-thiolate bonds 11

1.3. Metal-thiolate complexes for efficient electron transfer. 15

1.3.1. Copper-thiolate centers. 15

1.3.2. [Fe-S] clusters. 17

1.4. Reactivity of thiolates in metal-thiolate complexes. 21

1.4.1. S-reactions. 21

1.4.2. Activation of O_2 and derivatives. 22

1.4.3. NO activation. 24

1.4.4. S-alkylation. 24

1.4.5. Metal-based disulphide formation. 25

1.5. Metal-thiolate/sulphide centers for the activation of small molecules. 26

1.5.1. N_2O and N_2 reduction 26

1.5.2. CO_2 and CO activation 28

1.5.3. H_2 and H^+ activation. 29

Plan of the thesis. 30

References 32

Résumé

La chimie bio-inorganique est un domaine en pleine expansion. Elle combine la recherche fondamentale académique et les problèmes sociétaux important en utilisant une approche interdisciplinaire. Il s'agit de mimer, *via* des complexes moléculaires modèles, la structure et/ou la fonction du site actif d'une métalloprotéine d'intérêt entre autre à travers ses propriétés physico-chimiques (propriétés électroniques, propriétés redox, réactivité). Ces complexes modèles permettent de comprendre les systèmes biologiques par l'analyse du mécanisme à l'échelle moléculaire (caractérisation d'intermédiaires réactionnels) ainsi que le développement de nouveaux catalyseurs inspirés de ces systèmes biologiques. Dans ce contexte, les chimistes développent des séries de complexes dans le but de comprendre et d'optimiser leur réactivité. En étudiant ces complexes modèles par des méthodes, analytiques, spectroscopiques et théoriques, ils peuvent ainsi déterminer les facteurs structuraux, électroniques, et redox nécessaires à la réactivité (efficacité, sélectivité, spécificité). Cette approche permet aussi de définir des sondes de références (spectroscopiques et théoriques) ainsi que des corrélations magnéto-structurales, utiles pour l'identification d'espèces nouvelles telles que des intermédiaires réactionnels.

Certains éléments sont connus pour être essentiels pour la vie des plantes, des animaux et des bactéries. Seuls onze sont essentiels pour tous les organismes : hydrogène, carbone, azote, oxygène, sodium, potassium, calcium, magnésium, soufre et chlore. De plus, des ions métalliques, sous forme de trace, sont nécessaires à la survie de certaines espèces tels que : le vanadium, le chrome, le manganèse, le fer, le cobalt, le nickel, le cuivre, le zinc, le molybdène et le tungstène. Il a été estimé que parmi toutes les protéines, plus de 50% d'entre elles sont des métalloprotéines, pour lesquelles, le métal est essentiel pour un certain nombre de réactions qui ont lieu au sein du site actif comme : le transfert d'électron, l'activation des liaisons, le contrôle de réactions radicalaires, l'activation de petites molécules (O_2, H_2, N_2…), le transfert d'atome d'oxygène et des réactions non redox. Les sites actifs peuvent être considérés comme des complexes inorganiques organisés et sophistiqués, dans lequel l'ion métallique est directement lié à la protéine principalement par l'intermédiaire d'un atome d'azote, d'oxygène et dans une moindre mesure, par des atome de soufre issues des acides aminés. Parmi les 20 acides aminés, seuls deux d'entre eux contiennent des atomes de soufre sous forme de fonction thiolate (cystéine) et de thioéther (méthionine), la méthionine étant moins présente comme ligand dans les systèmes biologiques.

La cystéine figure parmi les acides aminés les moins abondants et est souvent retrouvée an tant que résidu hautement conservé dans le site actif des protéines. Sous sa forme thiolate (pKa~8.5), on peut la retrouver soit en tant que ligand monodentate, ou bien sous forme de ligand pontant entre deux

centres métalliques. Cette fonction thiolate présente des propriétés particulières qui permettent de conférer au centre métallique les propriétés désirées pour la réactivité ciblée : (i) nucléophilicité, (ii) haute affinité pour les ions métalliques, et/ou (iii) capacité de former des ponts disulfures.

Au cours de ce chapitre, nous allons décrire, aux travers d'exemples précis, les propriétés électroniques des liaisons métal-thiol. Dans un deuxième temps, les propriétés redox des systèmes métalliques les plus efficaces impliqués dans le transfert d'électrons, soit les complexes de cuivre-thiolates et les clusters [Fe-S], seront discutées. La troisième partie traitera de la réactivité de ces liaisons et enfin nous décrirons des familles de métalloenzymes contenant des liaisons métal-thiol impliquées dans l'activation de petites molécules.

Les atomes de soufre confèrent des propriétés électroniques uniques aux complexes métalliques de part une liaison métal-thiol hautement covalente. Ce degré de covalence implique différentes interactions orbitalaires, dont les trois orbitales de valence 3p du thiolate (Figure 1), avec une contribution majoritaire de l'orbital pseudo-σ.

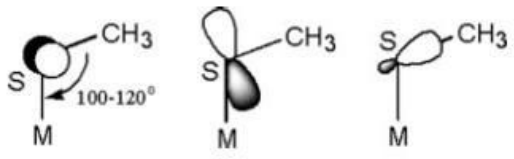

π pseudo-σ $\sigma_{S\text{-}C}$

Figure 1. Orbitales de valence 3p du soufre impliquées dans une liaison métal-thiolate.[5]

La covalence dépend également des propriétés électroniques du métal : sa configuration $3d^n$ ainsi que sa charge nucléaire effective (Z_{eff}) peuvent être estimées par différentes techniques spectroscopiques comme le dichroïsme circulaire magnétique (MCD), l'absorption UV-Visible, la résonance Raman (rR), et la spectroscopie d'absorption des rayons X (XAS au seuil K-du soufre). Au travers des séries de complexes **A** et **B** présentés sur la Figure 2 et la Table 1, il a pu être montré que ces complexes présentaient des bandes d'absorptions particulières et leur attribution (bandes d'absorption de transfert de charge (LMCT) dans la région du visible) a été réalisée grâce à des études complémentaires en MCD et rR. Pour les séries **A** et **B**, le degré de covalence suit l'ordre suivant: Fe^{II} –thiolate < Co^{II} –thiolate < Ni^{II} –thiolate <Cu^{II}–thiolate. La liaison Cu-thiolate est la liaison la plus covalente, en accord avec une faible énergie et de haute intensité pour la bande d'absorption LMCT. D'autre part, il a été montré que la liaison M-S était plus covalente pour les thiolates aromatiques (série **A**) que pour les alkyls thiolates (série **B**).

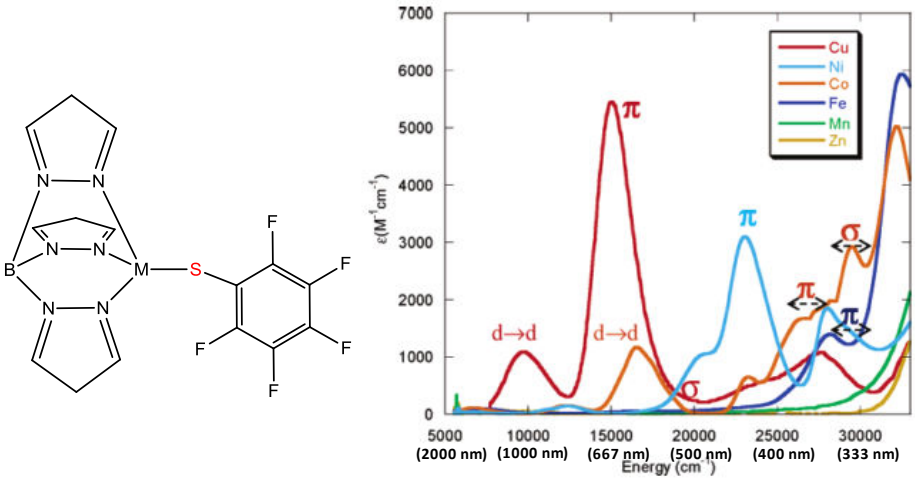

Figure 2. Spectres d'absorption UV-Vis des complexes $[ML(SC_6F_5)]$, **A** (M = Mn, Fe, Co, Ni, Cu, Zn) dans le cyclohexane.[9]

Table 1. Valeurs des transitions électroniques des spectres d'absorption UV-Vis pour la série **B**, $[M(S^{Me2}N_4(tren)]^+$ (M = Mn, Fe, Co, Ni, Cu, et Zn) dans MeCN.[1]

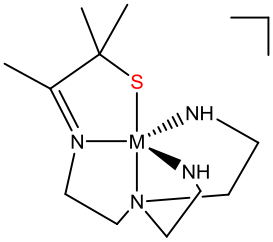

	λ_{max} (nm) (ϵ (M^{-1} cm^{-1}))	λ_{max} (nm) (ϵ (M^{-1} cm^{-1}))	λ_{max} (nm) (ϵ (M^{-1} cm^{-1}))
$[Mn^{II}(S^{Me2}N_4(tren))]^+$ (**5**)	240 (2910)		
$[Fe^{II}(S^{Me2}N_4(tren))]^+$ (**1**)	262 (4700)	357 (sh)	410 (sh)
$[Co^{II}(S^{Me2}N_4(tren))]^+$ (**6**)	236 (4570) 358 (990)	454 (215)	600 (100)
$[Ni^{II}(S^{Me2}N_4(tren))]^+$ (**4**)	275 (2394)	410 (330)	
$[Cu^{II}(S^{Me2}N_4(tren))]^+$ (**7**)	216 (3280) 236 (3400)	380 (3340)	618 (315)
$[Zn^{II}(S^{Me2}N_4(tren))]^+$ (**8**)	219 (4800)		

Un autre aspect important de la liaison métal-thiol est son implication dans le transfert d'électrons. Il s'agit d'un processus biologique essentiel nécessaire aux centres catalytiques redox. Les métaux de transition stables à différents degrés d'oxydation représentent ainsi de parfaits candidats. Les centres les plus efficaces dans le transfert d'électrons contiennent au moins une liaison M-thiolate. Il s'agit des « blue copper» protéines, le site dinucléaire de cuivre Cu_A et les clusters [Fe-S].

Les systèmes à base de cuivre sont divisés en deux familles : (i) les complexes mononucléaires de type T1 présents dans la plastocyanine (exemple d'une « blue copper » protéine) et (ii) les sites Cu_A présents dans la cytochrome *c* oxydase (CcO) et la N_2O réductase (N_2OR). Ces deux types de familles sont impliqués dans des transferts rapides d'électrons et présentent des liaisons Cu-thiolates hautement covalentes.

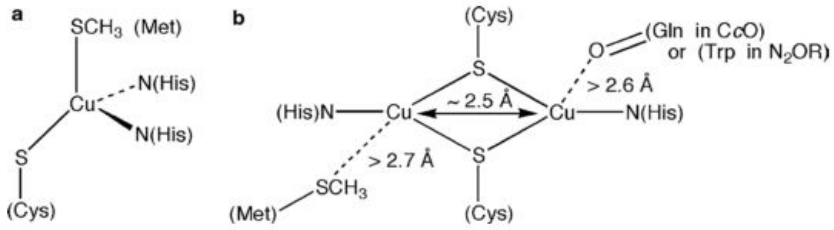

Figure 3. Représentation schématique a) du site T1 de la plastocyanine et b) du site Cu_A présent dans C*c*O et N_2OR.[5]

Les chimistes se sont donc intéressés à reproduire ces sites biologiques et se sont notamment focalisés sur la modélisation des complexes dinucléaires de Cu, dans le but de comprendre quels étaient les facteurs impliqués dans ce transfert rapide d'électrons et de comparer leurs systèmes modèles aux systèmes biologiques (Figure 3).

Les clusters [Fe-S] (Figure 4) sont principalement impliqués dans le transfert rapide d'électrons mais ont d'autres fonctions dont l'activation de substrats. Leur efficacité dans le transfert d'électrons vient de leur capacité à délocaliser leur densité électronique entre les atomes de Fe et de S. Il existe différentes familles de cluster [Fe-S] : les mononucléaires de Fe communément appelés rubrédoxines et les polynucléaires de Fe, les ferrédoxines : les clusters [2Fe-2S], [2Fe-2S] de la protéine Rieske, [3Fe-4S], [4Fe-4S], HiPiP [4Fe-4S] (High potential iron-sulfur protein) et le cluster [8Fe-7S] (Cluster P) composé de deux clusters [4Fe-3S] incomplets associé a un atome de soufre hexacoordonné (μ^6-S),[2] présent dans les nitrogénases. La synthèse de tels clusters a permis d'obtenir des informations complémentaires sur les propriétés redox des systèmes biologiques.

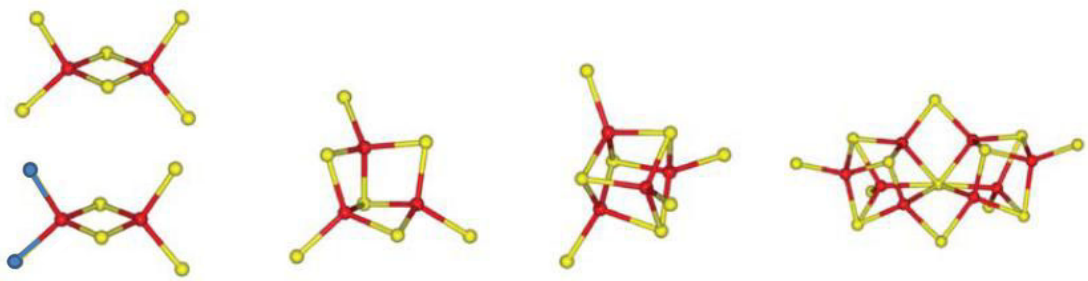

Figure 4. Structures et degrés d'oxydation des clusters [Fe-S].[23] Le Fe est en rouge, N en bleu et S en jaune. Le cluster avec les deux atomes N correspond au cluster de la protéine Rieske.

Il a été démontré que l'efficacité du transfert d'électrons entre ces clusters est associé à : (i) une configuration électronique haut spin pour le Fe^{II} et le Fe^{III}, (ii) une faible barrière d'activation au niveau de la sphère interne, et (iii) une conversion structural facile et rapide. Cela est dû aux propriétés de faible champ de ligand des thiolates et des soufres, ces derniers étant capables de rester à un degré d'oxydation S^{2-} même en présence d'ions Fe^{III}.

La coordination d'un alkyl-thiolate à un métal peut conduire à l'activation d'un atome de soufre pour promouvoir différents types de réactions telles que la S-alkylation, la S-oxygénation, la S-nitrosylation et la formation de ponts disulfures. Alors que les trois premières réactions nécessitent un substrat additionnel, c'est-à-dire, des dérivés alkyls, O_2 et ses dérivés ou encore NO, la formation de ponts disulfures à partir de thiolates coordonnés au métal ne nécessite que des processus intra- et inter-redox. Dans la nature, il a été montré que l'activation de petites molécules (dérivés alkyls, O_2 et ses dérivés ou encore NO) conduisent à des réactions centrées sur le soufre catalysées par le sites actifs spécifiques d'enzymes dont la méthionine synthase pour la S-alkylation), la nitrile hydratase ou la cystéine dioxygénase pour la S-oxygénation et des protéines héminiques ou des protéines de Cu de type I pour la S-nitrosylation. L'approche bio-inspirée a été fondamentale dans la compréhension des facteurs qui gouvernent une telle richesse de réactivité. De plus la conversion thiolate/disulfure est impliquée dans de nombreux processus biologiques avec entre autres, le repliement des protéines ou le contrôle de leur réactivité en tant que facteur de signalisation. L'idée que les ions métalliques puissent jouer un rôle actif dans cette conversion au sein de ces processus biologiques n'est que récente. Cependant, cette hypothèse n'est pas encore complètement comprise à ce jour (voir Chapitre III).

Les liaisons métal-thiol sont également impliquées dans le site actif de protéines responsables de l'activation d'autres petites molécules. Certaines enzymes vont être engagées dans le cycle de l'azote (la N_2O réductase (N_2OR), la nitrogénase), dans le cycle du carbone (la CO déshydrogénase (CODH), l'acétylcoenzyme A synthase (ACS)) (Figure 5) ou dans la réduction des protons ou l'oxydation de H_2 (les hydrogénases).

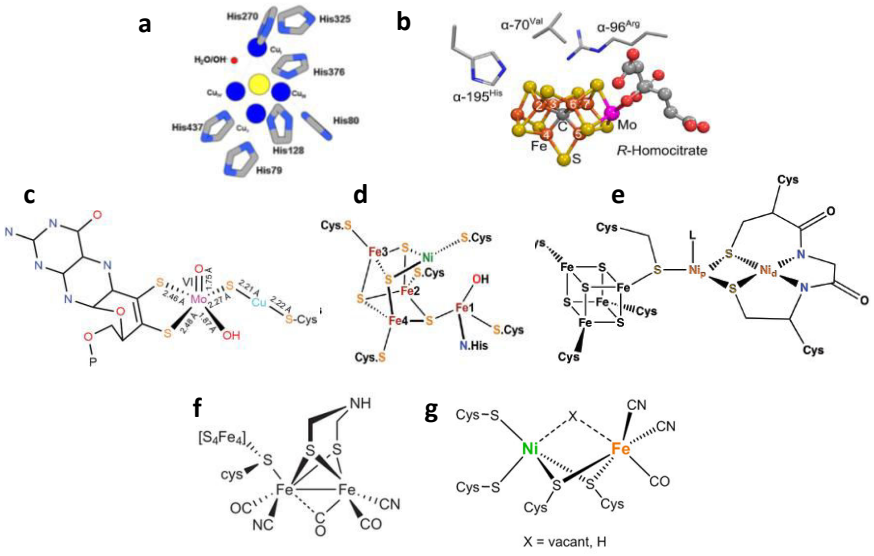

Figure 5. Représentation des enzymes impliqués dans le cycle de l'azote (haut), du carbone (milieu) et hydrogène (bas) : a) N_2OR, b) nitrogénase, c) Mo/Cu CODH, d) Ni/Fe CODH e) ACS f) hydrogénase à [Fe-Fe], g) hydrogénase à [NiFe].

La N_2OR catalyse la réduction du N_2O en N_2 et la nitrogénase la réduction de N_2 en ammoniac (NH_3). En ce qui concerne la N_2OR, la présence de soufre entre deux ions Cu du site actif va permettre (i) de délocaliser l'électron contribuant à une faible énergie de réorganisation au cours du processus catalytique et (ii) d'optimiser l'arrangement géométrique des ions Cu pour permettre au N_2O de se lier aux ions métalliques. Quant à la nitrogénase, les soufres vont permettre la communication entre les différents ions Fe de l'enzyme facilitant ainsi la rupture de la liaison N-N. Dans le cas de ces deux enzymes, des modèles moléculaires ont été nécessaires pour comprendre les phénomènes chimiques qui se déroulent au sein de leur site actif et comprendre les relations structures/activité.

L'oxydation du CO en CO_2 permet aux organismes de survivre sous atmosphère de CO, ce dernier étant source de carbone et d'énergie. Ce processus est assuré par la CODH présente chez les bactéries aérobies (Mo/Cu CODH) et anaérobies (Ni/Fe CODH). La Ni/Fe CODH est souvent associée à l'ACS (complexe dinucléaire de Ni) dans un cluster bi-fonctionnel qui catalyse la formation de la liaison C-C à partir de groupements méthyles et de CO_2 généré par la CODH. Cela génère ainsi un intermédiaire métabolique clé, l'acétylcoenzyme A.

Le rôle des thiolates au sein de la CODH n'est pas complètement compris. Néanmoins, au niveau de la Mo/Cu CODH, la présence d'un soufre pontant entre le Mo et le Cu forme deux liaisons fortement covalentes. Il est proposé que ce soufre permette de favoriser la délocalisation de l'électron entre les centres métalliques. Il existe énormément de complexes modèles de la CODH mais aucun d'entre eux n'est réactif en présence de CO. Quant aux modèles de l'ACS, la plupart d'entre eux tentent de reproduire une réactivité centrée sur le Ni comme dans l'enzyme.

Quant aux hydrogénases, ces enzymes catalysent la réduction réversible des protons en H_2. L'hydrogénase [NiFe] sera décrite dans l'introduction du chapitre I. Quant à l'hydrogénase [FeFe], sa particularité est d'être composée de deux ions Fe reliés entre eux par un ligand azadithiolate. La sphère de coordination de ces deux ions métalliques est complétée par des ligands carbonyles et cyano. Un cluster [4Fe-4S] est lié à cette unité bimétallique par un résidu cystéine. Dû à son environnement de coordination peu commun, les chimistes se sont intéressés à reproduire le site actif de cet enzyme par la synthèse de modèles structuraux et/ou fonctionnels. A ce jour aucun d'entre eux n'est capable de rivaliser avec les performances de l'enzyme en matière de production de H_2.

Notons que dans ce chapitre, la réactivité des enzymes à porphyrine et les molibdoptérines ne sera pas abordée.

1.1. Introduction.

Bio-inorganic chemistry is presently a field in expansion. It mixes fundamental academic research and important societal issues combining interdisciplinary approaches.[3] It consists of mimicking *via* small synthetic metal complexes the structure or/and the function of the active site of a metalloprotein of interest through its physico-chemical properties (electronic properties, redox properties, reactivity). Model compounds allow the understanding of biological systems by investigating mechanism at a molecular scale (intermediate characterization) and also the development of new bio-inspired catalysts. In this context, chemists develop series of complexes with the aim of understanding and optimizing targeted properties. By studying these model complexes with analytical, spectroscopic and theoretical methods, the structural, electronic and redox factors required for the reactivity (efficiency, selectivity, specificity) are determined. This approach also allows the definition of reference probes (spectroscopic and theoretical) and thus magneto-structural correlations that are useful for the identification of unknown species such as highly reactive intermediate species.

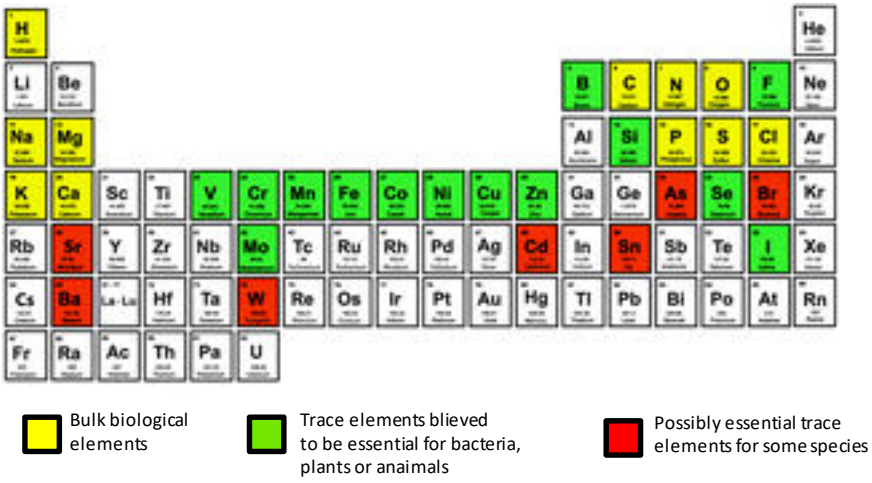

Figure 1. Elements essential for life.[79]

Few elements in hearth's crust appear to be essential for plants, animals and microbial life (Figure 1). Only eleven are essential in all known organisms and plants: hydrogen, carbon, nitrogen, oxygen, sodium, potassium, calcium, magnesium, sulphur and chlorine. Besides, metals, especially metal ions are needed by some species as trace elements: vanadium, chromium, manganese, iron, cobalt, nickel, copper, zinc, molybdenum and tungsten. It has been estimated that among all proteins, over 50% are metalloproteins,[4] for which the metal-based functional site is essential for promoting different kinds of reactions such as electron transfer, strong bond activation, controlled radical reaction, activation of small molecules (molecular dioxygen, hydrogen, and dinitrogen), oxo transfer and non-redox reactions. The active sites can be considered as well-organized and sophisticated inorganic complexes, in which the metal ion is directly bound to the protein mainly via nitrogen,

oxygen and to a lesser extent, sulphur donors issued from amino acid residues. Among the 20 amino acids, only two contain sulphur donor atoms: thiolate function for cysteine, and thioether for methionine (Figure 2),[3,5] but methionine is less present as metal ligand in biology than cysteine.

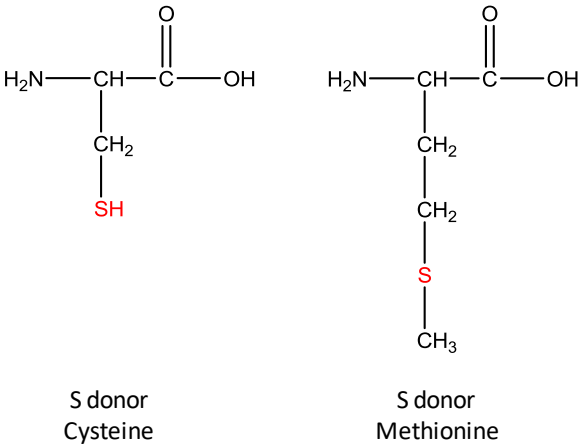

Figure 2. S- donor ligands from amino acids.

Cysteine is one of the least abundant amino acids and often found as a highly conserved residue in the functional site of proteins. In its thiolate form (pKa~8.5), it can act as monodentate or bridging ligand between two metal centers. It presents specialized properties, including high-nucleophilicity, high affinity for transition metal ions, and/or capacity to form disulphide bonds (by oxidation), to confer to the metal site the required properties for the targeted reactivity. The first part of the introduction will give an overview of the electronic properties of the metal-thiolate bond based on studies carried out on model complexes. Then, the redox properties of the most efficient natural metal-based electron transfer systems, i.e. copper-thiolate complexes and [Fe-S] clusters, will be discussed. While the third part will focus on the reactivity of the thiolate-metal bonds, the final one will deal with selected metalloenzymes containing active sites with thiolate metal complexes involved in the activation of small molecules. Note that the reactivity of porphyrin and molibdopterin proteins will not be discussed in this chapter.

1.2. Electronic properties of complexes with metal-thiolate bonds

Sulphur donor atoms give unique electronic properties of the corresponding metal complexes because of the high covalency of the M-thiolate bond. In metal-thiolate complexes, different orbital interactions are involved, implicating the three valence 3p orbitals of the thiolate. The carbon-sulphur σ bond ($\sigma_{S\text{-}C}$) cannot interact with the metal in an efficient way, thus contributing poorly to the covalency of the M-thiolate bond (Figure 3, right).

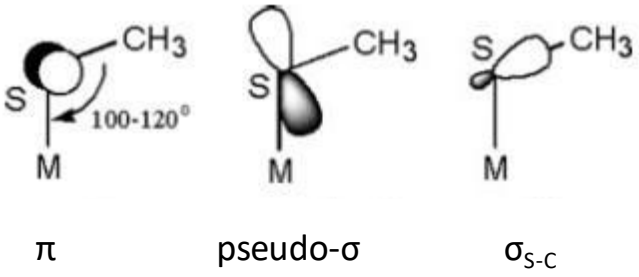

Figure 3. Sulphur-based valence orbitals of a metal-thiolate bond.[5]

The two other orbitals are perpendicular to the S-C bond and influence the thiolate interaction with the metal center. The 3p orbital located out of the C-S-M plane is involved in the π bonding (Figure 3, left), while the 3p pseudo-σ orbital in the C-S-M plane binds to the metal. Because the C-S-M angle is usually greater than 90° (100-120°), the sulphur electron density is shifted to the S-M bond (Figure 3, middle), explaining the so-called "pseudo" term for the latter orbital. The degree of covalency that can be estimated by different spectroscopic techniques (magnetic circular dichroism (MCD), UV-Vis absorption, Resonance Raman (rR), and S K-edge X-Ray absorption spectroscopy (XAS)), is also influenced by the electronic properties of the metal ion: its $3d^n$ configuration and its effective nuclear charge (Z_{eff}).

The covalent character of the metal-thiolate bond has been investigated through series of metal complexes. For example, two series (Figure 4) are discussed below: models **A** ($[M^{II}L(SC_6F_5)]$, where L = *hydrotris*(3,5-diisopropyl-1-pyrazolyl)borate anion) and M = Mn, Fe, Co, Ni, Cu and Zn characterized by X-ray crystallography)[6-8,7,10] contain a monodentate aromatic thiolate, while for **B** ($[M(S^{Me2}N_4(tren)]^+$, tren = *tris*(2-aminoethyl)amine), M = Mn, Fe, Co, Ni, Cu and Zn) the pentadentate ligand contains one alkyl thiolate.[11]

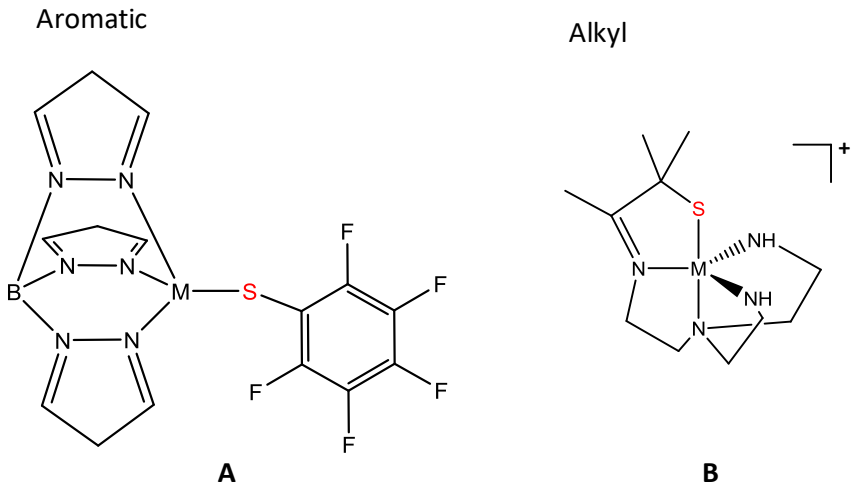

Figure 4. Series of metal aromatic thiolate **A** $[ML(SC_6F_5)]$,[8,10] and metal alkyl thiolate **B** $[M(S^{Me2}N_4(tren)]^+$.[1] (M^{II} = Mn, Fe, Co, Ni, Cu and Zn complexes**.**

Both series of complexes display peculiar absorption transitions and their attribution is based on complementary spectroscopic investigations including MCD and resonance Raman. As an example, the absorption spectra of the **A** series are shown in Figure 5 and the spectroscopic data are reported in Table 1 for the B series. All metal-thiolate complexes display intense low energy Ligand to Metal Charge Transfer transitions (LMCT) (noted either as π or σ in Figure 5) and low intensity d-d transitions at lower energies (except for d^{10} Zn^{II} and high spin d^5 Mn^{II} complexes because either the d-orbitals are filled or the transitions are both Laporte- and spin-forbidden).[7,1,8,9,10]

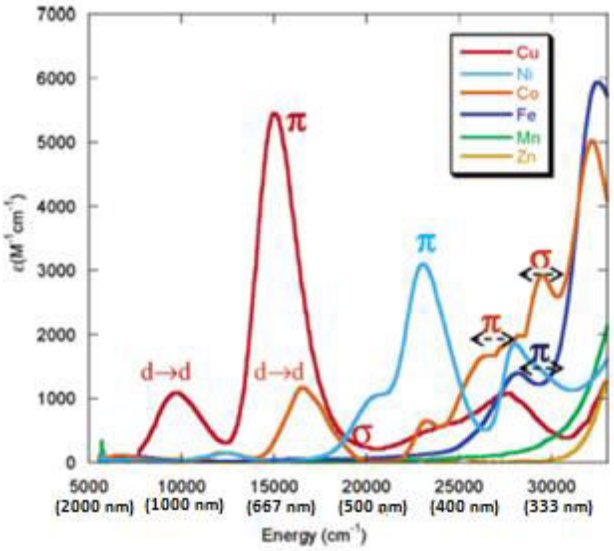

Figure 5. Electronic absorptions spectra of $[ML(SC_6F_5)]$, **A** (M = Mn, Fe, Co, Ni, Cu, Zn) in cyclohexane.[9]

Table 1. Electronic absorption transition for the series **B**, $[M(S^{Me2}N_4(tren)]^+$ (M = Mn, Fe, Co, Ni, Cu, and Zn) in MeCN.

	λ_{max} (nm) (ϵ (M^{-1} cm^{-1}))	λ_{max} (nm) (ϵ (M^{-1} cm^{-1}))	λ_{max} (nm) (ϵ (M^{-1} cm^{-1}))
$[Mn^{II}(S^{Me2}N_4(tren))]^+$ (**5**)	240 (2910)		
$[Fe^{II}(S^{Me2}N_4(tren))]^+$ (**1**)	262 (4700)	357 (sh)	410 (sh)
$[Co^{II}(S^{Me2}N_4(tren))]^+$ (**6**)	236 (4570) 358 (990)	454 (215)	600 (100)
$[Ni^{II}(S^{Me2}N_4(tren))]^+$ (**4**)	275 (2394)	410 (330)	
$[Cu^{II}(S^{Me2}N_4(tren))]^+$ (**7**)	216 (3280) 236 (3400)	380 (3340)	618 (315)
$[Zn^{II}(S^{Me2}N_4(tren))]^+$ (**8**)	219 (4800)		

It can be observed that each complex (except for Mn^{II} and Zn^{II}) displays LMCT transitions, attributed to a S-thiolate to metal transition in the visible region. The LMCT transitions shift to lower energy as the metal ion is changed from Fe^{II} to Cu^{II} and increase in intensity. Concerning the **B** series, the LMCT transitions are observed at higher energy with lower intensity with respect to the **A** series.[1] This is consistent with a lesser covalency for the alkyl-thiolate complexes compared to the aromatic-thiolate

complexes. As an example, the Cu-thiolate bond in series **B** is less covalent compared to that in the series **A** as attested by higher energy (26315 cm^{-1}) and lower extinction coefficient for the LMCT. Regarding the effect of the metal, the covalency follows the following trend for both series: Fe^{II} – thiolate < Co^{II} –thiolate < Ni^{II} –thiolate <Cu^{II}–thiolate.

Resonance Raman is another probe to estimate the covalency of M-thiolate bonds. Covalency can be related to a dominant strong peak at 400-421 cm^{-1}, associated with M-S stretching. A strong intensity of the signal is characteristic of a strong covalency. The Cu^{II}-thiolate bond presents the highest intensity in resonance Raman followed by the Ni-thiolate and the Co-thiolate consistently with the absorption properties of the complexes.

Although MCD is mainly used to assign absorption bands in UV-visible spectra, it also can give more insights into the covalency of the M-thiolate bond. Indeed, the MCD intensity of a LMCT transition related to M-thiolate bond is directly related to its covalency: the more negative, the more covalent.

Sulphur K XAS spectroscopy is certainly the most direct method to quantify the covalency of M-thiolate bonds. Two main regions can be observed in XANES spectra: the pre-edge and the edge. The sulphur K pre-edge corresponds to a transition from the 1s orbital of a sulphur atom to an unoccupied orbital bearing both S 3p and M 3d character. The pre-edge features are thus observed at lower energy with respect to the edge ones (between 2469.7-2471.4 eV and 2471.8-2272.8 eV, respectively for the **A** series as shown in Figure 6). The pre-edge energy is controlled by two factors: the ligand field and the Z_{eff} of the metal ion. Its energy position varies in the following trend: Cu^{II} < Ni^{II} < Co^{II}. Interestingly, the intensity of the S K-pre edge features provides an experimental measure of the thiolate covalency. In particular, the area of the pre-edge peak directly probes the M-thiolate covalency: the largest integrated area, the highest covalency. For the **A** series, the M-thiolate covalency follows this trend: Fe^{II} < Co^{II} < Ni^{II} < Cu^{II}, in agreement with the other spectroscopic investigations (see above).

The edge consists of a core 1s electron absorbing energy equal or greater than its binding energy (1s->4p). As observed for the pre-edge, S K-edge transitions shift to higher energy with the following trend: Zn^{II} < Mn^{II} < Fe^{II} < Co^{II} = Ni^{II} < Cu^{II}. This can be explained by a decrease in the negative charge on the sulphur atom resulting from a covalent donation from the thiolate to the metal 3d orbitals.

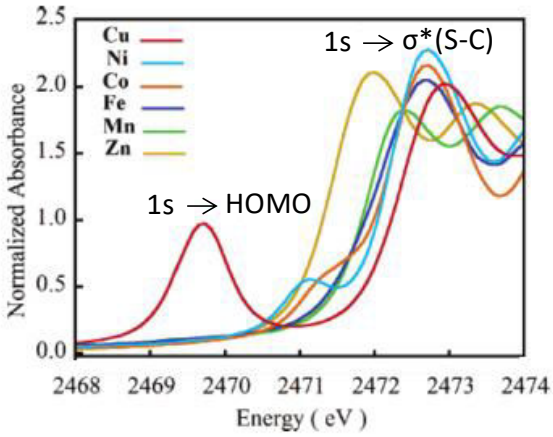

Figure 6. Normalized S K-edge XAS spectra of [M-S(C_6F_5)], (M = Mn^{II}, Fe^{II}, Co^{II}, Ni^{II}, Cu^{II} and Zn^{II}).

Sulphur K-edge XAS experiments also provide information on the oxidation state of the metal ions. In a simplified model, it is expected that the pre-edge transition shifts to lower energies when the oxidation state of the metal ion increases, because the M(3d) orbitals are stabilized in presence of a higher positive charge on M (the S(1s) energy remaining virtually unchanged).

1.3. Metal-thiolate complexes for efficient electron transfer.

Electron transfer is an essential biological process required for all catalytic redox centers which would be defunct without a steady, reliable and rapid supply in electron.[11] Transition metals, involved in multiple oxidation states, are well suited to fulfill this role. The most efficient centers involved in electron transfer contain at least one M-thiolate bond i.e. the blue copper sites (in cupredoxins), the mixed valent binuclear Cu_A site and iron-thiolate sulphur complexes, also called iron-sulphur clusters (in ferredoxins).

1.3.1. Copper-thiolate centers.

Biological copper-based electron transfer centers are divided into two families depending on their geometric and spectroscopic properties: mononuclear type 1 (T1) copper complexes present in blue copper proteins (plastocyanin and azurin, for example)[6] and dinuclear Cu_A found in cytochrome *c* oxidase (C*c*O) and in nitrous oxidase reductase (N_2OR) (Figure 7).[7,12,13] Both types are involved in rapid and efficient electron transfer and both present highly covalent copper-thiolate bond(s).[7,11] The oxidation state of the T1 sites cycles between Cu^{II} and Cu^{I}, while that of the bis(μ-thiolato) dicopper Cu_A complex between $Cu^{1.5}Cu^{1.5}$ and $Cu^{I}Cu^{I}$.

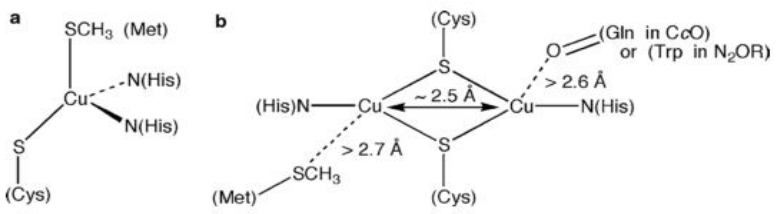

Figure 7. Schematic representation of (a) the mononuclear copper site in plastocyanine and (b) the binuclear Cu_A centers in cytochrome *c* oxidase (C*c*O) and in nitrous oxide reductase (N_2OR).[7]

The higher electron self-exchange rates (*k*) for Cu_A[14] compared to plastocyanine[15] (2.2 x 10^8 $M^{-1}.s^{-1}$ and 1.5 x 10^5 $M^{-1}.s^{-1}$, respectively) demonstrate that the electron transfer is more efficient in the dinuclear Cu_A site than in the mononuclear T1 site.[16,17] This has been rationalized by the fact that a better delocalization of the unpaired electron over the $\{Cu_2S_2\}^+$ core occurs in the oxidized state of Cu_A (due to thiolate bridges and to a direct Cu-Cu bond) with respect to the mononuclear T1 Cu^{II} site,[13] implicating a lower reorganization energy in the case of Cu_A. Blue copper proteins have high reduction potentials, in the range of +0.15 to +0.80 V *vs* NHE,[7] and the dinuclear Cu_A center a narrower redox potential range of +0.10 to + 0.42 V.[13,18,19]

Even if both T1 and Cu_A sites have attracted the attention of chemists, I decided to focus more on the dinuclear mimics due to the uncommon structure and exceptional efficiency of the Cu_A as electron transfer. In the 90's, the Tolman's group reported the first complex with a $\{Cu_2(\mu\text{-}SR)_2\}^+$core that mimics the structural and electronic properties of Cu_A. The low coordination number (<5), thiolate bridges and the atypical distorted trigonal geometry are factors that contributed to the stabilization of this delocalized mixed-valence compound.[20] However, it couldn't be stabilized at the Cu^ICu^I redox state (Figure 8).

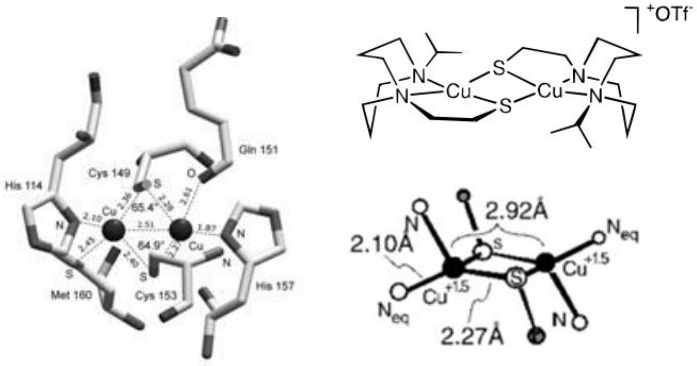

(a) (b)

Figure 8. (a) Structure of the Cu_A center of C*c*O issued from *Thermus thermophilus* in the mixed-valence state.[20] (b) Mixed valence model with a $\{Cu^2(\mu\text{-}SR)^2\}^+$ core.[80]

Duboc *et. al.* have isolated and characterized the first dicopper system with a $\{Cu_2S_2\}$ core stable at the two oxidation states (I,I) and (1.5, 1.5) well mimicking the biological Cu_A site (Figure 9).[17] They reported that the estimated *k* value of 1.37 x 10^6 $M^{-1}.s^{-1}$ indicates that the model could achieve electron transfer faster than the mononuclear T1 site such as that one in plastocyanin, but slower than Cu_A because of the lack of a Cu-Cu bond in the mixed valent state. The redox potential of -0.79 V *vs* Fc^+/Fc of the $Cu^{1.5}Cu^{1.5}/Cu^ICu^I$ redox system of the model complex is much lower than that of Cu_A, in accordance with weaker axial bonding interactions in the biological site due to the methionine ligand.[21]

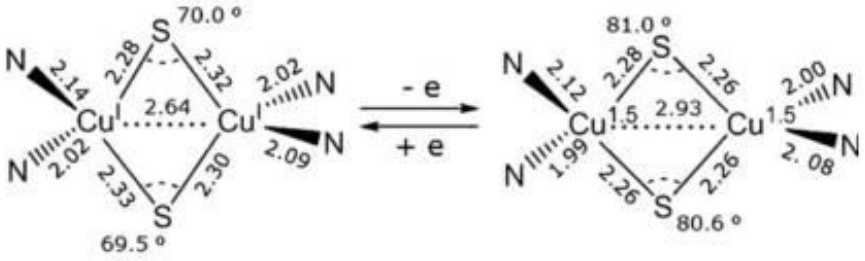

Figure 9. Representation with principal distances of the $\{Cu_2S_2\}$ core of the dinuclear copper complex model.[17]

They also reported a mononuclear Cu complex with the same dithiolate ligand, displaying a reversible Cu^{II}/Cu^{I} redox couple of -1.3 V vs Fc^{+}/Fc.[13] This low redox potential, compared to that of the dinuclear complex can be attributed to a difference in charge donation with two thiolate ligands per Cu in the case of the mononuclear complex vs only one thiolate ligand per Cu for the dimer (Figure 10).[17]

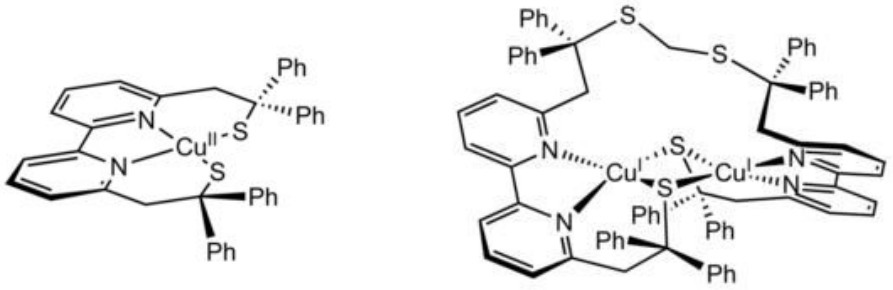

(a) (b)

Figure 10. (a) Mononuclear Cu complex and (b) a dinuclear Cu complex, models of Cu-based proteins.[13]

In order to evaluate the capability of both systems to transfer electrons (Figure 10), their reorganization energies (λ) have been calculated (parameters related to the electron transfer kinetics). The calculated λ values of 43.5 and 169.0 $kJ.mol^{-1}$ for the monomer and the dinuclear Cu complexes, respectively, are consistent with the fact that the mononuclear system is faster than the dinuclear one. Contrarily, in the biological system, it has been shown that the reorganization energy is larger for the blue copper proteins (21-81 $kJ.mol^{-1}$) than for Cu_A (15-50 $kJ.mol^{-1}$).[22,23] The rigidity of the dithiolate ligand prevents important structural modifications allowing a faster electron transfer for the mononuclear Cu complex with respect to the dinuclear Cu complex. On the other hand, the notable increase of the Cu-Cu distance during the oxidation process of the dinuclear Cu complex delays the electron transfer.[13]

1.3.2. [Fe-S] clusters.

[Fe-S] clusters are ubiquitous and origin from ancient prosthetic groups required for fundamental life processes.[24] These clusters are mainly involved in electron transfer, but also in substrate

binding/activation, iron-sulphur storage and regulation of gene expression. Their efficiency to transfer electrons arises from their ability to delocalize electron density over both Fe and S atoms. These [Fe-S] clusters are composed of Fe ions and inorganic sulphide (S^{2-}) with cysteinates generally completing tetrahedral coordination at each Fe site. The Fe-S bond is highly covalent and displays unexpected mechanical lability, i.e the Fe and S atoms can (de)coordinate very rapidly in physiological conditions. This lability can be quantified by the measure of the mechanical rupture force: the mechanical rupture force of the Fe-S bond (200 pN) is particularly low compared to the Au-S bond (while the covalency of these two bonds are comparable) or to the S-S bond (> 1 nN) perceived as a weaker covalent bond.[25] The clusters are generally bound to proteins via the cysteinate functions. There are two families of [Fe-S] centers: (i) the Fe monomers coordinated to 4 cysteines, commonly named rubredoxins (Rd), which do not properly belong to [Fe-S] clusters but will be considered as such in the following, [26] and (ii) the [Fe-S] clusters, present in ferredoxin proteins and composed of at least two Fe ions and two inorganic sulphides. There are several types of clusters depending on the number of Fe ions and S^{2-} ions, the coordination sphere of the Fe and the redox properties of the clusters: [2Fe-2S] and Rieske [2Fe-2S], [3Fe-4S], [4Fe-4S] and HiPiP [4Fe-4S] (High potential iron-sulphur protein) and [8Fe-7S] (Cluster P) consisting of two incomplete [4Fe-3S] cubane units linked by a six-coordinate sulphur atoms $(\mu^6\text{-S})^2$ present in nitrogenase (Figure 11). In all clusters, the oxidation state of the Fe ion cycles between +II and +III.

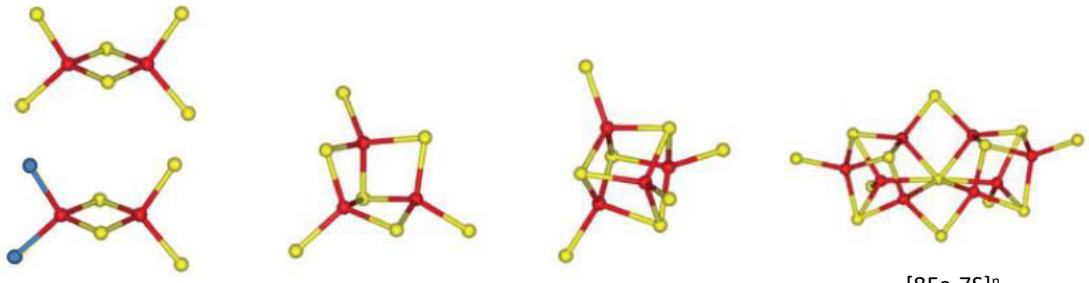

Figure 11. Structure, core oxidation states of crystallographically defined [Fe-S] clusters and their oxidation states. Iron is shown in red nitrogen in bleu and sulphur in yellow.[24] (The [Fe-S] cluster with two nitrogen atoms, corresponds to the Rieske protein).

There are two kinds of [2Fe-2S] clusters: (i) one with only S-donor atoms and (ii) one with two histidines instead of two cysteines leading to a N2S2 coordination sphere for one Fe site.[27] The latter corresponds to the Rieske protein (Figure 11). There are also two types of [4Fe-4S] clusters: the [4Fe-4S] clusters in which three S^{2-} can interact with the lateral peptidic chain via hydrogen bonding(s), and the more hydrophobic HiPiP [4Fe-4S] clusters.

[Fe-S] clusters mainly provide specifically one-electron transfer, except the double cubane [8Fe-7S] cluster found only in nitrogenase (P cluster) that can act as a two-electron carrier due to the presence of two associated clusters.[24,25] The electron transfer redox potential can vary from ~0.5 to ~-0.7 V *vs* NHE including the all types of clusters (Figure 12).[26] The redox potential range of clusters issued from the same families can be very large. Concerning the [2Fe-2S] clusters, the Rieske proteins display a higher redox potential range for $[2Fe\text{-}2S]^{2+/+}$ (-0.1-(+)0.4 V *vs* NHE) compared to those in ferredoxins (-0.4-(-)0.2 V *vs* NHE). This difference comes from the presence of two histidines in the Rieske proteins coordinated the one Fe instead of two cysteines in the ferredoxins, modifying the electronic environment of the overall cluster. Two different types of [4Fe-4S] clusters present also a large range of redox potentials but they involve different oxidation states: HiPiP (High potential iron-sulphur protein) $[4Fe\text{-}4S]^{3+/2+}$, $[4Fe\text{-}4S]^{2+/+}$ and thus share only one oxidation state, $[4Fe\text{-}4S]^{2+}$. As HiPiP $[4Fe\text{-}4S]^{3+/2+}$ clusters involved higher oxidation states, they are oxidized at higher redox potentials compared to $[4Fe\text{-}4S]^{2+/+}$ (Figure 12). The performance of the P cluster to transfer electron remains unclear. It is proposed that the P cluster can undergo different physiological oxidation states (+4, +3, +2). The redox potential of $[8Fe\text{-}7S]^{4+/3+}$ has been found to be pH dependent, while the redox potential of $[8Fe\text{-}7S]^{3+/2+}$ remains unchanged with pH variation, demonstrating that the protonation has no effect on the $[8Fe\text{-}7S]^{3+/2+}$ oxidation states.[28]

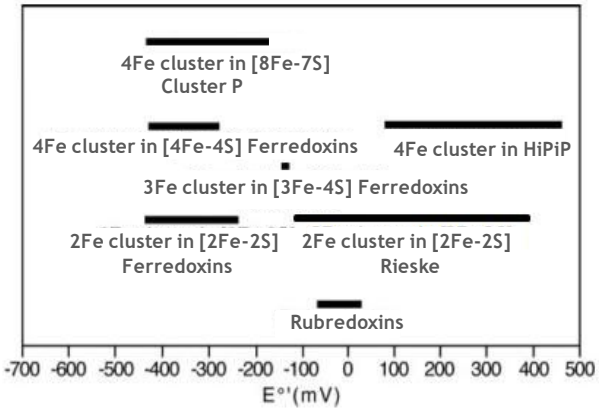

Figure 12. Experimental range of reduction potential (*vs* HNE) of various subclasses of Fe-S proteins ($Rd^{3+/2+}$, $[2Fe\text{-}2S]^{2+/+}$, HiPiP $[4Fe\text{-}4S]^{3+/2+}$, $[4Fe\text{-}4S]^{2+/+}$, $[3Fe\text{-}4S]^{+/0}$, $[8Fe\text{-}7S]^{4+/3+}$, $[8Fe\text{-}7S]^{3+/2+}$.[26,81,28]

Synthesis of low nuclearity iron-sulphur clusters permits to get more insights into the protein sites through the investigations of original structures and the examination of their reactivity. By chemical models, it has been demonstrated that the efficiency of the electron transfer rate is related to (i) the high-spin electronic configuration in two accessible oxidation states, (ii) the low inner-sphere barriers to electron transfer, and (iii) the easy structural conversion. These abilities are due to the weak-field properties of thiolate and sulphide, sulphide having the capacity to maintain the effective S^{2-} oxidation states even in the presence of one or several Fe^{III} ions.

The first synthetic models of the [FeS] proteins have been reported in the 1970s, especially with

mimics of rubredoxin. As an example, $[Fe(SCH_2CH_2OH)_4]^{-/2-}$ has a redox potential of -0.11 V in water, close to the 0.10 to –0.10 V range found of most native rubredoxin proteins.[37] The Meyer's group reported the best synthetic analogue of the Rieske cluster that undergoes fast concerted proton and electron transfer at a rate of 9.5 ±1.2 10^4 $M^{-1}.s^{-1}$ (Figure 13). The E_{pc} redox potential of this compound is -1.50 V vs Fc^+/Fc (converted at -0.73 V vs NHE) in MeCN and is shifted to -1.27 V in the presence of protons confirming their roles in the Rieske proteins.[38]

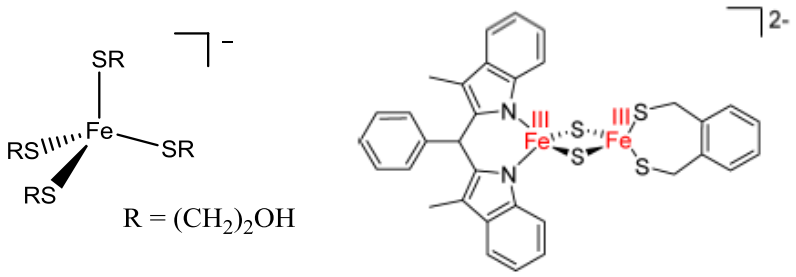

(a) (b)

Figure 13. (a) $[Fe(SCH_2CH_2OH)_4]^-$ complex,. Rubredoxin model.[37] (b) Rieske model: differic cluster $Fe_N^{III}Fe_S^{III}$.[38]

Models of the P cluster with different sizes and topologies have been synthesized in order to understand its peculiar properties.[39] Among these mimics, the group of Tatsumi reported a series of [8Fe-7S] clusters composed of two or four thiolate ligands (Figure 14). The redox properties of these clusters reveal two quasi-reversible one-electron reduction processes. The oxidation states involved in these processes are the same than in the P cluster, i.e. $6Fe^{II}2Fe^{III}$ for the oxidized form and $8Fe^{II}$ for the reduced one. This series exhibits two quasi-reversible one-electron processes: the redox potentials vary from -1.18 to -1.89 V *vs* Ag^+/Ag for the first redox system and to -1.51 to -2.25 V for the second redox system, the potential shifts depending on the coordination sphere of the clusters.[2] The replacement of neutral thiourea by thiolate anion results in a negative shift, because the negative charge makes the reduction more difficult. On the contrary, the substitution of the thiolate by amide ligand leads to a positive shift attributed to a strong σ/π donation from the amide ligand.

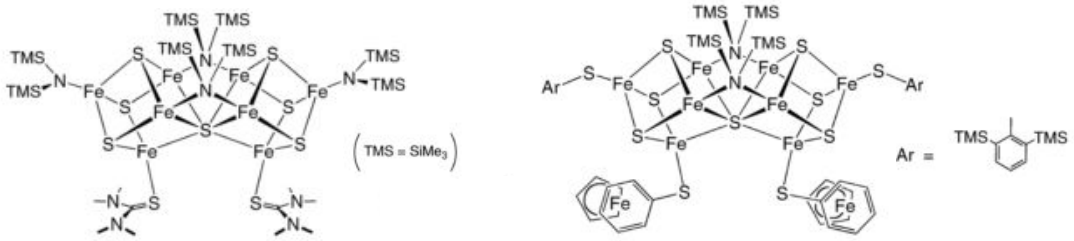

Figure 14. Examples of the P cluster models with two amides and two thiolates (left) and four thiolates (right).[2]

Holm and co-workers reported a series of [4Fe-4S] clusters and evidenced the existence of the [4Fe-

4S]^{0} oxidation state in the iron protein of nitrogenase, raising the issue of the physiological presence of such reduced state in proteins. However, the redox potentials of the synthetic [4Fe-4S]$^{+/0}$ are much smaller than those of the [4Fe-4S] clusters found in nitrogenases (≤ -1.5 V *vs* NHE and -0.46 V vs NHE, respectively).[40]

In the [NiFe] hydrogenase (see below), the active site formed by a NiFe complex site is close to an [4Fe-4S] cluster. Recently, a complete investigation including biochemical, electrochemical, spectroscopic and X-Ray crystallographic analysis on the O_2 tolerant [NiFe] hydrogenase has been carried out to evaluate the role this [FeS] cluster on its O_2 tolerance. It has been demonstrated that this proximal [FeS] cluster is notably different from the cluster present in the O_2-sensitive [NiFe] hydrogenase. While conventional [4Fe-4S] clusters are coordinated to four cysteine residues, that in the O_2 tolerant [NiFe] hydrogenase is ligated to six cysteine residues leading to an open and flexible cyst$_6$[4Fe-3S] configuration. The peculiarity of such a cluster is its ability to provide two electrons, while in regular [4Fe-4S] cluster could only be involved in one electron transfer. This ability seems to be a crucial factor in detoxification of O_2.[41]

1.4. Reactivity of thiolates in metal-thiolate complexes.

The coordination of an alkyl thiolate to a metal can lead to the activation of the sulphur atom for promoting different types of reactions including S-alkylation, S-oxygenation, S-nitrosylation and disulphide formation. While the three first processes require an additional substrate, i.e. alkyl derivatives, O_2 or derivative species and NO, respectively, the formation of metal-bound disulphides from metal-thiolate complexes only necessitates an intra- or intermolecular redox process. Therefore these two types of reactivity will be distinguished in the following part as “S-reactions” and “disulphide formation”.

1.4.1. S-reactions.

In Nature, it has been shown that the activation of small molecules such as alkyl derivatives, O_2 and derivatives or NO lead to these S-reactions catalyzed by specific active sites of metalloenzymes: S-alkylation[42] by the Ada protein or methionine synthase for examples, S-oxygenation by nitrile hydratases (NHase) or cysteine dioxygenase[43] and S-nitrosylation by haem proteins and type I Cu proteins (Figure 15). Interestingly, the activation of small molecules such as O_2 and derivatives or NO by metal-thiolate complexes can lead to products that differ from those generated *via* S-reactions. As examples, Ni superoxide dismutase[44] (SOD) or superoxyde reductase (SOR) react with the highly reactive $O_2^{\bullet-}$ without altering the cysteine residue(s) bound to their respective metal, while the metal-bound thiolates in the active site of the nitrile hydratases are oxidized using O_2 as oxidant. In

the same vein, NO can react with haem proteins possessing an axial cysteine to generate either metal-NO or metal-S(NO)-cysteine complexes.[45] What are the factors that govern such reactivity? The bio-inspired approach has been very fruitful to give insights to this fundamental question.

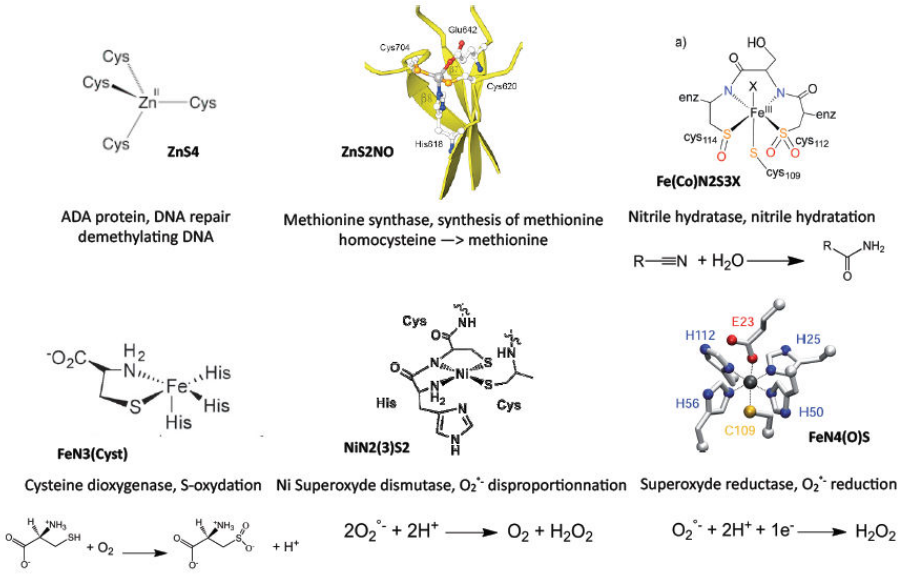

Figure 15. Active site and activity of enzymes discussed in this paragraph.

1.4.2. Activation of O_2 and derivatives.

While the mechanism of the NiSOD, at a molecular level, is not fully established, especially on the controversial question of an inner *versus* outer sphere reactivity, the characterization of Fe^{III}-hydroperoxo (Fe^{IV}-oxo) species during the catalytic cycle of the SOR (mutant) unambiguously demonstrates that $O_2^{\bullet-}$ is directly activated by the metal center (Figure 16).[46] The biomimetic models of the SOR developed by Kovacs et al. have shown that the Fe-bound cysteine is protected against S-oxygenation because the thiolate is located in a *trans* position with respect to the peroxo, promoting the protonation and release of H_2O_2 (Figure 16).[47] The same reactivity is also observed for the cytochrome P450, which reacts with O_2 and has an apical thiolate *trans* to the open coordination site (Figure 16). However the O-O cleavage promoted by the cysteinate is favored in the case of the CytP450, while for the SOR, the spin state of the Fe^{III}-hydroperoxo leads to a preferential Fe-O cleavage (Fe^{III}-hydroperoxo: $S = 5/2$ in SOR *vs* $S = 1/2$ in CytP450).

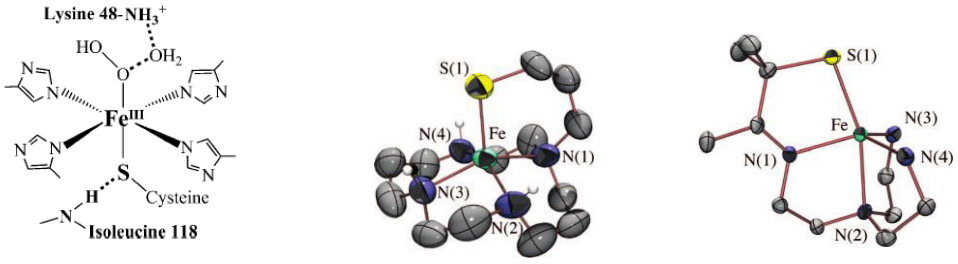

Figure 16. (left) Fe^{III}-hydroperoxo intermediate in SOR characterized by X-ray diffraction;[46] (middle) Fe^{II}-*trans*-thiolate SOR model; (right) Fe^{II}-*trans*-thiolate SOR model.[47] (*cis* and *trans* with respect to the vacant position)

The chemistry of the NiSOD has been explored *via* the development of either metallopeptides-based or small Ni-based mimics.[48–50] These works highlighted the role of the thiolates. In combination with the amine/amidate donor set, they tune the Ni^{III}/Ni^{II} redox couple to a physiological window of the superoxide redox potentials. Besides, their protonation leads to a stabilization of the S-based orbitals and thus, to a global decrease of the S-reactivity (Figure 17). Furthermore, kinetic studies of mimics in the presence of H_2O_2 have revealed that the S-oxygenation is kinetically limited and thus inefficient in physiological conditions.[44]

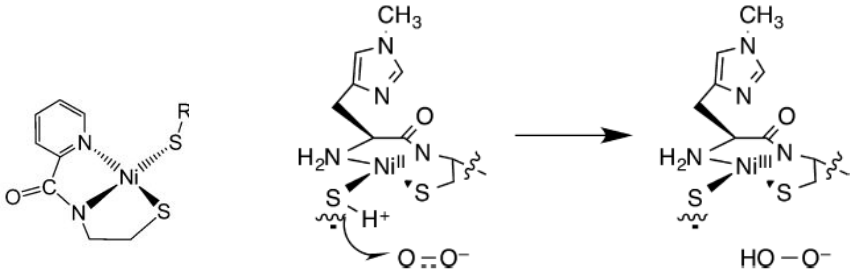

Figure 17. (left) Example of a Ni-based mimic of the NiSOD;[48–50] (right) metallopeptide based mimic of the NiSOD with the proposed role of the protonation of one cysteine residue during the catalytic cycle.[48]

NHase requires an activation process to be active towards the hydration of nitriles, involving the S-oxygenation of two metal (Fe or Co)-bound cysteinates into sulphinate and sulphenate species, respectively. This unusual reactivity combined with the unprecedented structure of the corresponding active sites has attracted the attention of chemists.[51,52,53] Based on these results, it is suggested that the final active complex is obtained after the sequential S- oxygenation of each of the cysteinate with an intermediate species containing one sulphinate and one thiolate (Figure 18). Such conclusion corroborates the current proposed mechanism for nitrile hydratation catalyzed by the NHases, in which the sulphenate is directly involved in the reaction as nucleophile agent, the O-atom of the SO^- group being thus exchangeable (Figure 18).[54,55] It was also evidenced that the oxidized thiolate ligands are crucial to maintain the low spin state of the metal, which is essential for the binding and activation of nitrile substrates. On the other hand, the S-oxygenation mechanism is still

not well understood because this complicated maturation process involves several protein partners and neither their role nor their intervention sequences are known.

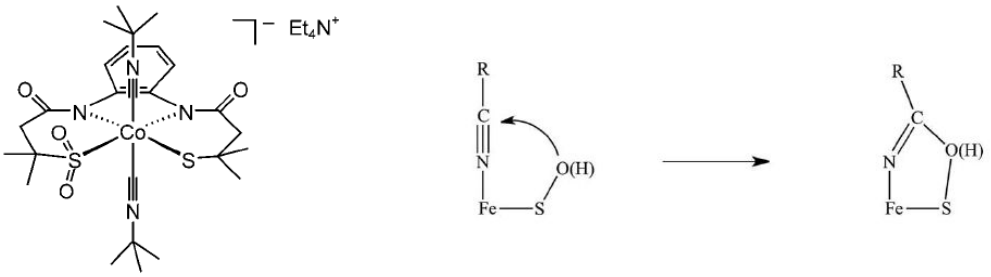

Figure 18. (left) Example of a Co-based mimic of the NHase highlighting the sequential S- oxygenation process,[52] (right) proposed mechanism for the NHase evidencing the role of the sulphenate as nucleophile agent.[55]

1.4.3. NO activation.

NO is an important gasotransmitter involved in a variety of physiological processes. In particular, NO is implicated in dynamic post-translational regulation of proteins via S-nitrosylation that requires one electron oxidation of the complex formed between the thiol and NO. It has been proposed that redox active metals could act as electron acceptors. While the direct binding of NO to the metal before its subsequent reaction with the thiolate has been largely described as in the case of haem proteins, the reversible insertion of NO into a Cu-bound thiolate *via* the generation of the unprecedented [Cu^{I}](κ^1-N(O)SR) motif has been recently reported (Figure 19).[56,57] This demonstrates that metal-bound thiolate could directly activate NO to form S-nitrosylated products. The reversibility of the process suggests physiological signaling action of NO to control the electron transfer at copper-thiolate redox center

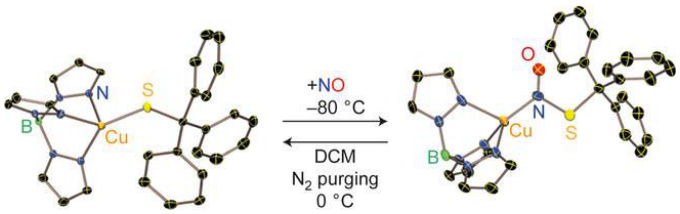

Figure 19. Reversible insertion of NO into a Cu-bound thiolate *via* the generation of the unprecedented [Cu^{I}](κ^1-N(O)SR) motif.[56]

1.4.4. S-alkylation.

In biology S-alkylation, mainly mediated by Zn-containing enzymes, is fundamental as it is involved in the biosynthesis of the methionine and in DNA repair, for instance. S-alkylation exploits the nucleophilicity of the thiolate sulphur atom and two different mechanisms can be envisaged with respect to the charge of the complex: (i) a dissociative pathway for anionic species, i.e. the metal-sulphur bond is split, followed by a SN_2 reaction and (ii) an associative pathway for neutral species, i.e. a SN_2 reaction involving the metal-bound thiolate. The reactivity of synthetic metal-thiolate

complexes towards S-alkylation has been extensively investigated (see an example in Figure 20) especially to analyze the covalency of the metal-thiolate bond as it is directly related to the nucleophilicity of the thiolate in order to understand why the Nature preferably chooses Zn^{II} for such reactivity. These studies have highlighted two points. First, in series of complexes, the kinetics of the reaction is always better or comparable with Zn^{II} compared to other metals such as Ni^{II}, Co^{II}, Fe^{II}, Cu^{II}. Second, the decoordination of the alkylated product rapidly occurs after S-alkylation predominantly with Zn^{II}, while it remains bound to the other metals.[13,58,59]

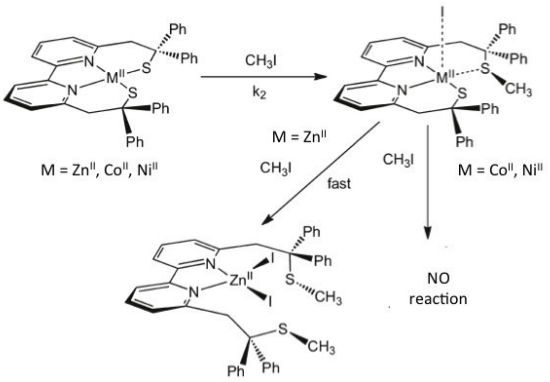

Figure 20. S-alkylation processes with a series of dithiolate complexes with M = Zn^{II}, Co^{II} and Ni^{II}.[13,58]

1.4.5. Metal-based disulphide formation.

Thiolate/disulphide interconversion is involved in many essential physiological processes including folding of proteins and control of the reactivity of a protein as a signaling factor. More recently, the idea that metal ions, especially Cu, can be involved in such a process has emerged. It has been evidenced that Sco proteins are implicated in the assembly of the Cu_A complex of the human mitochondrial cytochrome c oxidase but can also act as redox signaling and regulation of copper homeostasis in eukaryotes via a proposed Cu^{II}-thiolate/ Cu^{I}-disulphide interconversion.[60] Besides, it is also argued that the β-amyloid peptide implicated in Alzheimer's disease predominantly binds Zn^{II} in non-pathologic conditions leading to a normal concentration in reactive oxygen species owing to a transmetallation process. This process occurs *via* the interaction of a Cu^{II}-β-amyloid and a Zn^{II}-containing metallothionein generating a Zn^{II}-β-amyloid and a Cu^{I}-containing metallothionein, in which the cysteine residues have been oxidized into disulphide in order to sequester Cu. Such biological observations and hypothesis pushed chemists to better understand the role of the metal and the external stimulus to control the thiolate /disulphide interconversion. Because part of the work presented in this thesis deals with a related project, this part is developed in the introduction of chapter III (see below).

1.5. Metal-thiolate/sulphide centers for the activation of small molecules.

M-S (S= thiolate/sulphide) bond can be involved in the active site of enzymes responsible for the activation of small molecules, including enzymes implicated in the activation of O_2 and derivatives (see above), of N_2 by the nitrogenase or N_2O by the N_2O reductase, of CO and/or CO_2 by the CO dehydrogenase (CODH) and acetyl CoA synthase (ACS), and of H_2 and H^+ by the hydrogenases (Figure 21). While a short description of these enzymes is proposed below, the [NiFe] hydrogenase is introduced in chapter I in more details.

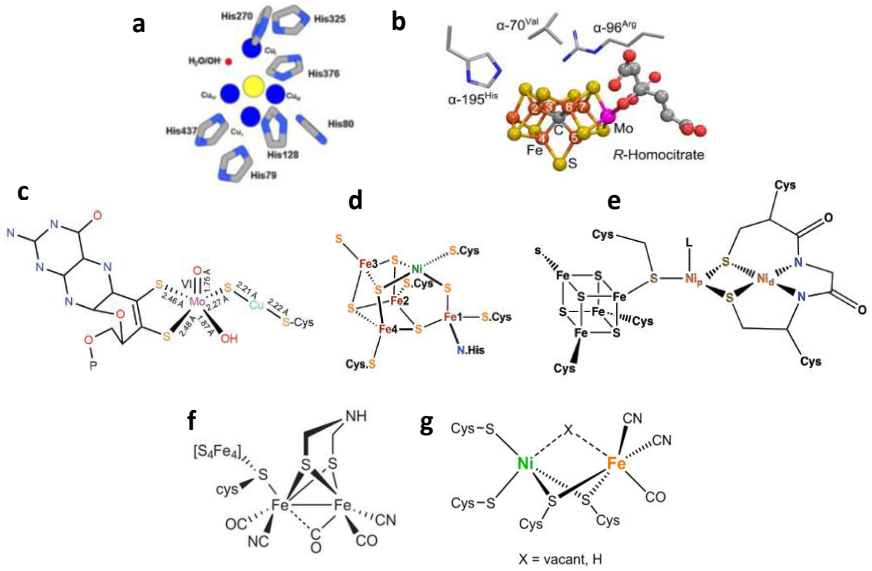

Figure 21. Representation of the enzymes involved in the cycle of nitrogen (up), carbon (middle) and hydrogen (down): a) N_2OR,[61] b) nitrogenase,[62] c) Mo/Cu CODH,[63] d) Ni/Fe CODH,[63] e) ACS,[64] f) [Fe-Fe] hydrogenase[65] and g) [NiFe] hydrogenase.[66]

1.5.1. N_2O and N_2 reduction

The different biochemical processes of the global nitrogen cycle are performed by bacteria in their effort to harvest energy or to accumulate useful forms of nitrogen for their growth. Among these transformations, two occur by means of metalloenzymes containing metal-thiolate/sulphide bonds in their active sites, i.e.: i) the reduction of nitrous oxide (N_2O) to molecular nitrogen (N_2) by nitrous oxide reductases (N_2OR)) and ii) the "fixation" of N_2 into ammonia (NH_3) by nitrogenases (Equation 1 and 2, respectively) shown in Figure 21.

$N_2O + 2H^+ + 2e^- \rightarrow N_2 + H_2O$ (Equation 1)

$N_2 + 6H^+ + 6e^- \rightarrow 2NH_3$ (Equation 2)

N_2OR contains two copper sites: a binuclear Cu_A electron transfer site, and an unprecedented tetranuclear copper sulphide-bridged cluster called 'Cu_Z', (Figure 21a) bound to seven His residues, which is believed to be the site of N_2O binding and reduction. The presence of a sulphide in the active

site may be responsible for (i) promoting electron delocalization, which should stabilize the transient oxidized state, thus contributing to lower the reorganization energy of the redox processes accompanying catalysis and (ii) placing the coppers in a geometrical arrangement well adapted to favor the bent geometry of the bridged N_2O molecule. Investigations on model complexes helped to get insights into catalytic intermediates of N_2OR and to understand structure–function relationships.[61,67]

The Mo-dependent nitrogenase[68] (Figure 21b) is a two-component system: the MoFe protein contains the iron–molybdenum cofactor (FeMoco) as an unprecedented [Fe_7CS_9Mo;homocitrate] cluster, identified as the catalytic site, and a P-cluster, which shuttles electrons from the Fe protein to FeMoco. The seven iron centers of the FeMoco are all 4-coordinated and their trigonal prismatic arrangement generates three open Fe_4S_4 faces, one of which is proposed to host the N_2 binding and reduction site. The currently proposed mechanism for N_2 binding and reduction to NH_3 by FeMoco involves a key intermediate generated by a transient protonation of the sulphide ligands, so that they could act as proton relays assisting ammonia formation (Figure 22). Sulphides are also key players to assure a geometric and electronic communication between multiple Fe centers, which may facilitate cooperation between multiple Fe centers for labilizing and breaking the N-N bond.

Only recently the first Fe model complexes containing sulphur ligands that are also able to bind and activate N_2 have been described, with aryl thiolate being the best reported models for the sulphides of FeMoco (Figure 22).

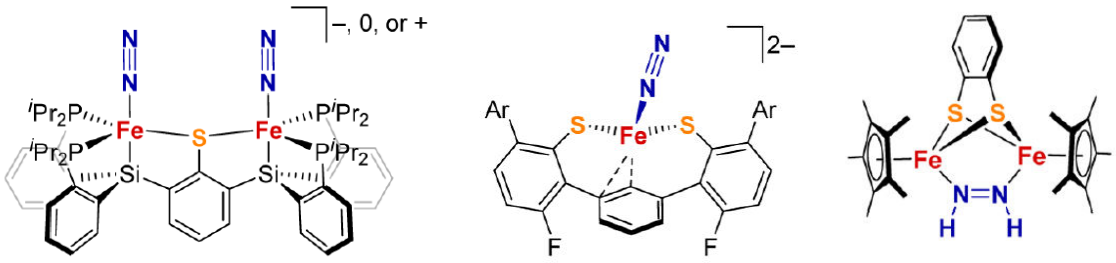

(a) (b) (c)

Figure 22. Thiolate–iron–N_2 (or related) model complexes.[39]

The first example of a thiolate–iron–N_2 species is the binuclear complex of Figure 22a, stable in three oxidation states, which generates ammonia after treatment with excess KC_8 and $[H(OEt2)_2]BArF_4$. A terminal mononuclear Fe-N_2 complex (Figure 22b) features partial coordination of an arene group, thus displaying close coordination of two S and one C: this is also a plausible N_2 binding mode for FeMoco. Other thiolate-iron complexes, as the thiolate-bridged one of Figure 22c are able to activate and reduce diazene and hydrazine, even if they don't bind N_2.

However, synthetic model chemistry is only in its first stages in the attempt of fully understanding the N_2 binding and reduction process by FeMoco and of identifying reaction intermediates.

1.5.2. CO_2 and CO activation

The oxidation of CO to CO_2 (Equation 3) allows organisms to grow on CO atmosphere as a sole source of carbon and energy. This process is catalyzed, close to the thermodynamic potential, by two different forms of CO dehydrogenase (CODH), one present in aerobic bacteria (Mo/Cu-containing CODH), and the other one active in anaerobic bacteria (Ni/Fe-containing CODH) (Figure 21).[69]

$CO + H_2O \rightarrow CO_2 + 2H^+ + 2e^-$ (Equation 3)

Anaerobic CODH is frequently associated to acetyl-CoA synthase (ACS) in a bifunctional cluster (CODH/ACS) that catalyzes C–C bond formation from a methyl group and the carbon monoxide generated from CO_2 by CODH, generating the metabolic intermediate acetyl-CoA from the Coenzyme A (CoA) (Equation 4).[64]

$CO + CH_3\text{-}Co + CoA \rightarrow CH_3\text{-}CO\text{-}CoA$ (Equation 4)

Remarkably, all these enzymes contain metal-bound thiolates and/or sulphides in their active sites. The bridging sulphide in the Mo/Cu CODH[69] (Figure 21c) between the two metallic sites, is proposed to be the key player to achieve the high delocalization between the two metal centers forming strongly covalent Mo-S and Cu-S bonds. In the Ni/Fe CODH (Figure 21d), the thiolates and sulphides from the cubane may contribute to an apparent planar T-shaped geometry. In the active site of ACS, the A-cluster (Figure 21e), the nickel Ni_p center is thiolate-bridged to a Fe_4S_4 cluster and to the second nickel Ni_d site, forming a T-shaped tris-thiolate coordination capable of coordinating the CO substrate. Due to the three coordinated thiolates, Ni_P is in a favorable environment to coordinate CO and to activate it.

Even if many structural models have been reported for aerobic CODH, no reactivity towards CO has been reported so far, and no functional models that include a sulphur-rich coordination environment. Concerning biomimetic chemistry of Ni/Fe-CODH, the obtaining of Ni-Fe heterometallic clusters has proven to be a big synthetic challenge. Few examples of $NiFe_3S_4$ cubane complexes are now reported in the literature, including the two most relevant examples that are shown in Figure 23.[64] However, all these clusters lack a pendant iron like that of the C-cluster. In addition, none of the reported model complexes has yet been reported to be active for catalytic interconversion between CO and CO_2

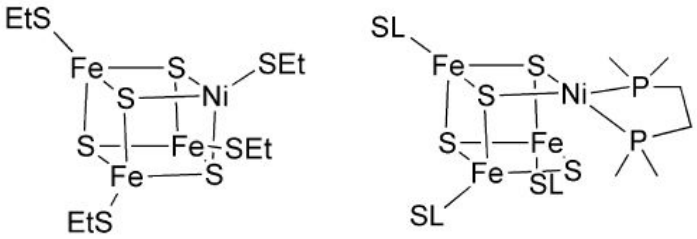

Figure 23: Most relevant structural models the Ni/Fe-CODH active site.[64]

Biomimetic studies of the active site of ACS have focused on reproducing the Ni_p or the bimetallic Ni_p–Ni_d environment, omitting the $[Fe_4S_4]$ complex.[64] The ensemble of these studies confirms the chemical inertness of Ni_d and the high reactivity (substrate binding, reducibility) of the labile Ni_p. Among the reported model complexes, the dinuclear Ni complex of Figure 24a includes one nickel atom in a bis-amide/bis-thiolate environment that structurally mimics Ni_d, and a second Ni center (in a P2S2 coordination sphere) that reproduces in part the reactivity of Ni_p. Indeed, its reduced $Ni^{I}Ni^{II}$ form can bind CO and be further reduced to the $Ni^{0}Ni^{II}$ state. As a further step, the $Ni^{I}Ni^{II}$ complex of Figure 24b was shown to accept a methyl group from methylcobaloxime to generate a thioether upon reaction with CO, thus mimicking the reaction catalyzed by the acetyl-CoA synthase.[70]

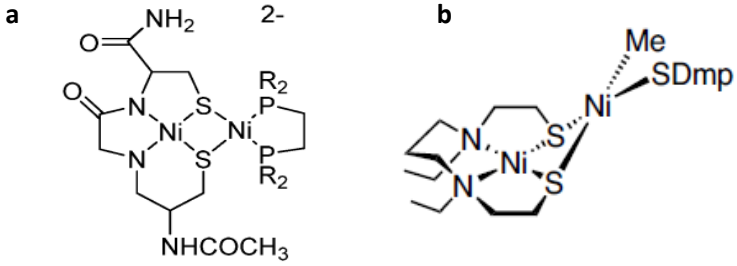

Figure 24. Most relevant structural/functional model of the ACS enzyme.[64,70]

1.5.3. H_2 and H^+ activation.

Hydrogenases play a key role in microbial energy metabolism,[71] since they catalyze the reversible reduction of protons into hydrogen (H_2). The multiple classes of hydrogenases are divided into three main families, based on the metal content of their active site, namely the [Fe], [FeFe] and [NiFe] hydrogenases. This section will mainly focus on the [FeFe] hydrogenase, because the [Fe]-hydrogenase [NiFe] hydrogenase will be fully described in the introduction part of chapter I. The [Fe] hydrogenase will be not further discussed in the context of this tutorial because it follows a complete different mechanism than that proposed for the two other families of hydrogenases. In the dinuclear Fe center (Figure 21), the two Fe ions are bridged by an unprecedented azadithiolate ligand in biology. The coordination sphere of both metallic ions is completed by carbonyl and cyanide ligands. A [4Fe-4S] cluster is linked to the diiron unit by a cysteinyl residue. Due to its uncommon

coordination environment, this active site has attracted attention of chemists that have developed number of diiron dithiolate mimics with the following aims: (i) synthesis of structural models, (ii) development of bio-inspired electro- and photocatalysts for H_2 production, (iii) investigation of the catalytic mechanism and (iv) biomimicry of intermediates such as hydride species.[72] In 2001, Rauchfuss reported the first diiron dithiolate complex capable to reduce protons electrochemically. This has opened the path to the synthesis of structural and/or functional model complexes. [73]

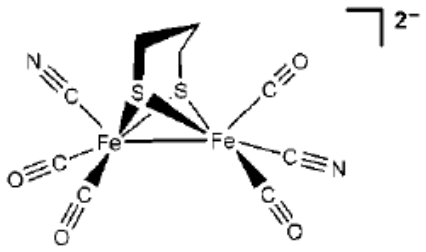

Figure 25. First diiron dithiolate complex capable of producing H_2, electrochemically.[73]

Currently, all diiron dithiolate models require significantly larger driving force and display lower activity than the [FeFe] hydrogenases for electrochemical production of H_2. This trend can be explained by differences between models and enzyme in structure and mechanism including (i) the replacement of CN^- by CO or phosphine derivatives that lowers the basicity of the Fe ions and then the stability of hydride species and (ii) the lack of an [4Fe-4S] cluster at close proximity to the diiron site, raising the importance of such a unit in the efficiency of this enzyme.

Plan of the thesis.

The purpose of the work described in this thesis is the synthesis and the characterization of bio-inspired molecular complexes containing metal-alkyl thiolate bonds for either modeling the active site of enzymes that activate small molecules, understanding the factors that influence the reactivity of the bound thiolates for thiolate/disulphide interconversion or defining the structural parameters that control the electronic and magnetic properties of the corresponding complexes. As described above, the synthesis of controlled nuclearity, low oxidation state complexes with alkyl-thiolate ligands is challenging due to their sensitivity to oxidation (S-oxygenation, disulphide bond formation). In this context, the tetradentate N2S2 (LS) ligand has been used (Figure 26) because it contains (i) the non-innocent bipyridine unit, well known to stabilize different oxidation states of a metal center, (ii) bulky substitutions on the α-carbon of the thiolate donor atoms to protect them and (iii) alkyl thiolates to correctly reproduce the redox and electronic properties of the M-S bonds involving cysteines.

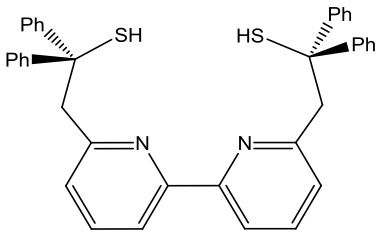

Figure 26. A schematic diagram of the ligand used in this thesis, LS

Before my arrival, researches have been carried out using this LS ligand in our group, with Cu^{II},[13,17] Ni^{II},[74,75] Zn^{II},[76] Co[17] and V[77] derivatives. From these studies, the corresponding complexes were used as structural mimics for thiolate containing metalloproteins or to develop new catalysts. These compounds were able to mimic some specific properties such as electronic properties and reactivity.

This thesis details the continuation and extension of the previously reported work with the activation of small molecules and the description of factors that influence the magnetic properties of such complexes. This manuscript is divided into four chapters. The two first chapters deal with activation of small molecules (H^+ and O_2, respectively), the third with the reactivity of metal bound thiolate toward disulphide formation, while the last reports on the magnetic properties of an unusual series of intermediate spin Co^{III} complexes.

The first chapter reports on the synthesis and characterization of two $Ni^{II}Fe^{II}$ complexes, along their catalytic activity toward proton reduction. The goal of this chapter was to mimic the active site of the [NiFe] hydrogenase and to understand the mechanism of its catalytic activity. A mechanistic investigation, using electrochemistry, UV-Vis, EPR, NMR, Mossbauer spectroscopies and computational calculations, has been carried out on the intermediate species involved during the catalysis. The inhibition of the catalytic activity in the presence of CO has been also investigated for both complexes.

Chapter II concerns the activation and the catalytic reduction of O_2 by a dinuclear Mn^{II}-thiolate complex to understand which factors influence a 2-electron *vs* 4-electron reduction promoting the production of H_2O_2 or H_2O, respectively. The O_2 activation and reduction pathways, under both stoichiometric and catalytic conditions, have been investigated. Finally, different high valent complexes arising from O_2 activation have been characterized and their role in the O-activation mechanism is discussed.

Chapter III reports the synthesis and characterization of a new dinuclear disulphide-bridged Mn^{II} complex, isostructural to a Co^{II}-parent compound.[78] Its reactivity with halide anions (in particular with iodide) has been investigated. The coordination of the halide to the metal ion induces a

disulphide to thiolate conversion with the concomitant oxidation of the metal from M^{II} to M^{III}, leading to mononuclear halide Co^{III} and Mn^{III} complexes. In combination with theoretical calculations, the reactivity of the cobalt and manganese systems are compared and discussed.

Chapter IV focuses on the magnetic properties of the penta-coordinated halide Co^{III} complexes described in chapter IIII. With the combination of experimental and calculations the intriguing magnetic behaviors of these intermediate S = 1 Co^{III} compounds have been rationalized and compared with the isostructural iodide Mn^{III} complex, which display an S = 2 ground spin state.

The crystallographic structures have been resolved by Jacques Pécaut (CEA Grenoble) and the structure of **$Ni^{II}Fe^{II}Cp^*$** by Christian Philouze (Université Grenoble Alpes). All reported quantum chemical calculations have been carried out in collaboration with Maylis Orio (Université Aix-Marseille, iSm2). In chapter II, the synthesis and the characterization of initial dinuclear Mn^{II} and Mn^{III} complexes have been carried out by Marcello Gennari (Université Grenoble Alpes, DCM). In chapter I, Mossbauer measurements have been performed by the Franc Meyer's group (Germany, Institute für Anorganische Chemie). The foot-of-the-wave analysis has been achieved by Nicolas Queyriaux and Vincent Artero (Université Grenoble Alpes, LCBM). XAS measurements for **Mn^{II}_2SH**, **Mn^{III}_2OH** have been performed by Serena DeBeer (Germany, MPI für Chemische Energiekonversion) and for **$Mn^{IV}_2(O)_2$** by Kallol.Ray.(Germany, Humboldt-Universität, Berlin) Magnetic measurements have been achieved by Rodolphe Clérac (Université de Bordeaux I)

References

1. Brines, L. . M. *et al. Inorg. Chem.* **2007**, *46*, 9267–9277 .
2. Ohki, Y. *et al. J. Am. Chem. Soc.* **2009**, *131***,** 13168–13178 .
3. Garner, C. D. *J. Chem. Soc. Dalt. Trans.***1997***,* 3903–3908.
4. Thomson, A. J. & Gray, H. B. *Curr. Opin. Chem. Biol.* **1999**, *2,* 155–158.
5. Solomon, E. I., Gorelsky, S. I. & Dey, A. *J. Comput. Chem.* **2006**, *27***,** 1415–1428.
6. Solomon, E. I., Szilagyi, R. K., George, S. D. & Basumallick, L. *Chem. Rev.* **2004**, *104***,** 419–458.
7. Belle, C., Rammal, W. & Pierre, J. L. Sulfur ligation in copper enzymes and models. *J. Inorg. Biochem.* **2005**, *99***,** 1929–1936.
8. Matsunaga, Y. *et al. SInorg. Chem.* **2005**, *44***,** 325–335.
9. Fox, D. C., Fiedler, A. T., Halfen, H. L., Brunold, T. C. & Halfen, J. A. E. *J. Am. Chem. Soc.* **2004**, *126***,** 7627–7638 .
10. Gorelsky, S. I. *et al. Inorg. Chem.* **2005***, 44,* 4947–4960 .
11. Wilson, T. D., Yu, Y. & Lu, Y. *Chem. Rev.* **2013**, *257***,** 260–276 .
12. Kroneck, P. M. H. *et al.FEBS Lett.* **1990**, *268,* 274–276.
13. Gennari, M., Pécaut, J., Collomb, M.-N. & Duboc, C. A. *Dalt. Trans.* **2012**, *41,* 3130.
14. Slutter, C. E. *et al.Inorganica Chimica Acta*. **1996**, *243,* 141–145.
15. Jensen, M. R., Hansen, F. & Led, J. J. *J. Am. Chem. Soc.* **2002**, *124,* 4093–4096.
16. Farver, O., Lu, Y., Ang, M. C. & Pecht, I. *Proc. Natl. Acad. Sci. U. S. A.* **1999**, *96,* 899–902.
17. Gennari, M. *et al. Angew. Chem. Int. Ed.* **2011**, *50,* 5662–5666.

18. Neehaul, Y. *et al. Biochim. Biophys. Acta - Bioenerg.* **2012**, *1817,* 1950–1954.
19. Sun, D., Wang, X. & Davidson, V. L. *Arch. Biochem. Biophys.* **2002**, *404,* 158–162.
20. Houser, R. P., Young, V. G. & Tolman, W. B. A. *J. Am. Chem. Soc.* **1996**, *6,* 10745–10746.
21. Ledesma, G. N. *et al. J. Am. Chem. Soc.* **2007**, *129,* 11884–11885.
22. Olsson, M. H., Ryde, U. & Roos, B. O. *Protein Sci.* **1998**, *7,* 2659–2668.
23. Olsson, M. H. M. & Ryde, U. *J. Am. Chem. Soc.* **2001**, *123,* 7866–7876.
24. Johnson, D. C., Dean, D. R., Smith, A. D. & Johnson, M. K. *Annu. Rev. Biochem.* **2005**, *74,* 247–281 ().
25. Zheng, P. & Li, H. *J. Am. Chem. Soc.* **2011**, *133,* 6791–6798.
26. Beinert, Herlmut. *Jbic* **2000**, *5,* 2–15.
27. Ali, M. E., Staemmler, V. & Marx, D. *Phys. Chem. Chem. Phys.* **2015**, *17,* 6289–6296.
28. Lanzilotta, W. N., Christiansen, J., Dean, D. R. & Seefeldt, L. C. *Biochemistry,* **1998**, *37,* 11376–11384.
29. Rao, P. V. & Holm, R. H. *Chem. Rev.* **2004**, *104,* 527–560.
30. Albers, A. *et al.* F*J. Am. Chem. Soc.* **2014**, *136,* 3946–3954.
31. Čorić, I. & Holland, P. L. *J. Am. Chem. Soc.* **2016**, *138*, 7200-7211.
32. Chaoyin Zhou, James W. Raebiger, Brent M. Segal, R. H. H. *Inorganica Chim. Acta.* **2000**, *302,* 892 – 902.
33. Fritsch, J., Lenz, O. & Friedrich, B. *Nat. Rev. Microbiol,* **2013**, *11,* 106–114.
34. Parkin, G. *Chem. Commun.* **2000**, 1971–1985
35. Jiang, Y., Widger, L. R., Kasper, G. D., Siegler, M. A. & Goldberg, D. P. *J. Am. Chem. Soc.* **2010**, *132,* 12214–12215.
36. Herdt, D. R. & Grapperhaus, C. A. *Dalt. Trans.* **2012**, *41,* 364–366.
37. Weichsel, A. *et al. Proc. Natl. Acad. Sci. U. S. A.* **2005**, *102,* 594–599.
38. Bonnot, F. *et al. Angew. Chem. Int. Ed.* **2014**, *53,* 5926–5930.
39. Kovacs, J. A. & Brines, L. M. *Acc. Chem. Res.* **2007**, *40,* 501–509.
40. Shearer, J. *Acc. Chem. Res.* **2014**, *47,* 2332–2341.
41. Shearer, J., Peck, K. L., Schmitt, J. C. & Neupane, K. P. *J. Am. Chem. Soc.* **2014**, *136,* 16009–16022.
42. Broering, E. P., Truong, P. T., Gale, E. M. & Harrop, T. C. *Biochemistry* **2013**, *52*, 4–18.
43. Dutta, A. *et al.* S *Inorg. Chem.* **2013**, *52,* 5236–5245.
44. Bourles, E., de Sousa, R. A., Galardon, E., Giorgi, M. & Artaud, I. *Angew. Chem. Int. Ed.* **2005**, *44,* 6162–6165.
45. Kovacs, J. A. *Chem. Rev.* **2004**, *104,* 825–848.
46. Yamanaka, Y. *et al. Angew. Chem. Int. Ed.* **2015**, *54,* 10763–10767.
47. Light, K. M., Yamanaka, Y., Odaka, M. & Solomon, E. I. S *Chem. Sci.* **2015**, *6,* 6280–6294.
48. Zhang, S., Melzer, M. M., Sen, S. N., Çelebi-Ölçüm, N. & Warren, T. H. *Nat Chem.* **2016**, *8,* 663–669.
49. Tian, S. *et al. Nat Chem*. **2016**, *8,* 670–677.
50. Gennari, M. *et al. Inorg. Chem.* **2011**, *50,* 10047–10055.
51. Fox, D. C., Fiedler, A. T., Halfen, H. L., Brunold, T. C. & Halfen, J. A. *J. Am. Chem. Soc.* **2004**, *126,* 7627–7638.
52. Banci, L., Bertini, I., Cavallaro, G. & Ciofi-Baffoni, S. *FEBS J.* **2011**, *278,* 2244–2262.
53. Pauleta, S. R., Dell'Acqua, S. & Moura, I. *Coord. Chem. Rev.* **2013**, *257,* 332–349.
54. Hoffman, B. M., Lukoyanov, D., Yang, Z. Y., Dean, D. R. & Seefeldt, L. C. The next stage. *Chem. Rev.* **2014**, *114,* 4041–4062.
55. Majumdar, A. *Dalt. Trans.* **2014**, *43,* 12135-12145.
56. Can, M., Armstrong, F. A. & Ragsdale, S. W. *Chem. Rev.* **2014**, *114,* 4149–4174.
57. Hunt, N. T., Wright, J. A. & Pickett, C. *Inorg. Chem.* **2016,** *55,* 399-410.
58. Canaguier, S., Artero, V. & Fontecave, M. *Dalt. Trans.* **2008***, 25,* 315–325.
59. Solomon, E. I. *et al.*. *Chem. Rev.* **2014**, *114***,** 3659–3853.
60. Hoffman, B. M., Lukoyanov, D., Yang, Z.-Y., Dean, D. R. & Seefeldt, L. C. *Chem. Rev.* **2014**, *114,*

4041–4062.
61. Hille, R., Dingwall, S. & Wilcoxen, J.*, J. Biol. Inorg. Chem.* **2015**, *20,* 243–251.
62. Ito, M., Kotera, M., Matsumoto, T. & Tatsumi, K. *Proc. Natl. Acad. Sci. U. S. A.* **2009**, *106,* 11862–11866.
63. Tard, C. & Pickett, C. J. *Chem. Rev.* **2009**, *109,* 2245.
64. Wang, N., Wang, M., Chen, L. & Sun, L. *Dalt. Trans.* **2013**, *42,* 12059.
65. Gloagueun, F, Lawrence, J. D. & Rauchfuss, T. B. *J. Am. Chem. Soc.* **2001**, *123*,9476–9477.
66. Gennari, M. *et al. Inorg. Chem.* **2010,** *49,* 6399–6401.
67. Gennari, M. *et al. Inorg. Chem.* **2011**, *50,* 3707–3716.
68. Gennari, M. *et al. Inorg. Chem.* **2011**, *50,* 10047–55.
69. Hall, N. *et al*. *Inorg. Chem.* **2013**, *52,* 13424–13431.
70. Brazzolotto, D. *et al. Chem. Eur. J.* **2016**, *22,* 925–933.
71. Element essential for life. *Metallomics,* **2012**, 1017–1019.
72. Gamelin, D. R. *et al. J. Am. Chem. Soc.* **1998**, *120,* 5246–5263.
73. Brown, E. N. *et al.*. *J. Biol. Inorg. Chem.* **2008**, *13,* 1301–1313.

Chapter I

Nickel centered proton reduction catalysis in a model of [NiFe] Hydrogenase.

Table of contents

Résumé 38

Introduction 42

Results and Discussion 47

1.1. Synthesis. 47

1.1.1. Synthesis of the bypiridine-bis-thiolate ligand. 47

1.1.2. Synthesis of the Ni^{II} unit 49

1.1.3. Synthesis of the Fe^{II} units 49

1.1.4. Synthesis of the **$Ni^{II}Fe^{II}$Cp** and **$Ni^{II}Fe^{II}$Cp***complexes 50

1.2. Structural characterization of the heterodinuclear $Ni^{II}Fe^{II}$ complexes 50

1.2.1. Structural characterization of the **$Ni^{II}Fe^{II}$Cp** complex 50

1.2.2. Structural characterization of the **$Ni^{II}Fe^{II}$Cp*** complex. 52

1.2.3. Mössbauer characterization of the **$Ni^{II}Fe^{II}$Cp** and **$Ni^{II}Fe^{II}$Cp *** complexes. 53

1.2.4. Optimized structures of **$Ni^{II}Fe^{II}$Cp** and **$Ni^{II}Fe^{II}$Cp***. 54

1.3. Solution properties of **$Ni^{II}Fe^{II}$Cp** and **$Ni^{II}Fe^{II}$Cp***. 54

1.3.1. Redox properties of **$Ni^{II}Fe^{II}$Cp** and **$Ni^{II}Fe^{II}$Cp***. 55

1.4. Electrocatalytic activity of **$Ni^{II}Fe^{II}$Cp** and **$Ni^{II}Fe^{II}$Cp*** for H_2 production 57

1.5. Investigation of the catalytic mechanism of **$Ni^{II}Fe^{II}$Cp** and comparison with the [NiFe] hydrogenase 61

1.5.1. Characterization of $Ni^{I}Fe^{II}$Cp, an active Ni-L model 61

1.5.2. Characterization of **$Ni^{II}Fe^{II}$Cp(H)**, an active Ni-R model 65

1.5.3. Towards **$Ni^{III}Fe^{II}$Cp(H)**, a Ni-C model 66

1.5.4. Identification of the two-electron reduced species of **$Ni^{II}Fe^{II}$Cp** 67

1.6. Effect of CO on H_2 production. 67

1.6.1. Electrocatalytic activity in the presence of CO. 67

1.6.2. EPR spectroscopy of **$Ni^{II}Fe^{II}$Cp*** in the presence of CO. 69

1.7. Discussion 70

Conclusion 75

References 76

Résumé

Le risque d'épuisement des ressources fossiles combiné aux problèmes environnementaux (émission de CO_2) témoigne du caractère non durable du modèle énergétique actuel. Dans un contexte où la demande en énergie est toujours croissante, il devient nécessaire d'orienter cette transition énergétique vers un nouveau modèle, impliquant de nouvelles sources d'énergie alternatives, pour stopper l'actuelle dépendance aux énergies fossiles, génératrice de pollution.

L'hydrogène moléculaire (H_2) représente un vecteur énergétique idéal et plus spécifiquement dans le secteur des transports. Même si le pouvoir calorifique volumique de l'hydrogène (H_2) est trois fois moins grand que le gaz naturel (~13 contre 40 $MJ.m^{-3}$), sa densité énergétique massique est 2,2 fois plus grande (120 contre 50 $Kj.g^{-1}$). Utilisé dans une pile à combustible, il permet la production d'électricité de manière propre et efficace. En effet, dans une pile à combustible sa réaction avec O_2 ne produit pas de sous-produits polluants, l'eau étant le seul déchet. Néanmoins, contrairement aux énergies renouvelables ou fossiles, H_2, sous sa forme moléculaire réduite n'est pas directement disponible dans la nature. Il n'est présent que sous forme oxydée comme dans H_2O ou dans les molécules organiques de la biomasse. Ainsi, bien que l'utilisation d'H_2 pose de nombreuses problématiques comme son stockage ou sa distribution, sa production reste le problème majeur car des réservoirs « indirects » de H_2 doivent être utilisés. De nos jours, 95 % d'H_2 est produit par reformage des hydrocarbures (principalement le gaz naturel) :[1a] ce processus est le moins cher mais il produit du dioxyde de carbone (CO_2). Par conséquent, ce procédé ne s'inscrit pas dans un schéma de développement durable et ne constitue pas une alternative à notre dépendance aux énergies fossiles. Une façon non polluante de produire H_2 se fait par électrolyse de l'eau, en utilisant l'électricité qui provient de ressources d'énergie renouvelables (solaire, éolienne…). Cependant, le catalyseur le plus utilisé dans les systèmes d'électrolyse à membrane polymérique (le système actuellement le plus prometteur du fait de sa compacité, de bon rendements et adaptables aux énergies renouvelables intermittentes) est composé de platine, un métal noble dont les ressources sont limitées.[2] Ce procédé est actuellement trop coûteux pour être utilisé à grande échelle. Dans ce contexte, la recherche de nouveaux catalyseurs qui ne contiennent pas de platine représente un défi majeur pour les chimistes.

La Nature a développé des catalyseurs actifs pour la production d'H_2. Ce sont les hydrogénases. Il existe deux classes d'hydrogénases, basées sur les métaux qui composent leur site actif : les [Fe-Fe] et les [Ni-Fe].[2] les hydrogénases catalysent la réduction réversible des protons en H_2 (Equation 1) à

[1a] Source : AFH2, Association Française de l'hydrogène.

des taux catalytiques très élevés, jusqu'à 3.10^4 cycles catalytiques par seconde à 30°C et à un potentiel proche de l'équilibre (-400 mV vs NHE, pH = 7).

$$H_2 \rightleftarrows 2H^+ + 2e^- \qquad \text{(Equation 1)}$$

Au cours de ce chapitre seule l'hydrogénase à [NiFe] sera discutée. Notons que ses performances rivalisent avec celles des catalyseurs à base de platine.

La première structure du site actif de l'hydrogénase [NiFe] a été caractérisée [1] en 1995 par Volbeda et al. Il s'agit un complexe hétérobimétallique original de NiFe composé d'un ion Fe coordonné à un ligand CO et deux CN^- (Figure 1), et d'un ion Ni coordonné à quatre résidus cystéines dont deux forment un pont entre les deux métaux.

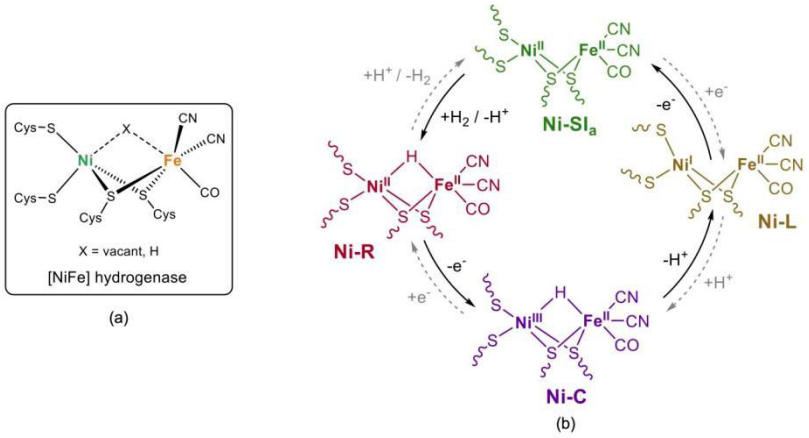

Figure 1. Site actif de l'hydrogénase [NiFe] (a) et le cycle catalytique proposé (b).

Après plusieurs décennies de recherches intensives, il a été communément proposé qu'il existe trois états intermédiaires actifs impliqués durant la catalyse (Figure 1), soit Ni-SI_a (vert), Ni-R (rouge) et Ni-C (violet). Au cours de ce cycle, H_2 se coordonne à l'état diamagnétique Ni-Si_a, dans lequel les deux métaux sont à l'état d'oxydation + II et à l'état bas spin (S = 0). Cette activation entraîne le clivage hétérolytique de H_2 et la formation concomitante de Ni-R, qui contient un ligand pontant hydrure déplacé vers l'ion Ni^{II}. L'oxydation à deux électrons de Ni-R[5,6] régénère l'état Ni-Si_a avec libération d'un second proton. L'espèce intermédiaire Ni-C[3,4] correspond à la forme mono-oxydée de l'état Ni-R et est attribué à un complexe $Ni^{III}Fe^{II}$ hydrure. Cet état intermédiaire a été notamment caractérisé par spectroscopie RPE en raison de son caractère paramagnétique. Très récemment, en 2015, il a été montré qu'un quatrième état actif, Ni-L, était impliqué dans le mécanisme, en particulier pour l'oxydation d'H_2.[8,9,47] L'état paramagnétique Ni-L avait été précédemment décrit car il peut être généré à très basse température à partir de Ni-C par exposition à la lumière visible. Ni-L a été attribué comme une espèce formelle $Ni^{I}Fe^{II}$.[9] Le centre nickel joue donc un rôle clé dans ce

mécanisme. Quant aux facteurs essentiels pour la libération de protons du centre actif et leur transfert à la surface de l'enzyme, ils ne sont pas encore clairement identifiés, bien que plusieurs modèles aient été proposés.

Reproduire la structure et les fonctions du site actif de l'hydrogénase [NiFe] par des mimes artificiels représente un réel intérêt pour les chimistes du fait de sa structure dissymétrique originale et de sa réactivité, notamment pour le développement d'application technologiques pour la production d'H_2. Malgré les grandes avancées dans la conception de modèles moléculaires dont la réactivité est localisé sur le Fe, il n'existe toujours pas de complexes qui miment précisément la structure et la réactivité centrée sur le Ni du site actif de l'hydrogénase [Ni-Fe].[10-13] Pour développer des complexes modèles de l'hydrogénase [NiFe] efficaces, la réactivité doit être localisée sur le Ni grâce à un environnement adéquat. La conception du ligand est donc primordiale dans le sens où il doit stabiliser l'ion Ni à différents degrés d'oxydation, tout en maintenant un système hétérodinucléaire stable. C'est pourquoi le ligand bispyridine-bisthiolate (LS) est particulièrement intéressant car il permet la formation de complexes de Ni stable aux trois degrés d'oxydation du Ni de +I à +III. Parallèlement, le synthon $\{FeCpCO\}^+$ a déjà été utilisé comme substitut pour mimer la partie $\{FeCO(CN)_2\}$ de l'enzyme pour la conception de modèles NiFe.[29-31]

Dans ce chapitre, nous présentons la synthèse et la caractérisation de deux complexes hétérodinucléaires de NiFe $[LSNi^{II}Fe^{II}Cp(*)(CO)]^+$ (**$Ni^{II}Fe^{II}Cp$** et **$Ni^{II}Fe^{II}Cp^*$**) qui miment le site actif de l'hydrogénase [NiFe] et qui produisent H_2 de manière catalytique. Ces composés présentent les meilleures performances en tant que modèle structural et fonctionnel parmi les systèmes reportés dans la littérature : constante catalytique du second ordre de 2.510^{-4} $M^{-1}s^{-1}$ pour **$Ni^{II}Fe^{II}Cp$**; fréquence de cycle catalytiques de 250 s^{-1} à 10 mM en concentration de H^+) en présence d'acide faible. Basé sur des résultats expérimentaux associés à des calculs DFT, un mécanisme électrocatalytique a été proposé pour **$Ni^{II}Fe^{II}Cp$**. (Figure 2) **$Ni^{II}Fe^{II}Cp$** subit une réduction à un électron pour générer **$Ni^{I}Fe^{II}Cp$**. Cette espèce est ensuite réduite pour donner l'espèce radicalaire **$LS^{\bullet}Ni^{II}Fe^{II}Cp$**, qui réagit ensuite avec un proton pour donner l'espèce hydrure **$Ni^{II}Fe^{II}Cp(H)$**. L'espèce hydrure réagit à nouveau avec des protons pour produire H_2 et régénérer le complexe initial **$Ni^{II}Fe^{II}Cp$**. Un tel mécanisme catalytique, impliquant des transferts découplés de protons et d'électrons, est similaire à ce qui est proposé pour l'enzyme, à l'exception que le transfert électron/proton conduisant à Ni-R/ **$Ni^{II}Fe^{II}Cp(H)$** à partir de Ni-L/ **$Ni^{I}Fe^{II}Cp$** est inversé. Par conséquent, la formation de **$Ni^{III}Fe^{II}Cp(H)$**, composé analogue à Ni-C est contournée dans notre système. Il est proposé que la protonation de **$Ni^{I}Fe^{II}Cp$** par Et_3NH^+ est soit thermodynamiquement non favorable, soit trop lente pour être observée à l'échelle de la voltammétrie cyclique. Cela peut s'expliquer par le faible caractère basique et nucléophile de **$Ni^{I}Fe^{II}Cp$** en comparaison à Ni-L du à (i) un environnement coordonnant moins donneur ($\{N_2S_2\}^{2-}$ pour

Ni^{I} vs. $\{S_4\}^{4-}$ dans l'enzyme enzyme) ; (ii) une délocalisation partielle de la SOMO sur la partie bipyridine (LS) et (iii) l'absence de relais de proton pour assister cinétiquement la protonation sur le centre Ni^{I}.

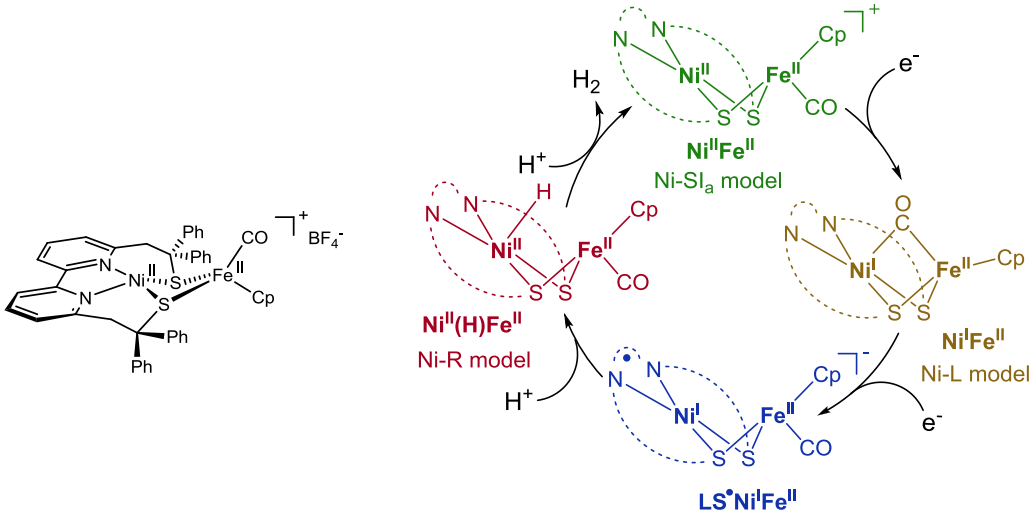

Figure 2. Représentation du complexe **$Ni^{II}Fe^{II}Cp$** (gauche). Mécanisme électrocatalytique proposé pour le complexe **$Ni^{II}Fe^{II}Cp$** (droite).

De plus, nous avons également démontré que le complexe parent **$Ni^{II}Fe^{II}Cp$*** représente un modèle de l'état Ni-CO de l'hydrogénase [NiFe]. En effet, à partir d'études électrochimiques, il a été montré qu'en présence de protons et de CO, l'activité catalytique de **$Ni^{II}Fe^{II}Cp$*** était inhibée alors qu'avec **$Ni^{II}Fe^{II}Cp$**, l'inhibition n'était que partielle. Comme dans l'enzyme, cette inhibition est réversible dans les deux cas. Cette différence de réactivité provient de la structure des espèces intermédiaires **$Ni^{I}Fe^{II}$** : alors que le CO est en position terminale sur le Fe dans **$Ni^{I}Fe^{II}Cp$***, il est pontant dans **$Ni^{I}Fe^{II}Cp$**, empêchant la coordination d'une deuxième molécule de CO sur le complexe.

Ces deux complexes décrits dans ce chapitre représentent de bons modèles structuraux et catalytiques pour la production d'H_2. Tout comme dans l'enzyme, le centre Fe de **$Ni^{II}Fe^{II}Cp$** est impliqué dans la modulation des propriétés électroniques du centre $\{N_2S_2\}$ avec une modification en potentiel de 540 mV. Une telle conclusion est confirmée par les expériences d'électrolyse (production d'H_2 plus importante en termes de vitesse et d'efficacité par rapport au complexe mononucléaire de Ni, **$Ni^{II}L$**) démontrant un effet coopératif du Fe sur la réactivité de l'unité {NiLS}.

Introduction

The risk of the fossil resources depletion combined with environmental issues testifies the non-lasting character of the current energetic model. In a context of constant growth in demand in energy, it is of urgent necessity to orientate an energetic transition towards another model, implying the research of new alternative resources of energy, to end our dependence to fossil fuels, generating pollution.[17]

In this context, molecular hydrogen (H_2) is an ideal energetic vector, especially in the transport sector. Even if the calorific volume power of H_2 is three times less big than the natural gas (~13 over 40 $MJ.m^{-3}$), its energetic mass density is 2.2 times higher (120 over 50 $KJ.g^{-1}$). Used in a fuel cell, it allows the production of electricity with a good yield and in a "clean" way. Its reaction with O_2 doesn't produce polluting by-products, water being the only waste. However, unlike renewable or fossil energies, H_2 is not directly available in nature. It exists in oxidized forms such as water (H_2O) or in the organic molecules of the biomass. Thus, H_2 production becomes an issue since indirect reservoirs of H_2 have to be used. Nowadays, 95 % of H_2 is produced by reforming hydrocarbons (mainly natural gas): [1a] this process is currently the less expensive one but releases carbon dioxide (CO_2). Therefore, it can't be considered in the scheme of sustainable development and doesn't constitute an alternative to our dependence to fossil fuels. Another "clean" strategy is to produce H_2 by water electrolysis, if the provided electricity comes from renewable resources (solar, wind power…).[2] However, the most promising catalysts used in water electrolysis systems are based on platinum, a noble and expensive metal that is of limited resources.[2] Such devices are thus too expensive to be used at a large scale. In this context, the research of new water reduction catalysts not implying platinum represents a major challenge.

On the other hand, Nature developed active catalysts for H_2 production, i.e. hydrogenases. The multiple classes of hydrogenases are divided into two main families, based on the metal content of their active site, namely the [FeFe] and [NiFe] hydrogenases.[2]

[NiFe] and [FeFe] hydrogenases are organometallic enzymes that catalyze the reversible reduction of protons into hydrogen (Equation 1), with performances that rival those of platinum. However, the [Fe-Fe] hydrogenase is usually committed to H_2 evolution.

$$\mathbf{H_2 \rightleftarrows 2H^+ + 2e^-} \qquad \text{(Equation 1)}$$

Indeed, hydrogenases produce H_2 at high catalytic rates (turnover frequencies, TOF, of up to 3.10^4 s^{-1} at 30°C) at a marginal potential beyond equilibrium (-400 mV vs NHE, pH = 7),[3] which is only matched by platinum.

The first hydrogenase, for which the structure has been determined crystallographically was from the prevalent [NiFe] hydrogenase class.[1] The structural elucidation in 1995 by Voldeba et al. revealed an original organometallic NiFe complex with CO and CN^- ligands bound to the Fe site (Figure 1). The Ni site is bound to four cysteine residues, two of them bridging the two metal ions. It has been demonstrated that the nickel center plays the critical role in hydrogen binding/H^+ activation and in redox chemistry occurring during the catalytic cycle.[2]

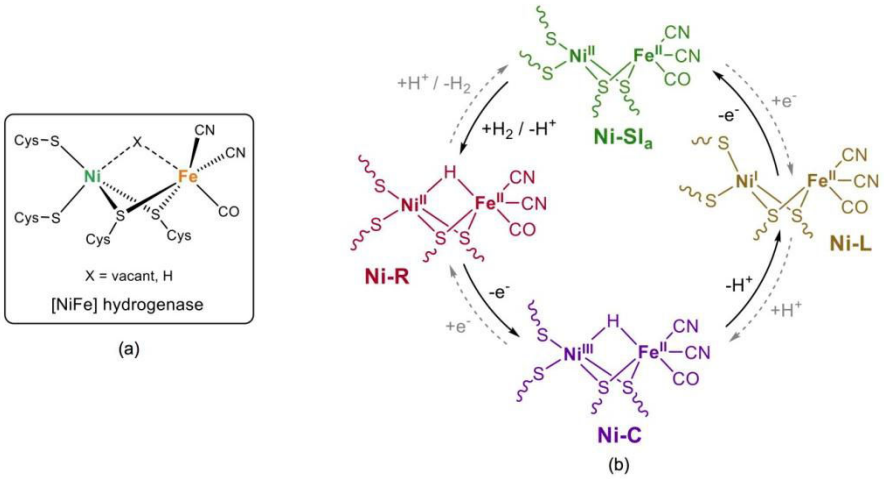

Figure 1. Active site of [NiFe] hydrogenase (a) and proposed catalytic cycle (b).

After two decades of intensive research, there is a general agreement that three different active states are involved during the catalysis, both in the case of H_2 oxidation and reduction of protons, namely Ni-SI_a, Ni-R and Ni-C (Figure 1). Considering H_2 oxidation, H_2 is activated through its binding to the diamagnetic Ni-SI_a state, in which both metal are at the +II oxidation state and in low spin state (*S* = 0). This activation leads to the heterolytic cleavage of H_2 and the concomitant formation of Ni-R, which contains a bridging hydrido ligand displaced toward the Ni^{II} ion. The two-electron oxidation of Ni-R[5,6] regenerates the Ni-SI_a state with the release of the second proton. The intermediate Ni-C[3,4] species corresponds to the one-electron oxidized form of Ni-R and is assigned to a $Ni^{III}Fe^{II}$ hydrido complex, which has been fully characterized especially by EPR spectroscopy owing to its paramagnetic character. Very recently, in 2015, evidence has been accumulated that a fourth active state, Ni-L, is involved in the mechanism, especially for H_2 oxidation.[8,9,47] The paramagnetic Ni-L state was previously described since it can be generated at cryogenic temperature from Ni-C under visible light exposure. Ni-L was assigned as a formal $Ni^{I}Fe^{II}$ species, and in 2013, it was proposed that Ni-L contains a metal-metal interaction with the unpaired spin density mainly localized on the Ni site.[9] The nickel centre is thus the key protagonist in this mechanism.

The residues essential for the proton release from the active center and their transfer to the surface of the enzyme are still not clearly identified, although several models have been proposed. Theoretical and mutational investigations as well as crystallographic evidence[53] suggest that the proton is first transferred from one of the terminal cysteines bound the Ni site to a nearby glutamate residue. Then the protons are transferred to the surface *via* either a network of water molecules or a glutamate chain.[65] A second hypothesis considers that protons are directly transferred to an arginine residue, which is located in an opposite position to the hydrido bridging ligand, and from there the protons can reach the surface *via* a histidine rich motif.[66]

In contrast, the electron transfer chain has been clearly identified and involves three [FeS] clusters, whose structural, redox and spectroscopic properties have been explored in depth. More precisely, the proximal and distal [4Fe4S] and the medial [3Fe4S] clusters allow the electron transfer from/to the active NiFe center to the surface of the protein (Figure 2).[67] While the distal cluster is exposed to the solvent region and is thought to be the final part of the electron transfer chain, the proximal cluster is proposed to have a key role during the catalysis. It has been recently shown that the redox state of this cluster controls the catalytic cycle, acting as a gate for the electron transfer flow from the NiFe active site to the redox partner.[68-70]

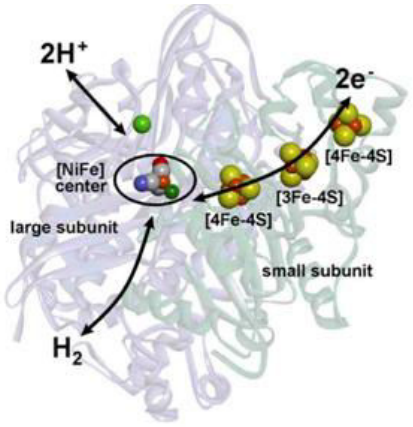

Figure 2. Structure of the [NiFe] hydrogenase the active site and the electron transfer. (Yellow: S, orange: Fe, dark green: Ni, light green: Mg^{2+}, red: oxygen, grey; carbon, bleu: N)

Reproducing the structure and function of the active site of [NiFe] hydrogenase in artificial mimics has for many years been a key challenge for synthetic chemists motivated by its original dissymmetric structure, its peculiar reactivity and the possible technological applications of efficient hydrogen production catalysts that may be developed. Despite tremendous advances in the design of NiFe models, there is still no complex that accurately mimics the structure, function and reactivity of the active site of [NiFe] hydrogenase.[10-13]

The first structural model was described by Darensbourg et. al. in 1996 (Figure 3A),[31] a mono-thiolate bridged complex with the Fe being bound to four CO ligands and the Ni hosted in a $\{N_2S_2\}$

environment. The groups of Tatsumi[71]and Schröder[30] have reported the first models with bridging dithiolate (Figures 3B and 3C, respectively) about 10 years later, illustrating the synthetic challenges in designing and isolating such systems. However, none of them displayed reactivity toward H^+ or H_2.

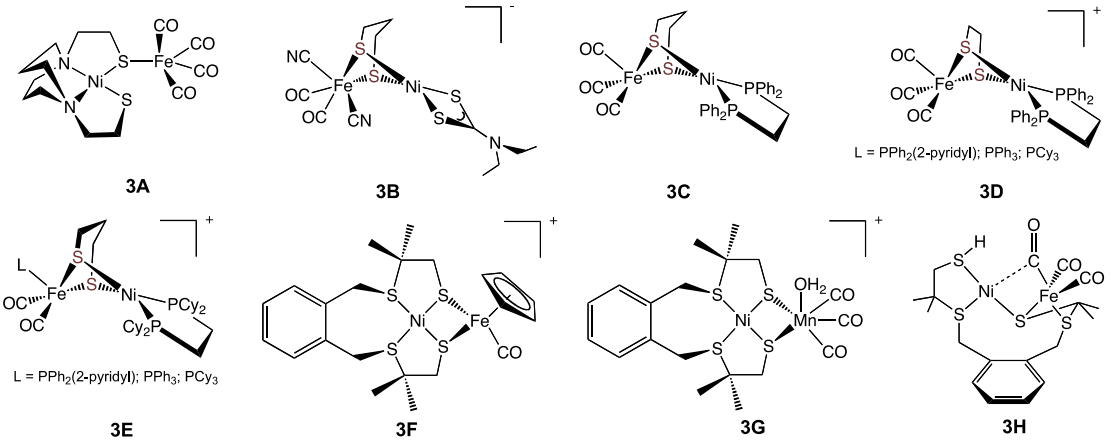

Figure 3. Relevant structural (3A-3C) and both structural/functional models of the [NiFe] hydrogenase.

From 2009 onwards, functional bio-inspired NiFe systems have been described that are active as H_2 evolution electrocatalysts. The most developed family of complexes reported by Rauchfuss & Stein is related to $Ni^{II}Fe^{I}$ complexes (Figures 3D & 3E)[72-74] with the Ni site being located in a $\{P_2S_2\}$ environment, while at least one CO is coordinated to the Fe site. Phosphine ligands have been often used to mimic the cyanide ligand in hydrogenases models. Mechanistic studies demonstrated that, in contrast to the enzyme, in all these active mimics the chemistry mainly occurs on the Fe site and not on the Ni site. Intermediates including a few metal-hydride species (Figure 4A and 4B)[16,21,23] have been isolated but the hydride ligand is strongly asymmetrically bound toward the Fe site or terminally bound to the Fe site.

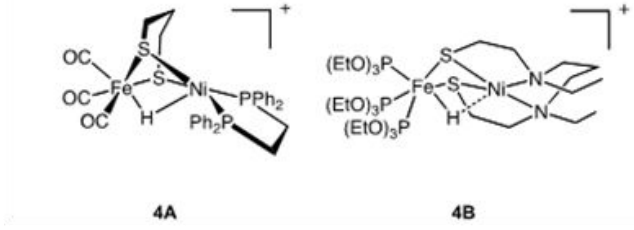

Figure 4. Ni-Fe hydride species (4A-4B).

The main drawback of most active mimics is that their chemistry is mainly centered on the Fe site[13] or on M (M = Mn[14,15] or Ru[16-19]) in heterodinuclear NiM models,[20] but not on the Ni site as in the enzyme. For instance, Ogo and Rauchfuss have evidenced that the formation of metal-hydride species in synthetic heterodinuclear NiFe/NiRu complexes is feasible,[16,21-23] but in all cases, including DFT-optimized models (DFT= Density Functional Theory),[14,24] the hydride ligand is either bridging[14,16,22-24] but displaced toward the Fe site, or terminal and bound to the Fe center.[21,25]

A family of catalysts described by Fontecave and Artero corresponds to **$Ni^{II}M^{II}$** complexes with M being Fe, Mn or Ru (3F, 3G).[14,17-19] In these catalysts, the Ni is hosted in $\{S_4\}$ environment and the M ion is in an organometallic environment. They have demonstrated that the production of H_2 with the NiRu catalyst follows a similar mechanism to that of the enzyme, but the bridging metal hydride intermediates proposed for these systems based on theoretical calculations are still asymmetrically bound toward the Fe/Ru site.

Finally, the model described by Lubitz et al (Figure 3H),[75] in which a Ni-bound terminal thiolate is protonated, opens on the idea that terminal cysteine protonation is relevant with respect to a proton relay function. Besides, it has been demonstrated that the presence of potential protonated sites located at proximity to the catalytic metal center can drastically enhance the performance of a catalyst. In the special case of the [FeFe] hydrogenase for example, the pendant amine group plays a crucial function as it participates in proton exchange, facilitating proton reduction to H_2.[76-77]

It has been shown that the [NiFe] hydrogenase can be inhibited by CO reversibly. X-Ray crystallography and Raman spectroscopy experiments evidenced that CO binds on the Ni site.[83] Two different CO inhibited states have been observed with distinct properties and electronic structures (Figure 5). The formation of these two states depends on the oxidation state of the Ni site. The paramagnetic form is known as Ni^{I}-CO, whereas the EPR-silent form is a Ni^{II} species, known as Ni^{II}SCO.[84] For both states, it has been shown that the CO can be photodissociated from the active site at near cryogenic temperature.

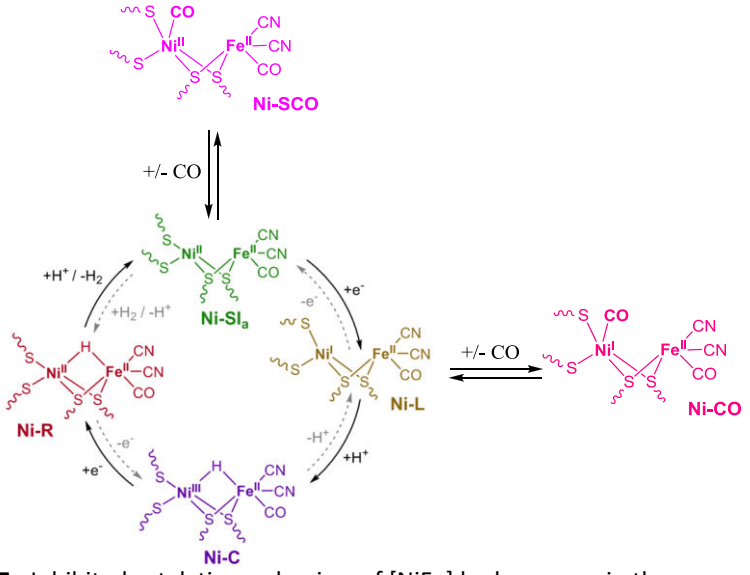

Figure 5. Inhibited catalytic mechanism of [NiFe] hydrogenase in the presence of CO.

In this context, the reactivity needs to be relocated to the Ni center with the aim of developing mimics of the active site of [NiFe] hydrogenase with a better efficiency. Ligand design can thus be exploited to promote redox flexibility on the Ni site (rather than on the Fe site), while maintaining a stable dinuclear framework in various oxidation states.

The bipyridine-bisthiolate ligand LS is particularly interesting since it forms quite stable nickel complexes in all three oxidation states from +I to +III.[27,28] Additionally, the $\{FeCpCO\}^+$ and $\{FeCp^*CO\}^+$ units (Cp = cyclopentadienyl, Cp* = pentamethylcyclopentadienyl) have previously been used as a surrogate for the $\{FeCO(CN)_2\}$ moiety of the natural cluster for the successful design of synthetic mimics.[29-31] (Figure 6)

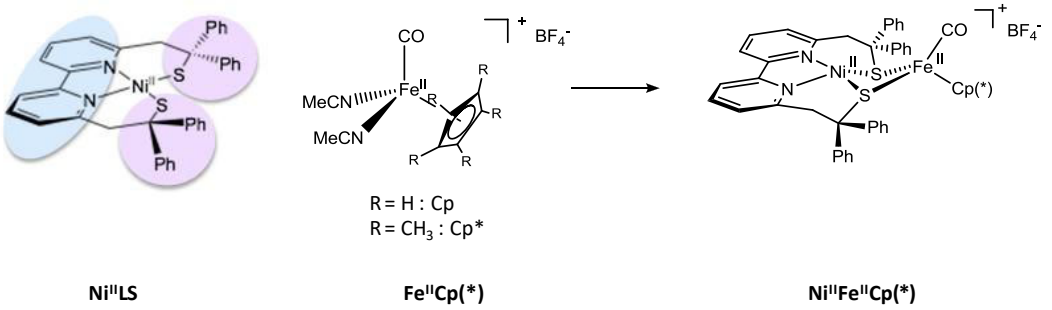

Figure 6. Ni^{II} and Fe^{II} complexes used as synthetic blocks for the synthesis of dinuclear NiFe models.

Starting from the **Ni^{II}LS** and **Fe^{II}Cp(*)** precursors, we report on the synthesis and characterization of two heterodinuclear NiFe complexes, $[(LS)Ni^{II}Fe^{II}Cp(CO)]^+$ and $[(LS)Ni^{II}Fe^{II}Cp^*(CO)]^+$ (**$Ni^{II}Fe^{II}$Cp** and **$Ni^{II}Fe^{II}$Cp***) (see below), that are models of the active site of [NiFe] hydrogenase and produces H_2 electrocatalytically at high rate. Intermediate species have been generated and characterized by different spectroscopic techniques in the case of **$Ni^{II}Fe^{II}$Cp**. Furthermore, the catalytic activity in the presence of CO for both $Ni^{II}Fe^{II}$ complexes has been investigated and is discussed.

Part of this work has been recently published in *Nature Chemistry*: doi:10.1038/nchem.2575.

Results and Discussion

1.1. Synthesis.

1.1.1. Synthesis of the bypiridine-bis-thiolate ligand.

The tetradentate ligand, 2,2'-(2,2'-bipyridine-6,6'-iyl)bis(1,1-diphenylethanethiolate) LS (Figures 7-9) has been synthesized by an adapted procedure from the Berg and Holm procedure.[79] This LS ligand contain terminal alkyl thiolates groups each one protected by two bulky phenyl groups on the C_α to limit the formation of disulphide bonds or complex polymerization. The bipyridine is well known as a good coordinating ligand because of its versatility in stabilizing high and low oxidation states (due to its ability to delocalize unpaired electrons on the aromatic rings of the bipyridine). This ligand was prepared *via* 3 steps: (i) synthesis of the thiol moiety, (ii) synthesis of the bipyridine moiety and (iii) condensation of the two synthons.

Synthesis of the thiolate moiety **b***.* **b** has been synthesized in a two-step reaction as shown in Figure 7; diphenylmethyl chloride was reacted with thiourea, and the product was then protected with tetrahydropyran. **b** will be used in step (vii).

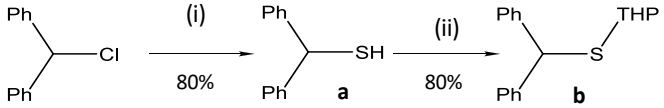

Figure 7. Synthesis of the thiol moiety: (i) thiourea, EtOH, reflux, NaOH; (ii) 2,3 dihydropyran, HCL 37%.

Synthesis of the bipyridine moiety **4***. S*ynthesis of the bipyridine moiety starts with step (iii) shown in Figure 8 which has been slightly modified from the published strategy.[80] Compound **1** was prepared using a Ullman coupling of the 2,6-bromopyridine. It is initiated with a lithium halogen exchange, which is a methathesis between 2,6-bromopyridine and *n*-butyllithium. The copper-catalysed oxidative coupling of the aryllithium intermediate at low temperature allows to obtain **1**. In the following step (iv) **1** is converted into the 6,6'-bis(methanoyl)-2,2'-bipyridine *via* a further lithiation reaction followed by a formylation reaction with DMF. **2** is then reduced with $NaBH_4$ to yield to 6,6'-bis(methanol)-2,2'-bipyridine. The next step (v) leads to the bromination of the alcohol using HBr as the brominating agent.

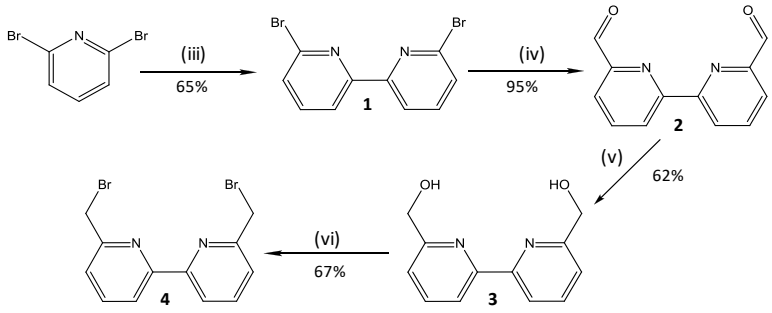

Figure 8. Synthesis of the bipyridine synthon: (iii) *n*-Buli 2.5 M at-78°C in Et_2O, $CuCl_2$, O_2; (iv) *n*-Buli 2.5 M at-78°C in THF, DMF; (v) $NaBH_4$ in MeOH; (vi) HBr 33% reflux.

Synthesis of the LS ligand. The synthesis of the LS (**6**) ligand begins with step (vii) as shown in Figure 9. In step (vii), **4** is coupled with **b** via a lithiation reaction in the presence of hexamethylphosphoramide (HMPA) to increase the basicity of *n*-BuLi. The final reaction consists of the deprotection of the thiolates which occurs in two steps. Firstly, the sulphurs of **5** are deprotected in the presence of the Lewis acid Ag^+, which leads to the formation of a Ag-thiolate complex. In a second step, Ag^+ is removed by protonation of the thiolates with H_2S to form Ag_2S. The compound **6** is thus obtained and handled under inert atmosphere due to its sensitivity to O_2 (Figure 8). The global yield of this multistep synthesis is 20%.

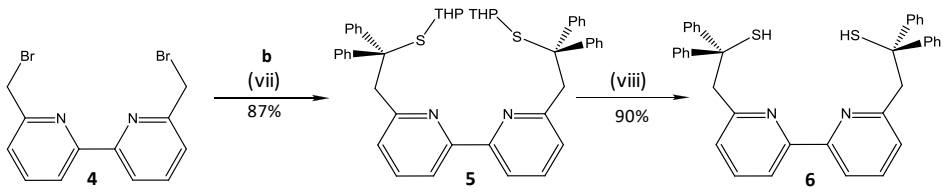

Figure 9. Synthesis of LS ligand: (vii) **b**,HMPA, *n*-Buli 2.5 M at-78°C in Et_2O, **4**, THF; (viii) $AgNO_3$/pyridine in MeOH/AcOEt, H_2S.

1.1.2. Synthesis of the Ni^{II} unit.

From the LS ligand, which has been deprotonated with NaH, [Ni^{II}(LS)] (**Ni^{II}LS**) complex was synthesized in the presence of $NiCl_2.6H_2O$ in THF as shown in Figure 10. The Ni^{II} center displays a distorted square planar geometry. **Ni^{II}LS** has been previously characterized by different techniques[27, 28] (X-Ray, UV-Vis absorption, and electrochemistry) by our group.

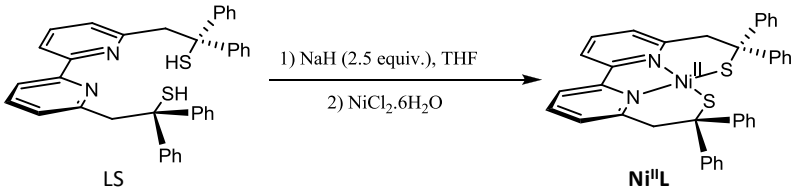

Figure 10. Synthesis of **Ni^{II}LS**.

1.1.3. Synthesis of the Fe^{II} units.

[$CpFe^{II}(CO)(MeCN)_2$]BF_4 and [$Cp^*Fe^{II}(CO)(MeCN)_2$]BF_4 (**Fe^{II}Cp** and **Fe^{II}Cp***) were synthesized in three steps by slightly modified previously published procedures.(Figure 11).[81]

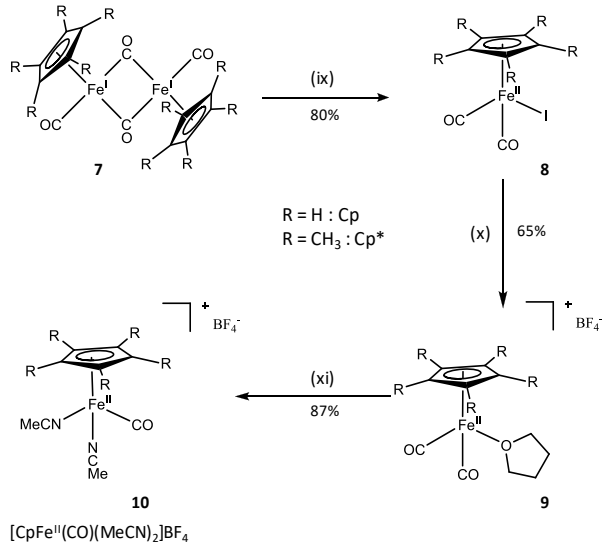

Figure 11. Synthesis of the Fe^{II} complex. (ix) I_2, $Na_2S_2O_3$, $CHCl_3$; (x) $AgBF_4$, THF; (xi) hν, MeCN.

The only difference between the two complexes is the presence of a cyclopentadienyl **(Cp)** or a pentamethyl-cyclopentadienyl **(Cp*)** group coordinated to Fe^{II}. All the syntheses have been performed under inert atmosphere due to the sensitivity of **Fe^{II}Cp(*)** to O_2.

Step (ix) consists of the oxidation of the commercial dinuclear Fe^{I} complex **7** with I_2 leading to two monomeric Fe^{II} complexes [Cp(*)Fe^{II}(CO)$_2$I], **8**. The following step (x) was to substitute the iodide with a tetrahydrofuran (THF) ligand using $AgBF_4$ and THF as solvent to obtain [Cp(*)Fe^{II}(CO)$_2$THF]BF_4, **9**.[61] In the last step (xi), the THF ligand and one carbonyl (CO) were replaced by two MeCN molecules, by exposure of a MeCN solution of the complex to a UV filtered Hg/Xe lamp to give [Cp(*)Fe^{II}(CO)(MeCN)$_2$]BF_4, **10**. During this reaction the flask was placed under a slight vacuum to favor the removal of one CO. The presence of CO in [CpFe^{II}(CO)(MeCN)$_2$]BF_4 and [Cp*Fe^{II}(CO)(MeCN)$_2$]BF_4 allows to follow the synthesis by IR spectroscopy. The final complexes [CpFe^{II}(CO)(MeCN)$_2$]BF_4 and [Cp*Fe^{II}(CO)(MeCN)$_2$]BF_4 present, a CO vibration at 2008 and 1976 cm^{-1}, respectively. The global yield is ~45% for both Cp and Cp* complexes.

1.1.4. Synthesis of the **$Ni^{II}Fe^{II}$Cp** and **$Ni^{II}Fe^{II}$Cp***complexes.

[Ni^{II}(LS)Fe^{II}(CO)Cp]BF_4 and [Ni^{II}(LS)Fe^{II}(CO)Cp*]BF_4 (**$Ni^{II}Fe^{II}$Cp** and **$Ni^{II}Fe^{II}$Cp***) have been isolated from the reaction between the two corresponding mononuclear units (Figure 6), i.e. the dithiolate Ni^{II} complex [Ni^{II}(LS)] **Ni^{II}LS** and the carbonyl Fe^{II} complex [Cp(*)Fe^{II}(CO)(MeCN)$_2$]BF_4 (**Fe^{II}Cp** or **Fe^{II}Cp***) (Figure 12) with a yield of ~70% for both complexes. This reaction was performed at 293 K in CH_2Cl_2 under inert atmosphere leading to a dark brown solution. Dark crystals were obtained after slow diffusion of diethyl ether and were characterized by X-ray crystallography. Once synthesized, both complexes are not sensitive to O_2. The synthesis can be followed by IR spectroscopy observing the appearance of a CO vibration of 1929 and 1926 cm^{-1} for **$Ni^{II}Fe^{II}$Cp** and **$Ni^{II}Fe^{II}$Cp***, respectively.

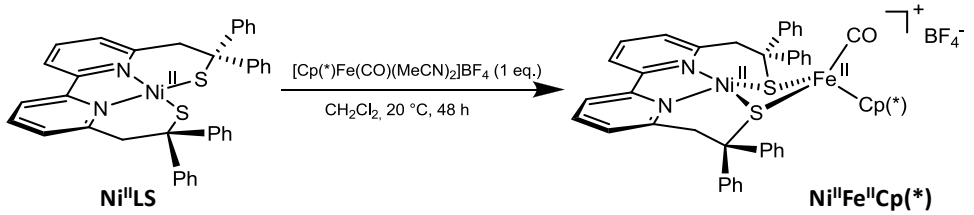

Ni^{II}LS **$Ni^{II}Fe^{II}$Cp(*)**

Figure 12. Synthesis of **$Ni^{II}Fe^{II}$Cp** and **$Ni^{II}Fe^{II}$Cp*** complexes.

1.2. Structural characterization of the heterodinuclear $Ni^{II}Fe^{II}$ complexes

1.2.1. Structural characterization of the **$Ni^{II}Fe^{II}$Cp** complex.

X-ray suitable dark-brown crystals corresponding to **Ni^{II}Fe^{II}Cp** were obtained by slow diffusion of diethyl ether into a CH_2Cl_2 solution of the product at 293 K. The X-ray structure of **Ni^{II}Fe^{II}Cp** is shown in Figure 13 and selected bond distances are given in Table 1. The **Ni^{II}Fe^{II}Cp** complex crystallizes as two crystallographically independent molecules with similar geometries. Only one of these molecules will be described.

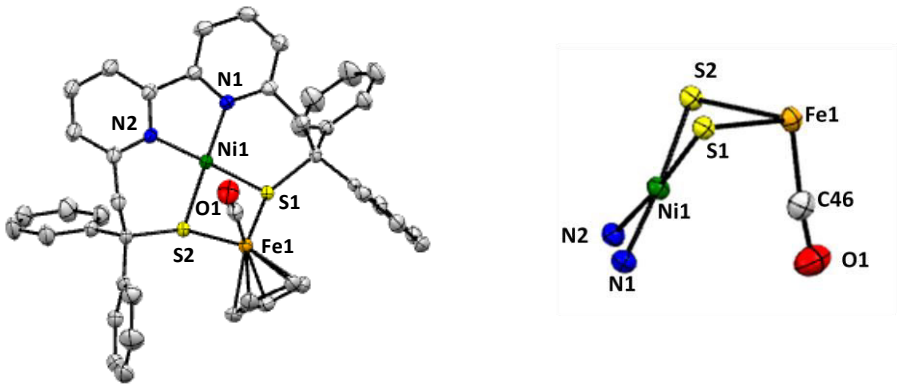

(a) (b)

Figure 13. (a) Molecular structure of Ni^{II}Fe^{II}Cp.BF_4^-.1.5Et_2O. (b) The {$NiFeS_2$} core. The thermal ellipsoids are drawn at 50% probability level. All hydrogen atoms, anions and solvent molecules are omitted for clarity.

The **Ni^{II}Fe^{II}Cp** cation consists in a dimercapto-bridged Ni-Fe heterodinuclear complex. Its structure contains a {$NiFeS_2$} core which is not planar with an angle between the S2NiS1 and S2FeS1 planes of 111.94(2)°, leading to a Ni...Fe distance of 2.91(7) Å, too long for a direct metal-metal interaction. Ni and Fe atoms display two different geometries. The Ni site presents a quasi-planar geometry with a small pseudotetrahedral twist angle of 5.47°, while the Fe site displays a tetrahedral geometry, with the CO occupying one of the fourth positions. The Fe centre is enclosed by a 18-electron shell, while a 16-electron shell encloses the Fe site of [NiFe] hydrogenase. The Ni-S and the Fe-S bond lengths implicated in the core (2.17-2.30 Å) are similar to those found in structurally related NiFe complexes with two bridging thiolates.[22] The Ni-N distances are comprised in the range 1.898-1.904 Å, consistent with the Ni^{II}-N distances previously observed with bipyridine-derivatives.[27, 28]

Table 1. Selected bond lengths (Å) and angles (°) for **Ni^{II}Fe^{II}Cp**$BF_4 \cdot 1.5Et_2O$ for the two crystallographically independent units and for **Ni^{II}Fe^{II}Cp***$BF_4 \cdot 0.7CH_2Cl_2 \cdot 0.15Et_2O \cdot 0.15H_2O$.

Ni^{II}Fe^{II}Cp (1)		**Ni^{II}Fe^{II}Cp** (2)		**Ni^{II}Fe^{II}Cp***	
Ni(1)-N(1)	1.904(3)	Ni(2)-N(51)	1.896(3)	Ni(1)-N(1)	1.9050(17)
Ni(1)-N(2)	1.898(3)	Ni(2)-N(52)	1.897(3)	Ni(1)-N(2)	1.9331(16)
Ni(1)-S(1)	2.1745(9)	Ni(2)-S(51)	2.1777(10)	Ni(1)-S(1)	2.1652(7)
Ni(1)-S(2)	2.1785(9)	Ni(2)-S(52)	2.1719(9)	Ni(1)-S(2)	2.1691(6)
Fe(1)-C(46)	1.755(4)	Fe(2)-C(96)	1.755(4)	Fe(1)-C(46)	1.761(2)
Fe(1)-C(Cp)	2.074(4)-2.117(4)	Fe(2)-C(Cp)	2.059(4)-2.101(4)	Fe(1)-C(Cp*)	2.101(2)-2.139(3)
Fe(1)-S(1)	2.3050(10)	Fe(2)-S(51)	2.3035(9)	Fe(1)-S(1)	2.3257(7)
Fe(1)-S(2)	2.2975(9)	Fe(2)-S(52)	2.3118(10)	Fe(1)-S(2)	2.2995(10)
O(1)-C(46)	1.149(5)	O(51)-C(96)	1.147(5)	O(1)-C(46)	1.149(2)
Ni(1)-Fe(1)	2.9181(7)	Ni(2)-Fe(2)	2.8421(7)	Ni(1)-Fe(1)	3.396(6)
[(S1Ni1S2)(S1Fe1S2)	111.92(4)	[(S51Ni2S52)(S51Fe2S52)	107.22(4)	[(S1Ni1S2)(S1Fe1S2)	152.52 (4)

1.2.2. Structural characterization of the **Ni^{II}Fe^{II}Cp*** complex.

X-Ray suitable dark-brown crystals corresponding to **Ni^{II}Fe^{II}Cp*** were obtained by slow diffusion of diethyl ether into a solution of the product in CH_2Cl_2 at 293 K. The X-ray structure of **Ni^{II}Fe^{II}Cp** is given in Figure 14 and selected bond distances and angles are shown in Table 1. Interestingly, the structure of this complex is notably different from its parent **Ni^{II}Fe^{II}Cp** complex. The structural difference of the $\{NiFeS_2\}$ core in both complexes arises from the bulkiness of Cp* with respect to Cp leading to an increase of the distance between the two metallic units (3.396 Å vs 2.918 Å for **Ni^{II}Fe^{II}Cp**). As the **Ni^{II}Fe^{II}Cp**, the **Ni^{II}Fe^{II}Cp*** cation consists in dimercapto-bridge Ni-Fe heterodinuclear complex. Its structure contains a planar $\{NiFeS_2\}$ core, (the NiFeS2 atoms deviate less than 0.18 Å from the mean plane that they formed) with an angle between the S2NiS1 and S2FeS1 plans of 152.52(2)° (vs 111.94° for **Ni^{II}Fe^{II}Cp**).

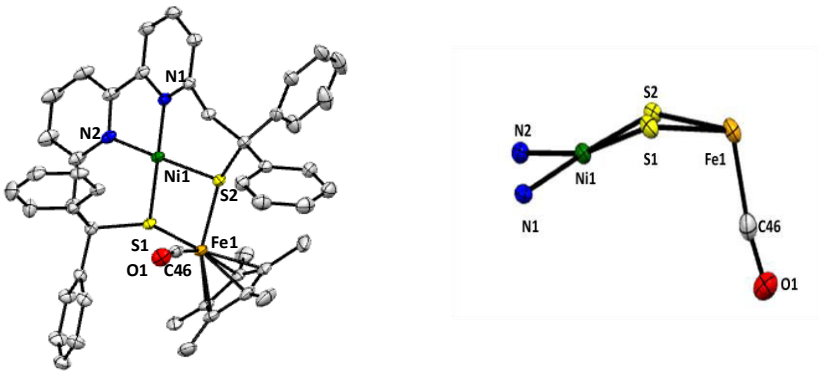

(a) (b)

Figure 14. (a) Molecular structure of **Ni^{II}Fe^{II}Cp***.$BF_4 \cdot 0.7CH_2Cl_2 \cdot 0.15Et_2O \cdot 0.15H_2O$. (b) The $\{NiFeS_2\}$ core. The thermal ellipsoids are drawn at 50% probability level. All hydrogen atoms, anions and solvent molecules are omitted for clarity.

The Ni-Fe distance is notably longer than in the previous complex suggesting that this compound is less stable and more reactive. The other distances (Ni-S, Ni-N, Fe-S) remain approximately unchanged in comparison to those of **Ni^{II}Fe^{II}Cp**. The distorted square planar geometry around the Ni site is characterized by a pseudotetrahedral twist angle (13.87°), notably smaller than in the mononuclear Ni precursor (29.15°), but much larger than in **Ni^{II}Fe^{II}Cp** (5.47°), probably due to the bulkiness of the Cp* ligand. The iron site displays a similar geometry in both heterodinuclear NiFe complexes.

1.2.3. Mössbauer characterization of the **Ni^{II}Fe^{II}Cp** and **Ni^{II}Fe^{II}Cp *** complexes.

Mössbauer measurements have been recorded on powder for both complexes to validate the oxidation state and determine the spin state of the Fe center. The spectra are characteristic of low-spin Fe^{II} ion, i.e doublets with isomer shift δ = 0.39 mm·s^{-1} for both complexes, and quadrupole splitting ΔE_Q = 1.82 mm·s^{-1} and 1.96 mm·s^{-1} for **Ni^{II}Fe^{II}Cp** and **Ni^{II}Fe^{II}Cp***, respectively as shown in Figure 15.

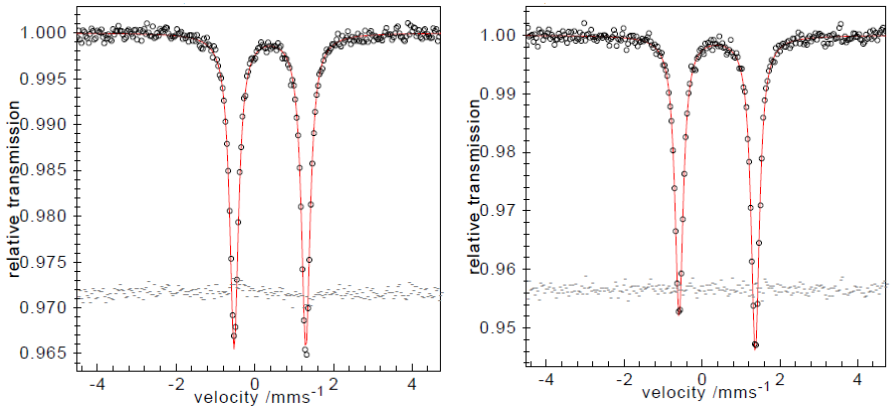

Figure 15. Mössbauer spectra of (a) **Ni^{II}Fe^{II}Cp** and (b) **Ni^{I}Fe^{II}Cp*** recorded at 80 K obtained on solid samples. The red solid line through the experimental data (empty black circles) is a simulation using Lorentzian line doublets with the following parameters **Ni^{II}Fe^{II}Cp:** δ = 0.39 mm·s^{-1} and ΔE_Q = 1.82 mm·s^{-1}; **Ni^{II}Fe^{II}Cp*:** δ = 0.39 mm·s^{-1} and ΔE_Q = 1.96 mm·s^{-1}.

1.2.4. Optimized structures of **Ni^{II}Fe^{II}Cp** and **Ni^{II}Fe^{II}Cp***.

The crystallographic structures have been optimized by DFT calculation for both complexes.

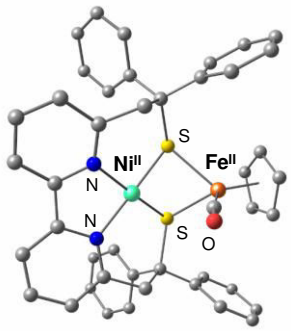

$\bar{\nu}_{CO}$ = 1929 cm^{-1} (1937 cm^{-1})
ΔEQ = 1.79 mm.s^{-1} (1.76 mm.s^{-1})
δ = 0.44 mm.s^{-1} (0.48 mm.s^{-1})

d (Å)	Ni^{II}Fe^{II}Cp	Ni^{II}Fe^{II}Cp$_{calc}$
Ni-Fe	2.9187(7)	3.034
Ni-N1	1.904(3)	1.936
Ni-N2	1.898(3)	1.936
Ni-S1	2.1745(9)	2.213
Ni-S2	2.1785(9)	2.211
Fe-S1	2.3050(10)	2.384
Fe-S2	2.2975(9)	2.382

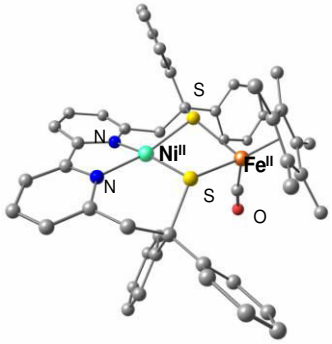

$\bar{\nu}_{CO}$ = 1926 cm^{-1} (1940 cm^{-1})
ΔEQ = 1.96 mm.s^{-1} (1.71 mm.s^{-1})
δ = 0.39 mm.s^{-1} (0.47mm.s^{-1})

d (Å)	Ni^{II}Fe^{II}Cp*	Ni^{II}Fe^{II}Cp*$_{calc}$
Ni-Fe	3.396(6)	3.400
Ni-N1	1.9050(17)	1.919
Ni-N2	1.9331(16)	1.977
Ni-S1	2.1652(7)	2.202
Ni-S2	2.1691(6)	2.230
Fe-S1	2.3257(7)	2.352
Fe-S2	2.2995(10)	2.309

Figure 16. DFT-optimized structure of **Ni^{II}Fe^{II}Cp** (left) and **Ni^{II}Fe^{II}Cp*** (right), with the corresponding experimental (calculated) spectroscopic parameters and selected bond distances of **Ni^{II}Fe^{II}Cp$_{calc}$** and **Ni^{II}Fe^{II}Cp*$_{calc}$**.

For both complexes, **Ni^{II}Fe^{II}Cp** and **Ni^{II}Fe^{II}Cp***, the distances of the optimized structure (Figure 16) are well consistent with the ones measured from the crystallographic structure. The calculated infrared spectroscopic parameters (1937; 1940 cm^{-1}) and the Mossbauer parameter (δ = 0.48; 0.47 mm.s^{-1} and ΔE = 1.76; 1.71 mm.s^{-1}) for **Ni^{II}Fe^{II}Cp** and **Ni^{II}Fe^{II}Cp***, respectively, are in agreement with experimental data (Figure 15). As the crystallographic structure and all spectroscopic parameters are reproduced by theoretical calculations performed on the optimized **Ni^{II}Fe^{II}Cp$_{calc}$** and **Ni^{II}Fe^{II}Cp*$_{calc}$** structure using the DFT approach, this demonstrates the viability of our theoretical approach for further analysis.

1.3. Solution properties of **Ni^{II}Fe^{II}Cp** and **Ni^{II}Fe^{II}Cp***.

The solution properties of **Ni^{II}Fe^{II}Cp** and **Ni^{II}Fe^{II}Cp*** have been investigated by using different techniques. First of all, the dinuclear structure is maintained in solution. This has been attested by electrospray ionization mass spectrometry (ESI-MS; 785.2 *m/z* and 855.2 *m/z*, respectively). From Nuclear Magnetic Resonance (NMR) measurements and Electron Paramagnetic Resonance (EPR), both heterodinuclear NiFe complexes are diamagnetic.

1.3.1. Redox properties of **Ni^{II}Fe^{II}Cp** and **Ni^{II}Fe^{II}Cp***.

The cyclic voltammogram (CV) of **Ni^{II}Fe^{II}Cp** and **Ni^{II}Fe^{II}Cp*** and the UV-Vis spectra recorded in MeCN are shown in Figure 17).

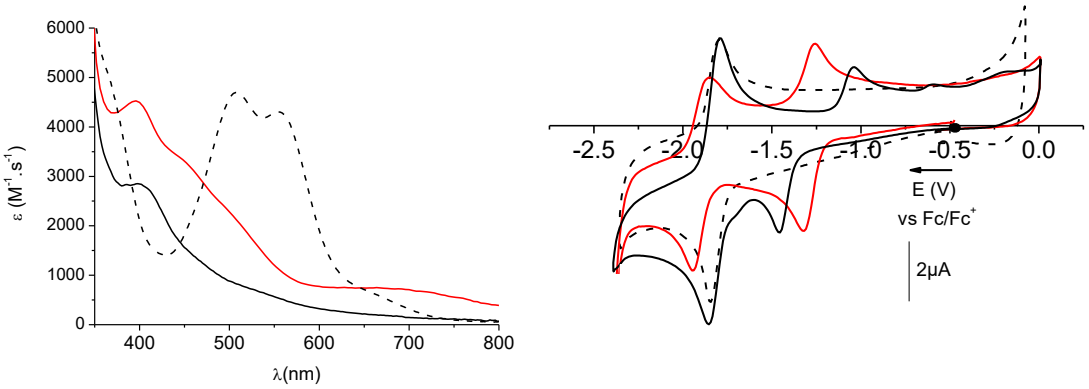

(a) (b)

Figure 17. (a) Visible absorption spectra of **Ni^{II}LS** (---) in CH_2Cl_2, **Ni^{II}Fe^{II}Cp** (—) and of **Ni^{II}Fe^{II}Cp*** (—) in MeCN (b) CVs of of **Ni^{II}LS** (---), **Ni^{II}Fe^{II}Cp** (—) and **Ni^{II}Fe^{II}Cp** (—) (0.18 mM) in MeCN solution, 0.1 M n-Bu_4NClO_4, on a glassy carbon electrode at 100 mV s^{-1} vc Fc^+/Fc

Table 2. Redox potential (V) of **Ni^{II}Fe^{II}Cp**, **Ni^{II}Fe^{II}Cp*** and **Ni^{II}LS** in MeCN*vs* Fc^+/Fc (*vs* SCE).

	E_{pC}^1	E_{pC}^2
Ni^{II}Fe^{II}Cp	-1.29 (-0.91)	-1.91 (-1.53)
Ni^{II}Fe^{II}Cp*	-1.46 (-1.08)	-1.86 (-1.48)
Ni^{II}LS	-1.86 (-1.48)	

The electronic absorption spectrum of the brown solution of **Ni^{II}Fe^{II}Cp** shows a broad band at 700 nm, two shoulders at 500 and 450 nm and a transition at 400 nm while **Ni^{II}Fe^{II}Cp*** displays a unique transition at 403 nm, which extends to 600 nm. Both spectra notably differ to that of **Ni^{II}LS**, which displays two main transitions at 503 and 556 nm.

The CV of **Ni^{II}LS** displays a reversible one-electron reduction Ni^{II}/Ni^{I} wave at E_{pc}=-1.86 V.[27] In comparison, the CV of **Ni^{II}Fe^{II}Cp** recorded in MeCN (Figure 17, b) displays two reversible and diffusion controlled one-electron reduction waves at E_{pc}^1= –1.29 V and E_{pc}^2=–1.91 V *vs* Fc^+/Fc (-0.91 and -1.53 V vs SCE) (Table 2). These waves can be assigned to the successive reductions of the Ni^{II} ion to Ni^{I} (formation of **Ni^{I}Fe^{II}Cp**) and of the bipyridine moiety in LS (to form the radical form of the ligand). This attribution arises from DFT calculations (see below). (Equations 1 and 2)

Ni^{II}Fe^{II}Cp + e- → **Ni^{I}Fe^{II}Cp** (Equation 1)

Ni^{I}Fe^{II}Cp + e- → **LS$^{\bullet}$Ni^{I}Fe^{II}Cp** (Equation 2)

Concerning the redox properties of **$Ni^{II}Fe^{II}Cp^*$**, its CV recorded in MeCN displays two one electron reduction processes (Figure 17). An irreversible peak is located at E_{pc}^{1} = -1.46 V *vs* Fc^+/Fc, assigned to the reduction of Ni^{II} into Ni^{I} (see above). The corresponding **$Ni^{I}Fe^{II}Cp^*$** complex undergoes a fast chemical reaction as evidenced by the appearance on the reverse scan of an irreversible reduction peak at E_{pa} = -0.94 V. A quasi-reversible wave at E_{pc}^{2}= -1.86 V is also observed, which can be tentatively assigned to the reduction of the bipyridine moiety in LS, leading to the formation of a **$LS^{\bullet}Ni^{I}Fe^{II}Cp^*$** species (Equations 3 and 4). This peak is twice intense than the peak of the first redox system. This can be explained by the fact that the diffusion rate of the double reduced species is slower than the first reduced species. Besides, the potential is identical to the redox system of the Ni^{II}LS complex, suggesting that there could be a mixture of the reduced species of **$Ni^{I}Fe^{II}Cp^*$** and Ni^{II}LS resulting from partial degradation of **$Ni^{I}Fe^{II}Cp^*$**.

$Ni^{II}Fe^{II}Cp^* + e^- \rightarrow Ni^{I}Fe^{II}Cp^*$ (Equation 3)

$Ni^{I}Fe^{II}Cp^* + e^- \rightarrow LS^{\bullet}Ni^{I}Fe^{II}Cp^*$ (Equation 4)

This electrochemical behavior notably differs from that of **$Ni^{I}Fe^{II}Cp$**, for which the two reduction processes were reversible. Interestingly, while a cathodic shift of the Ni^{II}/Ni^{I} reduction process compared to **$Ni^{II}Fe^{II}Cp$** (E_{Pc} = –1.29 V) is observed, an anodic shift of the ligand based reduction process (**$Ni^{II}Fe^{II}Cp$**, $E_{1/2}$ = –1.90 V) occurs. Cp* being a more electron donating ligand than Cp, the Ni-bound thiolate ligands in **$Ni^{II}Fe^{II}Cp^*$** bear a larger electron density leading to the expected cathodic shift observed on the first Ni-based reduction process. Regarding the anodic shift observed on the second reduction process and the irreversibility vs reversibility of the Ni^{II}/Ni^{I} redox process in **$Ni^{II}Fe^{II}Cp^*$** and **$Ni^{II}Fe^{II}Cp$**, this could be due to the fact that the two one-electron reduced species are structurally different. Consequently, the redox potentials of the second reduction process cannot be directly compared. The different redox properties between these two complexes nicely illustrate how the organometallic iron unit can modulate the electronics of the nickel center, as in the [NiFe] hydrogenase. Indeed, the redox potential of the Ni^{II}/Ni^{I} couple of the mononuclear Ni^{II} complex, **$Ni^{II}LS$**, is shifted from -1.86 V *vs* Fc^+/Fc to -1.29 and -1.46 V with a ΔE = 0.55 V and ΔE = 0.38 V for **$Ni^{II}Fe^{II}Cp$** and **$Ni^{II}Fe^{II}Cp^*$**, respectively. The Ni unit thus becomes more easily reducible, and the Ni^{I} oxidation state is stabilized by interaction with the Fe unit.

1.4. Electrocatalytic activity of $Ni^{II}Fe^{II}Cp$ and $Ni^{II}Fe^{II}Cp^*$ for H_2 production.

The electrocatalytic activity of both complexes for proton reduction has been investigated. Upon addition of Et_3NHBF_4 as a proton source (pKa = 18.6 in MeCN),[37] a catalytic process (E_{cat} = –1.91 V and -1.86 V vs Fc^+/Fc, measured at the half-wave) is developed on the top of the second reversible wave for **$Ni^{II}Fe^{II}Cp$** (Figure 18, left) and **$Ni^{II}Fe^{II}Cp^*$** (Figure 18, right), respectively.

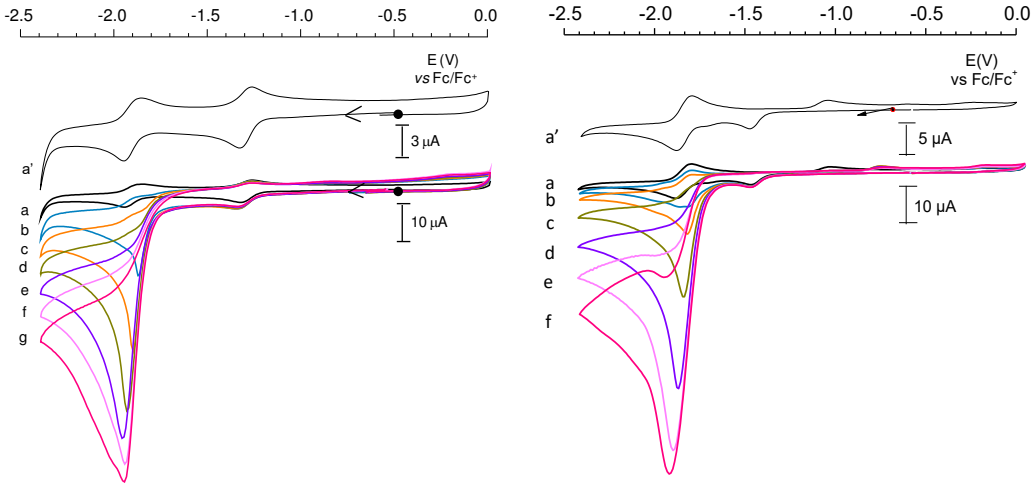

Figure 18. CVs of **$Ni^{II}Fe^{II}Cp$** (left) (0.18 mM) before (a and a') and after (b-g) addition of various amounts of Et_3NHBF_4 in MeCN solution, 0.1 M n-Bu_4NClO_4, on a glassy carbon electrode at 100 mV s^{-1}: (b) 5 equiv.; (c) 10 equiv.; (d) 15 equiv.; (e) 20 equiv.; (f) 25 equiv; (g) 30 equiv; CVs of **$Ni^{II}Fe^{II}Cp^*$** (right): (b) 1 equiv.; (c) 5equiv.; (d) 10 equiv.; (e) 15 equiv.; (f) 20 equiv.

Bulk electrolysis experiments performed at –1.85 V vs Fc^+/Fc on Hg-pool cathode confirm electrocatalytic production of H_2 (16 turnovers (TON) achieved, turnover frequency (TOF) = 10 h^{-1}, 70% conversion within 100 minutes) with faradic yields of 70% from Et_3NHBF_4 (50 equiv.) solution in the presence of **$Ni^{II}Fe^{II}Cp$**. In the same conditions, with **$Ni^{II}Fe^{II}Cp^*$**, 17 TON were achieved with 72% conversion within 100 minutes (TOF = 11 h^{-1}), with faradic yields of 76 % from Et_3NHBF_4 (50 equiv.) solution (Figure 19).

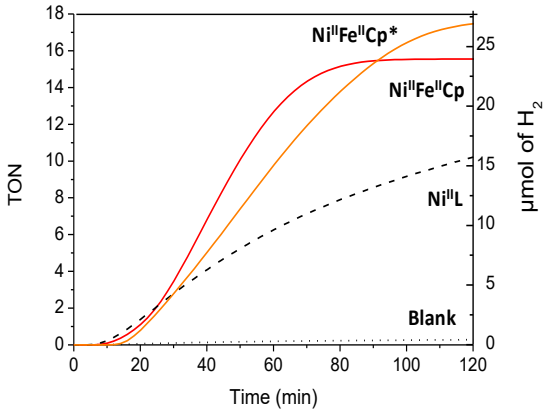

Figure 19. Dihydrogen production during bulk electrolysis at -1.86 V on Hg-pool cathode in the presence of **Ni^{II}Fe^{II}Cp** (—), **Ni^{II}Fe^{II}Cp*** (—) and **Ni^{II}L** (0.20 mM) and Et_3NHBF_4 (50 equiv.) in MeCN solution, 0.1 M *n*-Bu_4NClO_4.

While the mononuclear Fe^{II} precursor, $[CpFe^{II}(CO)(MeCN)_2]^+$, displays no reactivity toward proton reduction under similar conditions, $[Ni^{II}L]$ produces H_2 but with a minor activity (9 turnovers achieved within 100 minutes, TOF = 6 h^{-1}). Both heterodinuclear NiFe complexes have comparable reactivities. In the following part, all experimental data have been carried out with **Ni^{II}Fe^{II}Cp**.

When electrocatalytic studies are carried out on GC electrode, rinse test experiments and Scanning Electron Microscopy (SEM) has been performed. These experiments show that the CV profile of a solution of Et_3NHBF_4 (solution 2, second scan, —) is analogous when the GC electrode was previously cycled into solution 1 (acid + catalyst, —) after washing with CH_2Cl_2 or into the same solution 2 (acid only, first scan).

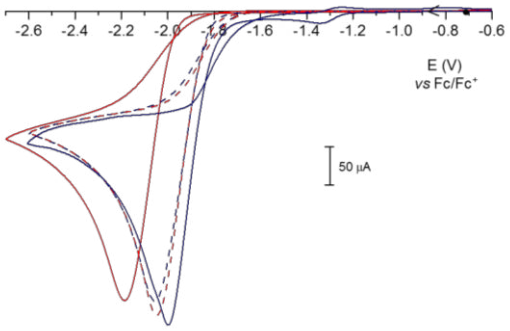

Figure 20. CV of **Ni^{II}Fe^{II}Cp** (—, 1.0 mM) in the presence of Et_3NHBF_4, 20 equiv. in MeCN solution, 0.1 M *n*-Bu_4NClO_4 (solution 1), compared to the CVs of Et_3NHBF_4, 20 equiv. (solution 2, first — and second --- scan, respectively) and of solution 2 after modifying the GC electrode by a CV scan into solution 1 followed by washing with CH_2Cl_2 (---).

This electrochemical study confirms that there is no metal-based surface-confined species responsible for the observed catalytic activity (Figure 20). In the same vein, two glassy carbon electrodes have been analyzed by SEM: (i) after recording a CV in the presence of $EtNHBF_4$ (20 equiv.) and washed with MeCN and (ii) after recording a CV in the presence of Et_3NHBF_4 (20 equiv.) and

washed with MeCN and CH_2Cl_2. On both pictures, no deposition is observed (Figure 21), confirming the absence of surface-confined species.

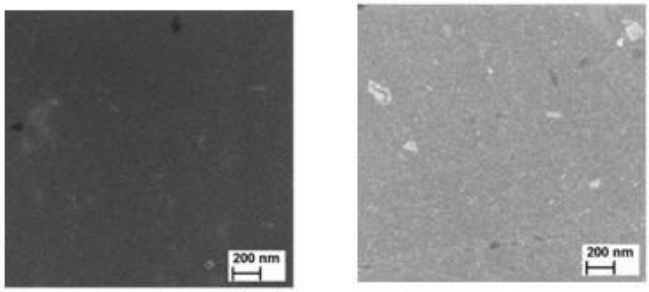

Figure 21. Scanning electron micrographs of glassy carbon electrodes subjected to electrocatalysis in dry acetonitrile solution of **$Ni^{II}Fe^{II}Cp$** (0.20 mM), Et_3NHCl (20 equiv.) and $n Bu_4NClO_4$ (0.1 M) and further rinsed with MeCN and CH_2Cl_2: right and left, respectively)

Kinectic rates associated to catalytic reactions is important for the comprehension of the efficiency of a catalyst. Therefore, electrochemical methods have been developed to extract such information. When the catalytic reaction speed rate is large enough, the establishment of a steady state is observed at which the diffusion of the electrogenerated species is compensated by its rapid reaction with the substrate. This happens in the so called "pure kinetics" conditions. For a two-electron multi-step catalytic reaction, such as proton reduction, the form of the catalytic wave is a sigmoid where a maximum is reached, called "plateau current" (Figure 22). This characteristic behavior has been explained by Savéant et al.[38] However, secondary phenomena including deactivation of the catalyst, consumption of the substrate or passivation process at the electrode surface by the product modify the sigmoid shape of the CV. In this context, kinetic values given by the analysis of the plateau current are not easily accessible. The foot of the wave analysis (FOWA) has been thus developed. It is based on the fact that at the foot of the wave, the measured currents are mainly under the control of the catalyzed reaction, allowing the negligence of secondary phenomena for the determination of kinetic rates.

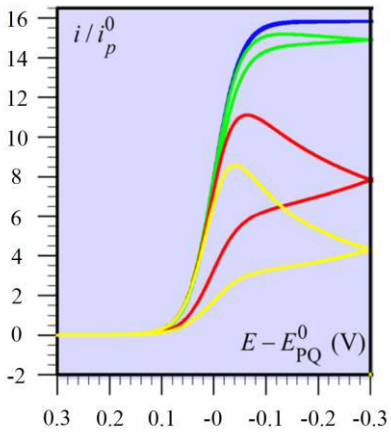

Figure 22. Different behavior of electrocatalytic waves for a typical system: sigmoid wave in "pure kinetics" conditions (bleu), and consumption of the substrate (green, red, yellow), v = 100 $Mv.s^{-1}$, [C] 0 =1 mM,.[38] Note that in this figure, the reduction currents are positive.

To gain more insight into the kinetics of the electrocatalytic hydrogen production with **$Ni^{II}Fe^{II}Cp$ and $Ni^{II}Fe^{II}Cp^*$**, FOWA has been carried out[38] and allowed the determination of a second-order rate constant (k_{cat}) of 2.5 ± 0.3 10^4 $M^{-1}{\cdot}s^{-1}$ and 7.7 ± 0.4 10^3 $M^{-1}{\cdot}s^{-1}$, respectively which rank both catalysts high in the series of H_2-evolving systems for which such rate constants were measured (10^6 - 10^4 $M^{-1}{\cdot}s^{-1}$ range, the best being iron-porphyrin).[14,39-41.] **$Ni^{II}Fe^{II}Cp$** appears to be faster than the **$Ni^{II}Fe^{II}Cp^*$** complex. This can be explained by a lack of stability of the latter complex

Under the same conditions the mononuclear **$Ni^{II}LS$** catalyst gives a k_{cat} value of 2.2± 0.3 10^3 $M^{-1}{\cdot}s^{-1}$, that is one order of magnitude lower than that of **$Ni^{II}Fe^{II}Cp$**. From these numbers and the conditions used for bulk electrolysis experiments ([$EtNHBF_4$] = 1.10^{-2} M), turnover frequency (TOF) values of 250 s^{-1} and 22 s^{-1} can be determined for **$Ni^{II}Fe^{II}Cp$** and **$Ni^{II}LS$**, respectively. These values reflect the intrinsic activity of the catalysts. They are significantly larger than those tentatively derived from bulk electrolysis experiments (10 h^{-1} and 6 h^{-1} for **$Ni^{II}Fe^{II}Cp$** and **$Ni^{II}LS$**, respectively). Such a discrepancy arises from the fact that not all the catalyst present in the bulk solution is active but only the fraction present in the convection-reaction layer at the immediate vicinity of the electrode. In addition, the current measured during bulk electrolysis experiments is limited by mass transport and consumption of the proton source.

The experimentally determined k_{cat} values can be translated into extrapolated TOF_{max} values in 1M acid solution (the standard condition proposed for a rational benchmark of performances of H_2 evolution catalysts using catalytic Tafel plot) assuming that the reaction remains first order in acid.[39] The TOF_{max} values of **$Ni^{II}Fe^{II}Cp$** and **$Ni^{II}Fe^{II}Cp^*$** of 2.5.10^4 s^{-1} and 7.7.10^3, respectively are larger especially for **$Ni^{II}Fe^{II}Cp$** compared to **$Ni^{II}LS$** (TOF_{max} value o= 2.2.10^3 s^{-1}). Based on an EECC mechanism (as proposed below, with E corresponding to an electron transfer step and C to a chemical reaction, here protonation) together with a E_{cat} value of –1.90 V *vs* Fc^+/Fc for both NiFe complexes and an apparent equilibrium potential of the H^+/H_2 couple (–1.21 V *vs* Fc^+/Fc),[85] we could depict the red trace in the catalytic Tafel plot shown in Figure 23, relating turnover frequency and driving force of the reaction, i.e. the overpotential related to H_2 evolution under the conditions used.[39] Overpotential is defined as the difference between the applied and the tabulated values of the standard potential of H^+/H_2.

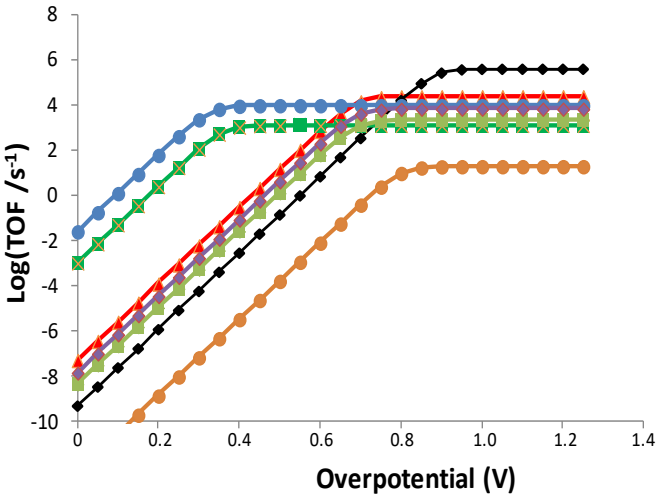

Figure 23. Catalytic Tafel plots relating turnover frequency and driving force of H_2 evolution, and performances of **$Ni^{II}Fe^{II}Cp$** with previously reported H_2-evolving electrocatalysts: **$Ni^{II}Fe^{II}Cp$** (red); **$Ni^{II}Fe^{II}Cp^*$** (purple); **$Ni^{II}LS$** (light green); $[Mn(mesbpy)(CO)_3(MeCN)](OTf)$ (mesbpy=6,6'-dimesityl-2,2'- bipyridine) (dark green);[6] $[Ni(xbsms)Mn(CO)_3(H_2O)]^+$ ($xbsms^{2-}$ a S4 donor ligand) (light green);[41] FeTPP(black);[14,39,62] $[Ni^{II}(P_2^{Ph}N_2^{C6H4X})_2]^{2+}$ (X= $CH_2P(O)$) (orange);[39] $Co^{II}(dmgH)_2py$ (blue).[39]

Although not rivaling with DuBois' bio-inspired Ni complexes,[42] **$Ni^{II}Fe^{II}Cp$** and **$Ni^{II}Fe^{II}Cp^*$** complexes displays significant catalytic activity ($log(TOF)/s^{-1}$)>1) for overpotential values larger than 500 mV and therefore compares well with other electrocatalysts based on non-noble metals,[39,43] including FeTPP,[40] a mononuclear Mn complex[41] or a $Ni^{II}Mn^{I}$ mimic[14] of the active site of [NiFe] hydrogenase.

1.5. Investigation of the catalytic mechanism of **$Ni^{II}Fe^{II}Cp$** and comparison with the [NiFe] hydrogenase.

With the aim of better understanding the electrocatalytic mechanism of H_2 production, efforts have been carried out to generate and characterize potential intermediate species. This work has been only carried out with **$Ni^{II}Fe^{II}Cp$,** because the intermediates with **$Ni^{II}Fe^{II}Cp^*$** are much less stable.

1.5.1. Characterization of $Ni^{I}Fe^{II}Cp$, an active Ni-L model.

The reaction between **$Ni^{II}Fe^{II}Cp$** and 1 equiv. of cobaltocene leads to the precipitation of a dark violet powder (Figure 24a). Suitable X-ray crystals couldn't be obtained because of their instability in solution, even at low temperature. However, this paramagnetic species has been assigned to one electron reduced species $[(LS)Ni^{I}\mu(CO)Fe^{II}Cp]$, **$Ni^{I}Fe^{II}Cp$**, based on several spectroscopic results described below. **$Ni^{I}Fe^{II}Cp$** is only soluble in THF and has been characterized by UV-Vis spectroscopy (Figure 24b). **$Ni^{I}Fe^{II}Cp$** displays two transitions at 570 nm and at 800 nm. The transition at 800 nm suggests that there is delocalization of the charge through the two metallic centers.

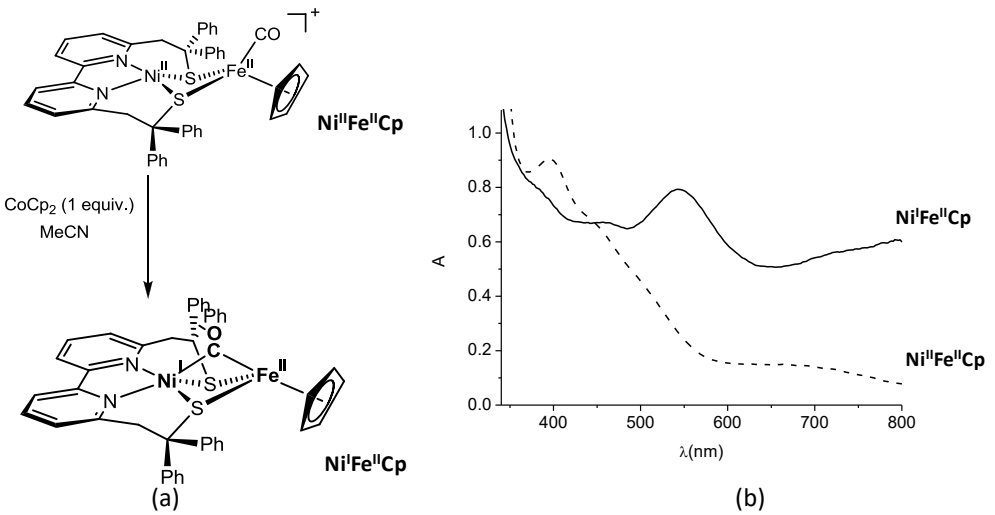

Figure 24. (a) Synthesis of **Ni^{I}Fe^{II}Cp** from **Ni^{II}Fe^{II}Cp** in the presence of cobaltocene (b) Visible absorption spectra of **Ni^{II}Fe^{II}Cp** (---, 1 mM in MeCN, d = 2 mm) and of **Ni^{I}Fe^{II}Cp** (—, 1 mM in THF, d = 2 mm).

The oxidation state of the **Ni^{I}Fe^{II}Cp** complex was attested by EPR and Mössbauer spectroscopy. The *S* = ½ EPR signature powder exhibits a characteristic axial signal of a Ni^{I}-based compound with a $g_{//}$ = 2.168 and $g_{\perp}$ = 2.060 (Figure 26). The Mössbauer doublet is characterized by δ = 0.44 mm·s^{-1} and ΔE_Q = 1.79 mm·s^{-1} parameters, which are similar to those of the initial **Ni^{II}Fe^{II}Cp** (Figure 25) demonstrating that the Fe site remains a low spin Fe^{II} ion with a similar coordination sphere.

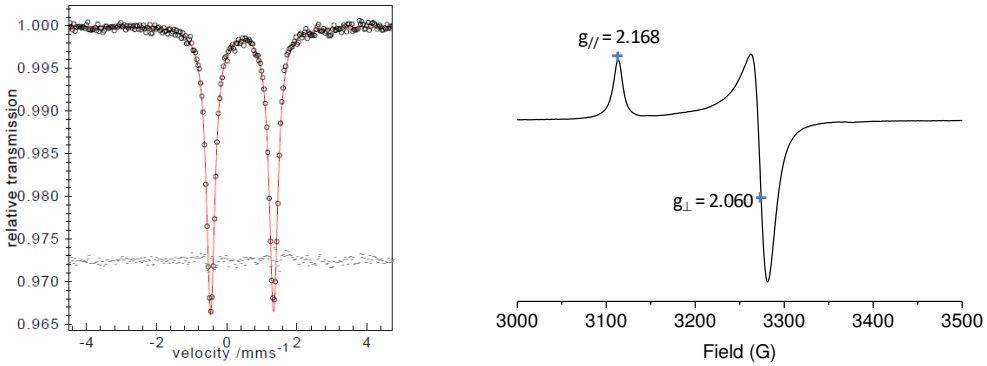

Figure 25. (a) Mössbauer spectrum of **Ni^{I}Fe^{II}Cp** recorded at 80 K obtained on solid samples. The red solid line through the experimental data (empty black circles) is a simulation using Lorentzian line doublets with the following parameters **Ni^{I}Fe^{II}Cp:** δ = 0.44 mm·s^{-1} and ΔE_Q = 1.79 mm·s^{-1}; (b) X-band EPR spectrum of **Ni^{I}Fe^{II}Cp** (powder, 100 K).

The CO vibration is shifted from 1929 cm^{-1} (**Ni^{II}Fe^{II}Cp**) to 1770 cm^{-1} in agreement with a bridging CO between the Fe and the Ni ions. It has been observed that in the course of bulk electrolysis experiments performed in wet MeCN ([H_2O > 0.5 M] at -1.3 V) **Ni^{I}Fe^{II}Cp** adsorbs at the surface of GC electrodes. This species can indeed be redissolved in THF and displays the same spectroscopic properties that the powder obtained from the reaction of a MeCN solution of **Ni^{II}Fe^{II}Cp** with one equiv. of cobaltocene (Figures 24, 25).

During cobaltocene reduction of **$Ni^{II}Fe^{II}Cp$,** another minor side-product co-precipitates with **$Ni^{I}Fe^{II}Cp$** with a CO vibration at 1888 cm^{-1} (Figure 26). The relative intensity of this feature (1888 cm^{-1}) can be slightly modulated as a function of several parameters including the amount of water. Based on this IR-vibration and on the fact that no additional feature can be observed by neither EPR nor Mössbauer spectroscopy, a theoretical structure has been calculated initiated from **$Ni^{I}Fe^{II}Cp_{calc}$** (see below), in which one water molecule has been added on the Ni site, **$Ni^{I}Fe^{II}Cp(OH_2)_{calc}$**.

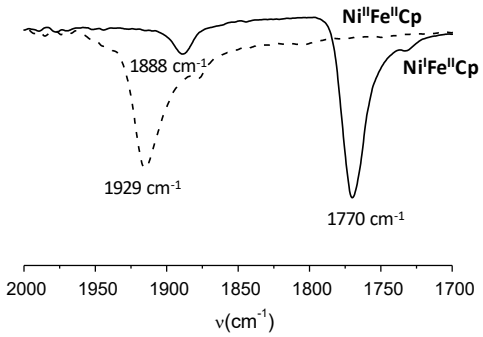

Figure 26. Infrared spectra (CO stretching region) of **$Ni^{II}Fe^{II}Cp$** before (---) and (—) after addition of cobaltocene.

During the optimization process, the CO is shifted to a terminal position at the Fe site, and the predicted CO vibration (1849 cm^{-1}) is consistent with the experimental 1888 cm^{-1} one. Furthermore, the Ni ion remains at the +I oxidation state in **$Ni^{I}Fe^{II}(H_2O)_{calc}$** and the iron site a low spin Fe^{II} (Figure 26, 27). Consequently, the CO vibration (1888 cm^{-1}) can be assigned to the $[(LS)Ni^{I}(OH_2)Fe^{II}(Cp)(CO)]^{+}$ complex, **$Ni^{I}Fe^{II}Cp(OH_2)$**.

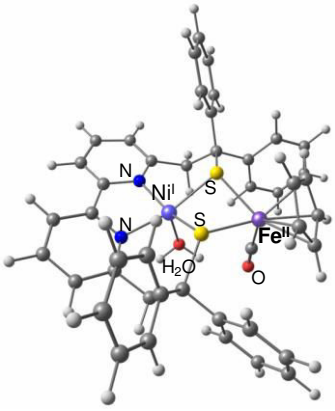

$\bar{\nu}_{CO}$ = 1888 cm^{-1} (1849 cm^{-1})

d (Å)	**$Ni^{I}Fe^{II}Cp\text{-}(H_2O)_{calc}$**
Ni-Fe	3.308
Ni-N1	1.949
Ni-N2	1.957
Ni-S1	2.235
Ni-S2	2.256
Fe-S1	2.338
Fe-S2	2.338
Ni-H_2O	2.200

Figure 27. DFT optimized structure of $[(LS)Ni^{I}(OH_2)Fe^{II}(Cp)(CO)]^{+}$, **$Ni^{I}Fe^{II}Cp(H_2O)_{calc}$** and selected bond distances of **$Ni^{I}Fe^{II}Cp(H_2O)_{calc}$**.

The structure of **$Ni^{I}Fe^{II}Cp$** has been confirmed by DFT calculations. The CO ligand indeed bridges the Ni and the Fe sites. All calculated spectroscopic parameters on its optimized structure (**$Ni^{I}Fe^{II}Cp_{calc}$**) are in reasonable to excellent agreement with the experimental data (Figure 28).

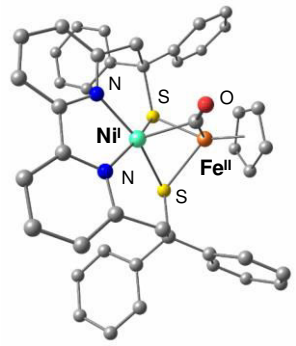

$\bar{\nu}_{CO}$ = 1770 cm^{-1} (1788 cm^{-1})
ΔE_Q = 1.82 $mm \cdot s^{-1}$ (1.83 $mm \cdot s^{-1}$)
δ = 0.39 $mm \cdot s^{-1}$ (0.46 $mm \cdot s^{-1}$)
$g_\perp$ = 2.05, $g_\parallel$ = 2.16
(g_x = 2.06, g_y = 2.07, g_z = 2.15)

d (Å)	$Ni^{I}Fe^{II}Cp_{calc}$
Ni-Fe	2.516
Ni-N1	1.985
Ni-N2	1.985
Ni-S1	2.332
Ni-S2	2.324
Fe-S1	2.336
Fe-S2	2.341
Ni-CO	2.064

Figure 28. DFT-optimized structure of the one-electron reduced form, **$Ni^{I}Fe^{II}Cp$**, with the corresponding experimental (calculated) spectroscopic parameters and selected bond distances of **$Ni^{I}Fe^{II}Cp_{calc}$**.

Upon reduction, the Ni···Fe distance is shortened to 2.52 Å likely due to the presence of the bridging carbonyl (Ni-CO: 2.064 Å and Fe-CO: 1.803 Å). The single occupied molecular orbital (SOMO, Figure 29) is mainly centered on the Ni ion (76 and 1 % on the Ni and Fe sites, respectively, *vs* 81 and 15 % in Ni-SI_a)[44] with partial delocalization on the bipyridine moiety of LS (7% on the N atoms). This confirms that the Ni is at its +1 oxidation state.

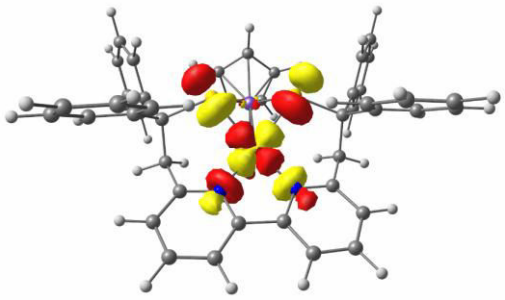

SOMO composition: 76% Ni, 1% Fe, 12% S, 7% N and 4% remaining ligand

Figure 29. Localized Singly Molecular Orbital (SOMO) of **$Ni^{I}Fe^{II}Cp_{calc}$**.

1.5.2. Characterization of **Ni^{II}Fe^{II}Cp(H)**, an active Ni-R model.

Our next attempt was focused on the detection of a metal-hydride species (Figure 30).

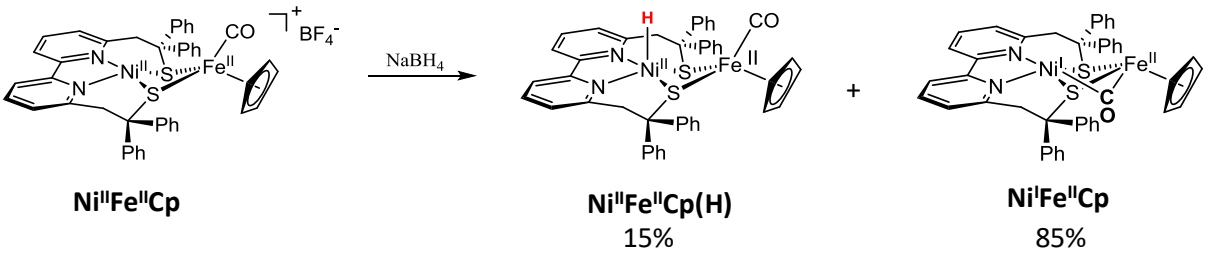

Figure 30. Synthesis of **Ni^{II}Fe^{II}Cp(H)** from **Ni^{II}Fe^{II}Cp** in the presence of an excess of $NaBH_4$ in MeCN. During this reaction, 85 % of **Ni^{I}Fe^{II}Cp** is produced.

When an excess of $NaBH_4$ (6 equivalents) is added to a MeCN solution of **Ni^{II}Fe^{II}Cp**, the IR spectrum of the solution displays a new CO vibration (1838 cm^{-1}), in addition to those (1770 and 1888 cm^{-1}) attributed to **Ni^{I}Fe^{II}Cp** and its aquo adduct, respectively. While the formation of **Ni^{I}Fe^{II}Cp** simply reflects the reducing nature of BH_4^- ions, the new feature at 1838 cm^{-1}, which shifts to 1844 cm^{-1} when using $NaBD_4$, can be confidently assigned to a hydride derivative (Figure 31).

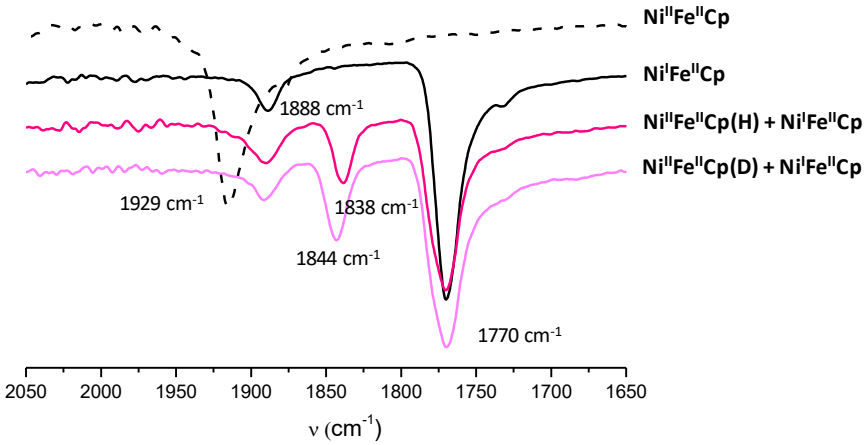

Figure 31. Infrared spectra (CO stretching region) of **Ni^{II}Fe^{II}Cp** before (---) and after addition of (—) $CoCp_2$, (—) $NaBH_4$, (—) $NaBD_4$.

In the ^{1}H NMR spectrum (Figure 32), a sharp peak at –6.80 ppm is observed consistent with a diamagnetic species containing a metal-bound hydride ligand, named **Ni^{II}Fe^{II}Cp(H)** hereafter. Based on the relative intensity of this peak with those accounting for **Ni^{I}Fe^{II}Cp**, **Ni^{II}Fe^{II}Cp(H)** represents maximum 15% of the sample.

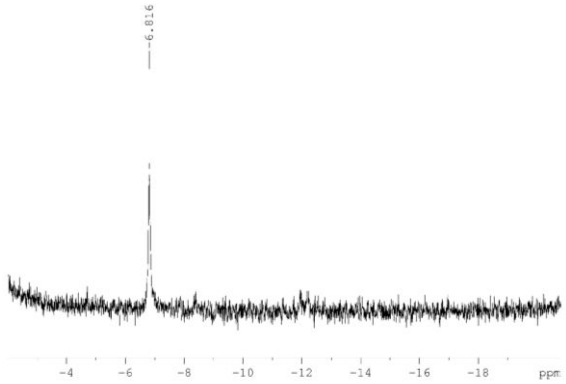

Figure 32. ^{1}H (hydride region) NMR spectrum (400 MHz, d_8-thf) of the product of reaction between **Ni^{II}Fe^{II}Cp** and $NaBH_4$.

The optimized **Ni^{II}Fe^{II}Cp(H)$_{calc}$** structure indicates that the hydride ligand is terminally bound to the Ni^{II} site and that the CO ligand remains terminally bound to the Fe^{II} site (Figure 33). The optimized distance between the Ni and the Fe sites is of 3.336 Å, thus longer than the Ni-Fe distance in **Ni^{II}Fe^{II}Cp.**

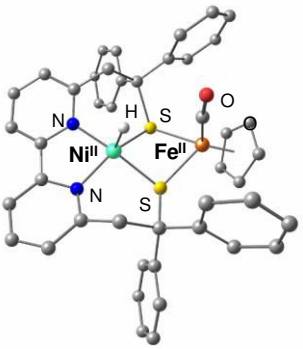

$\bar{\nu}_{CO}$ = 1838 cm^{-1} (1866 cm^{-1})
^{1}H NMR: -6.80 ppm (-3.90 ppm)

d (Å)	**Ni^{II}Fe^{II}Cp(H)$_{calc}$**
Ni-Fe	3.336
Ni-N1	1.866
Ni-N2	1.928
Ni-S1	2.297
Ni-S2	2.179
Fe-S1	2.321
Fe-S2	2.287
Ni-H	1.548

Figure 33. DFT-optimized structure of **Ni^{II}Fe^{II}Cp(H)**, with the corresponding experimental (calculated) spectroscopic parameters and selected bond distances of **Ni^{II}Fe^{II}Cp(H)$_{calc}$**.

The DFT-predicted spectroscopic parameters (IR and NMR) agree well with the experimental data (Figure 33) validating the theoretical model. According to the **Ni^{II}Fe^{II}Cp(H)$_{calc}$** optimized structure, the hydride is bound to the Ni site in a terminal position with Ni-H of 1.55 Å and the CO remains terminally bound to the Fe site. Both Ni and Fe ions are at the +II oxidation state.

1.5.3. Towards **Ni^{III}Fe^{II}Cp(H)**, a Ni-C model.

After the characterization of **Ni^{I}Fe^{II}Cp** and **Ni^{II}Fe^{II}Cp(H)**, models of the Ni-L and the Ni-R states, respectively, the next target was to obtain a model of the Ni-C state. As no reaction is obvious from the CV recorded in the presence of Et_3NH^+, addition of a stronger acid was tested. Addition of HBF_4 (pKa = 0.1)[37] to **Ni^{I}Fe^{II}Cp** in MeCN yields 0.40 equiv of H_2 (80% yield, as determined by gas

chromatography analysis *vs* proton concentration) with the concomitant regeneration of **Ni^{II}Fe^{II}Cp** (Figure 34, Equation 2).

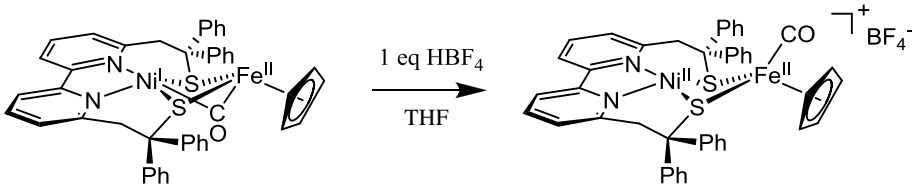

Ni^{I}Fe^{II}Cp **Ni^{II}Fe^{II}Cp**

Figure 34. Synthesis of **Ni^{II}Fe^{II}Cp** from **Ni^{I}Fe^{II}Cp** in the presence of 1 equiv. of HBF_4 in THF.

$$2\ Ni^{I}Fe^{II}Cp + 2\ H^{+} \rightarrow 2\ Ni^{II}Fe^{II}Cp + H_2 \qquad \text{Equation 2}$$

Such a reactivity suggests the transient formation of the **Ni^{III}Fe^{II}Cp(H)** species under these conditions, which either evolves H_2 in a homolytic bimolecular fashion, or reacts with a proton to produce H_2 heterolytically after *in situ* reduction to **Ni^{II}Fe^{II}Cp(H)** by a neighboring molecule of **Ni^{I}Fe^{II}Cp**. Nevertheless, despite strong efforts, we didn't succeed in detecting **Ni^{III}Fe^{II}Cp(H)**.

1.5.4. Identification of the two-electron reduced species of **Ni^{II}Fe^{II}Cp**.

In the CV of **Ni^{II}Fe^{II}Cp**, the second reversible wave is attributed to the reduction of the bipyridine moiety to form **LS$^{\bullet}$Ni^{I}Fe^{II}Cp** (Figure 17). This is attested by a DFT optimized structure of the one-electron reduced form of **Ni^{I}Fe^{II}Cp** that displays a strong radical character on the bipyridine ligand bound to the Ni^{I} site. This double-reduced species displays two unpaired electrons distributed in two SOMOs (Single Occupied Molecular Orbitals). The electronic density is mainly localized on the Ni for SOMO1, while the second electron is localized on the ligand at 89% for SOMO2 (Figure 35).

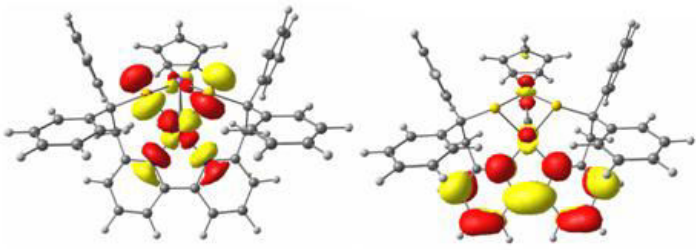

SOMO1 composition: 59% Ni, 3% Fe, 16% S, 11% N and 11% remaining ligand
SOMO2 composition: 6% Ni, 4% Fe, 1% S, 22% N and 67% remaining ligand

Figure 35. Magnetic orbitals of **LS$^{\bullet}$Ni^{I}Fe^{II} Cp**.

1.6. Effect of CO on H_2 production.

1.6.1. Electrocatalytic activity in the presence of CO.

In a first attempt to characterize the effect of CO on both NiFe complexes, electrochemical studies were performed in the presence of CO (Figure 36, Table 3). The redox properties of both complexes

are influenced by the presence of CO, but in a different manner. With **Ni^{II}Fe^{II}Cp** (at -1.91 V), the second reduction process is mainly modified, while in the case of **Ni^{II}Fe^{II}Cp*** the first reducing system (at -1.29 V) becomes fully irreversible. This implies that CO interacts with **Ni^{I}Fe^{II}Cp*** and with **LS$^{\bullet}$Ni^{I}Fe^{II}Cp.**

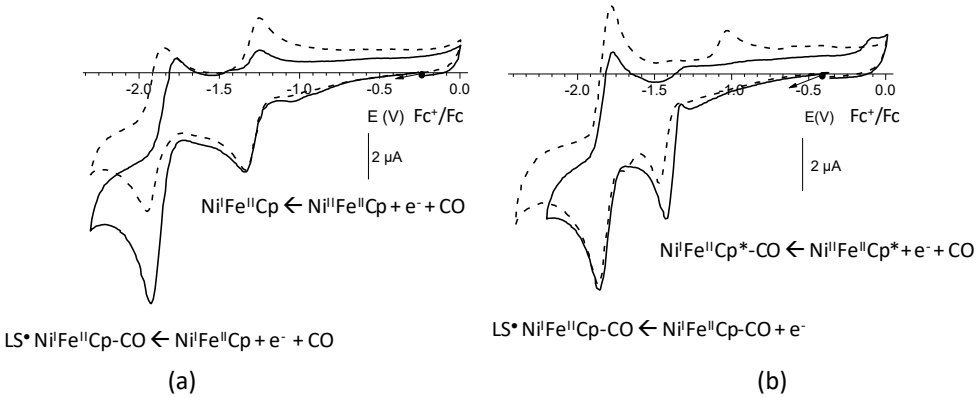

Figure 36. (a) CVs of **Ni^{II}Fe^{II}Cp** before CO (---) and after CO (—). (b) CVs of **Ni^{II}Fe^{II}Cp*** before CO (---) and after CO (—); [**Ni^{II}Fe^{II}Cp** and **Ni^{II}Fe^{II}Cp***]= 0.2 Mm in MeCN.

Table 3. Redox potential (V) of **Ni^{II}Fe^{II}Cp**, **Ni^{II}Fe^{II}Cp*** and **Ni^{II}LS** in MeCNvs Fc^{+}/Fc.

	E_{pc}^{1}	E_{pc}^{2}
Ni^{II}Fe^{II}Cp	-1.29	-1.91
Ni^{II}Fe^{II}Cp*	-1.46	-1.86
Ni^{II}Fe^{II}Cp + CO	-1.29	-1.91
Ni^{II}Fe^{II}Cp* + CO	-1.4	-1.86

As described previously, both complexes present a catalytic effect at -1.91 V and -1.86 V for **Ni^{II}Fe^{II}Cp** and **Ni^{II}Fe^{II}Cp***, respectively, in the presence of Et_3NHBF_4 (Figure 37a and 37b).

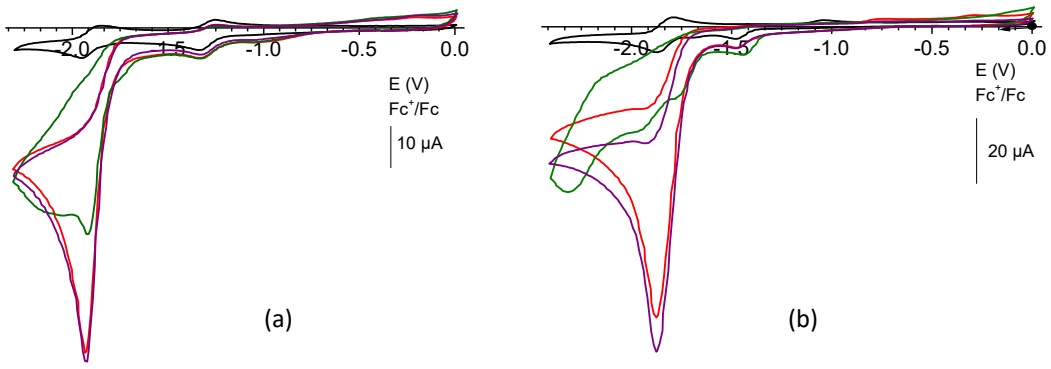

Figure 37. (a) CV of **Ni^{II}Fe^{II}Cp** (—), in the presence of 15 equiv. of EtNHBF$_4$ (—), and CO (—), CO removed (—).(b) CV of **Ni^{II}Fe^{II}Cp*** (—), in the presence of 15 equiv. of Et_3NHBF_4 (—), and CO (—), CO removed (—). [**Ni^{II}Fe^{II}Cp(*)**] = 0.2 mM.

For **Ni^{II}Fe^{II}Cp** (Figure 37a), when CO is bubbled into the solution containing 15 equiv. of Et_3NHBF_4, only a partial inhibition is observed (CV in green) but the activity is fully recovered when CO is

replaced by argon (CV in purple). Unlike **Ni^{II}Fe^{II}Cp**, the activity **Ni^{II}Fe^{II}Cp*** (Figure 37b) is almost fully inhibited in the presence of CO and recovered when CO is removed from the solution. Consequently, CO inhibits the catalytic activity of **Ni^{II}Fe^{II}Cp*** in the presence of protons.

1.6.2. EPR spectroscopy of **Ni^{II}Fe^{II}Cp*** in the presence of CO.

In order to get more insights into the inhibition mechanism by CO, EPR experiments have been carried out in the case of **Ni^{II}Fe^{II}Cp*** (Figure 38) for which a stronger effect of CO has been observed combined with a more pronounced modification of the first reduction process in the presence of CO.

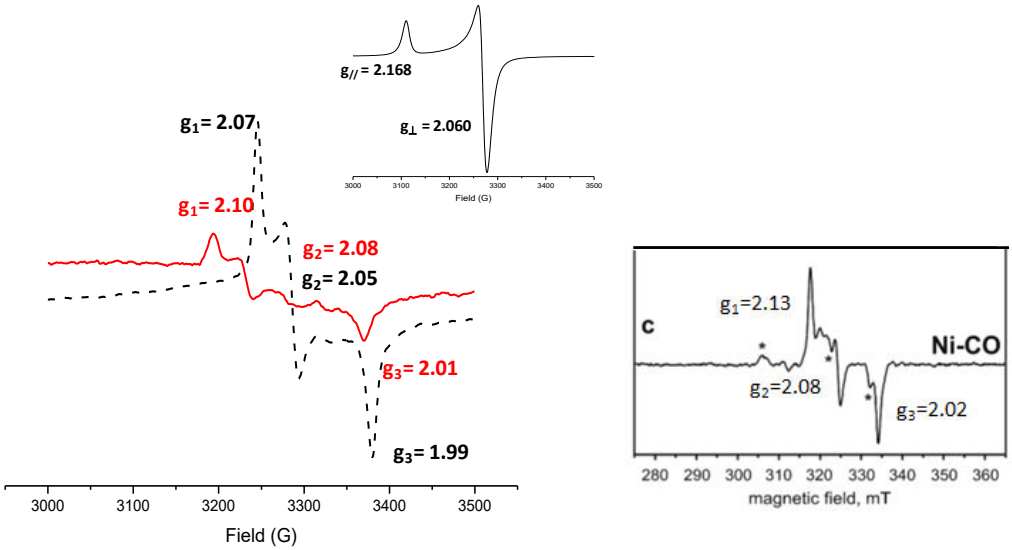

Figure 38. (a) X-band EPR spectra of **Ni^{I}Fe^{II}Cp*** (1 mM solution of **Ni^{II}Fe^{II}Cp*** was reduced with 1 equiv. of cobaltocene), (---) in MeCN and after CO bubbling in MeCN (—) (Zoom x 3) recorded at 100 K. Inset: X-band EPR spectrum of **Ni^{I}Fe^{II}Cp** (see Figure 26), (b) EPR spectra of the [NiFe] hydrogenase from *D. vulgaris* Miyazaki at 40 K for the Ni-CO state. [86]

When the diamagnetic **Ni^{II}Fe^{II}Cp*** complex is reduced with one equiv. of cobaltocene, it gives a reduced species, characterized by EPR spectroscopy. This species is much less stable compared to **Ni^{I}Fe^{II}Cp**. This is attested by the fact that the spectrum of **Ni^{I}Fe^{II}Cp*** is ~30 times less intense than that of **Ni^{I}Fe^{II}Cp**, using a similar concentration of the starting **Ni^{II}Fe^{II}Cp*** complex (Figure 38). The *S* = 1/2 EPR spectrum (Figure 38, dash line) displays a rhombic signal (g_1 = 2.07, g_2 = 2.05, g_3 = 1.99), different from that recorded with **Ni^{I}Fe^{II}Cp** (Figure 25) which was axial. This means that the geometries between the two complexes are different. By using DFT calculations, we can attest that CO doesn't bridge the Ni and the Fe sites. To get more insight about the structure of this reduced compound, DFT studies are still in progress.

It has been observed that when CO is bubbled in a freshly prepared solution of **Ni^{I}Fe^{II}Cp***, the resulting EPR spectrum is modified into a new rhombic signal with g values of g_1 = 2.10, g_2 = 2.08, g_3 = 1.99. The exogenous CO may bind the Ni^{I} site modifying its environment of coordination. DFT calculations are in progress to confirm these preliminary results. In addition, we can observe that the

EPR spectrum of the **Ni^{I}Fe^{II}Cp*** with CO (Figure 38a, red line) is very closed to what is observed for the enzyme similar g values (g_1 = 2.13, g_2 = 2.08, g_3 = 2.02)[86] with a rhombic spectrum (Figure 38b). Interestingly, when CO was bubbled before the addition of cobaltocene, no reduction of **Ni^{II}Fe^{II}Cp*** was observed. This is consistent with what happens in the enzyme in which CO can bind to Ni-Si$_a$ (Ni^{II} state) and inhibits the catalytic cycle. Based on these preliminary experiments, **Ni^{I}Fe^{II}Cp*** in the presence of CO appears to be a good model of the Ni-CO state of the [NiFe] hydrogenase.

1.7. Discussion.

Based on all experimental data combined with DFT calculations, **Ni^{II}Fe^{II}Cp** and **Ni^{II}Fe^{II}Cp*** complexes are proposed to be two structural models of the active site of the [NiFe] hydrogenase and more specifically of the Ni-Si$_a$ model (Figure 39). The X-ray structure of **Ni^{II}Fe^{II}Cp** reveals a {NiFeS$_2$} core identical to that of Ni-SI$_a$ state with the two thiolates bridging the Ni^{II} and Fe^{II} ions and a Ni$^{\cdots}$Fe distance (2.92 Å) close to that (~2.8 Å) determined for Ni-SI$_a$ through DFT calculations.[32]

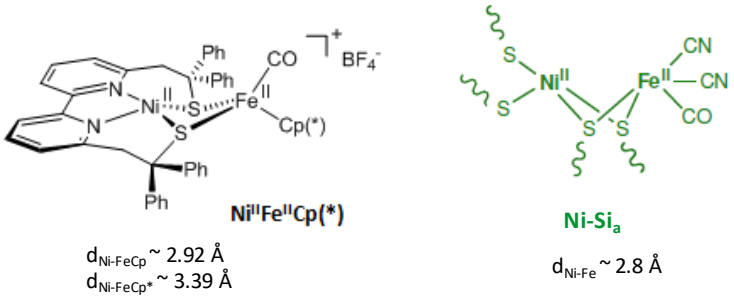

Figure 39. Ni^{II}Fe^{II}Cp(*), structural model of Ni-Si$_a$ (intermediate of [NiFe] hydrogenase).

The **Ni^{II}Fe^{II}Cp** complex also displays spectroscopic signatures similar to those measured for Ni-SI$_a$: (i) from Electron Paramagnetic Resonance (EPR) and Nuclear Magnetic Resonance (NMR) measurements, **Ni^{II}Fe^{II}Cp** is diamagnetic with both low-spin (S = 0) Ni^{II} and Fe^{II} ions as in Ni-SI$_a$. Accordingly, the Ni-S and Ni-N bond distances are similar to those measured in the low-spin **Ni^{II}LS** complex;[28] (ii) the Mössbauer spectrum of **Ni^{II}Fe^{II}Cp** displays a doublet with isomer shift δ = 0.39 mm·s^{-1} and quadrupole splitting ΔE_Q = 1.82 mm·s^{-1} characteristic of a low-spin Fe^{II} ion, even though the isomer shift is higher than the value reported for Ni-SI$_a$ (δ = 0.10 mm·s^{-1}, ΔE_Q = 1.60 mm·s^{-1})[33]; (iii) the CO stretching vibration ($\overline{\nu}_{CO}$ = 1929 cm^{-1}, of the carbonyl ligand coordinated to the Fe^{II} center is in the same range as for Ni-SI$_a$ (1925-1956 cm^{-1}).[2,34] All these data highlight that the electronic properties of the Fe unit in **Ni^{II}Fe^{II}Cp** and **Ni^{II}Fe^{II}Cp*** are close to those of the enzyme active site even if the coordination sphere is different (18-electron vs 16-electron shell for **Ni^{II}Fe^{II}Cp(*)** and [NiFe] hydrogenase, respectively).

Concerning **Ni^{II}Fe^{II}Cp***, it mimic less properly the Ni-SI$_a$ site, the Ni-Fe distance being of 3.396 Å. This is the consequence of the quasi planar {N$_2$S$_2$} core of the **Ni^{II}Fe^{II}Cp*** compared to **Ni^{II}Fe^{II}Cp**.

Despite some variations in the metal coordination spheres, the structural and spectroscopic properties of **Ni^{II}Fe^{II}Cp** closely resemble those of the enzyme's active site. The two terminal Ni-bound thiolates have been replaced by a bipyridine unit providing rigidity and preorganization essential for active catalysis and acting as an electron reservoir (see below), thus mimicking the proximal [4Fe4S] cluster. Essentially, the LS ligand affords an unsaturated four-coordinated Ni^{II} site appropriate for Ni-centered reactivity, as in the enzyme.

Concerning **Ni^{I}Fe^{II}Cp**, CO bridges the Ni and Fe units, whereas in the Ni-L state, the CO is bound to the Fe in a terminal position. While a large *g*-anisotropy is found in Ni-L (g_z = 2.046, g_y = 2.118 and g_x = 2.296 with Δg = 0.25),[3] Δg values in the range 0.09-0.16 are found in the model compounds,[26,45] including **Ni^{I}Fe^{II}Cp**. This discrepancy can be related to the different coordination spheres of the Ni^{I} ion. In Ni-L, the Ni^{I} ion is four-coordinate, while it is five-coordinate in the synthetic models. Stable four-coordinate Ni^{I} complexes are remarkably rare and require an appropriate ligand scaffold to avoid binding of a fifth ligand.[46] In Ni-L second coordination sphere effects probably play a crucial role in favoring this arrangement. Despite this difference, **Ni^{I}Fe^{II}Cp** represents the first mimic of the Ni-L state characterized (Figure 40) in the context of a full catalytic cycle, which supports the fact that Ni-L is indeed an active intermediate for [NiFe] hydrogenase.[9,47]

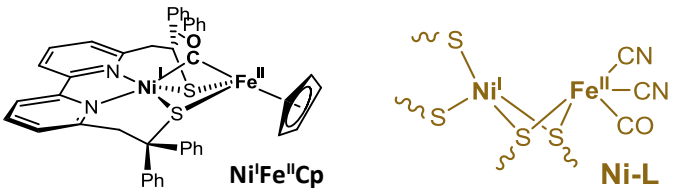

Figure 40. Ni^{I}Fe^{II}Cp, model of Ni-L (intermediate of the [NiFe] hydrogenase).

Ni^{II}Fe^{II}Cp(H) has a composition and redox state analogous to the Ni-R state of NiFe hydrogenase.

In Ni-R, the hydride bridges the two metals in a dissymmetrical manner and is displaced toward the Ni site as revealed by the Ni-H and Fe-H bond distances of 1.58 Å and 1.78 Å, respectively.[6] Interestingly, even if the hydride is terminally bound to Ni in **Ni^{II}Fe^{II}Cp(H)$_{calc}$**, the calculated Ni-H bond distance is similar (1.55 Å) to that in Ni-R and in the range of Ni-H length values found in the literature for terminal hydride ligands (1.33-1.65 Å).[48-50] Besides, the present model reproduces the notable dissymmetry observed in Ni-R between the two Ni-S$_{bridging}$ bonds (2.54 and 2.21 Å in Ni-R and 2.30 and 2.18 Å in **Ni^{II}Fe^{II}Cp(H)$_{calc}$**). In the three previously isolated Ni-R models, the hydride ligand binds in either a terminal mode to the Fe site[21] (Fe-H distance of 1.57 Å) or a dissymmetric bridging mode displaced toward the Fe ion (Δd (M-H) of 0.18 and 0.4 Å with Ni-H length of 1.64 and 1.89 Å, respectively) (Figure 41).[22,23]

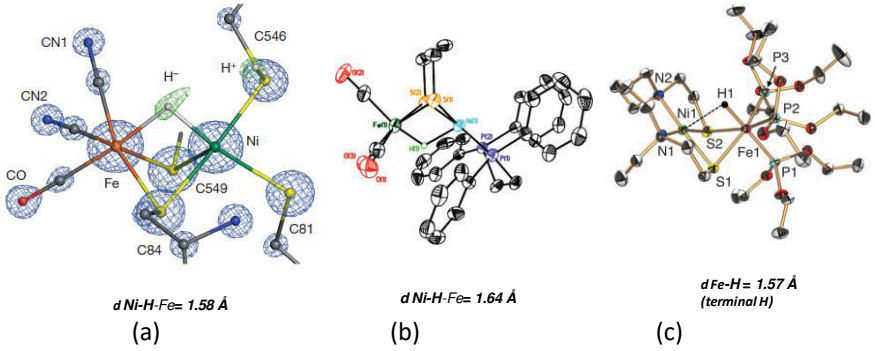

Figure 41. (a) The [NiFe] active site in the Ni-R form,[6] (b)[22] and (c)[23] two models of the Ni-R state.

With this unprecedented structure, **$Ni^{II}Fe^{II}Cp(H)$** thus represents the best active mimic of the Ni-R state involved in H_2 evolution catalysis to date (Figure 42).

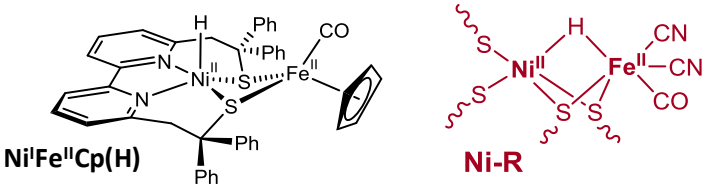

Figure 42. $Ni^{II}Fe^{II}Cp(H)$, model of Ni-R (intermediate of the [NiFe] hydrogenase).

The **$LS^{\bullet}Ni^{I}Fe^{II}Cp$** intermediate formed during the electrocatalytic pathway parallels the formation of a super-reduced state, implicated in the catalytic cycle of [FeFe] hydrogenase.[35,51] In this natural super-reduced state, the additional electron is located on the proximal [4Fe4S] cluster,[52,53] while in **$LS^{\bullet}Ni^{I}Fe^{II}Cp$** the bipyridine moiety acts as the electron reservoir. Whether [NiFe] hydrogenase could also exist in such a super-reduced state is an interesting question, but the present mechanism clearly demonstrates how the sequence of the various electron and proton transfer steps can be controlled in synthetic NiFe mimics through fine-tuning the redox and electronic properties of the system. A similar redox behavior has previously been observed in a diiron mimic of the active site of the [FeFe]-hydrogenase containing a bipyridine (Figure 43). They observed that at scan rates faster than 1 $V.s^{-1}$, the reductive peak was split into two reductive features. The first peak was assigned to Fe^{I}/Fe^{0} and the second one to the bpy^{0}/bpy^{-1}.[17]

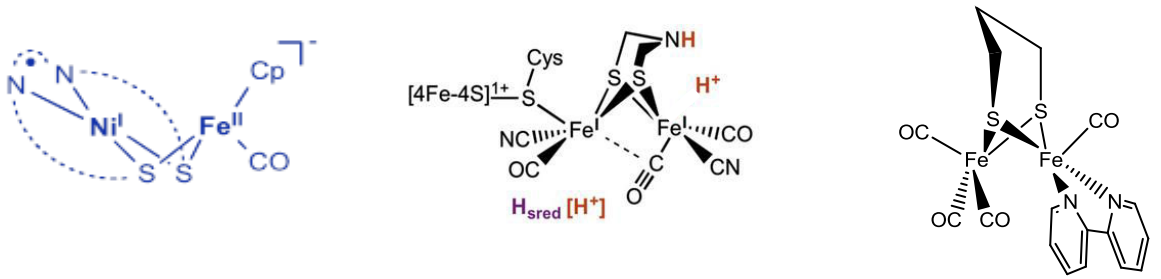

LS•NiIFeIICp (a) | **[FeFe] hydrogenase** (b) | **(μ-pdt)Fe$_2$(CO)$_4$(κ^2-bpy)** (c)

Figure 43. Comparison of (a) **LS•Ni^{I}Fe^{II}Cp**, (b) [FeFe] hydrogenase super-reduced state[35,51] and (c) a dinuclear iron model of the [FeFe] hydrogenase.[17]

After the characterization of all these intermediates, the electrocatalytic mechanism shown in Figure 44 can be proposed. **Ni^{II}Fe^{II}Cp** undergoes a one-electron reduction to generate **Ni^{I}Fe^{II}Cp**. This active species is further reduced to afford **LS•Ni^{I}Fe^{II}Cp**, which reacts with protons to yield **Ni^{II}Fe^{II}Cp(H)**. The metal-hydride species further reacts with protons to produce H_2, and to regenerate the initial **Ni^{II}Fe^{II}Cp** complex.

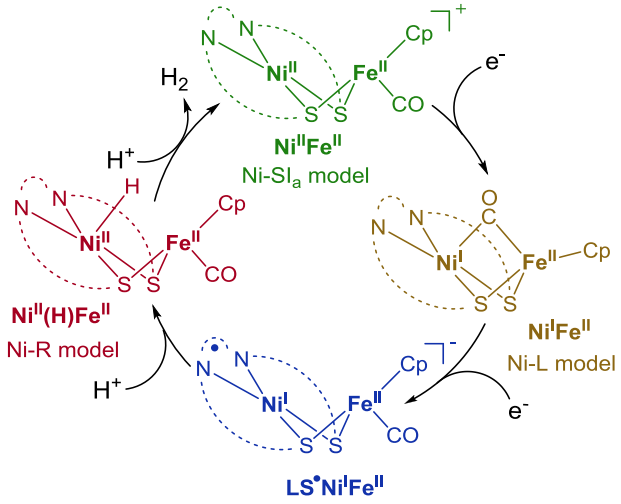

Figure 44. Proposed catalytic pathway for H_2 evolution mediated by **Ni^{II}Fe^{II}Cp** at the catalytic wave.

Such a catalytic cycle, involving decoupled electron and proton transfers, is similar to that proposed for the enzyme, except that the electron/proton transfer sequence yielding Ni-R/ **Ni^{II}Fe^{II}Cp(H)** from the one-electron reduced form, Ni-L/ **Ni^{I}Fe^{II}Cp** is inverted. As a consequence, the formation of a **Ni^{III}Fe^{II}Cp(H)** species, analogous to Ni-C, is bypassed in our system. It is hypothesized that protonation of **Ni^{I}Fe^{II}Cp** by Et_3NH^+ is either thermodynamically unfavorable or too slow to be observed on the timescale of a CV experiment. This can be rationalized by the poor basic and nucleophilic character of **Ni^{I}Fe^{II}Cp,** compared to Ni-L, due to (i) a much weaker electronic donor, coordination environment ($\{N_2S_2\}^{2-}$ for Ni^{I} vs. $\{S_4\}^{4-}$ in the enzyme); (ii) partial delocalization of the

SOMO on the bipyridine moiety of LS and (iii) the absence of any proton relay that could kinetically assist protonation of the Ni^{I} center.

The reversible electrochemical behavior of **$Ni^{II}Fe^{II}Cp$** is unprecedented among NiFe mimics, which generally displayed irreversible reduction processes, indicating strong structural reorganization at the metal site(s) possibly accompanied by ligand degradation *via* radical processes. The large anodic shift (530 mV) of the Ni^{II}/Ni^{I} redox potential (E_{pc} = -1.29 V) in **$Ni^{II}Fe^{II}Cp$**, compared to **$Ni^{II}LS$** (E_{pc} = -1.82 V),[21] nicely illustrates how the electronics of the nickel center can be modulated by the organometallic iron unit, in a similar fashion to the active site of [NiFe] hydrogenases. The presence of the Fe unit increases the efficiency of the $Ni^{II}Fe^{II}$ complex (16 -17 TON, TOF of 10-11 h^{-1}) compared to the **$Ni^{II}L$** complex (9 TON, TOF of 6 h^{-1}) towards proton reduction. The linkage of the cationic Fe moiety bearing the strong π-acceptor CO ligand withdraws electron density through thiolate ligands, which acquire thioether-like electronic properties.[36]

Despite the fact that **$Ni^{II}Fe^{II}Cp$*** is a less good structural mimic of the [NiFe] hydrogenase, it displays a good catalytic activity towards proton reduction. Interestingly, CO bubbling on **$Ni^{II}Fe^{II}Cp$*** modifies the redox properties of the complex. The complete loss of chemical reversibility of the first reducing system can be explained by the possible coordination of one CO molecule on the Ni site, leading to a shift of the E_{pc} potential from -1.46 V to -1.41 V *vs* Fc^{+}/Fc. The potential of the second reduction system remains unchanged, suggesting that the reduction is still occurring on the bipyridine ligand.

The complete loss of chemical reversibility of the first system is proposed to arise from coordination of a CO to Ni after reduction. Indeed, it is proposed that **$Ni^{I}Fe^{II}Cp$*** displays structural properties that allow the coordination of an exogenous CO on the Ni site, generating a terminally Ni bound CO, as CO cannot bridge between the Ni^{I} and the Fe^{II} (DFT calculation and EPR data). In the presence of protons, the electrocatalytic activity of **$Ni^{II}Fe^{II}Cp$*** is fully inhibited by CO bubbling and completely recovered by replacing CO by argon, as in the [NiFe] hydrogenase.

On the contrary, the first reduction system of **$Ni^{I}Fe^{II}Cp$** is only slightly modified by CO bubbling. This can be rationalized by the fact that the presence of a bridging CO between the Ni^{I} and Fe^{II} sites prevents the coordination of an exogenous CO. On the other hand, the second reduction system loses part of its reversibility and the potential is shifted from -1.91 V to -1.87 V. The optimized double reduced species, **$LS^{\bullet}Ni^{I}Fe^{II}Cp$** shows that there is no longer bridging CO on the NiFe complex. Consequently, the coordination of an exogenous CO to the Ni^{I} site can be envisaged explaining the partial inhibition of the electrocatalytic activity of **$Ni^{II}Fe^{II}Cp$** toward proton reduction in the presence of CO: Competition between the reaction of **$LS^{\bullet}Ni^{I}Fe^{II}Cp$** with H^{+} or with CO occurs. The proposed inhibition mechanisms of H_2 production for both **$Ni^{II}Fe^{II}Cp$** and **$Ni^{II}Fe^{II}Cp$*** are illustrated in Figure 45.

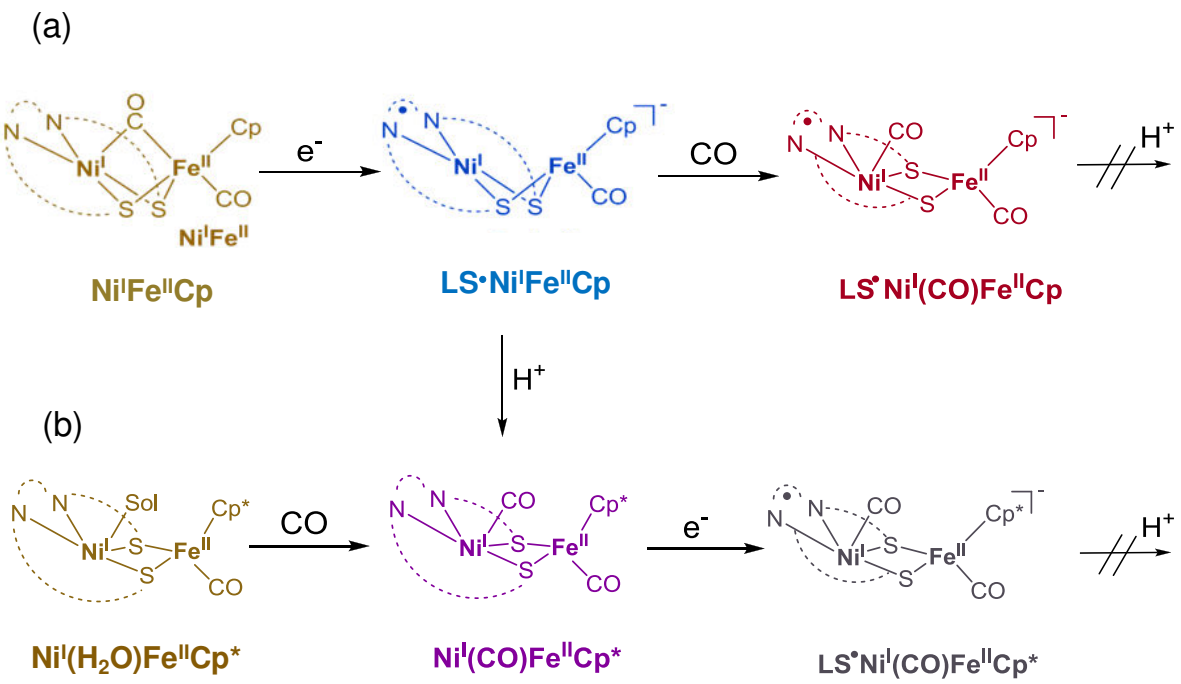

Figure 45. (a) Proposed mechanism of the inhibition of H_2 production in the presence of CO for **Ni^{II}Fe^{II}Cp** (competition between the fixation of H^+ and CO**)** and (b) for **Ni^{II}Fe^{II}Cp***.

As the electrocatalytic activity of **Ni^{II}Fe^{II}Cp*** is inhibited in the presence of CO, it represents a good model of the [NiFe] hydrogenase towards CO reactivity. The reduced species obtained with cobaltocene in the presence of CO (see EPR spectrum of Figure 36) can be considered as a model of the Ni-CO state. Further experiments will be performed in order to investigate the structure of these reduced species and the quantity of H_2 production in the presence of CO during electrocatalysis.

Conclusion

Ni^{II}Fe^{II}Cp displays the best performance of any reported [NiFe] hydrogenase mimics to date, with regards to electrocatalytic H_2 production. It is also the first heterodinuclear mimic, whose reactivity occurs on the Ni site. As in the enzyme, the Fe site of **Ni^{II}Fe^{II}Cp** is involved in the modulation of the electronic properties of the $\{N_2S_2\}$ core. Such a conclusion is further supported by electrolysis experiments (better H_2 production performances in terms of both efficiency and kinetics of **Ni^{II}Fe^{II}Cp** *vs* **Ni^{II}L**) demonstrating a cooperative effect of the Fe site on the reactivity of the {Ni(LS)} unit. In the presence of CO, the catalytic activity is partially inhibited and its reactivity is reversible when CO is removed from the solution. Despite a lack of accuracy in mimicking the $\{NiFeS_2\}$ core of the [NiFe] hydrogenase, **Ni^{II}Fe^{II}Cp*** complex shows a good catalytic activity comparable to **Ni^{II}Fe^{II}Cp**. Its catalytic activity is fully inhibited in the presence of CO and recovered when the solution is degassed with argon. **Ni^{II}Fe^{II}Cp*** thus represents a good model of the [NiFe] hydrogenase towards proton reactivity

especially considering its complete reversible inhibition in the presence of CO such as the Ni-CO state of the enzyme.

Other electrocatalytic experiments using a strong acid (HBF_4) are under investigation to test the reactivity of **$Ni^{I}Fe^{II}Cp$**. The preliminary results shows that there is a catalytic activity on the first reduced system suggesting that the mechanism may go through the formation of **$Ni^{III}Fe^{II}Cp(H)$**, thus mimicking the mechanism of the [NiFe] hydrogenase going through a Ni-C state.

References

1 Volbeda, A. *et al. Nature* **1995**, *373*, 580-587.
2 Lubitz, W., Ogata, H., Rüdiger, O. & Reijerse, E. Hydrogenases. *Chem. Rev.* 2014, *114*, 4081-4148.
3 Foerster, S. *et al. J. Am. Chem. Soc.* **2003**, *125*, 83-93.
4 Brecht, M., van Gastel, M., Buhrke, T., Friedrich, B. & Lubitz, W. *J. Am. Chem. Soc.* **2003**, *125*, 13075-13083.
5 George, S. J., Kurkin, S., Thorneley, R. N. F. & Albracht, S. P. J. *Biochemistry* **2004**, *43*, 6808-6819.
6 Ogata, H., Nishikawa, K. & Lubitz, W. *Nature* **2015**, *520*, 571-574.
7 van der Zwaan, J. W., Albracht, S. P. J., Fontijn, R. D. & Slater, E. C. *FEBS Lett.* **1985**, *179*, 271-277.
8 Murphy, B. J. *et al. J. Am. Chem. Soc.* **2015**, *137*, 8484-8489.
9 Hidalgo, R., Ash, P. A., Healy, A. J. & Vincent, K. A. *Angew. Chem. Int. Ed.* **2015**, *54*, 7110-7113).
10 Tard, C. & Pickett, C. J. *Chem. Rev.* **2009**, *109*, 2245-2274.
11 Ohki, Y. & Tatsumi, K. *Eur. J. Inorg. Chem.* **2011**, 973-985.
12 Simmons, T. R., Berggren, G., Bacchi, M., Fontecave, M. & Artero, V. *Coord. Chem. Rev.* **2014**, *270–271*, 127-150.
13 Kaur-Ghumaan, S. & Stein, M. *Dalton Trans.* **2014**, *43*, 9392-9405.
14 Fourmond, V. *et al.*. *Energy Environ. Sci.* **2011**, *4*, 2417-2427.
15 Song, L.-C., Li, J.-P., Xie, Z.-J. & Song, H.-B. *Inorg. Chem. 2013*, *52*, 11618-11626.
16 Ogo, S. *et al.*. *Science,* **2007**, *316*, 585-587 (**2007**).
17 Canaguier, S., Fontecave, M. & Artero, V. *Eur. J. Inorg. Chem.*, **2011**, 1094-1099.
18 Canaguier, S. *et al. Chem. Commun.* **2013***, 49*, 5004-5006.
19 Oudart, Y., Artero, V., Pécaut, J., Lebrun, C. & Fontecave, M. *Eur. J. Inorg. Chem.*, **2007**, 2613-2626.
20 Denny, J. A. & Darensbourg, M. Y. *Chem. Rev.* **2015**, *115*, 5248-5273.
21 Ogo, S. *et al. Science*, **2013**, *339*, 682-684.
22 Barton, B. E. & Rauchfuss, T. B. *J. Am. Chem. Soc.* **2010**, *132*, 14877-14885.
23 Barton, B. E., Whaley, C. M., Rauchfuss, T. B. & Gray, D. L. *J. Am. Chem. Soc.* **2009**, *131*, 6942-6943.
24 Vaccaro, L., Artero, V., Canaguier, S., Fontecave, M. & Field, M. J. *Dalton Trans.* **2010**, *39*, 3043-3049.
25 Simmons, T. R. & Artero, V. *Angew. Chem. Int. Ed.* **2013,***52*, 6143-6145.
26 Chambers, G. M. *et al. Inorg. Chem.* **2016**, *55,* 419-431.
27 Gennari, M. *et al. Inorg. Chem.* **2011**, *50*, 3707-3716.
28 Gennari, M. *et al. Inorg. Chem.* **2010**, *49*, 6399-6401.

29 Canaguier, S. *et alChem. Commun.* **2010**, *46*, 5876-5878.
30 Zhu, W. *et al. Proc. Natl. Acad. Sci. U. S. A.* **2005**, *102*, 18280-18285.
31 (a) Lai, C. H.; Reibenspies, J. H.; Darensbourg, M. Y. *Angew. Chem. Int. Ed.* **1996**, *35*, 2390. (b)Darensbourg, D. J., Reibenspies, J. H., Lai, C.-H., Lee, W.-Z. & Darensbourg, M. Y.. *J. Am. Chem. Soc.* **1997**, *119*, 7903-7904.
32 Pandelia, M.-E., Ogata, H. & Lubitz, W. *ChemPhysChem*, **2010**, *11*, 1127-1140.
33 Roncaroli, F. *et al. Chem. Sci.* **2015**, *6*, 4495-4507.
34 Lubitz, W., Gastel, M. V. & Gärtner, W. in (ed A. Sigel, Sigel, H., Sigel, R. K. O.) **2007**, 279-322 (John Wiley &Sons Ltd).
35 (a) Peters J. W., Schut G. J., Boyd E. S., Mulder D. W., Shepard E. M., Broderick J. B., King P. W. & Adams M. W. W. *BBA-Mol. Cell. Res.* **2015**, *1853,* 1350-1369. (b) Roy, S., Groy, T. L. & Jones, A. K. *Dalton Trans.* **2013**, *42,* 3843-3853.
36 Farmer, P. J., Reibenspies, J. H., Lindahl, P. A. & Darensbourg, M. Y. *J. Am. Chem. Soc.* **1993**, *115*, 4665-4674.
37 Izutsu, K. 1**990**, (Blackwell Scientific,.
38 Costentin, C., Drouet, S., Robert, M. & Savéant, J.-M. *J. Am. Chem. Soc.* **2012**, *134*, 11235-11242.
39 Artero, V. & Savéant, J.-M. *Energy Environ. Sci.* **2014**, *7*, 3808-3814.
40 Costentin, C., Dridi, H. & Savéant, J.-M. *J. Am. Chem. Soc.* **2014**, *136*, 13727-13734.
41 Sampson, M. D. & Kubiak, C. P. *Inorg. Chem.* **2015,** *54*, 6674-6676.
42 Shaw, W. J., Helm, M. L. & DuBois, D. L. *Biochim. Biophys. Acta, Bioenerg.* **2013**, *1827*, 1123-1139.
43 Van der Meer, M., Glais, E., Siewert, I. & Sarkar, B.. *Angew. Chem. Int. Ed.* **2015**, *54*, 13792–13795.
44 Kampa, M., Pandelia, M.-E., Lubitz, W., van Gastel, M. & Neese, F.. *J. Am. Chem. Soc.* **2013**, *135*, 3915-3925.
45 Perotto, C. U. *et al. Chem. Commun.* **2015**, *51*, 16988-16991.
46 Yoo, C., Oh, S., Kim, J. & Lee, Y. *Chem. Sci.* **2014**, *5*, 3853-3858.
47 Greene, B. L., Wu, C.-H., McTernan, P. M., Adams, M. W. W. & Dyer, R. B. *J. Am. Chem. Soc.* **2015**, *137*, 4558-4566.
48 Matson, E. M. *et al. Organometallics* **2015**, *34*, 399-407.
49 Breitenfeld, J., Scopelliti, R. & Hu, X. *Organometallics 31*, 2128-2136 (**2012**).
50 Boro, B. J., Duesler, E. N., Goldberg, K. I. & Kemp, R. A. *Inorg. Chem.* **2009**, *48*, 5081.
51 Peters, J. W. *et al. BBA-Mol. Cell. Res.* **2015**, *1853*, 1350-1369.
52 Adamska, A. *et al. Angew. Chem. Int. Ed.* **2012**, *51*, 11458-11462.
53 Chernev, P. *et al. Inorg. Chem.* **2014**, *53*, 12164-12177.
54 Ezzaher, S. *et al. Inorg. Chem.* **2007**, *46*, 3426-3428.
55 Mealli, C. & Rauchfuss, T. B. *Angew. Chem. Int. Ed.* **2007**, *46*, 8942-8944.
56 Barton, B. E., Olsen, M. T. & Rauchfuss, T. B. *J. Am. Chem. Soc.* **2008**, *130*, 16834-16835.
57 Olsen, M. T., Rauchfuss, T. B. & Wilson, S. R. *J. Am. Chem. Soc.* **2010**, *132*, 17733-17740**.**
58 Carroll, M. E., Barton, B. E., Rauchfuss, T. B. & Carroll, P. J *J. Am. Chem. Soc.* **2012**, *134,* 18843-18852.
59 Zaffaroni, R., Rauchfuss, T. B., Gray, D. L., De Gioia, L. & Zampella, G. *J. Am. Chem. Soc.* **2012**, *134*, 19260-19269.
60 Camara, J. M. & Rauchfuss, T. B. *Nature Chem.* **2012**, *4*, 26-30.
61 Reger, D. L. & Coleman, C. *J. Organomet. Chem.* 1**977**, *131*, 153-162.
62 Bhugun, I., Lexa, D. & Savéant, J.-M. *J. Am. Chem. Soc.* **1996**, *118*, 3982-3983.
63 Neese, F., Wennmohs, F., Hansen, A. & Becker, U. *Chem. Phys.* **2009**, *356*, 98-109.
64 Adamska, A.; Silakov, A.; Lambertz, C.; Ruediger, O.; Happe, T.; Reijerse, E.; Lubitz, W, *Angew. Chem. Int. Ed.* **2012**, *51*, 11458.
65 Dementin, S.; Burlat, B.; De Lacey, A. L.; Pardo, A.; Adryanczyk-Perrier, Guigliarelli, B.; Fernandez, V. M.; Rousset, M. *J. Biol. Chem.* **2004**, *279*, 10508.

66 (a)Szőri-Dorogházi, E.; Maróti, G.; Szőri, M.; Nyilasi, A.; Rákhely, G.; Kovács, K. L. *PLOS ONE* **2012**,*7*,34666.(b)M.; E. J.; S. A. M.; Nomerotskaia E.; Sargent F.; Carr S.B.; Phillips S. E. V.& Armstrong F. A., Nature Chemical Biology, **2016**, *12*, 46–50.
67 Ogata, H.; Hirota, S.; Nakahara, A.; Komori, H.; Shibata, N.; Kato, T.; Kano, K.; Higuchi, Y. *Structure* **2005**, *13*, 1635.
68 Karstens, K.; Wahlefeld, S.; Horch, M.; Grunzel, M.; Lauterbach, L.; Lendzian, F.; Zebger, I.; Lenz, O. *Biochemistry* **2015**, *54*, 389.
69 Tai, H.; Nishikawa, K.; Suzuki, M.; Higuchi, Y.; Hirota, S. *Angew. Chem. Int. Ed.* **2014**, *53*, 13817.
70 Abou Hamdan, A.; Burlat, B.; Gutiérrez-Sanz, O.; Liebgott, P.-P.; Baffert, C.; De Lacey, A. L.; Rousset, M.; Guigliarelli, B.; Léger, C.; Dementin, S., *Nature Chem. Biol.* **2013**, *9*, 15
71 Li, Z. L.; Ohki, Y.; Tatsumi, K. *J. Am. Chem. Soc.* **2005**, *127*, 8950.
72 Carroll, M. E.; Barton, B. E.; Gray, D. L.; Mack, A. E.; Rauchfuss, T. B. *Inorg. Chem.* **2011**, *50*,9554.
73 Schilter, D.; Nilges, M. J.; Chakrabarti, M.; Lindahl, P. A.; Rauchfuss, T. B.; Stein, M. *Inorg. Chem.* **2012**, *51*, 2338.
74 Schilter, D.; Rauchfuss, T. B.; Stein, M. *Inorg. Chem.* **2012**, *51*, 8931.
75 Schilter, D.; Rauchfuss, T. B. *Angew. Chem. Int. Ed.* **2013**, *52*, 13518.
76 Bourrez, M.; Steinmetz, R.; Gloaguen, F. *Inorg. Chem.* **2014**, *53*, 10667.
77 Wombwell, C.; Reisner, E. *Chem. Eur. J.* **2015**, *21*, 8096.
78 Gennari, M.; Orio, M.; Pécaut, J.; Neese, F.; Collomb, M.-N.; Duboc. C. *Inorg. Chem.* **2010**, 49, 6399-6401.)
79 Berg, J.; Holm, R. H. *J. Am. Chem. Soc.,* **1985**, *107*, 925-932.
80 Kamata, K.; Suzuki, A.; Nakai, Y. and Nakasawa, H. *Organometallics*, **2012**, *31*, 3825
81 Reger, D. L. & Coleman, C. *J. Organomet. Chem.*, 1**977**, *131*, 153.
82 Ogata, H.;. Mizoguchi, Y.; Mizuno, N.; Miki, K.; Adachi, S.; Yasuoka, N.; Yagi, T.; Yamauchi, O.; Hirota, S. and Higuchi, Y. *J. Am. Chem. Soc*, **2002**, *124*, 11628.
83 Pandelia, M-E.; Ogata, H.; Currell, L. J.; Flores, M.; Lubitz, W. *Biochimica et Biophysica Acta,* **2010**, *1797*, 304-313.
84 DeLacey, A. L.; Stadler, C; Fernandez, V. M; Hatchikian, E. C.; Fan, H.-J.; Li S. and Hall M. B. *J Biol Inorg Chem* , **2002**, *7*, 318.
85 Fourmond V. ; Jacques P-A. ; Fontecave M. and Artero V. *Inorg. Chem.*, **2010**, *49*, 10338–10347.
86 Pandelia, M.-E.,Ogata, H., Currell, L. J, Flores, M., Lubitz, W. *Biochimica et biophysica acta*, **2010**, *1797*, 304-313.

Chapter II

Dioxygen Activation and Catalytic Reduction to Hydrogen Peroxide by a Thiolate-Bridged Dimanganese(II) Complex with a Pendant Thiol.

Table of contents

Résumé 82

Introduction 86

Results and Discussion 90

2.1. Synthesis and structural properties of **Mn^{II}_2SH** and **Mn^{III}_2OH** 90

2.2.1. Synthesis of **Mn^{II}_2SH** and **Mn^{III}_2OH**. 90

2.1.2. Structural characterization of **Mn^{II}_2SH**. 90

2.1.3. Structural characterization of **Mn^{III}_2OH**. 92

2.2. Mn and S K-Edge XAS absorption of **Mn^{II}_2SH** and **Mn^{III}_2OH** 93

2.3. Magnetic properties of **Mn^{II}_2SH** and **Mn^{III}_2OH** 95

2.4. Solution properties. 96

2.4.1. Redox properties of **Mn^{II}_2SH**. 96

2.4.2. Redox properties of **Mn^{III}_2OH**. 98

2.5. Reactivity of **Mn^{II}_2SH** with dioxygen. 99

2.5.1. Reactivity of **Mn^{II}_2SH** with dioxygen in stoichiometric conditions. 99

2.5.2. Reactivity of **Mn^{II}_2SH** with dioxygen in catalytic conditions. 101

2.5.3. Characterization of the products of catalysis. 102

2.6. Reactivity of **Mn^{II}_2S** with dioxygen 103

2.6.1. Synthesis of **Mn^{II}_2S**. 103

2.6.2. Synthesis and structural properties of **$Mn^{IV}_2(O)_2$** and **$Mn^{IV}_2(O)(OH)$**. 104

2.7.1. ESI-mass spectrometry. 108

2.7.2. Acid/base properties 108

2.7.3. Mn K-Edge XAS absorption of **$Mn^{IV}_2(O)_2$**. 109

2.9. Mechanistic investigation of O_2 activation by **Mn^{II}_2S** 110

2.10. Proposed mechanism for O_2 activation and reduction. 111

2.10.1. **Mn^{II}_2SH**: An unusual metal-thiol system. 111

2.10.2. Proposed O_2 reduction pathways with **Mn^{II}_2SH** under stoichiometric and catalytic conditions. 111

Conclusion 115

References 116

Résumé

L'activation d'O_2 représente une étape critique dans de nombreux processus biologiques fondamentaux. En effet, l'oxygène représente 21% des composants de l'air que l'on respire. Il est nécessaire à la survie de nombreuses espèces vivantes comme les animaux, les plantes, les bactéries aérobies pour la production d'énergie ou le métabolisme, par exemple.[1b]

L'oxygène présent dans notre atmosphère est l'élément qui permet la formation d'un gradient d'énergie responsable du maintien de la vie sur Terre à travers un processus biologique appelé photosynthèse. Les organismes photosynthétiques stabilisent l'énergie éphémère contenue dans un photon en rompant et formant des liaisons chimiques. Ces organismes génèrent O_2 grâce à l'oxydation de l'eau. Les électrons libérés au cours de ce processus sont utilisés pour réduire le carbone inorganique en carbone organique dans le but de générer de nouvelles molécules. Cette énergie redox stockée peut être libérée par l'oxydation des nouvelles molécules synthétisées, permettant ainsi à l'oxygène d'être réduit à quatre électrons en présence de protons pour générer H_2O (équation 1). Ce phénomène est communément appelé respiration aérobie $O_2 + 4e^- + 4H^+ \rightarrow 2H_2O$ (Equation 1)

La réduction d'O_2 à quatre électrons est également impliquée pour la génération électrique d'énergie dans les systèmes de piles à combustibles (Figure 1).[6,7] Ces piles se divisent en deux compartiments (anode et cathode) reliés par des membranes représentant l'électrolyte. L'hydrogène, H_2, oxydé à l'anode (+) en protons traversent la membrane pour se retrouver du côté de la cathode (-). Les électrons, quant à eux, ne pouvant pas passer la membrane empruntent un circuit extérieur en générant un courant électrique. Ils vont ainsi se retrouver du côté de la cathode et ainsi participer à la réduction d'O_2 selon l'équation 1.

Il existe différents types de piles à combustible en fonction des composants de l'électrolyte comme le montre la Figure 1.

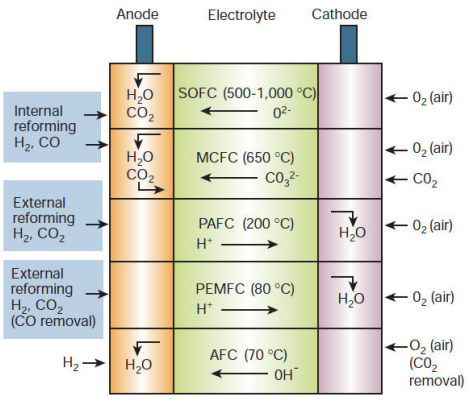

Figure 1. Schéma de différentes piles à combustible.[1b-82]

O_2 peut être également réduit à deux électrons générant ainsi H_2O_2, qui est un agent oxydant polyvalent et peu toxique pour l'environnement (Equation 2).[ref 8,9]

$O_2 + 2H^+ + 2e^- \rightarrow H_2O_2$ (Equation 2)

H_2O_2 se trouve être également un bon candidat comme vecteur énergétique dans les piles à combustible grâce à sa haute densité énergétique du fait de son état liquide à température ambiante. L'avantage d'utiliser le peroxyde d'hydrogène comme vecteur énergétique est que les sous-produits redox sont O_2 et H_2O. Il peut être considéré comme une alternative énergétique au pétrole ou H_2.[10-13]

Par ailleurs, les métaux de transitions sont connus pour leur capacité à faciliter et à contrôler l'activation d'O_2. Comment celui-ci peut être activé par des complexes métalliques demeure une question centrale pour les chimistes.[14,15] Dans ce contexte, l'étude de systèmes homogènes à base de métaux de transitions est particulièrement intéressante pour clarifier les détails mécanistiques de l'activation d'O_2.[16-25] Dans le cas spécifique de la réduction catalytique d'O_2, des études en solution sont essentielles pour obtenir des informations sur les facteurs qui contrôlent la compétition entre une réduction à deux ou quatre électrons.[19,26, 27]

Parmi les métaux de transition, le Mn présente une chimie de l'oxygène extrêmement riche. Un certain nombre de réactions vitales impliquant O_2 et ses dérivés ($O_2^{\cdot-}$, H_2O_2 et H_2O) sont gouvernées par des enzymes à Mn comme la lipoxygénase, la ribonucléotide réductase, la superoxyde dismutase, la catalase, ou bien le centre de dégagement de l'oxygène du Photosystème II.[28-33] Il existe également de nombreux complexes de Mn mimant la structure et/ou la réactivité de ces enzymes dans une approche de chimie bio-inspirée.[32, 34-36]

Il a, de plus, été montré que la nature du ligand joue un rôle fondamental dans la réactivité des complexes vis-à-vis d'O_2. En effet, la coordination de ligands thiolates à l'ion métallique peut promouvoir l'activation de l'oxygène[37] pour plusieurs raisons : (i) stabilisation des complexes métal-peroxo,[38-40],-hydroperoxo,[41]-alkylperoxo,[42-44] et –superoxo[45] du fait du caractère donneur des groupements thiolates; (ii) diminution de la barrière d'activation d'O_2 montré par des calculs théoriques[45,46]; (iii) l'assistance d'O_2 sur l'oxydation du métal en diminuant considérablement son potentiel redox[47]; (iv) augmentation de la basicité des substrats coordonnants en réduisant l'acidité de Lewis de l'ion métallique[48] générant ainsi des ligands oxo plus basique; et enfin (v) la stabilisation de complexes M^{II} présentant un site de coordination vacant avec la présence de ligands labiles en position *trans* des thiolates pour conduire à la libération des produits de manière concomitante.[47]

En plus de la nature du ligand et sa première sphère de coordination, le contrôle de la seconde sphère de coordination d'un complexe joue un rôle crucial dans la synthèse de composés hautement fonctionnels et chimiquement sélectifs. En particulier la présence de groupements acides (ou basiques) est connue pour promouvoir la réactivité *via* des liaisons hydrogènes transitoires, agissant alors comme des relais de protons durant le processus catalytique, mais aussi pour moduler le potentiel redox du centre métallique.[50] Ces concepts ont été validés dans le domaine de l'activation et de la réduction d'O_2. [51-54]

Quels sont les facteurs qui influencent une réduction à 2 ou 4 électrons demeure une question centrale, et notamment quels sont les facteurs qui vont promouvoir la rupture de la liaison O-O ou M-O pour récupérer des équivalents oxydants ?

Au cours de ce chapitre II, un nouvel exemple de complexe de Mn-thiolate capable d'activer l'oxygène moléculaire (O_2) et de le réduire soit à quatre électrons pour produire de l'eau en conditions stœchiométriques, soit de le réduire de manière catalytique, à deux électrons pour produire H_2O_2 est décrit. Le dimère de Mn^{II}-thiolate $[Mn^{II}_2(LS)(LSH)]ClO_4$ (**Mn^{II}_2SH**)a été synthétisé à partir du ligand (2,2-bipyridine-6,6'-diyl)bis-(1,1-diphenylethanethiolate) avec un sel de Mn^{II}. La présence inhabituelle d'un thiol protoné lié à un des Mn^{II} dans **Mn^{II}_2SH** a été observée que ce soit à l'état solide ou en solution. Le complexe **Mn^{II}_2SH** réagit avec O_2 dans l'acétonitrile conduisant à la formation d'un rare complexe dinucléaire de Mn^{III} mono-μ-hydroxo $[(Mn^{III}_2(LS)_2(OH)]ClO_4$ (**Mn^{III}_2OH**), dont la structure a été caractérisée par diffraction des rayons X. Quand **Mn^{II}_2SH** réagit ave O_2 en présence d'une source de proton comme 2,6-lutidinium tétrafluoroborate (jusqu'à 50 équivalents), une nouvelle espèce de Mn est formée. Il s'agit d'un complexe dinucléaire de Mn^{III} bis-μ-thiolate avec deux thiolates terminaux (**Mn^{III}_2**). H_2O_2 est formé de manière concomitante jusqu'à 40% versus **Mn^{II}_2SH**. L'addition d'une quantité catalytique **de Mn^{II}_2SH** à une solution saturée en O_2 contenant Me_nFc (n = 8 ou 10) et 2,6-lutidinium tetrafluoroborate résulte en une oxydation efficace et quantitative de Me_nFc (Figure 2). H_2O_2 est majoritairement produit dans ces conditions de réduction catalytique de O_2 avec un taux de conversion de 80-84%, faisant de **Mn^{II}_2SH** un rare exemple de catalyseur pour la réduction de l'oxygène à deux électrons. L'activation et la réduction de l'oxygène ont été étudiées en conditions stœchiométriques et catalytiques nous permettant d'analyser quels sont les facteurs qui vont contrôler la compétition entre une réduction à deux *vs* quatre électrons (Figure 3).

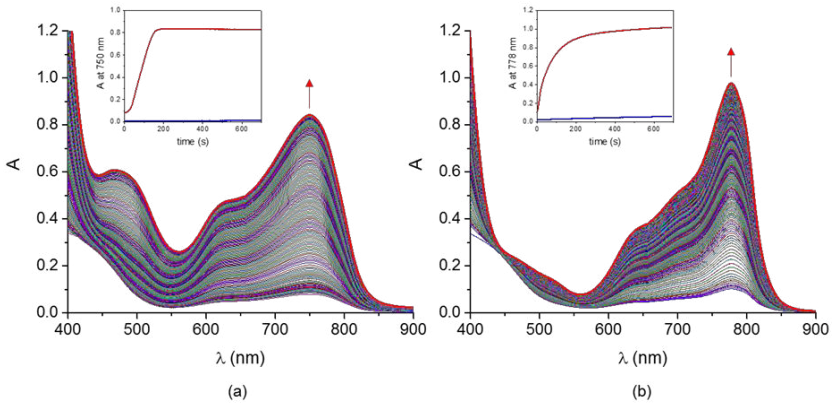

Figure 2. Changement spectral UV−vis observé pendant la réduction à 2 électrons catalysée par **Mn^{II}_2SH** avec Me_nFc ((a) n=8, (b) n=10) en présence de $LutHBF_4$, CH_3CN à 293 K (solution saturée en air, 2.0 mM Me_nFc, 15 mM $LutHBF_4$, 100 µM **Mn^{II}_2SH**, longueur de cuve 1 cm). L'insert montre le profil en fonction du temps pour la formation de Me_nFc^+ (n=8 ou 10) (—), absorbances respectives à 750 and 778 nm. les profils correspondants aux blancs sont aussi montrés (sans catalyseur) (—).

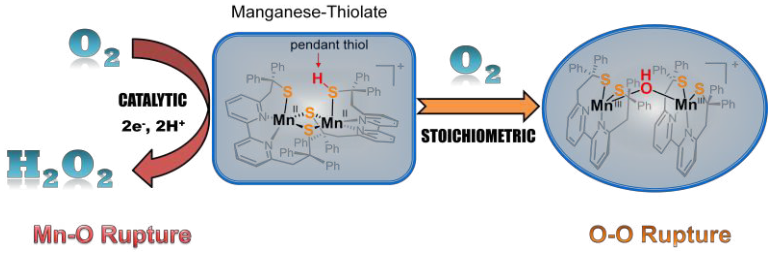

Figure 3. Schéma récapitulatif de la réactivité du complexe **Mn^{II}_2SH.**

Dans une deuxième partie, des complexes dinucléaires de Mn^{IV} sont décrits: $[Mn^{IV}_2(LS)_2(O)_2]$ **$Mn^{IV}_2(O)_2$** et $[Mn^{IV}_2(LS)_2(O)(OH)]ClO_4$ **$Mn^{IV}_2(O)(OH)$**. Le mécanisme de formation de ces composés a été étudié montrant qu'en fonction des conditions de synthèse, on peut obtenir soit **$Mn^{IV}_2(O)(OH)$** soit **$Mn^{IV}_2(O)_2$**. Les propriétés acido-basiques de ces composés ont été étudiées et ces complexes caractérisés par spectroscopie d'absorption UV-Visible (Figure 4).

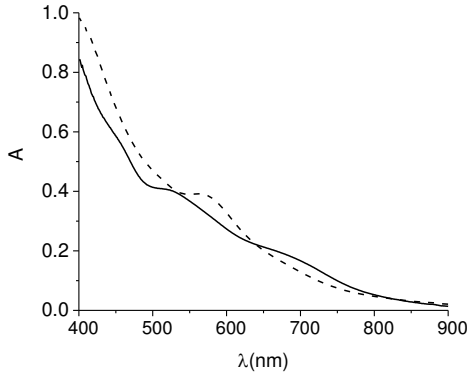

Figure 4. Profil UV-Vis de **$Mn^{IV}_2(O)_2$** (---) et après l'ajout de 1 équiv. de $LutHBF_4$ (—) 0°C (CH_2Cl_2, C b= 0.1mM, l = 1 cm).

Introduction

Dioxygen activation represents a critical step in numerous fundamental biological and industrial processes. Dioxygen represents 21% of the constituents of the air we breathe. It is mandatory to the survival of living species as animals, plants, aerobic bacteria for energy production, metabolism and their detoxification.[89]

Dioxygen is an inert molecule in its triplet ground state that is represented on the molecular orbital's diagram displayed in Figure 1.

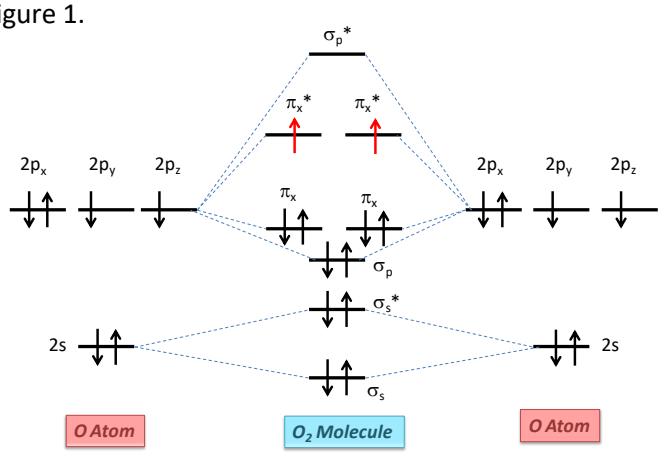

Figure 1. Molecular orbital's diagram of the O_2 molecule in its ground state.

It is a bi-radical in which unpaired electrons are located in two distinct orbitals in such way that the spin multiplicity is equal to 3. O_2 activation is a prerequisite for O_2-promoted selective oxidation and oxygenation of organic substrates[2,3] and for proton-assisted catalytic reduction of O_2. The 4-electron O_2 reduction process plays an essential role for sustaining life (aerobic respiration)[4,5] and generating electrical energy (in fuel cells).[6,7] (Equation 1)

$$O_2 + 4e^- + 4H^+ \longrightarrow 2\ H_2O \quad \text{(Equation 1)}$$

On the other hand, 2-electrons O_2 reduction generates hydrogen peroxide, a versatile and environmentally benign oxidizing agent[8,9] and also a promising candidate as an energy carrier in fuel cells.[10-13] (Equation 2)

$$O_2 + 2e^- + 2H^+ \longrightarrow H_2O_2 \quad \text{(Equation 2)}$$

Transition-metal ions are known for their ability to facilitate and control O_2 activation. In particular Fe-based systems especially with porphyrin ligands [74a] such as the cytochrome P450, [74b] have been largely developed and have displayed efficient reactivity. However, how dioxygen can be activated by metal complexes remains a central question for chemists.[14,15] In this regard, systematic studies of homogeneous metal-based systems are particularly useful for the clarification of mechanistic details of the dioxygen activation process.[16-25] In the specific case of catalytic O_2 reduction, investigations in solution are essential to obtain insights into the factors that control the competition between a 4- and 2-electron reduction processes.[19,26,27]

The reactivity of metal complexes with O_2 is mainly regulated by the nature of the transition metal ion, the donor atom set supplied by the supporting ligand, and finally by second coordination sphere effects. Among transition metals, manganese exhibits extremely rich oxygen chemistry, in both biological and synthetic systems. A number of vital reactions, involving dioxygen and its reduced derivatives (superoxide, peroxide and water) are promoted by Mn-dependent enzymes, including lipoxygenase,[28,29] ribonucleotide reductase, for which an activating process requires O_2 reduction,[30] superoxide dismutase,[31] catalases,[32] and the oxygen-evolving complex of Photosystem II (Figure 2).[33]

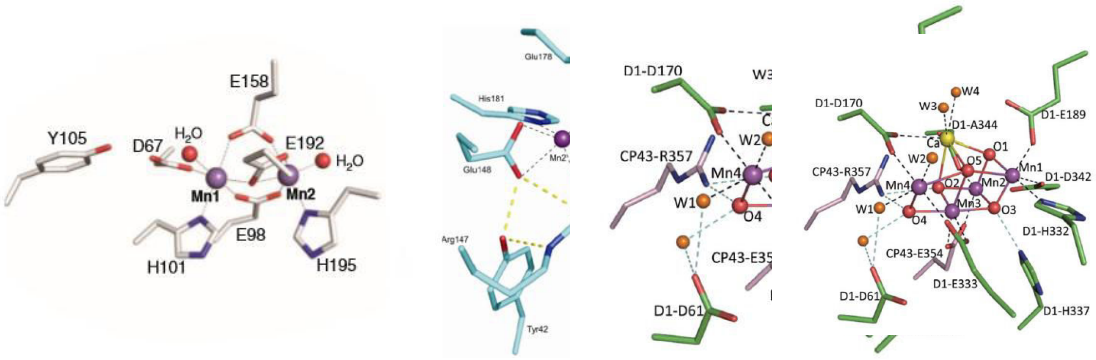

(a) (b) (c)

Figure 2. (a) Dinuclear Mn cofactor of the rinonucleotide reductase from *Escherichia Coli*,[30] (b)Dinuclear actives site of the Mn catalase from *L. plantarum* (adapted from PDB ID 1JKU) [36] and (c) structure of the Mn_4CaO_5 cluster of the oxygen evolving center.[33]

In addition, many synthetic Mn complexes mimic the structure and/or the reactivity of these enzymes based on a bio-inspired approach.[32,34-36] (Figure 3)

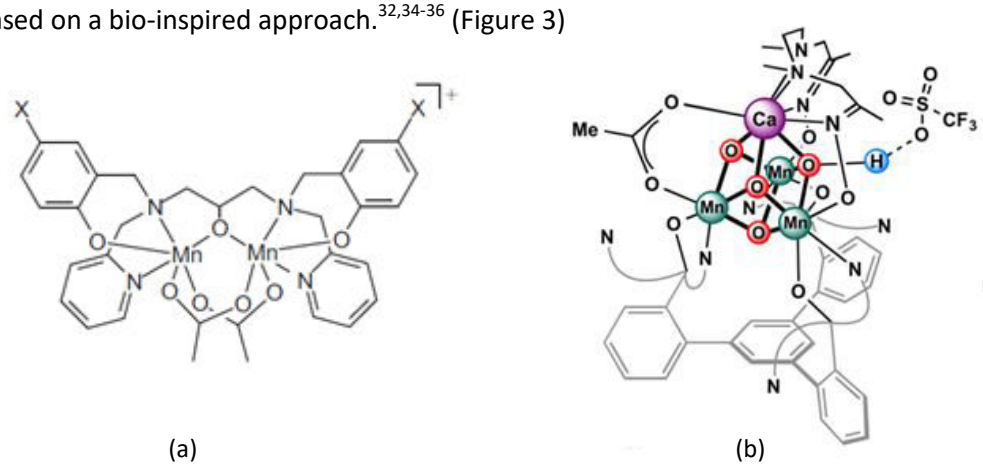

(a) (b)

Figure 3. Examples of manganese model complexes for (a) the active site of catalase[36] and (b) the oxygen evolving center.[90]

The nature of the supporting ligand also plays a key role in the reactivity of metal complexes with dioxygen. In particular, it has been shown that the coordination of thiolates to a metal ion can promote the activation of molecular oxygen[37] for several reasons: i) stabilization of metal-peroxo,[38-40] -hydroperoxo,[41] -alkylperoxo[42-44] and -superoxo[45] complexes, as a consequence of thiolate charge donation, ii) decrease of the activation barrier to O_2 binding, as shown by theoretical studies,[45,46] iii)

assistance of metal oxidation by O_2 by significantly lowering its redox potential,[47] iv) increase of the basicity of bound substrates by reducing the metal ion Lewis acidity (to generate more basic oxo ligands for instance)[48] and, finally v) stabilization of coordinatively unsaturated M^{II} complexes with the concomitant labilization of the *trans* sites to the thiolate for promoting product release.[47] This has been recently validated by the work of Kovacs et al. in the case of manganese complexes. They reported a series of mononuclear thiolate Mn^{II} complexes capable of activating and reducing O_2 stoichiometrically by generating mono-μ-oxo dinuclear Mn^{III} species (Figure 4a).[38,49] They also detected and characterized the first example of peroxo-bridged Mn^{III} dinuclear complex (Figure 4b).[38] Among Mn^{III} complexes, they recently reported a series of mononuclear alkylperoxo complexes including the first structure resolved by X-ray diffraction (Figure 4c). However, no catalytic studies (oxidation of substrates or dioxygen reduction) were performed on these systems.

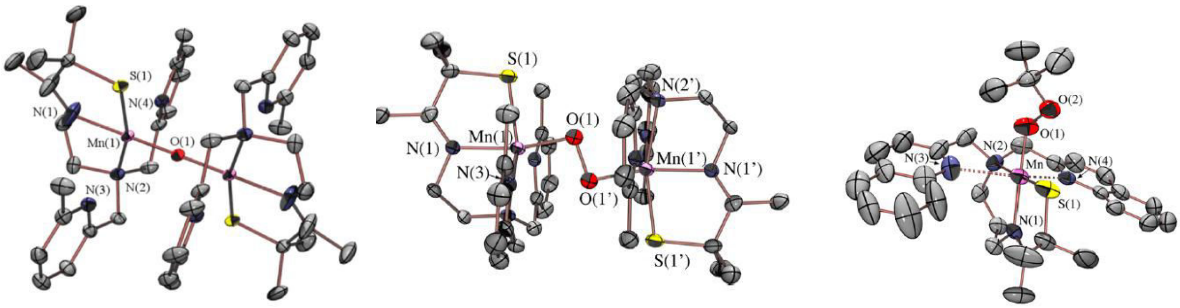

(a) (b) (c)

Figure 4. Examples of ORTEP diagrams of Mn-thiolate dinuclear –oxo[49](a), -peroxo[38](b), -alkylperoxo[43] (c) complexes.

In addition to the nature of the metal ion and its first coordination sphere, the control of the secondary coordination sphere of a complex is also crucial to achieve highly functional compounds and high chemical selectivity. In particular, the presence of pendant acids (or bases) is known to promote reactivity *via* transient hydrogen bonding interactions, to act as proton relay during a catalytic process, but also to modulate the redox potential of the metal center.[50] These concepts have also been validated in the domain of O_2 activation and reduction.[51-54] For instance, the group of Borovik, who,described Fe^{III} and Mn^{III} complexes, evidenced that the design of systems with rigid scaffold can play the same role of the second coordination sphere of a protein active site by positioning functional group to help the stabilization of oxygen-metal species *via* hydrogen bond (Figure 5).[51]

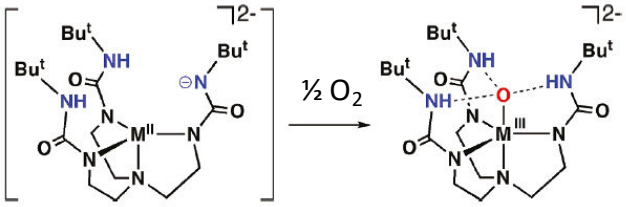

Figure 5. M^{III} (M=Fe, Mn) complexes obtained after exposition to ½ O_2, stabilized by H-bonding.[51]

What are the factors that influence a 2 versus 4 electron-reduction remains a central question and especially which are the factors that promote a O-O versus M-O cleavage to obtain oxydative agents?

In this chapter, the synthesis and characterization of a new manganese-thiolate complex, $[Mn^{II}_2(LS)(LSH)]ClO_4$ (**Mn^{II}_2SH**, Figure 6) bearing a pendant thiol group bound (in its -SH form) to one Mn^{II} ion is described. This complex is capable of activating dioxygen, and also acts as an active catalyst for selective 2-electron O_2 reduction in the presence of a one-electron reducing agent and a proton source. The O_2 activation and reduction pathways, under both stoichiometric and catalytic conditions, have been investigated and discussed here.

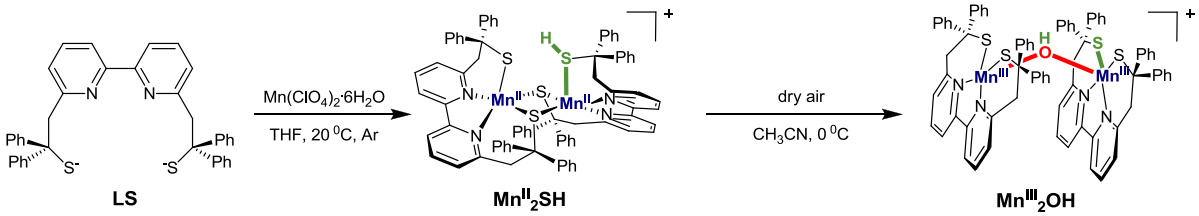

Figure 6. Synthesis of **Mn^{II}_2SH** and **Mn^{III}_2OH** from the LS ligand.

In a second part, high valent Mn^{IV} complexes $[Mn^{IV}_2(LS)(O)_2]$ and [MnIV2(LS)(O)(OH)]ClO_4 (**$Mn^{IV}_2(O)_2$** and **Mn^{IV}_2(O)(OH)**, respectively) obtained from **Mn^{II}_2SH** are discussed (Figure 7)**.** Their acid/base properties has been investigated and is discussed in this chapter.

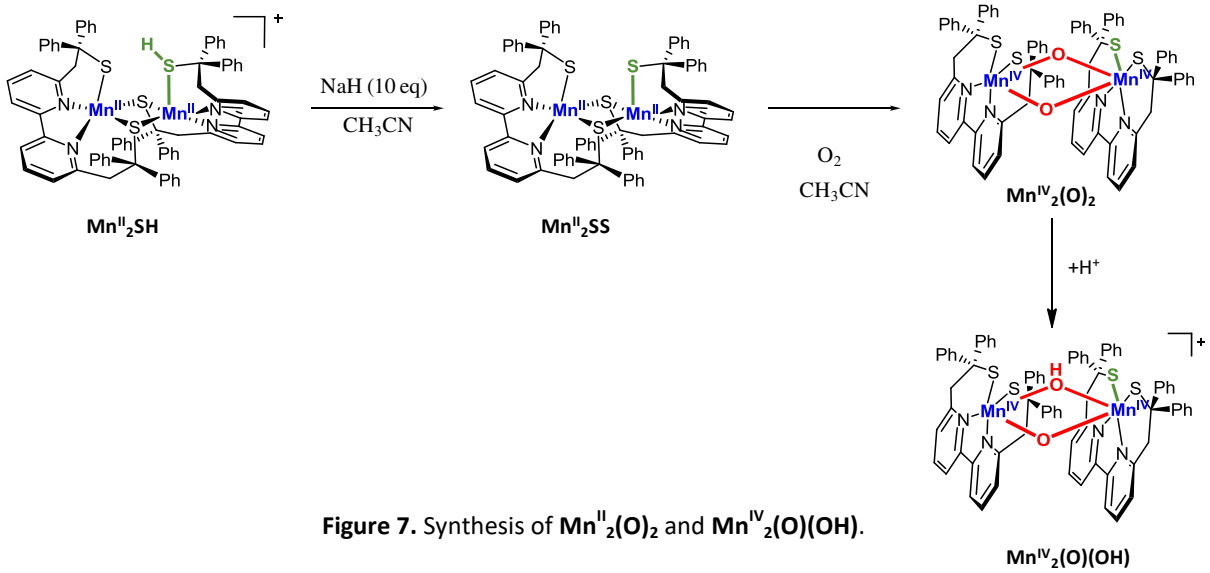

Figure 7. Synthesis of **$Mn^{II}_2(O)_2$** and **Mn^{IV}_2(O)(OH)**.

This project was already started before my arrival in the laboratory and the **Mn^{II}_2SH** and **Mn^{III}_2OH** previously isolated and characterized by M. Gennari. Part of this work has been recently published in *J. Am. Chem. Soc.* **2015**, 137, 8644–8653.

Results and Discussion

2.1. Synthesis and structural properties of **Mn^{II}_2SH** and **Mn^{III}_2OH**.

2.2.1. Synthesis of **Mn^{II}_2SH** and **Mn^{III}_2OH**.

The synthesis of the LS ligand (2,2'-(2,2'-bipyridine-6,6'-iyl)bis(1,1-diphenylethanethiolate))[55] has been described in chapter I. The potassium salt of LS reacts with an excess (2.5 equiv.) of $Mn(ClO_4)_2{\cdot}6H_2O$ in THF at 293 K under inert atmosphere, leading to a pale orange precipitate (Figure 6). The resulting powder corresponds to the dimercapto-bridged Mn^{II} dinuclear complex $[Mn^{II}_2(LS)(LSH)]ClO_4$ (**Mn^{II}_2SH**), as shown by single crystal X-ray diffraction data (vide infra). Surprisingly, in this compound, one of the metal-bound thiolates is protonated (*i.e.* the thiol form). The **Mn^{II}_2SH** complex reacts with O_2 in CH_3CN, leading to the formation of a dark red-purple precipitate, corresponding to the mono-μ-hydroxo dinuclear Mn^{III} complex $[(Mn^{III}_2(LS)_2(OH)]ClO_4$ (**Mn^{III}_2OH**), which has also been characterized by single crystal X-Ray diffraction.

2.1.2. Structural characterization of **Mn^{II}_2SH**.

X-Ray suitable orange-brown crystals corresponding to **Mn^{II}_2SH** were obtained by slow diffusion of diethyl ether into a solution of the product in acetonitrile at 293 K. The X-ray structure of **Mn^{II}_2SH** is shown in Figure 8 and selected distances are given in Table 1. The **Mn^{II}_2SH** cation consists of a dimercapto-bridged dinuclear Mn^{II} complex. Its structure contains a quasi-planar $\{Mn_2S_2\}$ diamond core (deviation from the S2Mn1S52Mn2 plane less than 0.017 Å, angle between the S2Mn1S52 and S2Mn2S52 planes of 2.36°). The two Mn sites are not equivalent and each Mn center is pentacoordinated, surrounded by an N2S3 donor set in a distorted square pyramidal geometry. The Mn···Mn distance of 3.1738(6) Å is too long for a direct metal-metal interaction. The discrepancy between the Mn1-S1 and Mn2-S51 bond lengths (2.4399(10) Å and 2.6462(10) Å, respectively) reflects the fact that S51 is protonated (S51-H51S = 1.61(3) Å) in agreement with the presence of electronic density of a proton found by Fourier transform near S51 (coordinated were refined and isotropic displacement parameter was fixed at 1.2 times that of S51). Coherently, S and Mn K-edge X-ray absorption spectroscopy (XAS) as well as magnetic susceptibility measurements (*vide infra*) demonstrate that both Mn ions are at the +II oxidation state. The S1···S51 distance of 3.772(3) Å is in agreement with a localized proton on one of the monodentate sulphur atoms in solid state.

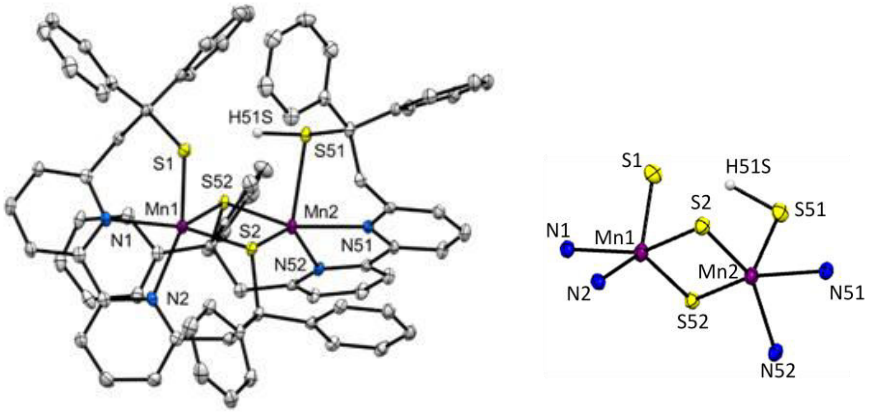

(a) (b)

Figure 8. (a) Molecular structure of **Mn^{II}_2SH**·1.55CH_3CN·0.45CH_3OH an (b) the {Mn_2S_2} core. The thermal ellipsoids are drawn at 30% probability level. All hydrogen atoms, except for H51S in **Mn^{II}_2SH**, anions and solvent molecules are omitted for clarity.

In the **Mn^{II}_2SH** complex, the distorted square pyramidal geometry around each Mn center is defined by τ_5 values of 0.35 and 0.25 for Mn1 and Mn2, respectively.[91] Each Mn is coordinated to five ligands and the geometry can be defined by τ_5 values. **τ** corresponds to an angular structural parameter that is defined and proposed as an index of trigonality. It is used as a general descriptor of five-coordinate centric molecules (Figure 9).

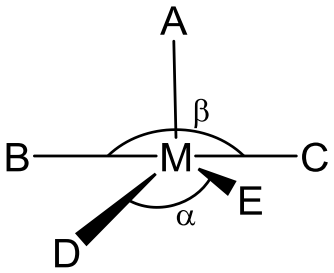

Figure 9. Definition of the angles in five-coordinated complex.

In a five-coordinated system, such as represented above, an ideal square-pyramidal geometry is associated with α=β=180°, where A is the axial ligand. Trigonal systems are characterized by a α=120° and BMC becomes the principal axis. In most of the cases, M is displaced out of the BCDE plan towards A in a square-pyramidal geometry where α=β<180°. The geometry can be described by the value of (β-α) which is 0 for a C_{4v}, and 60° for a D_{3h} or trigonal-bipyramidal geometry. It has thus been defined the geometric parameter τ=(β-α)/60 which is applicable to five-coordinate structures as an index of the degree of trigonality. τ is equal to zero for a perfect tetragonal geometry whereas it becomes one for a perfectly trigonal-bipyramidal geometry.[91]

The plane for Mn1(Mn2) is defined by the N1(51), N2(52) and S1(51) atoms, and the bridging aliphatic thiolate sulfur S52(2) atom. The axial position is occupied by the S2(52) atom. The Mn-N

distances are comprised in the range 2.172-2.229 Å, consistent with the Mn^{II}-N distances previously observed with bipyridine-derivatives. Concerning the Mn-S bonds, those implicated in the diamond core (2.4679-2.5075 Å) are similar to those found in structurally related complexes.[82] The μ-S bonds are longer than the terminal unprotonated Mn1-S1 bond, which is comprised in the range values of Mn-SR terminal bonds found in other alkyl thiolate-ligated Mn(II) complexes (2.36-2.45 Å).[82-85]

Table 1. Selected bond lengths (Å) for **Mn^{II}_2SH**·1.55CH_3CN·0.45CH_3OH and the two crystallographically independent units of **Mn^{III}_2OH$^{\#}$**·7.16CH_3CN.

Mn^{II}_2SH		**Mn^{III}_2OH$^{\#}$**			
Mn(1)-N(1)	2.172(2)	Mn(1)-N(1)	2.061(4)	Mn(3)-N(81)	2.101(4)
Mn(1)-N(2)	2.255(2)	Mn(1)-N(2)	2.082(4)	Mn(3)-N(82)	2.057(4)
Mn(1)-S(1)	2.4399(10)	Mn(1)-S(1)	2.2916(15)	Mn(3)-S(81)	2.2775(16)
Mn(1)-S(2)	2.5075(9)	Mn(1)-S(2)	2.2918(15)	Mn(3)-S(82)	2.2782(15)
Mn(1)-S(52)	2.4869(9)	Mn(1)-O(1)	2.034(3)	Mn(3)-O(2)	2.043(3)
Mn(1)-Mn(2)	3.1738(6)	Mn(2)-N(41)	2.097(4)	Mn(4)-N(121)	2.058(3)
Mn(2)-N(51)	2.181(2)	Mn(2)-N(42)	2.056(4)	Mn(4)-N(122)	2.089(4)
Mn(2)-N(52)	2.229(2)	Mn(2)-S(41)	2.2881(15)	Mn(4)-S(121)	2.2881(13)
Mn(2)-S(51)	2.6462(10)	Mn(2)-S(42)	2.2754(15)	Mn(4)-S(122)	2.2872(13)
Mn(2)-S(52)	2.4759(9)	Mn(2)-O(1)	2.041(3)	Mn(4)-O(2)	2.036(3)
Mn(2)-S(2)	2.4679(9)				

2.1.3. Structural characterization of **Mn^{III}_2OH**.

In order to obtain crystals of **Mn^{III}_2OH**, 1.5 equivalent of dioxygen were added into a 0.9 mM solution of **Mn^{II}_2SH** in acetonitrile at -18°C, in the presence of 0.02 M Bu_4NPF_6, without stirring. After few days, X-Ray-suitable dark red single crystals of the product were obtained. The X-ray structure of **Mn^{III}_2OH** is shown in Figure 10 and selected distances are given is table 1. The **Mn^{III}_2OH** complex crystallizes as a mixed-salt, $[(Mn^{III}L)_2(OH)](PF_6)_{0.81}(ClO_4)_{0.19}$ (**Mn^{III}_2OH$^{\#}$**) with two crystallographically independent molecules with similar geometries. **Mn^{III}_2OH** is a rare example of a dinuclear Mn^{III} complex with a unique hydroxo bridge and the first with thiolate ligands.[56-59] Each manganese(III) ion is surrounded by an N2S2O donor set in a distorted square pyramidal coordination sphere. The Mn^{III}-S distances - with S being unprotonated - are shorter than those in **Mn^{II}_2SH**, in agreement with the increase of the Mn oxidation state from +II to +III. The Mn-O(H)-Mn angles of 146.56(17) and 146.11(17)° and the Mn···Mn separation of 3.902(1) Å and 3.903(1) Å are in the range found in the other reported dinuclear μ-OH Mn^{III} complexes (141°<Mn-O-Mn<160° and 3.87 Å <Mn…Mn distance<3.99 Å).[56-59] A mono oxo-bridge can be excluded based on the Mn···Mn distance that is notably shorter in dinuclear mono μ-oxo Mn^{III} complexes (3.4-3.6 Å).[34,49,60]

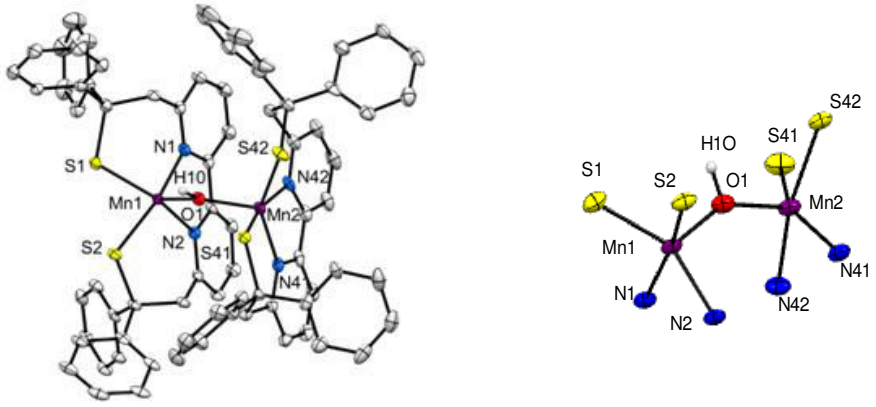

(a) (b)

Figure 10. (a) Molecular structure of $\mathbf{Mn^{III}_2OH^{\#}}\cdot 7.16CH_3CN$ and (b) the $\{Mn_2O(H)\}$ core. The thermal ellipsoids are drawn at 30% probability level. All hydrogen atoms, except for H10 in $\mathbf{Mn^{III}_2OH^{\#}}$, anions and solvent molecules are omitted for clarity. Only one crystallographically independent unit of $\mathbf{Mn^{III}_2OH^{\#}}$ is displayed.

The structure of $\mathbf{Mn^{III}_2OH}$ contains solvent accessible voids of 385 $Å^3$, corresponding to 48.125 $Å^3$ per complex unit. This can be attributed to the presence of an additional, completely disordered molecule of co-crystallized acetonitrile per $\mathbf{Mn^{III}_2OH}$. The distorted square pyramidal geometry around each Mn center is defined by τ_5 values in the range 0.27-0.40.[86] The plane is defined by the four coordinated atoms of LS, which presents a N2S2 donor set. The axial position is occupied by the O atom of the hydroxo bridge. The Mn-N distances (2.056-2.101 Å) are consistent with Mn^{III}-N distances previously observed with bipyridine-derivatives. The Mn-S bond lengths (2.2754-2.2918 Å) are comparable with those reported in other complexes with Mn^{III}-SR bonds.[85-87]

X-Ray diffraction data collection are given in the appendix for $\mathbf{Mn^{II}_2SH}$ and $\mathbf{Mn^{III}_2OH}$ complexes.

2.2. Mn and S K-Edge XAS absorption of $\mathbf{Mn^{II}_2SH}$ and $\mathbf{Mn^{III}_2OH}$.

Absorption spectroscopy by X-Ray (XAS) by atoms is nowadays a very powerful tool for studying structural and physicochemical properties of chemical compounds including the local geometry of the absorber (EXAFS) and/or its electronic structure (XANES). This method can be applied for crystal, amorphous or liquid samples. XAS data are obtained by tuning the photon energy at which a core electron can be excited. The name of the edge depends on the core electron which is excited (K, L, M…). Regarding the XANES spectrum, 2 main regions can be observed: (i) the pre-edge, which correspond to the transition from a core electron to the lowest unoccupied state (1s->3d); (ii) the edge, at which a core electron absorbs the energy which is equal or greater than its binding energy (1s->4p). Consequently, the energy increases as the effective nuclear charge on the metal increases. The pre-edge will give information about the electronic structure, the ligand type and the covalency, whereas the edge gives information about the oxidation state, the symmetry site and the coordination number.

Mn and S K-edge XAS experiments have been performed to assign the oxidation state of the Mn ions in both **Mn^{II}_2SH** and **Mn^{III}_2OH** complexes (Figure 11). Such investigation was crucial to indirectly confirm the protonation of one LS ligand in **Mn^{II}_2SH** and the hydroxo nature of the bridge present in **Mn^{III}_2OH**.

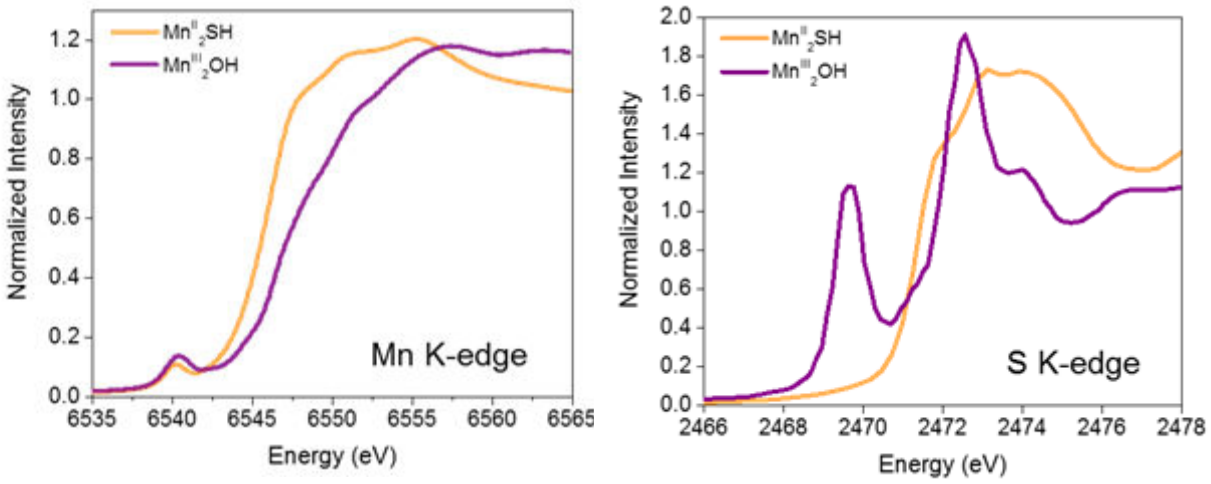

Figure 11. Mn and S K-edge XAS spectra recorded on powdered samples of **Mn^{II}_2SH** and **Mn^{III}_2OH**.

It has been previously shown that the energy of the Mn K-edge (and pre-edge), corresponding to a Mn(1s) → Mn(4p) transition (and Mn(1s) → Mn(3d) transition), is sensitive to the oxidation level of the Mn ions, *i.e*. the lower the energy, the lower the oxidation state.[61,62] This can be rationalized by considering that removing one electron from an atom that bears a higher positive charge is more difficult. In this specific case, the ~1.5 eV shift to lower energy of the edge inflection point measured for **Mn^{II}_2SH** with respect to that for **Mn^{III}_2OH** is consistent with a + II oxidation state in **Mn^{II}_2SH** *vs* +III in **Mn^{III}_2OH**. The same trend is observed for the much less intense Mn K pre-edge feature at ~6540 eV.

The sulfur K-edge XAS experiments also provide information on the oxidation level of the Mn ions. In a simplified model, the sulfur K pre-edge corresponds to a transition from the 1s orbital of a sulfur atom to an unoccupied orbital bearing both S 3p and Mn 3d character. It is thus expected that the pre-edge transition shifts to lower energies when the oxidation state of the Mn ion increases, as the Mn(3d) orbitals are stabilized in presence of a higher positive charge on Mn (the S(1s) energy remaining virtually unchanged). Accordingly, a sulfur K pre-edge is observed only in the case of **Mn^{III}_2OH**, at an energy of 2469.6 eV, while that of **Mn^{II}_2SH** is obscured by the edges above 2472 eV. For both complexes, the sulfur K-edge energies at approximately 2472 eV are consistent with reduced sulfurs as thiol or thiolate groups.

2.3. Magnetic properties of $\mathbf{Mn^{II}_2SH}$ and $\mathbf{Mn^{III}_2OH}$.

Variable-temperature magnetic susceptibility data were collected on powdered samples of $\mathbf{Mn^{II}_2SH}$ and $\mathbf{Mn^{III}_2OH}$ in the 1.8 to 300 K temperature range at 1000 Oe (Figure 12).

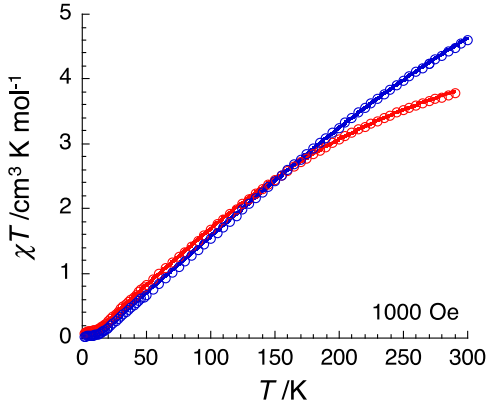

Figure 12. Temperature dependence of the χT product (where χ is the molar magnetic susceptibility equal to M/H per complex) measured at 1000 Oe for $\mathbf{Mn^{II}_2SH}\cdot 1.55CH_3CN\cdot 0.45CH_3OH$ (○) and $\mathbf{Mn^{III}_2OH^{\#}}\cdot 7.16CH_3CN$ (○). The solid lines are the best fits of the experimental data to the models described in the text.

For both systems, the steady decrease of χT product to nearly zero at 2 K suggests the presence of significant intra-complex antiferromagnetic exchange. Therefore, the magnetic data were analyzed by an isotropic spin-dimer Heisenberg model, $H = -2JS_AS_B$, assuming that the two metal ions are high spin Mn^{II} ($S_A = S_B = 5/2$) in $\mathbf{Mn^{II}_2SH}$, or high spin Mn^{III} ($S_A = S_B = 2$) in $\mathbf{Mn^{III}_2OH}$.[63] Concerning $\mathbf{Mn^{II}_2SH}$, the bridging thiolate ligands mediate antiferromagnetic interactions between Mn^{II} magnetic centers leading to a diamagnetic $S = 0$ ground state. The resulting best fit for $\mathbf{Mn^{II}_2SH}$ (solid blue line in Figure 3) gives $g_A = g_B = 2.05(8)$ and $J = -22(1)$ cm^{-1} (-31(1) K). The magnetic coupling between two Mn^{II} ions is typically small (J =< 10 cm^{-1}) regardless of the nature of the bridging ligand[32,64] (We note that phenolato bridges are an exception).[65] Therefore, the exchange interaction found in $\mathbf{Mn^{II}_2SH}$ is surprisingly high. In the literature, the number of polynuclear Mn^{II} complexes with thiolate bridge(s) is limited and, to the best of our knowledge, the magnetic properties have been reported only for one of those, *i.e.* a linear trinuclear Mn^{II} complex with a mono μ-thiolato bridge between each Mn ion, with a relatively strong antiferromagnetic interaction evaluated around -9.8 cm^{-1}.[66] Concerning $\mathbf{Mn^{III}_2OH}$, the resulting best fit affords $g_A = g_B = 2.00(5)$ and $J = -19(1)$ cm^{-1} (-27(1) K; solid red line in Figure 12). The magnetic properties of only two other mono μ-hydroxo dinuclear Mn^{III} complexes have been reported so far, both containing porphyrin-based ligands. In these two complexes, the antiferromagnetic exchange interaction is much larger, *i.e.* -71 cm^{-1} and -74 cm^{-1}, consistent with larger Mn-O-Mn angle values (152.73° and 160.4°, respectively, *vs* 146.56°/146.11° for $\mathbf{Mn^{III}_2OH}$).[56,57]

2.4. Solution properties.

The **Mn^{II}_2SH** compound has been studied in solution. We observed that the dinuclear solid-state structure is retained when it is dissolved in CH_3CN. This has been attested by electrospray ionization mass spectrometry (ESI-MS; 1267.2 *m/z*). The redox properties of **Mn^{II}_2SH** in solution have been investigated by cyclic voltammetry (CV).

2.4.1. Redox properties of **Mn^{II}_2SH**.

The cyclic voltammetry (CV) has been used to evidence the presence of the metal-bound SH group (Figure 13). A cathodic peak at -1.27 V *vs* Fc/Fc^+ is observed only in the CV of **Mn^{II}_2SH** recorded on Pt working electrode, but not on glassy carbon, GC. The well-known ability of platinum to lower the overpotential for proton reduction leads to the assignment of this peak to the reduction of the Mn-bound thiol proton into H_2.

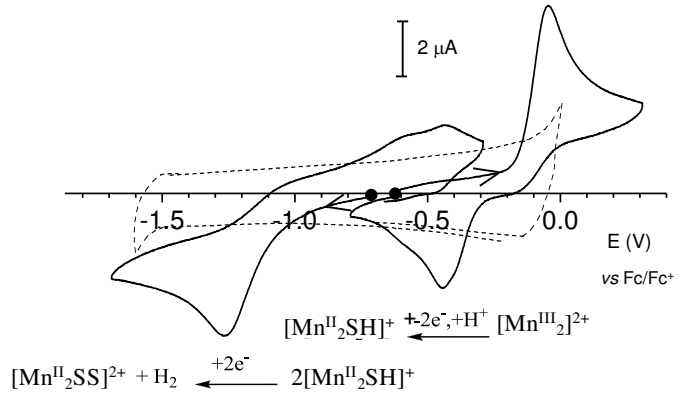

Figure 13. CV of **Mn^{II}_2SH** (0.6 mM) in CH_3CN, 0.1 M Bu_4NPF_6. Platinum working electrode (1 mm diameter), scan rate of 100 $mV{\cdot}s^{-1}$ (—). The proton (-SH) reduction peak at -1.27 V is shown. Carbon working electrode (3 mm diameter)(----).

The CVs of **Mn^{II}_2SH** recorded both on Pt or GC electrodes show an irreversible anodic peak at Ep_a = -0.01 V, assigned to a two-electron metal based oxidation, $Mn^{II}Mn^{II} \rightarrow Mn^{III}Mn^{III}$. The redox potential associated with the $Mn^{III}Mn^{III}/Mn^{II}Mn^{II}$ system suggests that **Mn^{II}_2SH** could be easily oxidized by O_2, in analogy to the mononuclear Mn^{II}-thiolate complexes reported by Kovacs (for which $E_{1/2}$ = +0.08 to +0.20 V *vs* Fc/Fc^+ for the Mn^{III}/Mn^{II} redox couples). The potential of the corresponding cathodic peak (Ep_c = -0.47 V) indicates that the electrochemically-generated $Mn^{III}Mn^{III}$ dinuclear complex (**Mn^{III}_2SH**) undergoes a fast chemical rearrangement, probably associated with the deprotonation of the thiol group to afford **Mn^{III}_2**.

A different redox behavior was observed in the case of a related dinuclear Cu^I complex containing an analogous bis-μ-thiolato bridge. The latter displayed a one-electron reversible $Cu^{1.5}Cu^{1.5}/Cu^ICu^I$ redox process, the mixed-valence species being stable and fully characterized.[67] In the case of **Mn^{II}_2SH**, the generation of the mixed-valence species is prevented presumably due to the fact that the redox potential of the $Mn^{III}Mn^{II}/Mn^{II}Mn^{II}$ couple is too close to that of the $Mn^{III}Mn^{III}/Mn^{III}Mn^{II}$ couple.

During the oxidative electrolysis of **Mn^{II}_2SH** in CH_3CN (at *E* = +0.05 V), the color of the solution turns from light orange to deep orange (**Mn^{III}_2**) and then evolves to light yellow (**Mn^{II}_2SS**) at 293 K (Figure 14). This final species corresponds to a Mn^{II}_2-disulfide **Mn^{II}_2SS** complex that has been isolated and characterized and that is discussed in chapter III. This species can be obtained from **Mn^{III}_2** after evolving with time (Figure 15).

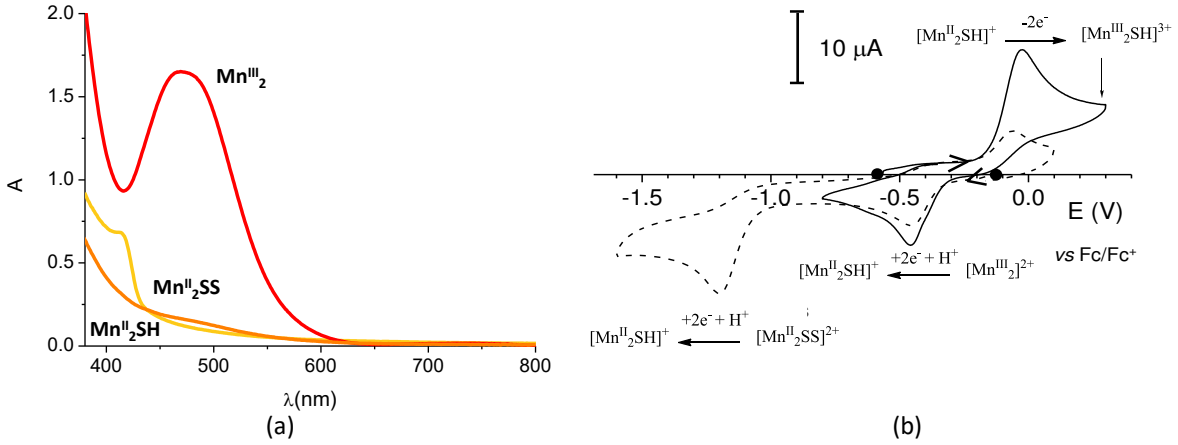

Figure 14. (a) UV-Vis spectrum absorption of **Mn^{III}_2** (—), **Mn^{II}_2SH** (—) and **Mn^{II}_2SS** (—) and (b) CV of **Mn^{II}_2SH** (0.7 mM) in CH_3CN, 0.1 M Bu_4NPF_6, before (—) and after (---) electrolysis at +0.05 V.

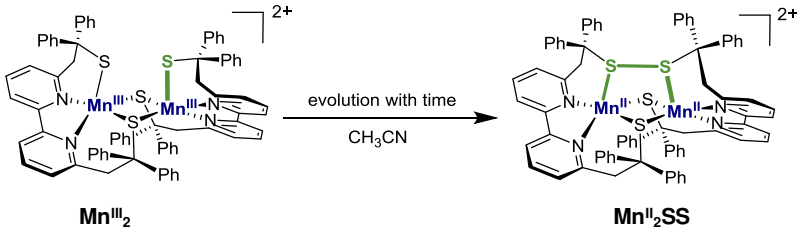

Figure 15. Obtention of **Mn^{II}_2SS** from **Mn^{III}_2** evolving with time.

On this basis, the deep orange intermediate species (that can be stabilized at 253 K) has been assigned to a bis μ-thiolato dinuclear Mn^{III} complex with two terminal thiolate groups (**Mn^{III}_2**), the isoelectronic form of the **Mn^{II}_2SS** complex. The deep orange color is due to a broad absorption band at ~475 nm (~6400 $M^{-1}cm^{-1}$, Figure 14 a) and was assigned to ligand to metal charge transfer (LMCT) contributions to the lower-energy d-d transitions based on time dependent density functional theory (TDDFT) calculations.

2.4.2. Redox properties of $\mathbf{Mn^{III}_2OH}$.

The solution properties of $\mathbf{Mn^{III}_2OH}$ have been investigated as well as the redox properties. When a light orange solution of $\mathbf{Mn^{II}_2SH}$ (1 mM) is exposed to air or to dry O_2 (~1 mM) in CH_3CN at 293 K, a dark red-purple solution is formed, containing the structurally characterized $\mathbf{Mn^{III}_2OH}$ complex as the main product (Figures 6 and 8). Based on the epsilon value of $\mathbf{Mn^{III}_2OH}$ at 527 nm (~3100 $M^{-1}cm^{-1}$) determined from the isolated product, about ~70% of $\mathbf{Mn^{III}_2OH}$ is generated under these conditions (Figure 16 a).

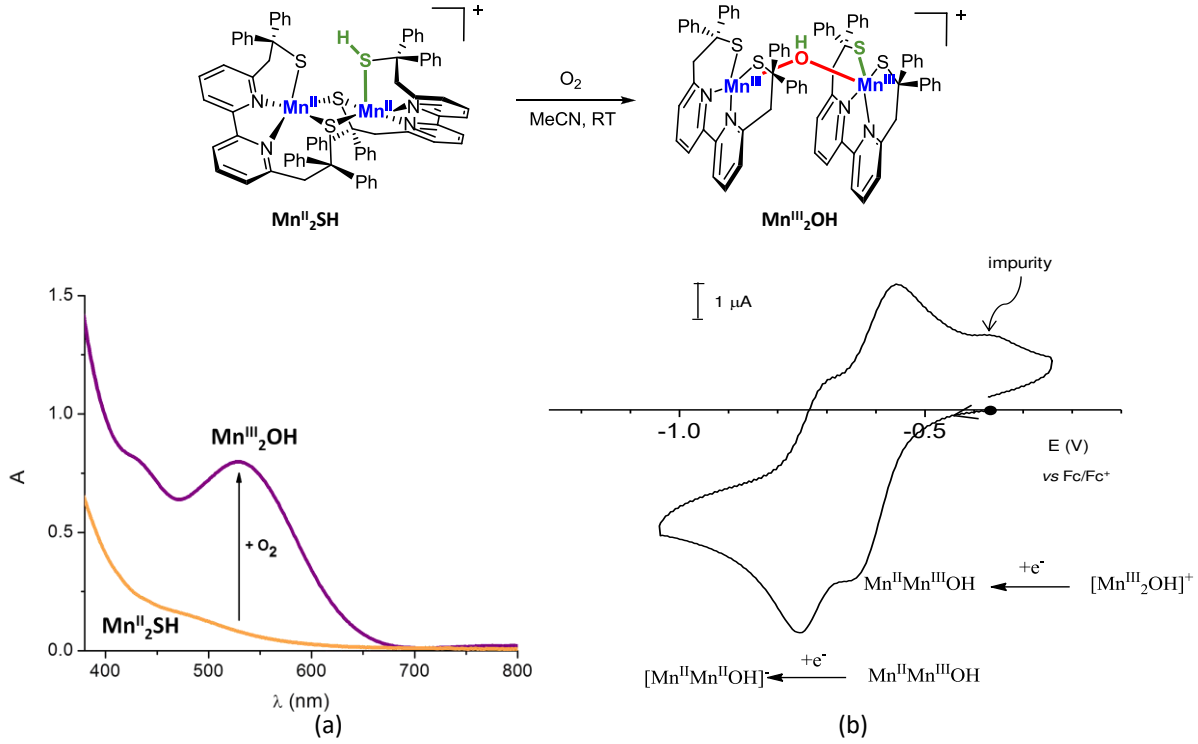

Figure 16. (top) Synthesis of $\mathbf{Mn^{III}_2OH}$. (a) UV-Vis spectrum of $\mathbf{Mn^{II}_2SH}$ (0.35 mM) in CH_3CN before (—) and after addition of 1 mM O_2 (—) to generate $\mathbf{Mn^{III}_2OH}$; 1 cm optical path length and (b) CV of a saturated solution of $\mathbf{Mn^{III}_2OH}$ in CH_3CN (~0.6 mM), 0.1 M Bu_4NPF_6, at 253 K. Glassy carbon working electrode (3 mm diameter), scan rate of 100 $mV{\cdot}s^{-1}$.

In agreement with its dinuclear structure, the CV of $\mathbf{Mn^{III}_2OH}$ displays two successive one-electron reduction processes at Ep = -0.60 V (ΔEp = 80 mV) and -0.75 V (ΔEp = 80 mV) corresponding to the stepwise reduction of the Mn^{III} dinuclear complex into the corresponding Mn^{II} analogue (Figure 16 b). The low stability of the product at 293 K can explain the non-quantitative character of the process as well as the possible presence of weak absorbers as side-products. Based on TDDFT calculations, the 527 nm absorption band has been assigned to a mixed d-d/intraligand charge transfer (ILCT) transition.

2.5. Reactivity of $\mathbf{Mn^{II}_2SH}$ with dioxygen.

2.5.1. Reactivity of $\mathbf{Mn^{II}_2SH}$ with dioxygen in stoichiometric conditions.

In an attempt to identify O_2 as the source of oxygen for the hydroxo bridge, $^{18}O_2$ was used to generate $\mathbf{Mn^{III}_2OH}$. Even though no labeled $\mathbf{Mn^{III}_2{}^{18}OH}$ compound was observed by ESI-mass spectrometry, H_2O has been excluded as the oxygen source in $\mathbf{Mn^{III}_2OH}$ based on the fact that no $\mathbf{Mn^{III}_2OH}$ is formed when $\mathbf{Mn^{III}_2}$ is electrochemically-generated in the presence of H_2O (Equation 3). The lack of ^{18}O-labeling in $\mathbf{Mn^{III}_2OH}$ when $^{18}O_2$ is used has been attributed to a fast exchange between the μ-^{18}OH bridge and adventitious water as previously reported for a $Mn^{III/IV}_4$-oxo complex of the photosystem II.[68,69] Such exchange has been further evidenced by adding $H_2{}^{18}O$ to $\mathbf{Mn^{III}_2OH}$ in CH_3CN (Equation 4) by using mass spectrometry (Figure 17)

$$Mn^{III}_2 + H_2O \not\longrightarrow Mn^{III}_2OH \qquad \text{(Equation 3)}$$

$$Mn^{III}_2OH + H_2{}^{18}O \longrightarrow Mn^{III}_2{}^{18}OH + H_2O \qquad \text{(Equation 4)}$$

In Figure 17a, the mass spectrum of $\mathbf{Mn^{III}_2OH}$ is shown with a major peak of 1283.3 m/z for $[(MnL)_2OH]^+$. After the addition of $H_2{}^{18}O$ in the same sample, a two-unit shift is observed with the 1285.2 m/z peak of Figure 17b that is characteristic of the presence of ^{18}O instead of ^{16}O. This is consistent with the $^{16}O/^{18}O$ exchange coming from the water.

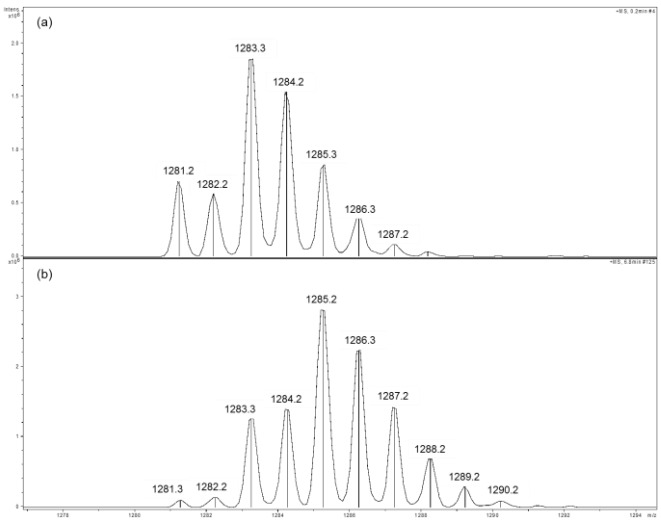

Figure 17. Molecular peak in the ESI-mass spectrum of a 0.8 mM solution of $\mathbf{Mn^{III}_2OH}$ in CH_3CN (1283.3 *m/z*) before (a) and after (b) addition of ^{18}O-water.

In order to evaluate the potential catalytic activity of $\mathbf{Mn^{II}_2SH}$ for proton-assisted O_2 reduction, the effect of proton addition during the oxygenation process has been monitored by visible absorption spectroscopy (Figure 18a) and CV (Figure 18b).

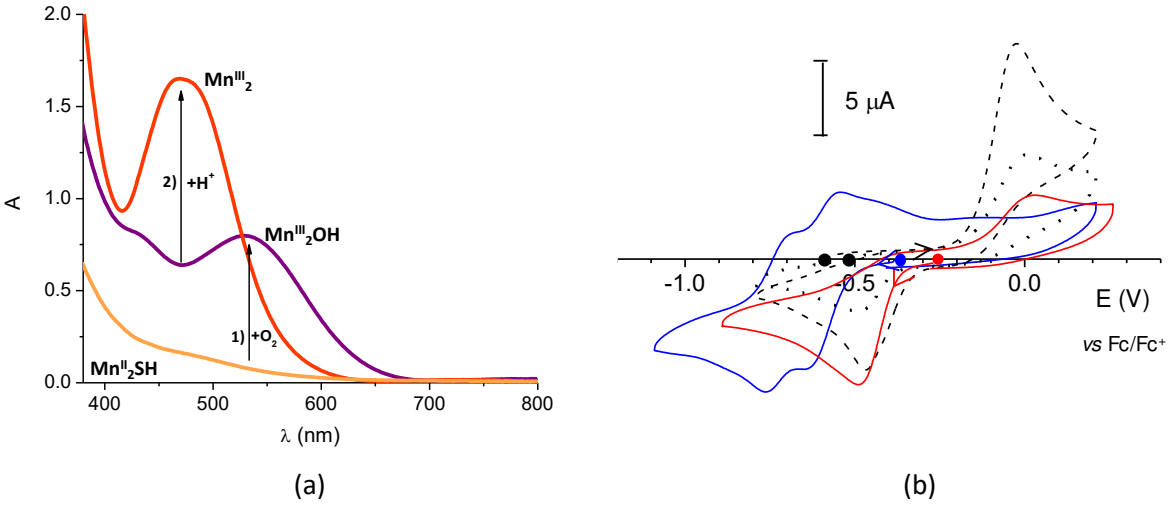

Figure 18. (a) UV-Vis spectrum of **Mn$^{II}_2$SH** (0.35 mM) in CH_3CN before (—) and after addition of 1 mM O_2 (—) to generate **Mn$^{III}_2$OH**. **Mn$^{III}_2$** is obtained after the addition of 2,6-lutidinium tetrafluoroborate (1 eq.) to **Mn$^{III}_2$OH**, spectrum (—); 1 cm optical path length. (b) CV of **Mn$^{II}_2$SH** (0.5 mM) in CH_3CN, 0.1 M Bu_4NPF_6, before (---) and after sequential addition of air (—) + $LutHBF_4$ (10 eq, —), followed by electrolysis at -0.7 V to partially regenerate the initial species (‴, ~35% yield). Glassy carbon working electrode (3 mm diameter), scan rates of 100 $mV{\cdot}s^{-1}$.

In a first step, **Mn$^{III}_2$OH** is generated from the reaction of **Mn$^{II}_2$SH** with O_2. The following addition of 2,6-lutidinium tetrafluoroborate ($LutHBF_4$) instantaneously leads to the protonation of **Mn$^{III}_2$OH** with the simultaneous production of H_2O as the main product and **Mn$^{III}_2$** (Figure 19a). Subsequently, the *in situ* generated **Mn$^{III}_2$** complex can be reduced by exhaustive electrolysis at E = -0.7 V *vs* Fc/Fc^+, to partially recover the initial **Mn$^{II}_2$SH** complex, thus completing one stepwise cycle. The incomplete recovery of **Mn$^{II}_2$SH** (only ~35%, as estimated by the initial and final CVs) can be mainly ascribed to the poor stability of **Mn$^{III}_2$** at 293 K (this species evolves to a Mn$^{II}_2$-disulfide complex, Chapter III) (Figure 18b).

Coherently, when **Mn$^{II}_2$SH** reacts with O_2 in the presence of $LutHBF_4$ (up to 50 eq.), the direct formation of **Mn$^{III}_2$** is observed (Figure 19b). Under such conditions, the concomitant production of H_2O_2, up to ~40% *vs* **Mn$^{II}_2$SH**, is attested by titration with the H_2O_2-specific Ti-TPyP reagent[70,71] (see experimental section).

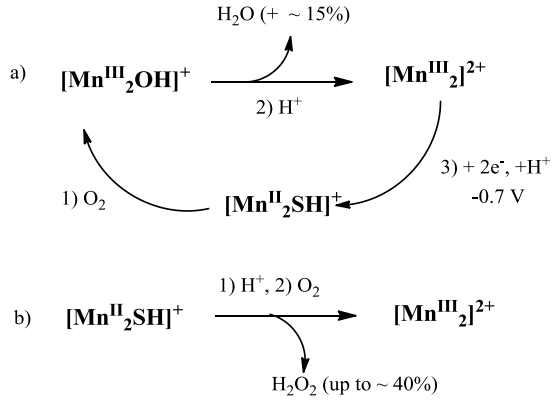

Figure 19. Reactivity of **Mn$^{II}_2$SH** in the presence of dioxygen a) before and b) after the addition of $LutHBF_4$.

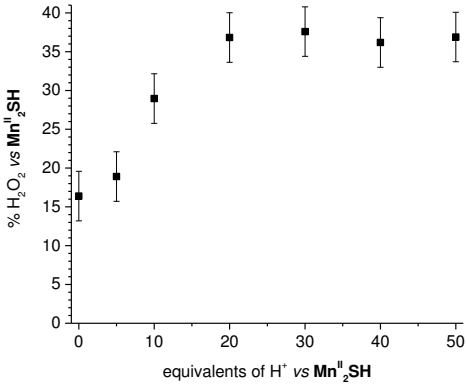

Figure 20. Plot of the amount (%) of H_2O_2 detected by the Ti-TPyP method in a 0.8 mM solution of **Mn^{II}_2SH** in CH_3CN after exposition to air in presence of different aliquots of $LutHBF_4$ (H^+).

The amount of H_2O_2 generated depends on the relative concentration of acid *versus* **Mn^{II}_2SH** (Figure 20): the higher isthe $LutHBF_4$: **Mn^{II}_2SH** ratio, the larger the amount of H_2O_2 with a plateau for 20:1 ratio corresponding to 40% of generated H_2O_2 (see below for the explanation). Production of 15% of H_2O_2 is detected in the absence of acid: this has been attributed to the fact that the Mn-bound pendant thiol can act as a proton source for a neighboring complex molecule.

2.5.2. Reactivity of **Mn^{II}_2SH** with dioxygen in catalytic conditions.

As a further step, we have investigated the catalytic activity of the **Mn^{III}_2/Mn^{II}_2SH** system for O_2 reduction using a sacrificial electron donor and protons.[16,19,72,73] As one-electron reducing agents, we have selected octamethylferrocene (Me_8Fc) and decamethylferrocene ($Me_{10}Fc$), for their standard potential ($E_{1/2}$ Me_8Fc^+/Me_8Fc = -0.40 V, $E_{1/2}$ $Me_{10}Fc^+/Me_{10}Fc$ = -0.49 V) that should be suitable to reduce **Mn^{III}_2** (E_{pc} = -0.47 V). The addition of a catalytic amount of **Mn^{II}_2SH** (100 µM) to an air-saturated CH_3CN solution of Me_nFc (n = 8 or 10, 2 mM, 20 equiv.) and $LutHBF_4$ (15 mM, 150 equiv.) at 293 K results in the quantitative and efficient oxidation of the ferrocene derivatives by O_2 to afford octamethylferricenium (Me_8Fc^+) and decamethylferricenium ($Me_{10}Fc^+$), respectively. Figure 21 shows the absorption spectral changes during the catalytic reaction and the corresponding time profiles for the generation of Me_8Fc^+ and $Me_{10}Fc^+$ (at 750 and 778 nm, respectively). In the absence of the catalyst, oxidation of the ferrocene derivatives occurs only to an insignificant extent.

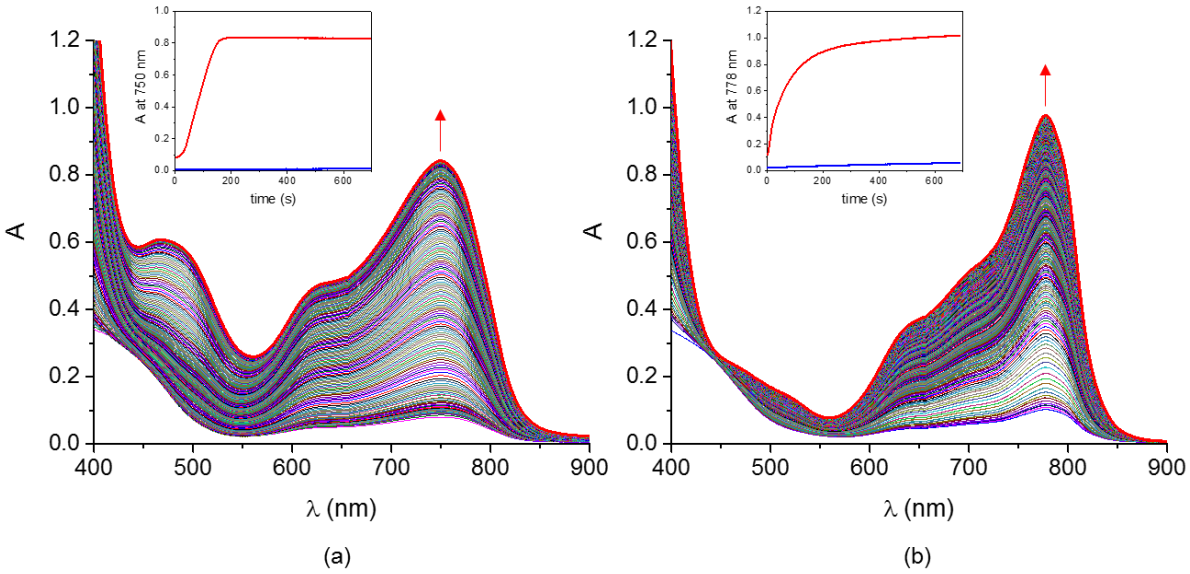

Figure 21. UV–vis spectral changes observed during the 2-electron O_2 reduction catalyzed by **Mn^{II}_2SH** with Me_nFc ((a) n=8, (b) n=10) in the presence of $LutHBF_4$ in CH_3CN at 293 K (air-saturated solution, 2.0 mM Me_nFc, 15 mM $LutHBF_4$, 100 µM **Mn^{II}_2SH**, 1 cm path length). The insets show the time profiles for Me_nFc^+ (n=8 or 10) formation (—, absorbance at 750 and 778 nm, respectively); the profiles of the corresponding blank samples (no catalyst) are also shown (—).

Under such conditions, the rate of electron transfer to **Mn^{III}_2** follows pseudo-zero-order kinetics in the case of Me_8Fc, whereas it becomes pseudo-first-order kinetics with $Me_{10}Fc$. This could be rationalized by a difference of steric hindrance between both reducing agents. $Me_{10}Fc$, which is the most hindered complex, limits its interaction with **Mn^{III}_2** explaining this difference of reactivity.

2.5.3. Characterization of the products of catalysis.

The nature of the oxygen-reduction product and the selectivity of the catalytic process have been investigated. After the completion of catalysis (see above), 0.6 mM (~ 80%) concentration of H_2O_2 was detected in the sample solution when the substrate was Me_8Fc (titration with the Ti-TPyP reagent).[70,71] In contrast, no H_2O_2 formation was observed in the case of $Me_{10}Fc$. It has, however, been shown that H_2O_2 can spontaneously decompose, partially or completely, in the presence of ferrocene derivatives.[19] We have estimated that under the present conditions about 30% of H_2O_2 formed during the catalytic oxidation of Me_8Fc is decomposed. By taking into account this correction, a ~43% yield of H_2O_2 *vs* Me_8Fc is produced by O_2 reduction at 293 K. In the case of $Me_{10}Fc$, low-temperature experiments have been carried out, in propionitrile and acetone at 223 K in order to prevent the direct oxidation of $Me_{10}Fc$ by H_2O_2 (Figure 22).

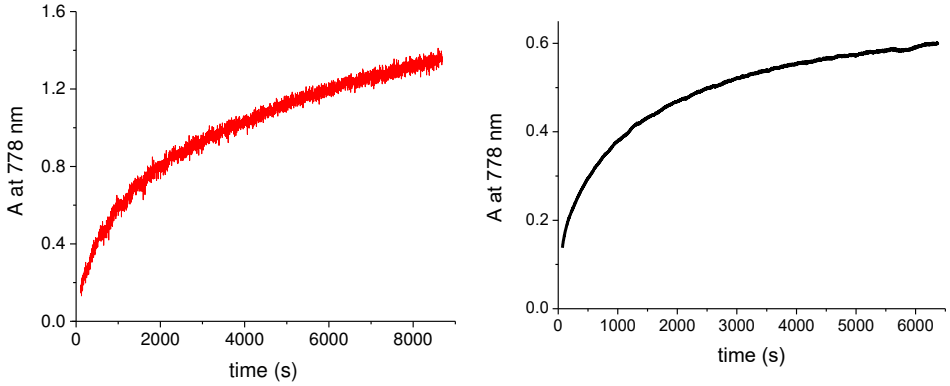

Figure 22. Time profile (absorbance at 778 nm) for catalytic oxidation of $Me_{10}Fc$ to $Me_{10}Fc^+$ by O_2 in the presence of **Mn^{II}_2SH** in propionitrile solution (red line) and in acetone solution (black line) at 223 K (air-saturated solution, 2.0 mM $Me_{10}Fc$, 15.0 mM $LutHBF_4$, 100 µM **Mn^{II}_2SH**, 1cm/0.5 cm path length, respectively).

Under these conditions, a ~40% of H_2O_2 *vs* $Me_{10}Fc$ is produced in both solvents. Taking into account the stoichiometry of the 2-electron reduction of O_2 by ferrocene derivatives (Equation 5), the amount of H_2O_2 detected corresponds to ~80-84% selectivity (we note that 50% H_2O_2 *vs* Me_nFc is expected for a completely selective process).

$$O_2 + 2\ Me_nFc + 2H^+ \rightarrow 2\ Me_nFc^+ + H_2O_2 \text{ (Equation 5)}$$

In summary, in the presence of **Mn^{II}_2SH** as catalyst, both Me_8Fc and $Me_{10}Fc$ are quantitatively oxidized by O_2 to give the corresponding Me_nFc^+ cations, with O_2 selectively reduced to hydrogen peroxide corresponding to a 2-electron-reduction.

2.6. Reactivity of **Mn^{II}_2S** with dioxygen.

2.6.1. Synthesis of **Mn^{II}_2S**.

The **Mn^{II}_2SH** complex can be deprotonated by using NaH as a base to afford **Mn^{II}_2S**. This compound has not been characterized in its powdered form but it has been characterized by electrochemistry. Interestingly, the deprotonation induces a remarkable decrease of the oxidation potential of the Mn^{II} dinuclear complex (of ~300 mV, Figure 23), resulting from the lower donor ability of a thiol functionality with respect to a thiolate.

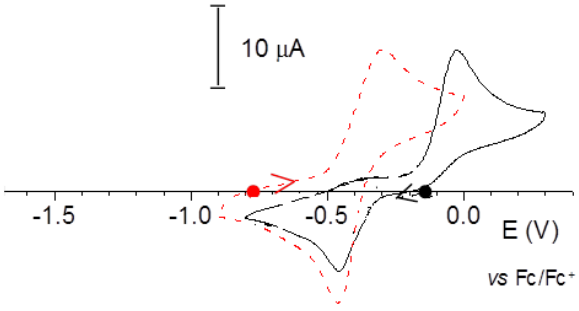

Figure 23. CVs of **Mn^{II}_2SH** (0.7 mM) in CH_3CN, 0.1 M Bu_4NPF_6, before (—) and after addition of 30 eq of 2,6-lutidine, (---) leading to **Mn^{II}_2**.

2.6.2. Synthesis and structural properties of $\mathbf{Mn^{IV}_2(O)_2}$ and $\mathbf{Mn^{IV}_2(O)(OH)}$.

After the deprotonation of $\mathbf{Mn^{II}_2SH}$ into $\mathbf{Mn^{II}_2S}$, the resulting brown suspension has been exposed to dioxygen leading to a dark brown precipitate corresponding to the bis-μ-oxo dinuclear Mn^{IV} complex $[Mn^{IV}_2(LS)(O)_2]$ ($\mathbf{Mn^{IV}_2(O)_2}$) (Figure 24) as shown by single crystal X-Ray diffraction (*vide infra*).

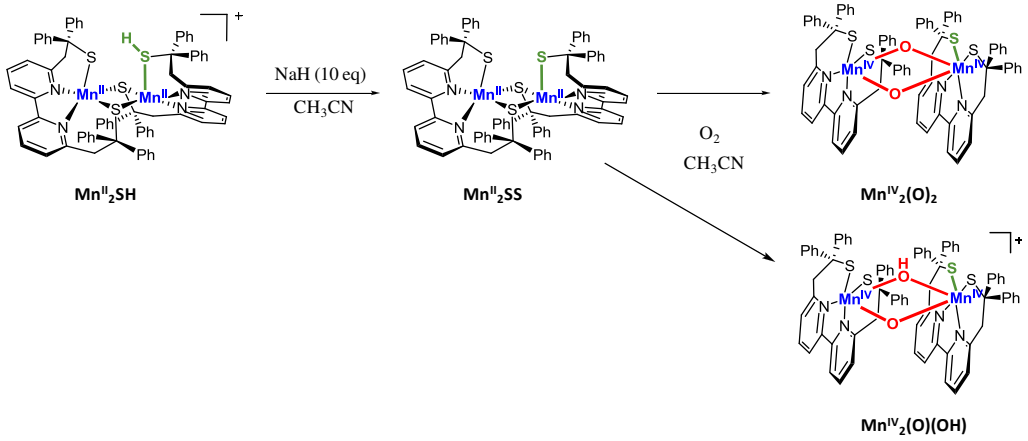

Figure 24. Synthesis of $\mathbf{Mn^{II}_2(O)2}$ and $\mathbf{Mn^{IV}_2(O)(OH)}$ from LS ligand.

Single crystals of the $\mathbf{Mn^{IV}_2(O)_2}$ suitable for X-Ray diffraction were obtained by recrystallization of the corresponding powder in CH_2Cl_2 by slow diffusion of MeOH at -40°C under argon. The X-ray structure of $\mathbf{Mn^{IV}_2(O)_2}$ is shown in Figure 25 and the selected bond lengths and angle are reported in Table 2. The $\mathbf{Mn^{IV}_2(O)_2}$ complex consists of a di-μ-oxo dinuclear Mn^{IV} complex. Its structure contains a perfect planar $\{Mn_2O_2\}$ core and the molecule is perfectly symmetric according to the C_2 axes. The two Mn sites are equivalent and each Mn is hexacoordinated surrounded by an N2S2O2 donor set in an octahedral geometry. The Mn···Mn distance of 2.7820(3) Å is too long for a direct metal-metal interaction but it appears to be shorter than the Mn-Mn distance in $\mathbf{Mn^{II}_2SH}$ (3.1738(6) Å) and $\mathbf{Mn^{III}_2OH}$ (3.902 Å). The Mn-N distances are comprised in the range 2.069-2.187 Å, consistent with the Mn^{IV}-N distances previously observed with Salen-derivatives[88] and closed to the distance for $\mathbf{Mn^{III}_2OH}$ (2.061-2.082). Concerning the Mn-S bonds, they are longer (in the range 2.3014-2.3554 Å) than those found in the structurally related $\mathbf{Mn^{III}_2OH}$ complex (in the range 2.2754-2.288). This is unexpected because of the +IV oxidation state of Mn. This can be explained by the *trans* effect of the oxo-bridges. O2Mn1O1 angle of 80.83(5)° and Mn1O2Mn1 angle of 100.50(7)° are consistent with the other Mn^{IV} di-oxo complexes (95.2° and 102.3°).[88]

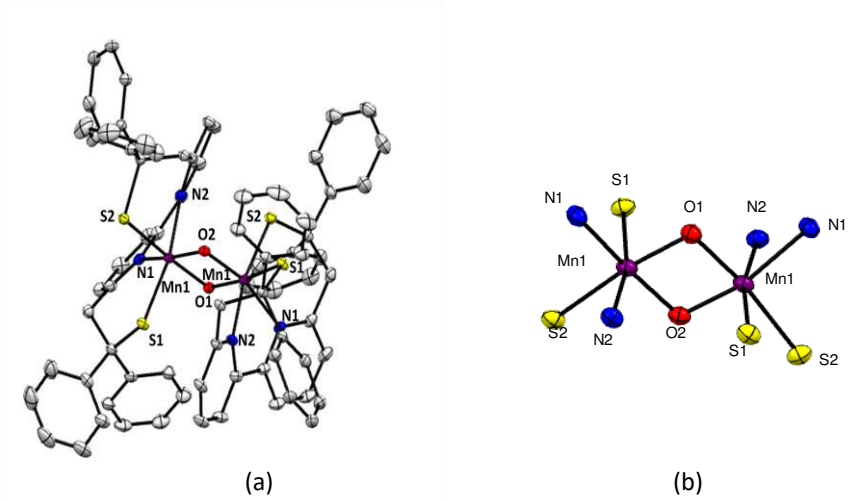

(a) (b)

Figure 25. (a) Molecular structure of $\mathbf{Mn^{IV}_2(O)_2}\cdot 0.64CH_2Cl_2.2.7H_2O$ and (b) the Mn2 unit with its first coordination sphere. The thermal ellipsoids are drawn at 30% probability level. All hydrogen atoms, anions and solvent molecules are omitted for clarity for (a).

Table 2. Selected bond lengths (Å) and angles (°) for $\mathbf{Mn^{IV}_2(O)_2}\cdot 0.64CH_2Cl_2\cdot 2.71H_2O$.

Mn(1)-N(1)	2.172(2)	Mn(1)- N(1)- Mn(1)	129.78(4)	O(2)-Mn(1)- N(2)	92.99(4)
Mn(1)-N(2)	2.255(2)	Mn(1)- N(2)- Mn(1)	95.60(5)	O(2)-Mn(1)-S2	91.24(5)
Mn(1)-S(1)	2.3014(6)	Mn(1)-O(1)-Mn(1)	41.08(4)	O(2)-Mn(1)-S(1)	97.40(3)
Mn(1)-S(2)	2.3584(6)	Mn(1)-O(2)-Mn(1)	39.75(4)	O(2)-Mn(1)-O()1	80.83(5)
Mn(1)-O(1)	1.8453(11)	Mn(1)- S(1)-Mn(1)	96.69(3)	N(2)-Mn(1)-S(2)	85.54(4)
Mn(1)-O(2)	1.8092(10)	Mn(1)- S(2)-Mn(1)	130.986(16)	N(2)-Mn(1)-S(52)	76.44(5)
		O(1)-Mn(1)- S2	172.03(3)	N(2)-Mn(1)-S(52)	76.44(5)
Mn(1)-Mn(1)	2.7820(13)	O(1)-Mn(1)-S(1)	92.72(3)	N(1)-Mn(1)-S(1)	94.46(4)
		O(1)-Mn(1)-N(1)	89.70(5)	N(1)-Mn(1)-S(2)	146.95(7)
		O(1)-Mn(1)-N(2)	95.57(4)	N(1)-Mn(1)-S(52)	98.23(4)
		S(1)-Mn(1)-S(2)	87.52(3)	N(2)-Mn(1)-S(1)	167.62(3)
		O(2)-Mn(1)-N(1)	165.12(5)	N(2)-Mn(1)-S(2)	85.54(4)

Depending on the experimental synthetic procedure, another complex has been isolated and characterized. The main difference between the two complexes concerns the crystallization procedure. Crystals of the second complex were obtained by diffusion of di-isopropyl ether into a dark brown solution of *in situ* prepared $\mathbf{Mn^{II}_2S}$ in the presence of O_2 at -40°. In this case, no precipitation was observed during O_2 bubbling. The new complex corresponds to the protonated form of $\mathbf{Mn^{IV}_2(O)_2}$, $[Mn^{IV}_2(LS)(O)(OH)]$, $\mathbf{Mn^{IV}_2(O)(OH)}$. $\mathbf{Mn^{IV}_2(O)(OH)}$ represents the first μ-oxo-μ-hydroxo dinuclear Mn^{IV} complex characterized by X-ray diffraction spectroscopy. This complex can also be obtained from $\mathbf{Mn^{IV}_2(O)_2}$ in the presence of one equiv. of $HClO_4$ in MeCN by slow diffusion of di-isopropylether at -40°C In the literature, Pecoraro reported a series of Mn^{IV} di-μ-oxo, μ-oxo-μ-hydroxo, di-μ-hydroxo dinuclear Mn^{IV} complexes, $[Mn^{IV}_2(salpn)_2(\mu\text{-}O)_2]$, $[Mn^{IV}_2(salpn)_2(\mu\text{-}O)(\mu\text{-}OH)]^+$

and $[Mn^{IV}_2(salpn)_2(\mu\text{-}OH)_2]^{2+}$, which were not characterized by X-ray crystallography but by EXAFS spectroscopy except for the $[Mn^{IV}_2(salpn)_2(\mu\text{-}O)_2]$ complex.[88]

The crystallographic structure of **$(Mn^{IV}_2(O)(OH)$** is shown in Figure 26 and selected bond lengths and angles are reported in Table 3.

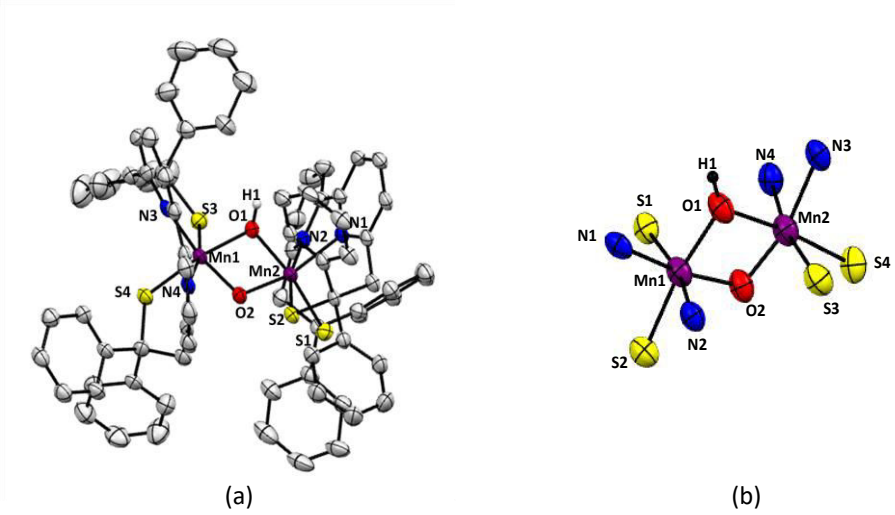

Figure 26. (a) Molecular structure of **$Mn^{IV}_2(O)(OH)$**· ClO_4.5.68CH_3CN.1.5H_2O and (b) the $\{Mn_2O(OH)\}$ core. The thermal ellipsoids are drawn at 30% probability level for (a). All hydrogen atoms, anions and solvent molecules are omitted for clarity.

The geometry of the **$Mn^{IV}_2(O)(OH)$** is different from **$Mn^{IV}_2(O)_2$** because of the hydroxo bridge. The **$Mn^{IV}_2(O)(OH)$** complex consists of μ-oxo-μ-hydroxo dinuclear Mn^{IV} complex. Its structure contains a quasi-planar $\{Mn_2O_2\}$ core (deviation from O2Mn1H1Mn1 plane of 0.35°, angle between Mn1O1Mn2 and Mn1O2Mn2 planes of 1.95°). The two Mn sites are not equivalent and each Mn is hexacoordinated, surrounded by N2S2(O)(OH) donor set in an octahedral geometry. The Mn…Mn distance of 2.9220(13) Å is too long for a direct metal-metal interaction and longer than in **$Mn^{IV}_2(O)_2$** due to the presence of the hydroxo bridge responsible of the elongation. In the same vein, Mn1O1Mn2 (107.22(12)°) and Mn1O2Mn2 (96.15(12)°) angles are increased with respect to **$Mn^{IV}_2(O)(OH)$** and as also observed in Pecoraro's compound.[88] Concerning the Mn-O(H) distances, they are about 10 pm longer (1.956(2)-1.969(3)Å) than the Mn-O distances (1.811(3)-1.819(4)Å) in **$Mn^{IV}_2(O)_2$.** It can be noticed that the Mn-O an Mn-O(H) bonds in **$Mn^{IV}_2(O)_2$** and **$Mn^{IV}_2(O)(OH)$** display similar lengths than those calculated by DFT for the Pecoraro's complexes (Figure 27).[88]

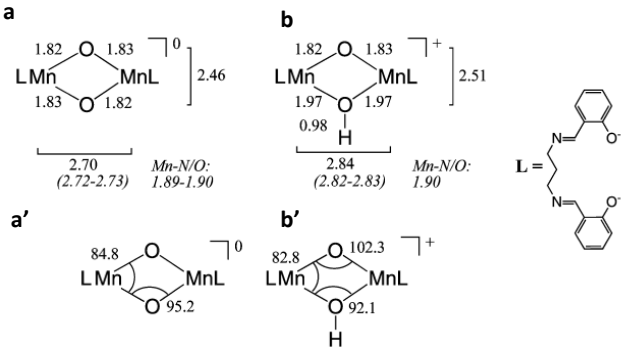

Figure 27. (a, b) DFT-optimized distances in Å and (a', b') selected angles (°) on Mn^{IV} dimer core. Distances from EXAFS are given in italic and L represents the salpn ligand.[88]

The Mn-N distances are in the same range of values for both Mn^{IV} complexes, (~2.1 Å). Regarding the Mn-S distances, those in **$Mn^{IV}_2(O)_2$** are shorter than in **$Mn^{IV}_2(O)(OH)$** (in the 2.2656(15)-2.2918(4) Å range). To compensate the longer Mn-O(H) bonds with respect to the Mn-O ones, a compression along the Mn-S bonds occurs.

Table 3. Selected bond lengths (Å) and angles (°) for **$Mn^{IV}_2(O)(OH)$**·ClO_4.5.68CH_3CN.1.5H_2O.

Mn(2)-S(4)	2.2782(13)	Mn(2)- S(4)- Mn(1)	129.87(5)	O(2)-Mn(2)-S(3)	93.24(10)
Mn(2)-S(3)	2.2656(15)	Mn(2)- S(3)- Mn(1)	95.23(4)	O(2)-Mn(2)-N(3)	165.12(12)
Mn(2)-O(1)	1.958(2)	Mn(2)-O(1)-Mn(1)	42.07(8)	O(2)-Mn(2)-N(4)	96.32(14)
Mn(2)-O(2)	1.819(3)	Mn(2)-O(2)-Mn(1)	36.30(7)	O(2)-Mn(1)- S(1)	93.45(10)
Mn(2)-N(3)	2.065(3)	Mn(2)- N(3)-Mn(1)	130.20(8)	O(2)-Mn(1)-S(2)	91.78(9)
Mn(2)-N(4)	2.052(4)	Mn(2)- N(4)-Mn(1)	96.22(9)	O(2)-Mn(1)-N(1)	165.57(13)
Mn(1)-S(1)	2.2918(14)	Mn(2)- N(1)- Mn(1)	130.26(9)	O(2)-Mn(1)-N(2)	97.07(13)
Mn(1)-S(2)	2.2832(13)	Mn(1)-O(1)-Mn(2)	41.79(7)	O(2)-Mn(2)-O(1)	78.35(11)
Mn(1)-N(1)	2.103(3)	Mn(1)-O(2)-Mn(2)	36.49(9)	O(2)-Mn(1)-O()1	78.26(11)
Mn(1)-O(1)	1.969(3)	Mn(1)- S(1)-Mn(2)	96.21(4)	S(3)-Mn(2)- S(4)	86.48(5)
Mn(1)-O(2)	1.811(2)	Mn(1)- S(2)-Mn(2)	128.23(4)	S(2)-Mn(1)-S(1)	86.23(5)
Mn(1)-N(2)	2.065(4)	Mn(1)- N(2)-Mn(2)	96.03(9)	N(3)-Mn(2)- S(4)	99.33(9)
		O(1)-Mn(2)- S(4)	171.58(9)	N(3)-Mn(2)-S(3)	94.89(11)
Mn(1)-Mn(2)	2.9220(13)	O(1)-Mn(2)-S(3)	96.30(10)	N(4)-Mn(2)-S(4)	86.61(9)
		O(1)-Mn(2)-N(3)	88.38(11)	N(4)-Mn(2)-S(3)	168.53(10)
		O(1)-Mn(2)-S(4)	91.83(12)	N(4)-Mn(1)- N(3)	77.23(14)
		O(1)-Mn(1)- S(1)	95.06(10)	N(1)-Mn(1)-S(1)	94.32(10)
		O(1)-Mn(1)-S(2)	170.01(8)	N(1)-Mn(1)-S(2)	100.85(9)
		O(1)-Mn(1)-N(1)	88.94(11)	N(2)-Mn(1)-S(1)	167.71(9)
		O(1)-Mn(1)-N(2)	93.30(13)	N(2)-Mn(1)-S(2)	87.09(10)
		O(2)-Mn(2)- S(4)	93.59(9)	N(2)-Mn(1)-N(1)	76.83(13)

Infrared spectroscopy has been a useful technique to distinguish the two complexes. As shown on Figure 28, the large triplet feature assigned for ν_{ClO_4} at 1090 cm^{-1} is only present in the cationic **$Mn^{IV}_2(O)(OH)$, $Mn^{IV}_2(O)_2$** being neutral. IR spectroscopy will thus be the appropriate tool to probe the protonation state of these dinuclear Mn^{IV} complexes.

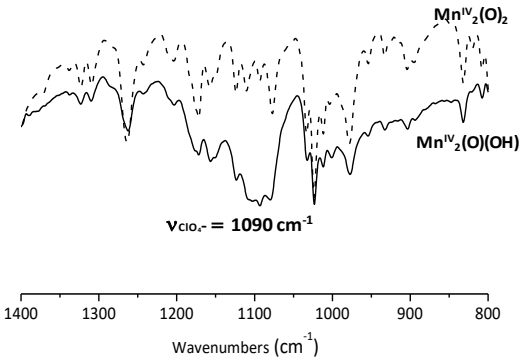

Figure 28. Infra-red spectra of **$Mn^{IV}_2(O)_2$** (---) and **$Mn^{IV}_2(O)(OH)$** (—).

2.7. Solution properties of $Mn^{IV}_2(O)_2$.

2.7.1. ESI-mass spectrometry.

In the attempt to identify the source of oxygen for the two oxo-bridges, $^{18}O_2$ was used to generate **$Mn^{IV}_2(O)_2$** in situ. Labeled **$Mn^{IV}_2(^{18}O)_2$** compound was quantitatively observed by ESI-mass spectrometry with a characteristic 4-unit shift in CH_2Cl_2 as seen in Figure 29. This experiment demonstrates that the two oxo-bridges come from molecular oxygen. The simulated spectra are well consistent with the experimental ones either with $^{16}O_2$ or $^{18}O_2$.

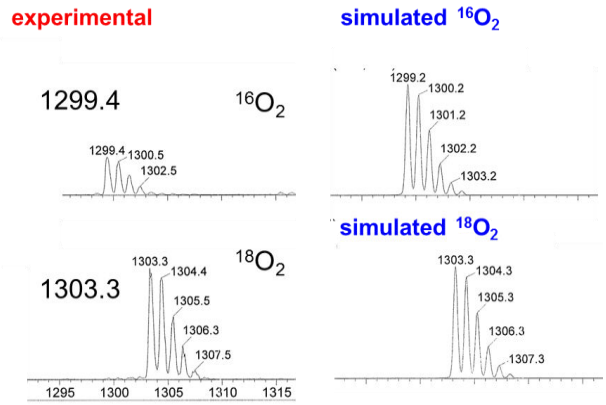

Figure 29. Experimental and simulated ESI-mass spectra of **$Mn^{IV}_2(O)_2$** with $^{16}O_2$ and $^{18}O_2$.

However, with ESI-mass it is difficult to attest the presence of the hydroxo-bridge. In order to identify the protonation state of these complexes in solution, UV-Vis absorption studies have been performed (Figure 30).

2.7.2. Acid/base properties.

The electronic absorption spectrum of **$Mn^{IV}_2(O)_2$** in CH_2Cl_2 displays a band at 574 nm (Figure 30). At room temperature, the solution is completely decomposed in less than 15 minutes whereas at 0°C, the solution remains stable for few hours. Acid/base properties have been thus investigated at 0°C. In the presence of one equivalent of 2,6-lutidinium tetrafloroborate ($LutHBF_4$) in CH_2Cl_2, two new

bands appear at 526 nm and 680 nm with the concomitant disappearance of that at 574 nm. These bands are proposed to be assigned to the **Mn^{IV}_2(O)(OH)** species. When 1 equiv. of strong bases (tBuOK and 18-crown-6/, n-Buli, LDA) are used, no deprotonation occurs, suggesting a very large pKa for **Mn^{IV}_2(O)(OH)**.

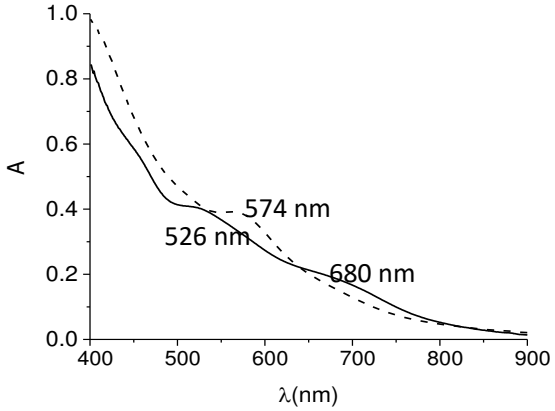

Figure 30. UV-Vis spectra of **$Mn^{IV}_2(O)_2$** at 0.1 mM (---) and after the addition of 1 equiv. of $LutHBF_4$ (—) at 0°C in CH_2Cl_2 (path length: 1 cm).

2.7.3. Mn K-Edge XAS absorption of **$Mn^{IV}_2(O)_2$**.

Mn K-Edge XAS experiments have been performed on a solution sample made in situ from **Mn^{II}_2S** and O_2 to assign the oxidation state of the Mn ion of **$Mn^{IV}_2(O)_2$**. Such investigation was important to confirm the +IV oxidation state. As explained previously for the K-Edge region, the upper energy, the higher oxidation state. Regarding the energy of **Mn^{II}_2SH**, **Mn^{III}_2OH** and **$Mn^{IV}_2(O)_2$**, a shift at higher energy is observed at 6654 eV for **$Mn^{IV}_2(O)_2$** compared to **Mn^{II}_2SH**, **Mn^{III}_2OH** (6648, 6551eV, respectively). Consequently, these Mn K-edge measurements are consistent with an increase of the oxidation states confirming the +IV oxidation state of **$Mn^{IV}_2(O)_2$** (Figure 31).

It would have been interesting to compare the two Mn^{IV} complexes (**$Mn^{IV}_2(O)_2$** and **Mn^{IV}_2(O)(OH)**) by XAS measurements. Indeed, the investigation of the Pecoraro's series has revealed that μ-oxo/μ-hydroxo bridges can be identified thanks to Mn K-Edge XAS measurements by analyzing the pre-edge region, while[88] the edge is not sensitive to such structural modification (Figure 30). Such measurements are planned in the following months.

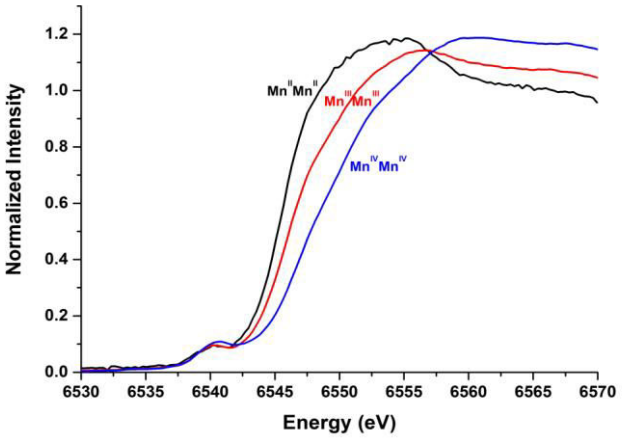

Figure 31. Mn K-edge XAS spectra recorded on solution samples of **Mn^{II}_2SH**, **Mn^{III}_2OH** and **$Mn^{IV}_2(O)_2$**.

2.9. Mechanistic investigation of O_2 activation by **Mn^{II}_2S**.

Under stoichiometric conditions, the reaction between **Mn^{II}_2SH** and O_2 generates the μ-oxo dinuclear Mn^{III} complex, **Mn^{III}OH** while in the presence of **Mn^{II}_2S**, **$Mn^{IV}_2(O)_2$** is obtained after exposure to oxygen at room temperature in MeCN (Figure 32).

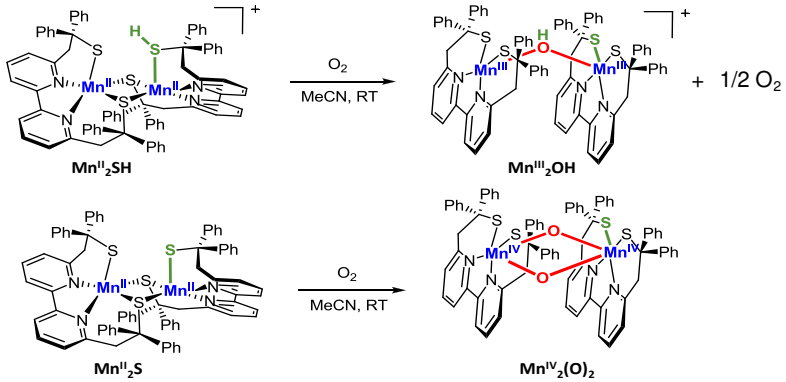

Figure 32. Synthesis of **Mn^{III}_2OH** from **Mn^{II}_2SH** (top) and **$Mn^{IV}_2(O)_2$** from **Mn^{II}_2S** in presence of O_2 at room temperature (RT).

On the other hand, **Mn^{III}_2OH** is obtained as the main product when **Mn^{II}_2S** is exposed to O_2 at -45°C instead at room temperature and when air is bubbled instead of O_2. Another experiment shows that in dilute conditions **Mn^{II}_2SH** can, lead to **$Mn^{IV}_2(O)_2$** after exposition to O_2.

Interestingly, we were able to demonstrate that when **$Mn^{IV}_2(O)_2$** reacts with **Mn^{II}_2SH** (or **Mn^{II}_2S**) at room temperature, **Mn_2^{III}OH** is formed quantitatively according to a comproportionation reaction (Figure 33).[92]

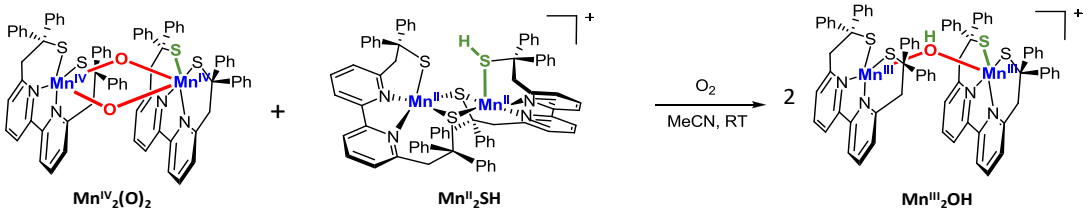

Figure 33. Comproportionation reaction between $\mathbf{Mn^{IV}_2(O)_2}$ and $\mathbf{Mn^{II}_2SH}$ giving $\mathbf{Mn^{III}OH}$ at room temperature.

2.10. Proposed mechanism for O_2 activation and reduction.

2.10.1. $\mathbf{Mn^{II}_2SH}$: An unusual metal-thiol system.

In coordination chemistry, although metal-bound thiolates (M-S) are very common; examples of metal bound thiols (M-SH) are relatively rare. Among the structurally characterized M-SH complexes, most examples are based on iron[32,33] or ruthenium.[34,35] The formation of transient metal-thiol bonds in the active sites of metalloenzymes, including [NiFe][36] and [FeFe][37] hydrogenases, nitrogenase,[38] and their biomimetic models, is often proposed (and in some cases established) to be an influential factor in their reactivity. In these systems, metal-bound thiols can act as proton relay during the catalytic process, but are also capable of tuning the redox potential of the active metal centers. Concerning the O_2 activation domain, one Mn^{I} complex containing a pendant thiol is reported to react with O_2 leading to the formation of a mononuclear O_2-side-on-bound Mn^{IV} complex.[39] However, in this case the pendant proton doesn't seem to take part to the reactivity of the system.

In $\mathbf{Mn^{II}_2SH}$, the presence of one coordinated thiol has been unambiguously demonstrated both in solid state (as evidenced by the Mn2-S51 distance in the X-ray structure and, indirectly, by magnetic and XAS measurements) and in solution (as shown by CV), with the hexaaqua Mn(II) as the most probable proton source. The uncommon stability of the terminal metal-bound thiol in solution could be attributed to an intramolecular SH···S-bond interaction between S1 and S51 (Figure 7).

2.10.2. Proposed O_2 reduction pathways with $\mathbf{Mn^{II}_2SH}$ under stoichiometric and catalytic conditions.

As explained previously, the obtained products from the reaction between $\mathbf{Mn^{II}_2SH}$ and O_2 are synthesized in different yields according to stoichiometric (H_2O is the main product) or catalytic conditions (H_2O_2 is the main product). Two proposed O_2 reductions pathways with $\mathbf{Mn^{II}_2SH}$ will be discussed.

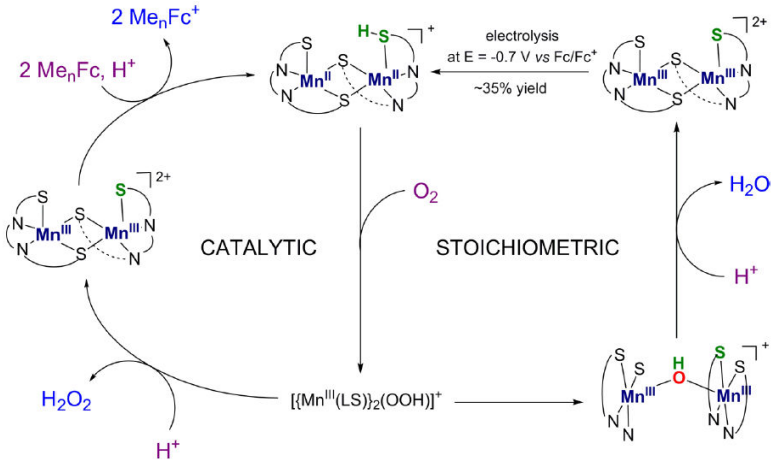

Figure 34. Proposed mechanism for O_2 activation and reduction by **Mn^{II}_2SH** in catalytic and stoichiometric conditions.

A) Under stoichiometric conditions.

Under stoichiometric conditions and in the absence of an external proton source (Figure 34, right), the reaction between **Mn^{II}_2SH** and dioxygen generates the μ-hydroxo complex **Mn^{III}_2OH**. In this case, the O-O bond reductive cleavage and full 4-electron reduction of O_2 are achieved. Dioxygen activation is probably promoted by the fact that a coordination vacancy can be created on each Mn center of **Mn^{II}_2SH** by breaking the two μ-S bridges. It can then be proposed that the formation of **Mn^{III}_2OH** follows an oxygenation process parallel to those described for Fe^{II} porphyrins.[74] In those systems, a Fe^{III}_2-peroxo intermediate evolves into a μ-oxo Fe^{III} dimer as a consequence of O-O bond cleavage *via* a bimolecular process. In this respect, Kovacs has recently isolated and crystallized the first example of peroxo-bridged Mn^{III} dinuclear complex.[38] (Figure 4b)

Efforts to detect and characterize a similar intermediate are ongoing and computations are being pursued in order to assess its energetic accessibility. Nevertheless, a mechanism is proposed as explained in Figure 35. **Mn^{II}_2SH** reacts with O_2 to give $[Mn^{III}_2(LS)_2OO(H)]CLO_4$, **$Mn^{III}$-OO(H)-$Mn^{III}$** as an intermediate species. The peroxo species is thus stabilized by a H-bonding coming from the pendant thiol.

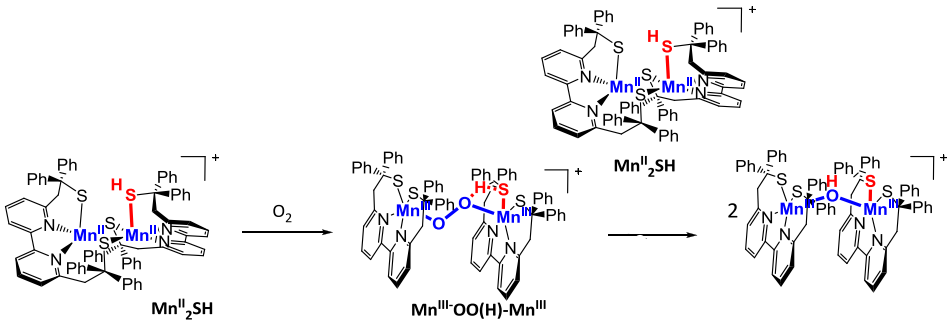

Figure 35. Proposed mechanism promoting the formation of **Mn^{III}_2OH**.

When protons ($LutHBF_4$) are added on a freshly prepared **Mn^{III}_2OH** solution, its μ-hydroxo bridge is immediately protonated to afford **Mn^{III}_2** and H_2O (Equation 6). In the case of the dinuclear μ-oxo thiolate Mn^{III} complexes described by Kovacs et al., concomitant addition of ROH is required to release water (Equation 7).[75] In our system, the release of water is driven by the tendency of the complex to form μ-S bridges.

$Mn^{III}_2OH + H^+ \rightarrow Mn^{III}_2 + H_2O$ (Equation 6)

$Mn^{III}_2O + ROH \rightarrow Mn^{III}OR + H_2O$ (Equation 7)[75]

When a proton source ($LutHBF_4$) is already present in the initial solution of **Mn^{II}_2SH**, an alternative reaction pathway can be followed (Figure 36).

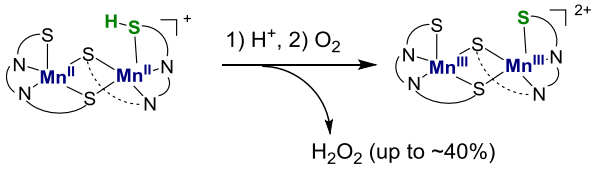

Figure 36. Reactivity of Mn^{II}_2SH in the presence of 1) H+ and 2) O_2 to give Mn^{III}_2.

Under these conditions the postulated Mn^{III}_2-(hydro)peroxo intermediate $[\{Mn^{III}(LS)\}_2(OOH)]^+$ (Figure 34) reacts with protons promoting the cleavage of the Mn-O bond and the subsequent formation of hydrogen peroxide (up to 40% *vs* **Mn^{II}_2SH** (step 2 in Figure 34). This 2-electron O_2 reduction pathway coexists with the reductive cleavage of the O-O bond leading to the same final **Mn^{III}_2** product. Two key factors regulate the competition between O-O and M-O rupture in metal-peroxo complexes: (i) the intrinsic strength of the O-O and M-O bonds and (ii) the presence of a proton source. Regarding the first aspect, the O-O bond lengths of previously reported thiolate Mn^{III}-peroxo and Mn^{III}-alkylperoxo complexes (1.431(5)-1.468(7) Å)[38,42,43] fall in the high limit of those observed for metal-peroxo complexes. These long bond distances are consistent with highly activated O-O bonds that are easy to cleave. On the other hand, regulation of proton delivery to a metal-peroxo species is also crucial in the competition between M-O *vs* O-O ruptures. As shown in the case of classical copper systems,[76,77] and also for a side-on peroxo-Mn^{III} mononuclear complex,[78] more acidic media favor M-O rupture, while in less acidic media, the O-O bond is cleaved. Our experimental data are in full agreement with previous findings: while the presence of thiolate ligands favors the O-O breaking, the addition of protons ($LutHBF_4$) promotes the M-O rupture.

A high valent **$Mn^{IV}_2(O)_2$** complex can also be generated from O_2 activation and the formation of **$Mn^{IV}_2(O)_2$** vs **Mn^{III}_2OH** depends on the experimental conditions, i.e. protonation state of the initial Mn^{II} complex, temperature and concentration. Considering all experimental data, an activation pathway is proposed promoting either Mn^{IV} or Mn^{III} dinuclear complexes as shown in Figure 37.

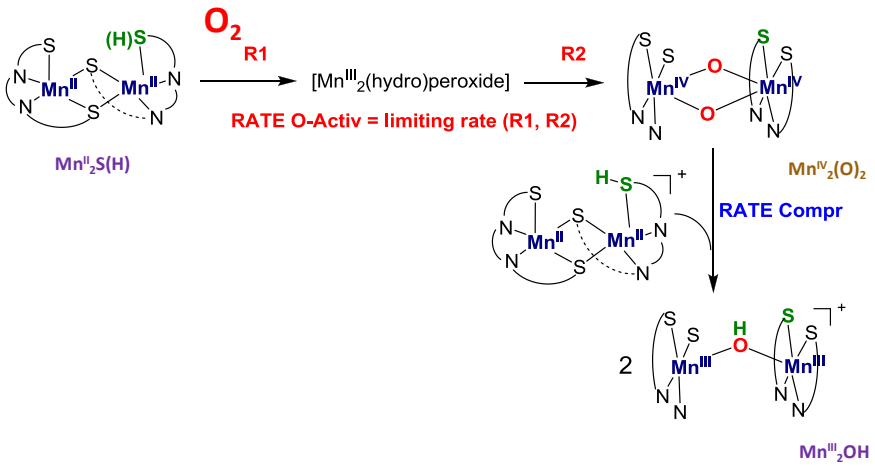

Figure 37. Proposed pathway for O_2 activation by **Mn^{II}_2S** in stoichiometric conditions.

The kinetics of generation of **$Mn^{IV}_2(O)_2$** thus depends on the O_2-activation rate with $R_2 \geq R_1$, the [Mn^{III}_2(hydro)peroxide] being not accumulated in the process. The following proposed reaction is the comproportionation between generated **$Mn^{IV}_2(O)_2$** and **$Mn^{II}_2S(H)$** to give **Mn^{III}_2OH**. When the O_2-activation rate is higher than the comproportionation rate, **$Mn^{IV}_2(O)_2$** is mainly produced. On the other hand, when the comproportionation rate is higher than the O_2-activation rate, **$Mn^{III}OH$** is the main product. When a diluted **Mn^{II}_2SH** solution in CH_3CN is exposed to "pure O_2", the O_2-activation rate is higher than the comproportionation rate, thus promoting the formation of **$Mn^{IV}_2(O)_2$**. This is because the amount of **Mn^{II}_2SH** is not enough compared to O_2 to react with generated **$Mn^{IV}_2(O)_2$**. On the other hand, when the initial complex is exposed to air, the O_2 concentration is too low to favor the formation of the **$Mn_2^{III}OH$**. At low temperature, the O_2-activation process is probably slowed down more than the comproportionation step. Once **$Mn^{IV}_2(O)_2$** is produced, it has enough time to react with **Mn^{II}_2SH** which has not been able to react with O_2.

B) Under catalytic conditions.

The catalytic O_2 reduction process presented in this part, in which Me_nFc are used as monoelectronic sacrificial donors and **Mn^{II}_2SH** as catalyst, represents a rare example of manganese-based molecular catalyst for 2-electron reduction of O_2 in homogeneous solution.[79,80,81]

The proposed mechanism of H_2O_2 formation, depicted in Figure 37, is most likely the same as that of the stoichiometric reaction in acidic medium. When compared to the stoichiometric process, the higher selectively for H_2O_2 is consistent with the presence of a larger excess of acid (200 equiv. *vs* the Mn-catalyst) and higher dilution conditions (100 µM of **Mn^{II}_2SH**) that disfavor the bimolecular process proposed to generate **Mn^{III}_2OH** (Figure 37). Regeneration of the initial complex (step 3 in Figure 34) occurs by electron transfer from Me_nFc (n=8,10) to **Mn^{III}_2**. This process should be

thermodynamically feasible in both cases (ΔG ≈ +0.05 eV and -0.04 eV for Me_8Fc $Me_{10}Fc$, respectively).[16] The process is further driven by protonation of the reduced product to afford **Mn^{II}_2SH**. Even though **Mn^{III}_2** is relatively unstable (as it slowly decays to a Mn^{II}_2-disulfide complex), under catalytic conditions the presence of an excess of Me_nFc (20 equivalents) permits its immediate reduction, thus circumventing its decomposition. It is worth noting that **Mn^{III}_2** is not accumulated during the catalytic process, as the corresponding absorption band at ~475 nm is not observed during the catalysis (Figure 21).

Conclusion

In this chapter, we have described a new thiolate-bridged dimanganese(II) complex, $[Mn^{II}_2(LS)(LSH)]ClO_4$ (**Mn^{II}_2SH**), which represents an unusual system with a metal-bound pendant thiol (M-SH). This complex is capable of binding and activating dioxygen. In particular, under stoichiometric conditions and in the absence of an external proton source, **Mn^{II}_2SH** reacts with dioxygen to generate a μ-hydroxo complex, $[(Mn^{III}_2(LS)_2(OH)]ClO_4$ (**Mn^{III}_2OH**). In this case the reductive cleavage of the O-O bond is achieved, leading to a 4-electron O_2 reduction process. Conversely, in the presence of a proton source and of a one-electron reducing agent, **Mn^{II}_2SH** selectively catalyzes the reduction of dioxygen to hydrogen peroxide. In this case, the rupture of the M-O bond in the putative manganese-peroxo intermediate is favored by the acidic medium, leading to 2-electron O_2 reduction. The **Mn^{II}_2SH** complex represents a rare example of manganese-based molecular catalysts for selective 2-electron O_2 reduction in homogeneous solution.[79-81]

It has been also observed that depending on the experimental conditions (protonation state of the initial Mn^{II} complex, temperature and concentration), a high valent bis-μ-oxo dinuclear Mn^{IV} complex can be generated that has been fully characterized. The investigation of its acid/base properties allowed us to isolate and characterize the μ-oxo-μ-hydroxo dinuclear Mn^{IV} derivate. A proposed mechanism explaining the competition between the formation of the dinuclear Mn^{III} and Mn^{IV} complexes during O_2 activation has been proposed that can rationalize all experimental observations. Currently, theoretical calculations are performed in collaboration with the group of De Visser to validate this mechanism, especially the role of the Mn-bound SH. Besides, we have shown that only the bis-μ-oxo complex displays hydrogen atom transfer reactivity in the presence of phenol substrates. Kinetic studies will be performed in the presence of such substrates in order to get more insights into the mechanism of the HAT reaction.

More recently, the group decided to study the role of the metal on the O_2 activation and reduction processes by replacing the Mn by Fe ions, A dinuclear Fe^{II} complex, isostructural to the dinuclear Mn^{II} complex with the metal-bound SH, has been isolated and its reactivity toward O_2 is currently under investigation.

References

1. (a) Simandi, L. I. *Advances in Catalytic Activation of Dioxygen by Metal Complexes. [In: Catal. Met. Complexes, 2003; 26]*; Kluwer Academic Publishers, 2003. (b) Hohmann-Marriott, M. F. & Blankenship, R. E. Evolution of photosynthesis. *Annu Rev Plant Biol,* **2011**, *62*, 515–548.
2. Arakawa, H.; Aresta, M.; Armor, J. N.; Barteau, M. A.; Beckman, E. J.; Bell, A. T.; Bercaw, J. E.; Creutz, C.; Dinjus, E.; Dixon, D. A.; Domen, K.; DuBois, D. L.; Eckert, J.; Fujita, E.; Gibson, D. H.; Goddard, W. A.; Goodman, D. W.; Keller, J.; Kubas, G. J.; Kung, H. H.; Lyons, J. E.; Manzer, L. E.; Marks, T. J.; Morokuma, K.; Nicholas, K. M.; Periana, R.; Que, L.; Rostrup-Nielson, J.; Sachtler, W. M. H.; Schmidt, L. D.; Sen, A.; Somorjai, G. A.; Stair, P. C.; Stults, B. R.; Tumas, W. *Chem. Rev.* **2001**, *101*, 953.
3. Shilov, A. E.; Shul'pin, G. B. *Chem. Rev.* **1997**, *97*, 2879.
4. Ferguson-Miller, S.; Babcock, G. T. *Chem. Rev.* **1996**, *96*, 2889.
5. Kaila, V. R. I.; Verkhovsky, M. I.; Wikstrom, M. *Chem. Rev.* **2010**, *110*, 7062.
6. Adler, S. B. *Chem. Rev.* **2004**, *104*, 4791.
7. Winter, M.; Brodd, R. J. *Chem. Rev.* **2004**, *104*, 4245.
8. Egami, H.; Oguma, T.; Katsuki, T. *J. Am. Chem. Soc.* **2010**, *132*, 5886
9. Hermans, I.; Spier, E. S.; Neuenschwander, U.; Turra, N.; Baiker, A. *Top. Catal.* **2009**, *52*, 1162.
10. Yamada, Y.; Fukunishi, Y.; Yamazaki, S.-i.; Fukuzumi, S. *Chem. Commun.* **2010**, *46*, 7334.
11. Mase, K.; Ohkubo, K.; Fukuzumi, S. *Inorg. Chem.* **2015**, *54*, 1808.
12. Mousavi Shaegh, S. A.; Nguyen, N.-T.; Mousavi Ehteshami, S. M.; Chan, S. H. *Energy Environ. Sci.* **2012**, *5*, 8225.
13. Yamazaki, S.-i.; Siroma, Z.; Senoh, H.; Ioroi, T.; Fujiwara, N.; Yasuda, K. *J. Power Sources* **2008**, *178*, 20.
14. Tolman, W. B.; Solomon, E. I. *Inorg. Chem.* **2010**, *49*, 3555.
15. Ray, K.; Pfaff, F. F.; Wang, B.; Nam, W. *J. Am. Chem. Soc.* **2014**, *136*, 13942.
16. Fukuzumi, S.; Okamoto, K.; Gros, C. P.; Guilard, R. *J. Am. Chem. Soc.* **2004**, *126*, 10441.
17. Rosenthal, J.; Nocera, D. G. *Acc. Chem. Res.* **2007**, *40*, 543.
18. Halime, Z.; Kotani, H.; Li, Y.; Fukuzumi, S.; Karlin, K. D. *Proc. Natl. Acad. Sci. U. S. A.* **2011**, *108*, 13990.
19. Tahsini, L.; Kotani, H.; Lee, Y.-M.; Cho, J.; Nam, W.; Karlin, K. D.; Fukuzumi, S. *Chem. - Eur. J.* **2012**, *18*, 1084.
20. Fukuzumi, S.; Mochizuki, S.; Tanaka, T. *J. Chem. Soc., Chem. Commun.* **1989**, 391.
21. Olaya, A. J.; Schaming, D.; Brevet, P.-F.; Nagatani, H.; Zimmermann, T.; Vanicek, J.; Xu, H.-J.; Gros, C. P.; Barbe, J.-M.; Girault, H. H. *J. Am. Chem. Soc.* **2012**, *134*, 498.
22. Peljo, P.; Murtomaki, L.; Kallio, T.; Xu, H.-J.; Meyer, M.; Gros, C. P.; Barbe, J.-M.; Girault, H. H.; Laasonen, K.; Kontturi, K. *J. Am. Chem. Soc.* **2012**, *134*, 5974.
23. Costas, M.; Mehn, M. P.; Jensen, M. P.; Que, L. *Chem. Rev.* **2004**, *104*, 939.
24. Decker, A.; Solomon, E. I. *Curr. Opin. Chem. Biol.* **2005**, *9*, 152.
25. Solomon, E. I.; Brunold, T. C.; Davis, M. I.; Kemsley, J. N.; Lee, S. K.; Lehnert, N.; Neese, F.; Skulan, A. J.; Yang, Y. S.; Zhou, J. *Chem. Rev.* **2000**, *100*, 235.
26. Liu, S.; Mase, K.; Bougher, C.; Hicks, S. D.; Abu-Omar, M. M.; Fukuzumi, S. *Inorg. Chem.* **2014**, *53*, 7780.
27. Kakuda, S.; Rolle, C. J.; Ohkubo, K.; Siegler, M. A.; Karlin, K. D.; Fukuzumi, S. *J. Am. Chem. Soc.* **2015**, *137*, 3330.
28. Hamberg, M.; Su, C.; Oliw, E. *J. Biol. Chem.* **1998**, *273*, 13080.
29. Su, C.; Sahlin, M.; Oliw, E. H. *J. Biol. Chem.* **2000**, *275*, 18830.
30. Boal, A. K.; Cotruvo, J. A., Jr.; Stubbe, J.; Rosenzweig, A. C. *Science* **2010**, *329*, 1526.
31. Miller, A.-F. *Curr. Opin. Chem. Biol.* **2004**, *8*, 162.
32. Wu, J.; Penner-Hahn, J. E.; Pecoraro, V. L. *Chem. Rev.* **2004**, *104*, 903.
33. Umena, Y.; Kawakami, K.; Shen, J.-R.; Kamiya, N. *Nature* **2011**, *473*, 55.
34. Mullins, C. S.; Pecoraro, V. L. *Coord. Chem. Rev.* **2008**, *252*, 416.

35. Pecoraro, V. L.; Baldwin, M. J.; Gelasco, A. *Chem. Rev.* **1994**, *94*, 807.
36. Signorella, S.; Hureau, C. *Coord. Chem. Rev.* **2012**, *256*, 1229.
37. Kovacs, J. A.; Brines, L. M. *Acc. Chem. Res.* **2007**, *40*, 501.
38. Coggins, M. K.; Sun, X.; Kwak, Y.; Solomon, E. I.; Rybak-Akimova, E. V.; Kovacs, J. A. *J. Am. Chem. Soc.* **2013**, *135,* 5631.
39. Lee, C.-M.; Chuo, C.-H.; Chen, C.-H.; Hu, C.-C.; Chiang, M.-H.; Tseng, Y.-J.; Hu, C.-H.; Lee, G.-H. *Angew. Chem. Int. Ed.* **2012**, *51*, 5427.
40. Namuswe, F.; Kasper, G. D.; Sarjeant, A. A. N.; Hayashi, T.; Krest, C. M.; Green, M. T.; Moenne-Loccoz, P.; Goldberg, D. P. *J. Am. Chem. Soc.* **2008**, *130*, 14189.
41. Jiang, Y.; Telser, J.; Goldberg, D. P. *Chem. Commun.* **2009**, 6828.
42. Coggins, M. K.; Kovacs, J. A. *J. Am. Chem. Soc.* **2011**, *133*, 12470.
43. Coggins, M. K.; Martin-Diaconescu, V.; DeBeer, S.; Kovacs, J. A. *J. Am. Chem. Soc.* **2013**, *135*, 4260.
44. Krishnamurthy, D.; Kasper, G. D.; Namuswe, F.; Kerber, W. D.; Narducci Sarjeant, A. A.; Moenne-Loccoz, P.; Goldberg, D. P. *J. Am. Chem. Soc.* **2006**, *128*, 14222.
45. Brown, C. D.; Neidig, M. L.; Neibergall, M. B.; Lipscomb, J. D.; Solomon, E. I. *J. Am. Chem. Soc.* **2007**, *129*, 7427.
46. Brines, L. M.; Shearer, J.; Fender, J. K.; Schweitzer, D.; Shoner, S. C.; Barnhart, D.; Kaminsky, W.; Lovell, S.; Kovacs, J. A. *Inorg. Chem.* **2007**, *46*, 9267.
47. Kitagawa, T.; Dey, A.; Lugo-Mas, P.; Benedict, J. B.; Kaminsky, W.; Solomon, E.; Kovacs, J. A. *J. Am. Chem. Soc.* **2006**, *128*, 14448.
48. Green, M. T.; Dawson, J. H.; Gray, H. B. *Science* **2004**, *304*, 1653.
49. Coggins, M. K.; Toledo, S.; Shaffer, E.; Kaminsky, W.; Shearer, J.; Kovacs, J. A. *Inorg. Chem.* **2012**, *51*, 6633.
50. DuBois, D. L. *Inorg. Chem.* **2014**, *53*, 3935.
51. Shook, R. L.; Borovik, A. S. *Inorg. Chem.* **2010**, *49*, 3646.
52. Shook, R. L.; Gunderson, W. A.; Greaves, J.; Ziller, J. W.; Hendrich, M. P.; Borovik, A. S. *J. Am. Chem. Soc.* **2008**, *130*, 8888.
53. Carver, C. T.; Matson, B. D.; Mayer, J. M. *J. Am. Chem. Soc.* **2012**, *134*, 5444.
54. Borovik, A. S. *Acc. Chem. Res.* **2005**, *38*, 54.
55. Kopf, M. A.; Varech, D.; Tuchagues, J. P.; Mansuy, D.; Artaud, I. *J. Chem. Soc., Dalton Trans.* **1998**, 991.
56. Cheng, B.; Cukiernik, F.; Fries, P. H.; Marchon, J.-C.; Scheidt, W. R. *Inorg. Chem.* **1995**, *34*, 4627.
57. Cheng, B.; Fries, P. H.; Marchon, J.-C.; Scheidt, W. R. *Inorg. Chem.* **1996**, *35*, 1024.
58. Biswas, S.; Mitra, K.; Adhikary, B.; Lucas, C. R. *Transition Met. Chem.* **2005**, *30*, 586.
59. Zhou, H. B.; Wang, H. S.; Chen, Y.; Xu, Y. L.; Song, X. J.; Song, Y.; Zhang, Y. Q.; You, X. Z. *Dalton Trans.* **2011**, *40*, 5999.
60. Mukhopadhyay, S.; Mandal, S. K.; Bhaduri, S.; Armstrong, W. H. *Chem. Rev.* **2004**, *104*, 3981.
61. Visser, H.; Anxolabéhère-Mallart, E.; Bergmann, U.; Glatzel, P.; Robblee, J. H.; Cramer, S. P.; Girerd, J.-J.; Sauer, K.; Klein, M. P.; Yachandra, V. K. *J. Am. Chem. Soc.* **2001**, *123*, 7031.
62. Roemelt, M.; Beckwith, M. A.; Duboc, C.; Collomb, M. N.; Neese, F.; DeBeer, S. *Inorg. Chem.* **2012**, *51*, 680.
63. O'Connor, C. J. *Prog. Inorg. Chem.* **1982**, *29*, 203.
64. Wieghardt, K. *Angew. Chem. Int. Ed. Engl.* **1989**, *28*, 1153.
65. Blanchard, S.; Blain, G.; Rivière, E.; Nierlich, M.; Blondin, G. *Chem. Eur. J.* **2003**, *9*, 4260.
66. Mikuriya, M.; Adachi, F.; Iwasawa, H.; Handa, M.; Koikawa, M.; Okawa, H. *Bull. Chem. Soc. Jpn.* **1994**, *67*, 3263.
67. Gennari, M.; Pécaut, J.; DeBeer, S.; Neese, F.; Collomb, M.-N.; Duboc, C. *Angew. Chem. Int. Ed.* **2011**, *50*, 5662.
68. Hillier, W.; Wydrzynski, T. *Coord. Chem. Rev.* **2008**, *252*, 306.
69. Hillier, W.; Messinger, J.; Wydrzynski, T. *Biochemistry* **1998**, *37*, 16908.

70. Matsubara, C.; Kawamoto, N.; Takamura, K. *Analyst* **1992**, *117*, 1781.
71. Takamura, K.; Matsubara, C.; Matsumoto, T. *Anal. Sci.* **2008**, *24*, 401.
72. Fukuzumi, S.; Kotani, H.; Lucas, H. R.; Doi, K.; Suenobu, T.; Peterson, R. L.; Karlin, K. D. *J. Am. Chem. Soc.* **2010**, *132*, 6874.
73. Kakuda, S.; Peterson, R. L.; Ohkubo, K.; Karlin, K. D.; Fukuzumi, S. *J. Am. Chem. Soc.* **2013**, *135*, 6513.
74. (a)Balch, A. L.; Chan, Y. W.; Cheng, R. J.; La Mar, G. N.; Latos-Grazynski, L.; Renner, M. W. *J. Am. Chem. Soc.* **1984**, *106*, 7779. (b) Luthra, A., Denisov, I. G., Sligar, S. G., *Archive of Biochemitry and Biophysics*, **2011**, *507*, 26-35.
75. Coggins, M. K.; Brines, L. M.; Kovacs, J. A. *Inorg. Chem.* **2013**, *52*, 12383.
76. Root, D. E.; Mahroof-Tahir, M.; Karlin, K. D.; Solomon, E. I. *Inorg. Chem.* **1998**, *37*, 4838.
77. Chen, P.; Fujisawa, K.; Solomon, E. I. *J. Am. Chem. Soc.* **2000**, *122*, 10177.
78. Ching, H. Y. V.; Anxolabehere-Mallart, E.; Colmer, H. E.; Costentin, C.; Dorlet, P.; Jackson, T. A.; Policar, C.; Robert, M. *Chem. Sci.* **2014**, *5*, 2304.
79. Jung, J.; Liu, S.; Ohkubo, K.; Abu-Omar, M. M.; Fukuzumi, S. *Inorg. Chem.* **2015**, Ahead of Print.
80. Sheriff, T. S. *J. Chem. Soc., Dalton Trans.* **1992**, 1051.
81. Bettelheim, A.; Ozer, D.; Parash, R. *J. Chem. Soc., Faraday Trans. 1* **1983**, *79*, 1555.
82. Schneider, J.; Schnautz, B.; Hauptman, R.; Henkel, G., *Acta Crystallogr. Sect. C-Cryst. Struct. Commun.* **1999,** *55*, 489-491.
83. Costa, T.; Dorfman, J. R.; Hagen, K. S.; Holm, R. H., *Inorg. Chem.* **1983,** *22*, 4091-4099.
84. Brines, L. M.; Shearer, J.; Fender, J. K.; Schweitzer, D.; Shoner, S. C.; Barnhart, D.; Kaminsky, W.; Lovell, S.; Kovacs, J. A., *Inorg. Chem.* **2007,** *46*, 9267-9277.
85. Coggins, M. K.; Toledo, S.; Shaffer, E.; Kaminsky, W.; Shearer, J.; Kovacs, J. A., *Inorg. Chem.* **2012,** *51*, 6633-6644.
86. Addison, A. W.; Rao, T. N.; Reedijk, J.; Vanrijn, J.; Verschoor, G. C., *J. Chem. Soc.,*
87. Seela, J. L.; Knapp, M. J.; Kolack, K. S.; Chang, H.-R.; Huffman, J. C.; Hendrickson, D. N.; Christou, G., *Inorg. Chem.* **1998,** *37*, 516-525.
88. Krewald, V.; Lassalle-Kaiser, B.;. Boron III,. T. T.; C. J. Pollock, C. J.; Kern, J.; Beckwith, M. A.; Yachandra, V. K.; Pecoraro, V. L.; Yano, J.; Neese, F. and DeBeer, S. *Inorg. Chem.* **2013**, *52*, 12904−12914.
89. Hohmann-Marriott, F.M. & Blankenship, R. E. *Annu Rev Plant Biol,* **2011**, *62***,** 515–548.
90. Kanady, J. S.; Lin, P.-H., Carsch, K. M.; Nielsen, R. J.; Takase, M. K.; Goddard III W. A.; and Agapie, T. *J. Am.Chem. Soc.*, **2014**, *136*, 14373-14476.
91. Yin, G. Danby, A. M. Kitko, D. Carter, J. D. Scheper, W. M. Busch, D. H. *J. Am. Chem. Soc,.* **2008**, *130*, 16245−16253.
91. Addison, A. W.; Rao, T. N.; Reedijk, J.; Vanrijn, J.; Verschoor, G. C., *J. Chem. Soc., Dalton Trans.* **1984**, 1349-1356.
92. A.L., Balch.,Y.W. Chan., Cheng, J., La Mar, G. N., Latos-Grazynski, L., Renner, M. W., *J. Am. Chem. Soc.*, **1984**, *106* , 7779–7785.

Chapter III

Effect of the metal on disulfide/thiolate interconversion: Manganese *vs* Cobalt.

Table of contents

Résumé 122
Introduction 127
Results and Discussion 130
3.1. Synthesis and characterization of Mn and Co complexes. 130
3.1.1. Synthesis of **Co^{II}_2SS** and **$Co^{III}I$**. 130
3.1.2 Synthesis of **Mn^{II}_2SS** and **$Mn^{III}I$**. 131
3.1.3. X-Ray characterization of **Co^{II}_2SS** and **$Co^{III}X$**. 132
3.1.4 X-Ray characterization of **Mn^{II}_2SS** and **$Mn^{III}I$**. 134
3.2. UV-Vis spectroscopic properties. 136
3.2.1. UV-Vis spectroscopy of **Co^{II}_2SS** and **$Co^{III}X$** complexes. 136
3.2.2. UV-Vis spectroscopy of **Mn^{II}_2SS** and **$Mn^{III}I$** complexes. 137
3.3. Magnetic properties. 138
3.2.1. **Mn^{II}_2SS** magnetic properties. 138
3.4. Reactivity with Iodide: disulphide/thiolate interconversion. 139
3.5. Electrochemical properties 141
3.6. Theoretical calculations. 143
Conclusion 146
References 147

Résumé

La conversion redox thiolate/disulfure est impliquée dans de nombreux processus biologiques essentiels[1] et notamment dans le repliement des protéines. Cette conversion joue un rôle important dans la régulation intracellulaire en agissant comme un interrupteur ON/OFF de la réactivité des protéines, c'est-à-dire en inhibant ou non leur activité. Différentes stratégies biologiques sont utilisées pour contrôler précisément cette balance thiolate/disulfure : il a été récemment proposé que des ions métalliques, et plus particulièrement des ions cuivre, puissent réguler cette conversion thiolate/disulfure. De tels systèmes à base de cuivre semblent être impliqués dans la délivrance du cuivre, comme par exemple au niveau de la Cytochrome c oxydase, oxydoréductase de la chaine respiratoire qui catalyse l'oxydation réversible du cytochrome c en présence d'O_2 Celle-ci contient une protéine membranaire interne Sco1, impliquée dans l'assemblage du centre Cu_A et qui est capable de fixer du Cu^{2+} ainsi que Cu^{+}.[2] (Figure 1)

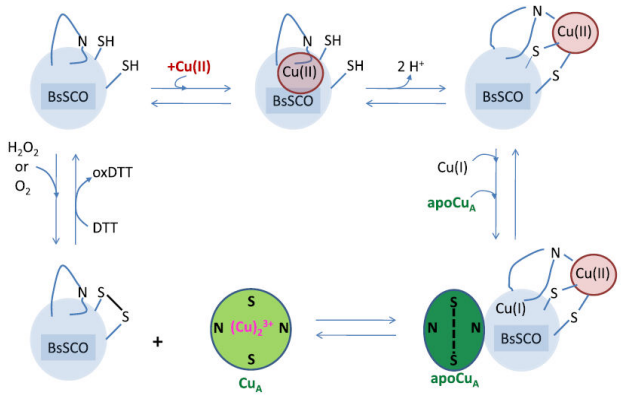

Figure 1. Exemple d'un système impliqué dans la deliverance du Cu de la Cytochrome *c* oxydase (Sco1) présent chez la bactérie *Bacillus subtilis* (i.e., BsSCO) .[2d] (DTT : dithiothreitol)

Il est également connu que le cuivre joue un rôle dans la formation d'espèces réactives de l'oxygène (ROS pour reactive oxygen species) dans la maladie d'Alzheimer.[3] Cette maladie est responsable d'une neurodégénération conduisant à la démence et se caractérise par la déposition de plaques amyloïdes au niveau du cerveau. Récemment, il a été mis en évidence que le Cu^{2+} une fois coordiné à l'amyloïde β (Aβ)[29] génèrent la production de ROS, conduisant à la formation d'agrégat et de plaques Aβ responsable de la neurotoxicité. Par contre lorsque le Zn^{2+} est coordiné au Aβ, il empêche la formation de ROS, et donc de plaques Aβ. En présence de Zn^{2+}, le Cu^{2+} s'échange au niveau de Aβ, jouant un rôle protecteur au niveau du cerveau. Cette régulation serait basée sur l'interconversion thiolate/disulfure activée par le cuivre.[3a] Au cours du processus, quatre cystéines de la métallothionéine (MT) sont oxydées par quatre ions Cu^{2+}, issus de Aβ, avec la formation concomitante de deux ponts disulfures entrainant la libération de Zn^{2+} qui se coordine alors au Aβ.[3e]

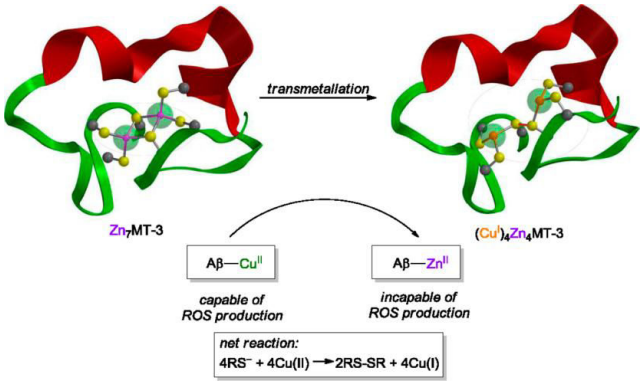

Figure 2. Exemple biologique d'une conversion thiolate/disulfure à base de Cu impliquée dans la Maladie d'Alzheimer's. Echange Cu/Zn entre une métallothionéine (MT) à Zn et le peptide amyloïde β (CuAβ). [3e]

Ces récentes investigations suggèrent que le Cu^{2+} intracellulaire aurait un rôle protecteur dans la régulation des fibres Aβ via des interférences dans les différents processus de régulation.[3b,30] Plus spécifiquement, des cultures cellulaires en présence de complexes de cuivre peuvent activer des voies de signalisation qui vont entrainer une augmentation de l'expression d'une protéase impliquée dans la dégradation des plaques Aβ diminuant ainsi leur formation.[3e]

La réactivité des disulfures ou des thiolates en présence d'un ion métallique a aussi attiré l'attention des chimistes comme un outil synthétique de choix pour la conception de molécules fonctionnelles originales comprenant des architectures moléculaires à base de métaux.[4] Les propriétés de coordination des soufres peuvent être employées pour la préparation de molécules variées. En présence d'un ion métallique, un pont disulfure peut (i) rester non coordonné, (ii) être impliqué dans des interactions faibles, ou (iii) subir des coupures réductrices de la liaison S-S. dans le dernier cas, les thiolates résultants peuvent agir comme ligand terminal ou pontant, générant ainsi des assemblages de molécules inorganiques avec un nombre de noyaux métalliques contrôlés ou infinis.
Dans ce contexte, les propriétés électroniques et redox de ces complexes doivent être finement réglées pour générer les motifs métal-thiol ciblés et/ou de contrôler l'équilibre thiolate/disulfure. Cependant, le rôle du métal ou du ligand soufré sur l'interconversion thiolate/disulfure en fonction n'a jamais été étudié, ces conversions moléculaires demeurant rares et majoritairement limitées à des complexes de Cu^{I}-disulfure/Cu^{II} thiolate.[5]

En 2014, notre groupe a publié le premier système ne contenant pas de Cu. Il s'agissait d'un complexe à base de cobalt capable de réaliser de manière propre et efficace une conversion Co^{II}-disulfure/ Co^{III} thiolate réguler par la coordination/décoordination d'un ion chlorure. L'avantage de ce système est d'être actif en condition aérobie et d'exister sous forme de dimère ou de monomère.

Il est donc intéressant d'étendre cette étude à d'autres métaux de transition pour comprendre leur impact sur de tels processus.[6] (Figure 3)

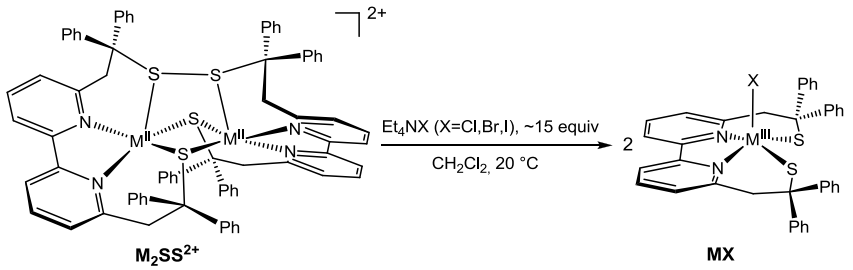

Figure 3. Interconversion M^{II} disulfure/ M^{III} thiolate régulée par la coordination/décoordination d'halogénures (M=Co, Mn), (X = Cl, Br, I).[6]

Dans ce sens, le manganèse est particulièrement intéressant, car il présente une plus faible affinité vis-à-vis des soufres que le cobalt ou encore que le cuivre. Si on s'intéresse aux propriétés électroniques des métaux de transitions, le caractère covalent de la liaison métal-thiol doit diminuer du Cu^{II} au Mn^{II}.

Dans ce contexte, ce chapitre rapporte la synthèse et la caractérisation d'un nouveau complexe dinucléaire de Mn^{II} présentant un pont disulfure $[Mn^{II}_2(LSSL)](PF_6)_2$ (**Mn^{II}_2SS**), isostructural au complexe de Co^{II}, $[Co^{II}_2(LSSL)](PF_6)_2$ (**Co^{II}_2SS**).[6] Ainsi cette étude s'intéresse à l'effet du métal coordinant (M) sur les propriétés d'interrupteur moléculaire M^{n+}-disulfure/ $M^{(n+1)+}$-thiolate. Comme son parent isostructural de Co, **Co^{II}_2SS**,[6] ce nouveau complexe dinucléaire de Mn^{II}-disulfure, **Mn^{II}_2SS**, peut réaliser une interconversion Mn^{II}-disulfure/ Mn^{III}-thiolate qui conduit au premier interrupteur moléculaire thiolate/disulfure basé sur le Mn. En particulier, la coordination de l'iodure sur l'ion métallique stabilise la forme oxydée du manganèse, Mn^{III}, alors que le disulfure stabilise sa forme réduite, Mn^{II}. Le processus inverse, qui implique la réduction de Mn^{III} en Mn^{II} avec l'oxydation concomitante des thiolates, nécessite la libération de l'iodure. Le complexe **Mn^{II}_2SS** réagit lentement avec Bu_4NI dans CH_2Cl_2 pour donner le complexe mononucléaire de **Mn^{III}I**. Le processus est beaucoup plus lent (16 h) et beaucoup moins efficace (30% de rendement), qu'avec le complexe de **Co^{II}_2SS** où la conversion **Co^{II}_2SS** en **Co^{III}I** est instantanée et quantitative dans les mêmes conditions expérimentales (Figure 4). Dans les deux cas, le processus inverse, soit la réduction du complexe de Mn^{III} en Mn^{II} avec l'oxydation concomitante des thiolates en disulfure est instantanée.

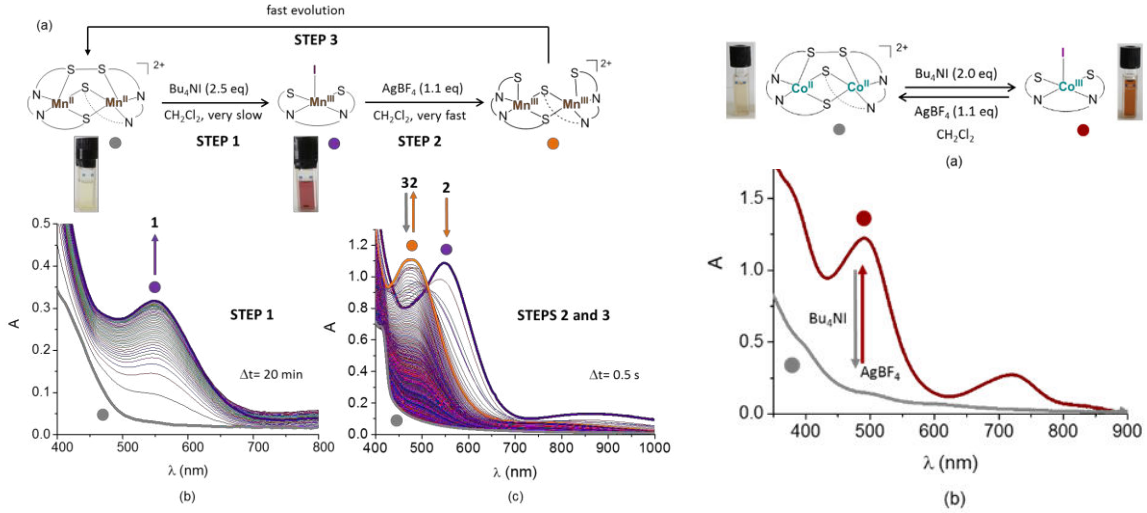

Figure 4. Spectres UV-Visible illustrant l'interconversion thiolate/disulfure, (gauche) Mn^{II}/Mn^{III}, (droite) Co^{II}/Col^{II}.

Ce comportement distinct peut être rationalisé en considérant les différentes propriétés électrochimiques du Co et du Mn ainsi que par des calculs DFT nous permettant de comprendre quels facteurs sont impliqués dans cette conversion disulfure/thiolate. Les énergies libres de Gibbs (ΔG° à 0 K) calculées pour les réactions de l'équation 1 peuvent être considérées comme des premières estimations de la force motrice pour la conversion M^{II}-disulfure/M^{III}-thiolate, en sachant que la coordination de l'iodure n'a pas les mêmes effets sur le métal (l'iodure n'étant pas pris en compte pour ses estimations).

$$[M^{II}_2(LSSL)]^{2+} = 2[M^{III}(LS)]^{+} \qquad \text{(Equation 1)}$$

Ces valeurs de ΔG°, en phase liquide (CH_2Cl_2) et en phase gaz sont présentées dans le tableau 1.

Tableau 1. Energies libres de Gibbs (ΔG^0), calculées à 0 K, pour les réactions de l'équation 3, en phase liquide (CH2Cl2) et en phase gaz.

	ΔG^0 *in vacuum* (kcal·mol^{-1})	ΔG^0 *in* CH_2Cl_2 (kcal·mol^{-1})
$[Mn^{II}_2(LSSL)]^{2+} = 2[Mn^{III}(LS)]^{+}$	+3.6	+7.9
$[Co^{II}_2(LSSL)]^{2+} = 2[Co^{III}(LS)]^{+}$	-31.0	-15.1

La dissociation du Co^{II}-disulfure en deux unités Co^{III}-thiolate est hautement exergonique (ΔG° = -15.1 kcal·mol^{-1} dans le CH_2Cl_2). La relative haute stabilité des unités monomériques $[Co^{III}(LS)]$, ainsi que celle du complexe dinucléaire de Co^{II}, $[Co^{II}_2(LSSL)]^{2+}$, est en bon accord avec une conversion rapide et efficace, comme cela a pu être observé expérimentalement. Quant au complexe de Mn, les énergies libres calculées sont positives témoignant de la faible réactivité du système dinucléaire à base de Mn.

La coordination de l'iodure au Mn^{III} stabilise la forme mononucléaire, ce qui favorise tout de même sa formation.

Pour chacun des systèmes de Mn et de Co, l'interconversion M^{II}-disulfure/M^{III}-thiolate est réversible. Quand l'iodure est décoordiné du métal en présence d'Ag^{+}, le complexe de $\mathbf{M^{II}_2SS}$ est régénéré, bien que de manière plus lente pour les complexes de Mn que pour ceux de Co. La coordination de l'ion iodure diminue le potentiel redox du couple Co^{III}/Co^{II} de manière à ce que les ions Co^{II} puissent réduire le pont disulfure en thiolate. Inversement, le potentiel redox du couple LSSL/2 LS pour le complexes de Mn est étonnamment plus bas que pour le complexe de Co (-1,17 et -0,74 V, respectivement). Par conséquent, la coordination de l'ion iodure ne diminue pas suffisamment le potentiel redox du couple Mn^{III}/Mn^{II} pour permettre une conversion efficace, contrairement aux complexes de Co.

Nous décrivons ici deux rares exemples d'interrupteurs moléculaires impliqués dans la conversion disulfure/thiolate et plus particulièrement, des complexes qui (i) ne sont pas à base de Cu mais de Co et de Mn, dont les propriétés électroniques du métal jouent un rôle sur l'efficacité de cette interconversion. Ce travail montre également qu'un stimulus externe (comme l'ajout d'un ion iodure) peut conduire à un fin contrôle des propriétés électroniques de l'ion métallique permettant ainsi un déplacement de l'équilibre disulfure/thiolate.

Introduction

Thiolate/disulphide redox conversion is implicated in various essential biological processes[1]including the folding of most proteins. Thiolate/disulphide redox conversion also plays a key role in the intracellular regulation by acting as a switch that turns ON or OFF the reactivity of a protein by inhibiting or not its activity. Different biological strategies are employed to precisely control the thiolate/disulphide balance; it has been recently proposed that metal ions, especially copper, can mediate thiolate/disulphide interconversion. Such copper-based systems seem to be implicated in the delivery of copper from the human Sco1, an inner membrane protein involved in the assembly of the Cu_A center in the Cytochrome c oxidase (Figure 1), an enzyme of the respiratory chain that catalyzes the reversible oxidation of the cytochrome c in the presence of dioxygen.[2]

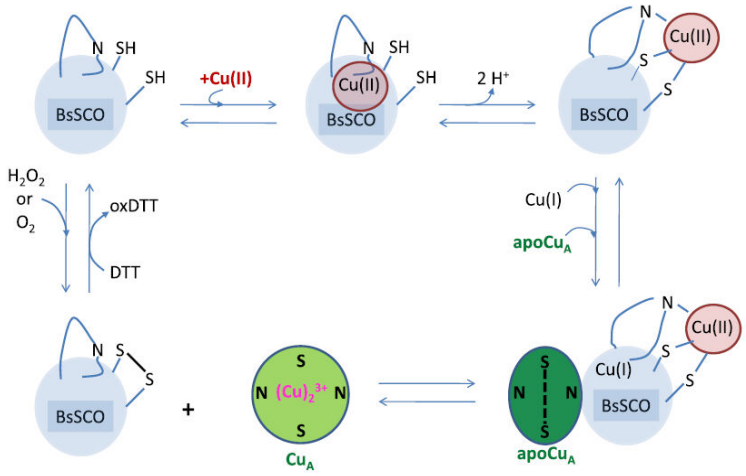

Figure 1. Example of copper-based delivery system in the Cytochrome c oxidase of the *Bacillus subtilis* involving Sco1.[2d] (i.e., BsSCO); (DTT : dithiothreitol))

Copper-based systems are also involved in the protection of cells against reactive oxygen species (ROS) such in Alzheimer's disease[3]. This disease is known to be a progressive neurodegenerative disease and involved in cause of dementia. This pathology is characterized by the deposition of cerebral amyloid plaques. It has been recently evidenced that once Cu^{2+} is coordinated to Amyloid β (Aβ), the Cu^{II} Aβ complex produces ROS that causes the Aβ aggregation into plaques at the origin of the neurotoxicity.[29] On the other hand, when Zn^{2+} is coordinated to Aβ, it prevents the formation of ROS and thus of Aβ plaques. In the presence of Zn^{2+}, the Aβ-bound Cu^{2+} ion is exchanged, playing a protective role by preventing the toxicity of ROS produced by Cu^{2+}. This regulation is based on a Cu-based thiolate/disulphide interconversion involving a multifunctioning living system.[3a] During this process, four cysteine-thiolate of the metallothioneine (MT) are oxidized by 4 Cu^{2+} ions, originating

from Aβ, with the concomitant formation of two disulphide bonds that leads to the release of Zn^{2+} that is then coordinated to Aβ(Figure 2).[3e]

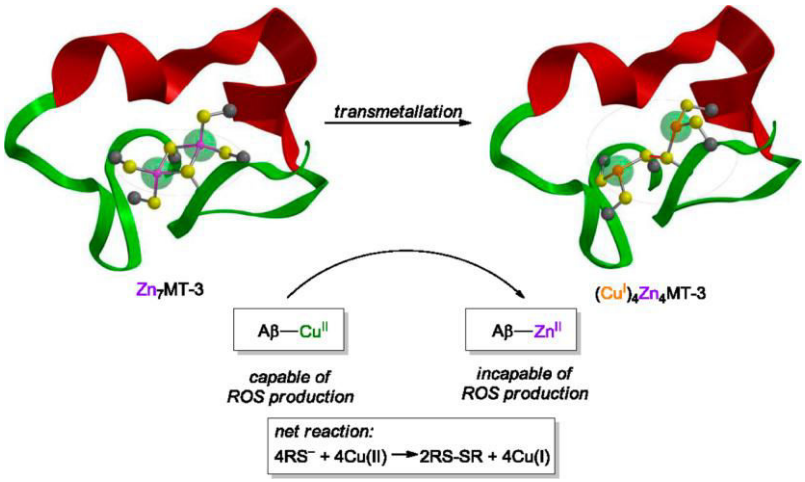

Figure 2. Biological example of a postulated thiolate/disulphide interconversion in Alzheimer's disease.[3e] Cu/Zn exchange between metallothionein (MT) and Cu^{2+}-bonded amyloide peptide (Cu^{2+} Aβ complex)

The reactivity of disulphides or thiolates in the presence of a metal ion has also attracted the attention of chemists as an interesting synthetic tool for the conception of functional materials and original metal-based molecular architectures, enrolling in the biomimetic area.[4] Actually, the coordinating properties of sulphur display a remarkable versatility that can be employed for the preparation of various molecular assemblies. In the presence of a metal, the disulphide atoms could (i) remain uncoordinated, (ii) be involved in weak interactions, or (iii) undergo a reductive cleavage of the S-S bond. In the last case, the resulting thiolates could act as terminal or bridging ligands to generate many types of molecular inorganic auto-assemblages with controlled or infinite nuclearity.

In this context, the electronic and redox properties of metal complexes should be accurately fine-tuned to generate the targeted metal-sulphur motifs and/or to control the thiolate/disulphide equilibrium. The nature of the metal should play a key role in driving M^{n+}-disulphide/ $M^{(n+1)+}$-thiolate interconversion. However, such investigation in thiolate/disulphide interconversion has never been reported. So far, these molecular switches remain rare and mainly limited to Cu^{I} disulphide/ Cu^{II} thiolate based systems (Figure 3).[5]

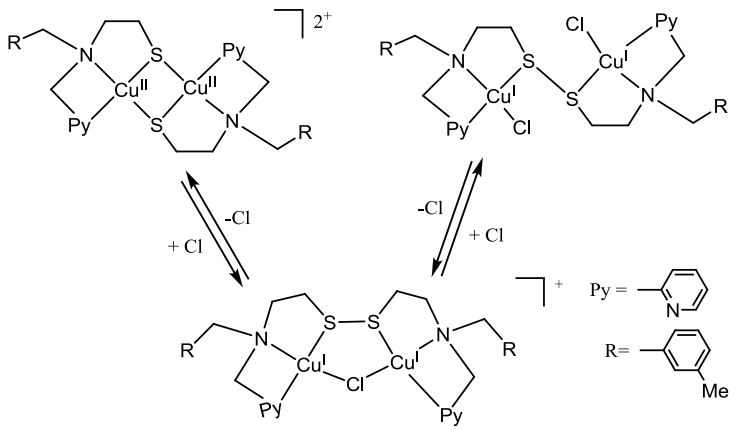

Figure 3. One example of Cu-based disulfide/thiolates switch implicated the coordination/release of chloride anions. [5]

In 2014, the group has reported the first system that does not contain copper, a Co-based switch implying a very clean, quantitative and reversible Co^{II} disulphide/ Co^{III} thiolate interconversion implicated the coordination/release of chloride anions which acts under aerobic conditions and involves systems with different nuclearity.[6] Interestingly, its extension to other transition metal ions is thus mandatory to better understand the impact of the metal ion on such fundamental processes (Figure 4).

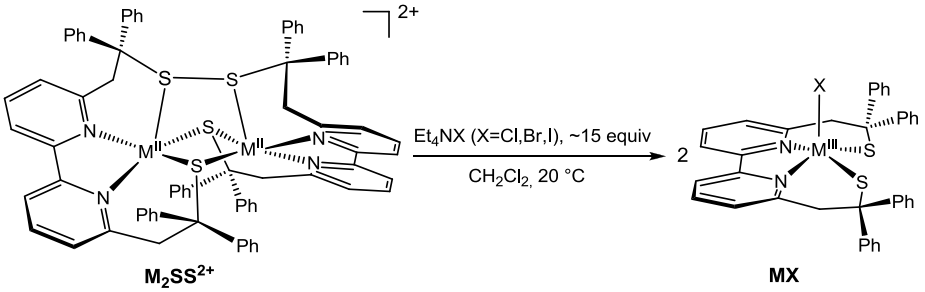

Figure 4. M^{II} disulphide/ M^{III} thiolate interconversion implicated the coordination/release of halide anions (M=Co, Mn), (X = Cl, Br, I).

In this sense, manganese is very attractive, as it should have a notably lower sulphur affinity with respect to the late transition copper or cobalt metal ions, as well as very distinctive electronic properties due to a decrease of the covalent character of the metal-sulphur bond from Cu^{II} to Mn^{II}. The reactivity of thiolates in the presence of Mn complexes has only been investigated in the case of the anionic $[Mn^{I}(CO)_3(SPhS)]^-$ complex (SPhS = 1,2 benzenedithiol) with aromatic thiolates, which is converted into a dinuclear $[Mn^{I}_2(CO)_6(SPhSSPhS)]$ in the presence of protons with the concomitant formation of H_2 (Figure 5).[7]

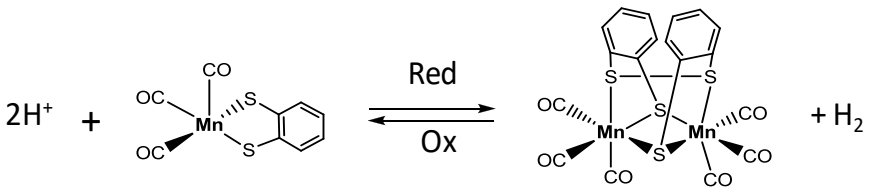

Figure 5. Mn^{I} thiolate/ Mn^{I} dissulfide interconversion by the coordination/release of protons on the thiolates.[7]

In this chapter III, the synthesis and characterization of a new dinuclear disulphide-bridged Mn^{II} complex, $[Mn^{II}_2(LSSL)](PF_6)_2$ (**Mn^{II}_2SS**) (Figure 4), isostructural to Co^{II}-parent compound, $[Co^{II}_2(LSSL)](PF_6)_2$ (**Co^{II}_2SS**) are reported.[6] The reactivity of **Mn^{II}_2SS** with halide anions (in particular with iodide) has been investigated. As in the case of **Co^{II}_2SS**, coordination of the halide to the metal ion induces a disulphide to thiolate conversion and the concomitant oxidation of M^{II} to M^{III}. Even though the process occurs in a much lower efficiency, the process remains reversible. With the help of theoretical calculations, the reactivity of the cobalt and manganese systems is finally compared and discussed.

This work has been recently published in *Chem. Eur. J.*, **2015**, *21(51)*, 18770-18778 and *Chem. Eur. J.* **2016**, *22*, 925-933.)

Results and Discussion

3.1. Synthesis and characterization of Mn and Co complexes.

3.1.1. Synthesis of **Co^{II}_2SS** and **Co^{III}I**.

Co^{II}_2SS has been synthesized from the potassium salt of the ligand H_2L= 2,2′-(2,2′-bipyridine-6,6′-diyl)bis(1,1-diphenylethanethiol)) complexes in THF in the presence of $Co(BF_4)_2.6H_2O$ leading to a dark brown precipitate corresponding to the mononuclear **Co^{II}L** complex which has been characterized by X-Ray spectroscopy. **Co^{II}_2SS** can be electro-generated by an exhaustive electrolysis of **Co^{II}L**, carried out in CH2Cl2 at 0 V *vs* Fc^+/Fc (Figure 6).

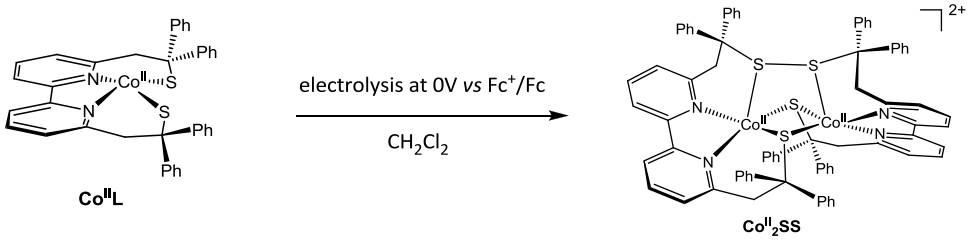

Figure 6. Electro-synthesis of the described dinuclear Co^{II}_2SS complex.

Different synthetic methods have been reported for the synthesis of **Co^{III}Cl** (chemical and electrochemical paths), including a procedure that can be generalized to potentially allow for the

synthesis of series of penta-coordinated mononuclear Co^{III} complexes (Figure 7). The reaction of the dinuclear **Co^{II}_2SS** complex in the presence of two equivalents of Et_4NCl leads to **Co^{III}Cl** in a good yield of 72%.[6] In this reaction, the coordination of one chloride anion on each Co^{II} center in **Co^{II}_2SS** leads to the reduction of the disulfide bridge and the concomitant oxidation of the Co^{II} ions. Following the same procedure, addition of two equivalents of Et_4NBr and Et_4NI to **Co^{II}_2SS** leads to the formation of [Co^{III}L(Br)] (**Co^{III}Br**) and [Co^{III}L(I)] (**Co^{III}I**), in a good yield of 70% and 84%, respectively.

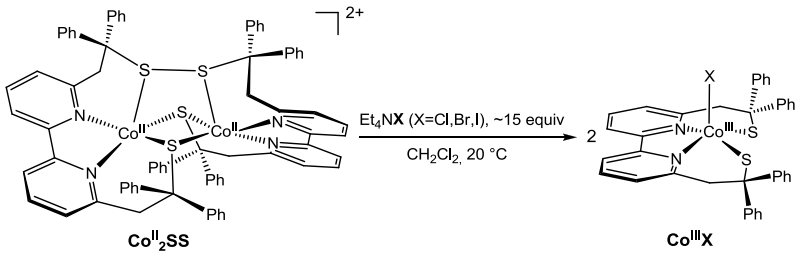

Figure 7. Synthesis of the mononuclear **Co^{III}X** complex (X = Cl, Br, I).

The reactions which lead to **Co^{III}X** are efficient and quantitative and will be studied in details. The differences of synthesis and especially the electronic properties between Mn and Co complexes will be explained chapter IV.

3.1.2 Synthesis of **Mn^{II}_2SS** and **Mn^{III}I**.

The [Mn^{II}_2(LSSL)]$(PF_6)_2$ complex (**Mn^{II}_2SS**) has been obtained from the oxidative electrolysis of [Mn^{II}_2(LS)(LSH)]ClO_4 (**Mn^{II}_2SH**, containing a pendant thiol) in CH_3CN at E = +0.05 V vs Fc^+/Fc (Figure 8). The synthesis and the redox properties of **Mn^{II}_2SH** complex have been previously described in chapter II.

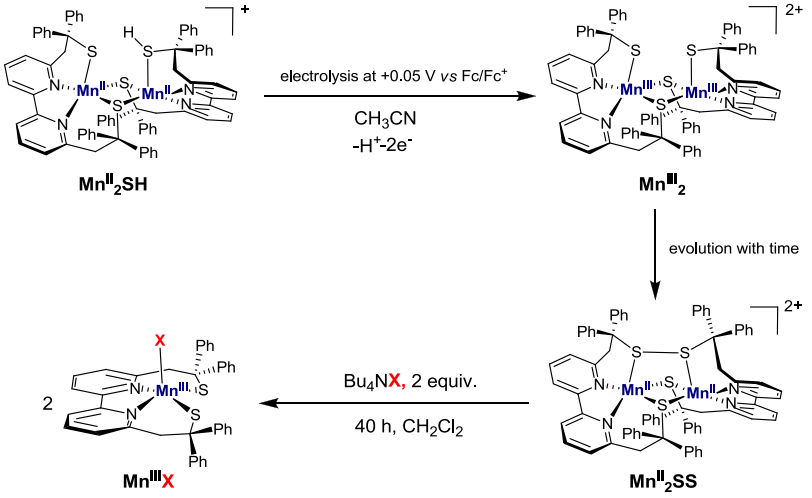

Figure 8. Synthesis/ electrosynthesis of the described manganese sulphur complexes, (X = Cl, Br, I).

During the oxidative electrolysis at +0.05 V of **Mn^{II}_2SH**, the color of the solution turns from light orange to deep orange, which corresponds to the formation of **Mn^{III}_2**. Then, this species evolves to a

light yellow solution with time. This final complex has been isolated and identified as **Mn^{II}_2SS**, an isoelectronic form of **Mn^{III}_2**, by single crystal X-ray diffraction (See below). **Mn^{II}_2SS** reacts with halides (X=Cl, Br, I) in CH_2Cl_2 (Figure 8) to mainly afford mononuclear Mn^{III} complexes [Mn^{III}(LS)X] (**Mn^{III}X**) after several hours. Only [Mn(LS)I] (**Mn^{III}I**), as a dark violet species, has been fully studied thank to its particular stability among the series.

3.1.3. X-Ray characterization of **Co^{II}_2SS** and **Co^{III}X**.

A) X-Ray characterization of Co^{II}_2SS.

In order to obtain X-Ray suitable single crystals, diethyl ether was layered on a solution of **Co^{II}_2SS** in a solution of CH_2Cl_2:CH_3CN (9:1).

The X-ray structure of **Co^{II}_2SS** (Figure 9) displays a {Co_2S_2(SS)} core, with a disulfide binding the two Co^{II} ions in a cis-μ-1,2 mode. The slightly shorter Co-N distances in **Co^{II}_2SS** in are consistent with the +II oxidation state for both Co ions. A C2 axis is at the origin of the structural equivalence of the two Co^{II} centers. Each Co^{II} ion displays a highly distorted square-pyramidal geometry, with two N atoms and two μ-S atoms of the ligand forming the square planar base and one S atom of the disulphide bridge in axial position. As expected, the axial Co^{II}-$S_{S\text{-}S}$ bond (2.5341(8) Å) is significantly longer than the basal Co^{II}-(μ-$S_{thiolate}$) bonds (2.3796(8) and 2.3272(7) Å), the latter being in the expected range (2.21–2.39 Å).[31] The long distance between the two Co ions (3.1188(5) Å) implies the absence of a direct metal–metal bond. Selected bond distances and angles are listed in Table 2.

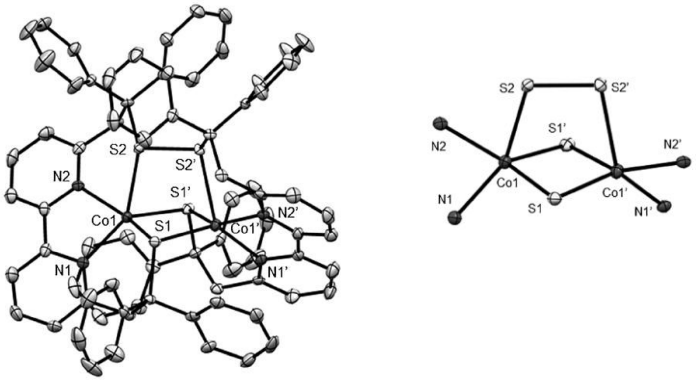

Figure 9: ORTEP-type views (thermal ellipsoids set at 30% probability, hydrogen atoms removed for clarity) of **Co^{II}_2SS** (left) and the binuclear {$N_4Co_2S_2$(SS)} core of **Co^{II}_2SS** (right).

Table 2. Selected bond lengths (Å) and angles (°) of **Co^{II}_2SS**.

$Co^{II}_2SS.(PF_6)_2.CH_3CN$			
	Bond distances (Å)		**Angle (°)**
Co(1)-N(1)	2.072(2)	N(1)-Co(1)-N(2)	78.92(9)
Co(1)-N(2)	2.111(2)	N(1)-Co(1)-S(1)	91.80(6)
Co(1)-S(1)	2.3795 (7)	N(1)-Co(1)-S(1)'	133.34(7)
Co(1)-S(1)'	2.3272(8)	N(1)-Co(1)-S(2)	137.88 (6)
Co(1)-S(2)	2.5342(8)	N(2)-Co(1)-S(1)	144.91(6)
S(1)-S(2)	2.0242(13)	N(2)-Co(1)-S(1)'	113.77(6)
		N(2)-Co(1)-S(2)	83.90(6)
		S(1)-Co(1)-S(2)	81.41(3)
		S(1)'-Co(1)-S(2)	88.78(3)

B) X-Ray characterization of $Co^{III}X$ (X=Cl, Br, I).

The X-ray structures of complexes **$Co^{III}Cl$**, **$Co^{III}Br$** and **$Co^{III}I$** (Figure 10 and Table 3) show that the three compounds are isostructural. In **$Co^{III}Br$** and **$Co^{III}I$** as in the case of **$Co^{III}Cl$**, the N2S2 coordination sphere insured by L^{2-} is completed by the halide anion, leading to a distorted square pyramidal geometry around the Co^{III} ion. The two nitrogen and two sulfur atoms of L^{2-} are located in the equatorial plane, whereas the halide ion occupies the axial position. The Co^{III} ion is shifted approximately 0.485 Å, 0.464 Å and 0.435 Å from the mean equatorial plane (formed by N2S2) toward the axial halide ligand in **$Co^{III}Cl$**, **$Co^{III}Br$** and **$Co^{III}I$**, respectively. The equatorial Co-N and Co-S bond lengths are not sensitive to the nature of the halide (less than 3.5 pm of difference), whereas the Co-X distance increases significantly from **$Co^{III}Cl$** to **$Co^{III}I$** (2.3336(5) Å, 2.4888(7) Å and 2.6938(18) Å, respectively). The Co-S and the Co-N bond distances in all complexes are slightly shorter than those in **Co^{II}_2SS**, consistent with the difference of the ionic radii for Co^{II} and Co^{III}. The valence angles of the equatorial plane evidence strong distortions in the plane as attested by the S1-Co-N2 and S2-Co-N1 angles of 142.15(4)° and 163.72(5)° in **$CoI^{II}Cl$**, 143.48(9)° and 164.65(9)° in **$Co^{III}Br$** and 145.7(3)° and 165.6(3)° in **$Co^{III}I$**. From these two angles, the index of the degree of trigonality of a penta-coordinated geometry can be determined by the τ_5 which has been already described in chapter II. The τ_5 values are 0.360, 0.353 and 0.332 for **$Co^{III}Cl$**, **$Co^{III}Br$** and **$Co^{III}I$**, respectively, in agreement with a distorted square pyramidal geometry in all cases.

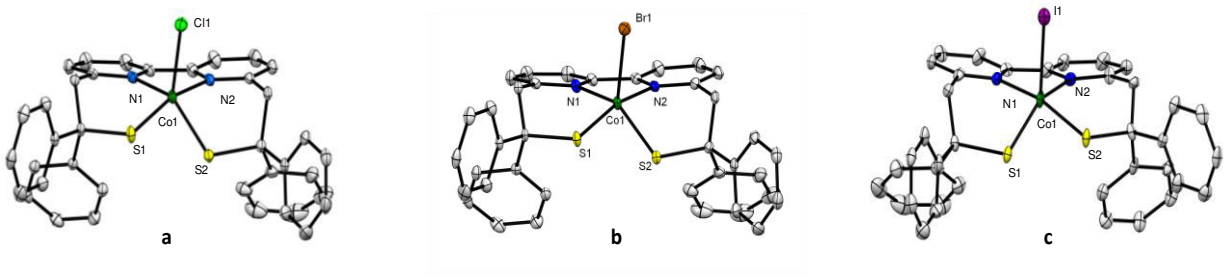

Figure10. ORTEP-type views of (a) **Co^{II}Cl**, (b) **Co^{III}Br**, (c) **Co^{III}I** (thermal ellipsoids set at 30% probability, hydrogen atoms removed for clarity)

Table 3. Structural properties of **CoX** with X = I, Br, Cl.

	Co^{III}Cl[a]	**Co^{III}Br**	**Co^{III}I**
Co-S1	2.1957(5)	2.1898(10)	2.178(3)
Co-S2	2.2056(5)	2.1984(9)	2.187(3)
Co-N1	1.9915(14)	1.993(3)	1.984(8)
Co-N2	2.0267(14)	2.022(3)	2.016(8)
Co-X	2.3336(5)	2.4888(7)	2.6938(18)
S1-Co-S2	78.427(19)	78.60(4)	78.91(12)
S1-Co-N1	92.57(5)	93.01(9)	93.9(3)
S1-Co-N2	142.15(4)	143.48(9)	145.7(3)
S2-Co-N1	163.72(5)	164.65(9)	165.6(3)
S2-Co-N2	97.73(4)	98.14(8)	98.2(3)
N1-Co-N2	80.99(6)	80.88(11)	80.6(4)
S1-Co-X	118.80(2)	118.34(3)	118.41(10)
S2-Co-X	104.64(2)	103.25(3)	101.86(10)
N1-Co-X	91.57(4)	92.03(8)	92.5(2)
N2-Co-X	98.73(4)	97.93(9)	95.7(3)

[a] *data issued from*[6]

3.1.4 X-Ray characterization of **Mn$^{II}_2$SS** and **Mn^{III}I**.

*A) X-Ray characterization of **Mn$^{II}_2$SS**.*

The single crystal X-ray structures of **Mn$^{II}_2$SS**.2CH_3CN and **Mn^{III}I** are shown in Figure 11, while selected bond distances are collected in Table 4. X-Ray suitable orange-yellow single crystals have been obtained in the presence of few drops of acetonitrile in CH_2Cl_2 after slow diffusion of diethyl ether. The **Mn$^{II}_2$SS** complex (Figure 11, left) consists in a μ-1,2-dimercapto-bridged dinuclear Mn^{II} complex containing a rare example of $\{Mn_2S_2(SS)\}$ core. Such of an arrangement has been previously found only in a few carbonyl disulphide Mn^{I}_2 complexes.[7, 9] This new complex is isostructural to the described Co^{II}-parent compound, **Co$^{II}_2$SS**, displaying the same symmetry.[6] As in the case of **Co$^{II}_2$SS**, the disulphide remains coordinated to the metal ions despite the fact that only a weak interaction is expected between a disulphide and d^5 Mn^{II} ions. The $\{Mn_2S_2\}$ plane is quasi planar (deviation from the S1Mn1S1'Mn1' plane is less than 0.059 Å and the angle between the S1Mn1S1' and S1Mn1'S1'

planes is 8.53°). The Mn sites are equivalent because of a C_2 symmetry axis, orthogonal to the average $\{Mn_2S_2\}$ plane. The manganese ions are not involved in a direct metal-metal interaction (Mn…Mn distance of 3.1469(10) Å). Each manganese site is penta-coordinated surrounded by an N2S3 donor set in a distorted square pyramidal geometry with a τ_5 value of 0.07.[10]

While the plane is defined with the four donor-atoms of one LS^- unit of LSSL, the axial position is occupied by the $S_{thiolate}$ atom of the second LS^- unit. A larger distortion from the square pyramidal geometry is observed in the isostructural Co complex with a τ_5 value of 0.13. All metal-ligand distances are slightly longer in the Mn derivative (in the range 8 pm - 16 pm) in comparison with the Co analogue, in agreement with the periodic table trend, as well as the S-S bond (2.0357(17) Å vs 2.0243(13) Å in the Co complex). **Mn^{II}_2SS** displays structural properties also similar to those of **Mn^{II}_2SH**, except the fact that the terminal Mn-bound sulphurs have been oxidized into a disulphide bridge in **Mn^{II}_2SS**. The short S2-S2' distance of 2.0357(17) Å is typical of a disulphide bond and is remarkably shorter than in the reported complexes containing a $\{Mn^{I}_2S_2(SS)\}$ core (between 2.206 Å and 2.224 Å).[7, 9a, b] The Mn1(1')-S2(2') bond lengths (2.6947(10) Å) are comparable to those of the Mn-S(H) bond found in **Mn^{II}_2SH** (2.6462(10) Å).

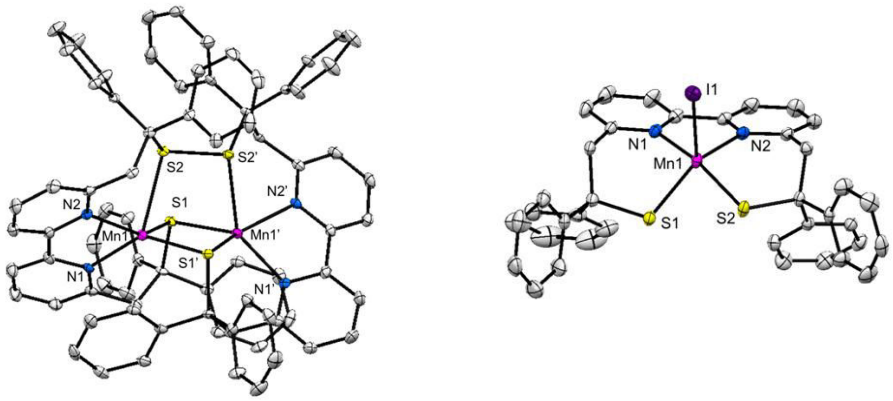

Figure 11. Molecular structure of **Mn^{II}_2SS**·$2CH_3CN$ (left) and **Mn^{III}I** (right). The thermal ellipsoids are drawn at 30% probability level. All hydrogen atoms, counter anions and solvent molecules are omitted for clarity.

B) X-Ray characterization **Mn^{III}I**.

X-Ray suitable dark-violet crystals were obtained in CH_2Cl_2 after slow diffusion of di-isopropylether.

The X-ray structure of the mononuclear **Mn^{III}I** complex (Figure 11, right) shows that the Mn^{III} ion is penta-coordinated, centered around a distorted square pyramidal N_2S_2I coordination sphere with the two N and two S atoms of the LS ligand located in the equatorial plane and the I^- ion occupying the axial position. Mononuclear penta-coordinated Mn^{III} complexes are quite uncommon, and mainly obtained in the presence of salen,[11] porphyrin[12] or cyclam[13] supporting ligands. The **Mn^{III}I** complex is isostructural to the previously described Co^{III} parent **Co^{III}I**,[6] displaying the same symmetry. The Mn^{III}

ion is shifted approximately 0.489 Å from the mean N_2S_2 plane toward the axial I ligand, slightly more than in the case of the Co analogue (0.435 Å). The valence angles of the equatorial N_2S_2 plane evidence strong distortions in the plane as attested by the S1-Mn-N2 and S2-Mn-N1 angles of 144.21(12)° and 163.31(13)°. The corresponding τ_5 value[10] is 0.318, consistent with a slightly less distorted square pyramidal geometry with respect to the isostructural **Co^{III}I** complex (τ_5 =0.332).

Table 4. Selected bond lengths (Å) for **Mn^{II}_2SS**·$2CH_3CN$ and **Mn^{III}I**.

Mn_2SS·$2CH_3CN$		**MnI**	
Mn(1)-N(1)	2.151(3)	Mn(1)-N(1)	2.059(4)
Mn(1)-N(2)	2.194(3)	Mn(1)-N(2)	2.091(4)
Mn(1)-S(1)	2.4940(10)	Mn(1)-S(1)	2.2792(16)
Mn(1)-S(2)	2.6947(10)	Mn(1)-S(2)	2.2846(15)
Mn(1)-S(1)'	2.4340(9)	Mn(1)-I(1)	2.7450(12)
Mn(1)-Mn(1)'	3.1469(10)		
S(2)-S(2)'	2.0357(17)		

3.2. UV-Vis spectroscopic properties.

3.2.1. UV-Vis spectroscopy of **Co^{II}_2SS** and **Co^{III}X** complexes.

The UV-visible absorption spectra of the three **Co^{III}X** complexes recorded in CH_2Cl_2 display three main transitions 477-493 nm (1), 675-718 nm (2) and 804-857 nm (3) ranges (Figure 12 and Table 3). Both the energy and intensity of these features are sensitive to the nature of the axial halide in a similar manner. While their intensity notably increases from the chloride to the iodide derivative, their respective energy decreases. In particular, the energies of transitions (2) and (3) are noticeably more affected than that of (1) by the nature of the halide. TD-DFT calculations have been performed to assign these transitions (Table 5). A good agreement between the calculated and experimental data have been found and the observed tendencies have been reproduced. The two high-energy transitions (1 and 2) have been attributed to ligand to metal ion charge transfer transitions (LMCT), whereas the lower energy features (3) to a mixed d-d/intraligand charge transfer (ILCT) transition. Figure 12 clearly evidences the strong influence of the halide ligand on this last transition, with a larger contribution for the iodide with respect to the chloride or bromide.

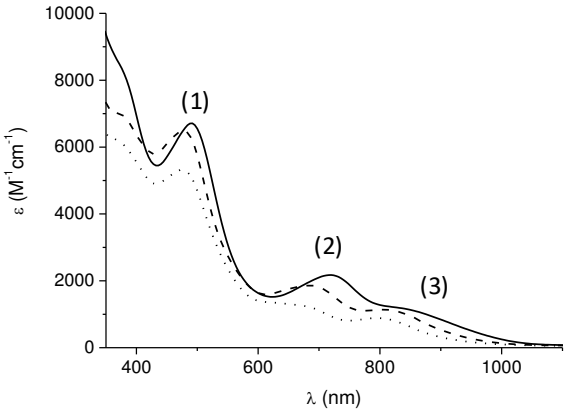

Figure 12. UV/Vis spectra of **Co^{III}Br** (---) and **Co^{III}I** (—), compared to that of **Co^{III}Cl** (····) (0.19 mM solutions in CH_2Cl_2, 1 cm path length, 20 °C, aerobic conditions).

Co^{III}Cl, λ = 760 nm **Co^{III}Br, λ = 798 nm** **Co^{III}I, λ = 862 nm**

Figure 13. Difference electron density sketches of transition (3) for **Co^{III}I, Co^{III}Br** and **Co^{III}Cl** (yellow = negative, red = positive).

Table 5. Experimental and TD-DFT calculated UV-Visible absorption properties of **Co^{III}X** with X = I, Br, Cl in CH_2Cl_2.

	λ_{exp} in nm (ε_{exp} in $M^{-1}cm^{-1}$)			λ_{calc} in nm (f_{calc})		
Co^{III}Cl[a]	477 (5318)[a]	675 (1250)[a]	804 (875)[a]	472 (0.056)	690 (0.026)	760 (0.009)
Co^{III}Br	486 (6400)	688 (1860)	814 (1135)	489 (0.050)	710 (0.034)	798 (0.004)
Co^{III}I	493 (6800)	718 (2250)	857 (1140)	508 (0.024)	741 (0.019)	862 (0.008)

[a] *data issued from* [6]

3.2.2. UV-Vis spectroscopy of **Mn$^{II}_2$SS** and **Mn^{III}I** complexes.

The electronic absorption spectrum of the light yellow solution of **Mn$^{II}_2$SS** displays no visible band in CH_2Cl_2 whereas the electronic absorption spectrum of the violet solution of **Mn^{III}I** shows a transition at 550 nm (ε =2250 $M^{-1}.cm^{-1}$) in the visible region and second less intense broad band at 870 nm. The transition at 550 nm can be attributed to a charge transfer band due its large epsilon value, while the other one to d-d a transition because of its low epsilon value (ε = 231 $M^{-1}.cm^{-1}$) involving both the

metal ion and the thiolate (Figure 14). Regarding **$Mn^{III}Br$** and **$Mn^{III}Cl$**, the UV-Vis absorption spectra are not available because of their lack of stability.

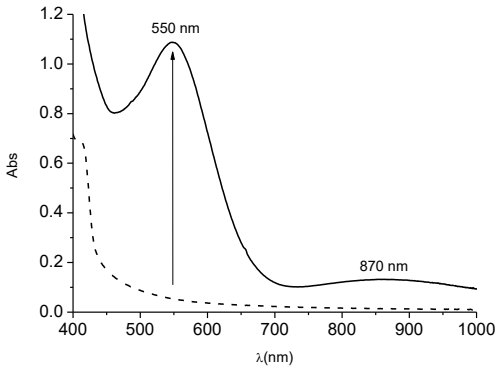

Figure 14. Electronic absorption spectra of **Mn^{II}_2SS** and **$Mn^{III}I$** complexes. (0.4 mM, solution in CH_2Cl_2, 1cm pathlength, 20°C, anaerobic conditions).

3.3. Magnetic properties.

3.2.1. Mn^{II}_2SS magnetic properties.

The magnetic properties of a powdered sample of **Mn^{II}_2SS** were studied between 1.8-300 K at 1000 Oe (Figure 15).

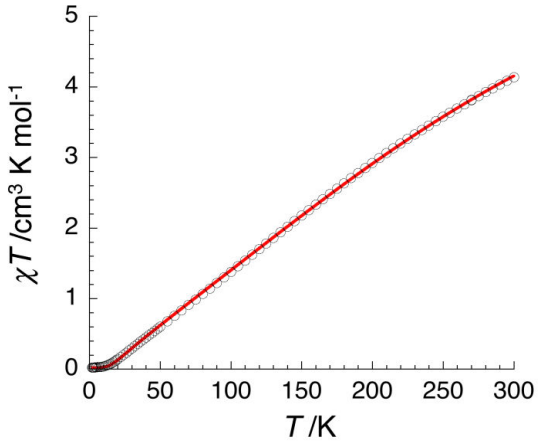

Figure 15. Temperature dependence of the χT product (where χ is the molar magnetic susceptibility equal to M/H per complex) measured at 1000 Oe for **Mn^{II}_2SS**. The solid line is the best fit of the experimental data to the isotropic S = 5/2 spin dimer model described in the text.

The steady decrease of χT product to nearly zero at 2 K suggests the presence of significant antiferromagnetic exchange occurring in the dinuclear complex, as in the case of the Co analogue, **Co^{II}_2SS**. The magnetic data were analysed in the frame of an isotropic spin-dimer Heisenberg model with the following Hamiltonian: $H = -2JS_AS_B$, assuming that the two metal ions are high spin Mn^{II} centres ($S_A = S_B = 5/2$). The resulting best fit for **Mn^{II}_2SS** is shown in Figure 15 with $g_A = g_B = 2.02(5)$ and J = -23(2) cm^{-1} (-33(3)K). This value is in excellent agreement with the calculated J value (J_{calc} = -23.5 cm^{-1}) for the optimized $[Mn^{II}_2(LSSL)]^{2+}$ complex. Thus, the bridging thiolate ligands mediate an

antiferromagnetic exchange interaction between the two Mn^{II} centres leading to a diamagnetic *S* = 0 ground spin state. Remarkably, the $\{Mn_2S_2\}$ core in **Mn^{II}_2SS** and **Mn^{II}_2SH** (*J* = -22 (1) cm^{-1}) leads to large magnetic couplings, such interactions between two Mn^{II} ions being generally low in magnitude (less than 15 cm^{-1}).[14] In the literature, the number of polynuclear Mn^{II} complexes with thiolate bridge(s) is limited and, to the best of our knowledge, the magnetic properties have been reported for only one of these, *i.e.* a linear trinuclear Mn^{II} complex with a mono μ-thiolato bridge between each Mn ion with a magnetic interaction estimated at -9.8 cm^{-1}.[15]

The magnetic susceptibility of **Mn^{II}_2SS** has been compared with the magnetic susceptibility of a powdered sample of **Co^{II}_2SS** studied between 1.8-300 K at 1000 oe.[6] The magnetic behaviour is consistent with the presence of two high spin Co^{II} ions (S=3/2). A strong anti-ferromagnetic coupling is observed with a *J* = -286(5) cm^{-1}, g = 2.37(5). The effective magnetic moment determined in CH_2Cl_2 solution of 3.77 μ_B at 20°C corresponding to a χT of 1.8 $cm^3.K.mol^{-1}$ is consistent with the magnetic properties measured on the powder. Once again, the bridging thiolate ligands mediate an antiferromagnetic exchange interaction between the two Co^{II} centres leading to a diamagnetic *S* = 0 ground spin state. The magnetic properties of mononuclear **Mn^{III}I** and **Co^{III}X** complexes will be discussed in chapter IV.

3.4. Reactivity with Iodide: disulphide/thiolate interconversion.

The reaction of the Mn^{II}–disulphide complex **Mn^{II}_2SS** with Bu_4NI gives a more stable Mn^{III}-thiolate adduct, **Mn^{III}I**, with respect to the chloride and bromide derivatives. We have thus thoroughly investigated this iodide-induced intramolecular redox process by UV-Vis absorption (Figure 16).

At 20 °C, the **Mn^{II}_2SS** complex (clear yellow solution) slowly reacts with Bu_4NI (2.5 eq.) in CH_2Cl_2 under argon to afford the **Mn^{III}I** complex (dark violet solution). The formation of **Mn^{III}I** is evidenced by the progressive increase in the absorbance of a visible band at 550 nm, a maximum amount of product being obtained after approximately 16 hours. **Mn^{III}I** is generated only in a ~30% yield, based on the epsilon value of **Mn^{III}I** at 550 nm (~2250 $M^{-1}cm^{-1}$). The further step was to investigate the backward process *i.e.* the possibility to regenerate the initial **Mn^{II}_2SS** complex by removing the iodide anion from **Mn^{III}I** *via* its reaction with $AgBF_4$.

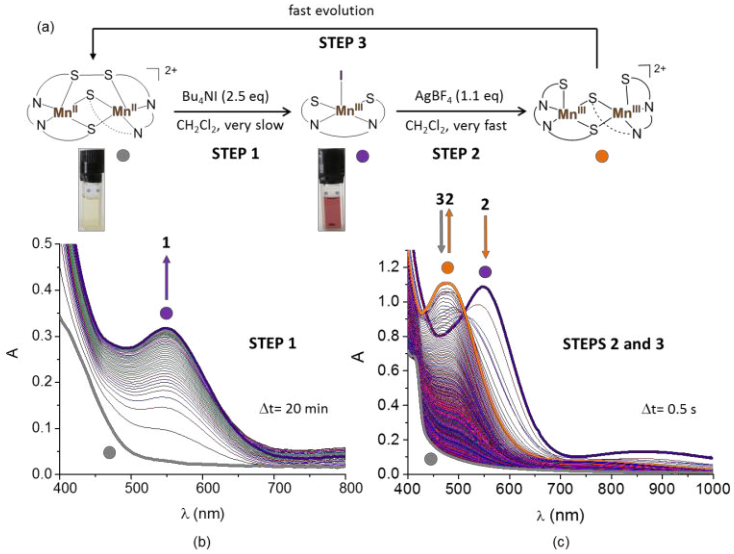

Figure16. UV-Vis spectral evolution of: (b) a **Mn^{II}_2SS** solution (0.5 mM) in CH_2Cl_2 after the addition of Bu_4NI (2.5 eq) to afford **$Mn^{III}I$** (0.5 cm path length); (c) a **$Mn^{III}I$** solution (0.5 mM) in CH_2Cl_2 after the addition of $AgBF_4$ (1.1 eq, 0.1 M in MeCN), to recover **Mn^{II}_2SS** (1.0 cm path length). The experimental data are rationalized in (a).

For **$Mn^{III}I$** complex the process is completely reversible, as the addition of a stoichiometric amount of $AgBF_4$ is sufficient to quantitatively regenerate the corresponding dinuclear **Mn^{II}_2SS** complex. This reversibility is attested by the complete disappearance of any feature typical of M^{III} ions in the respective final visible spectra and by the concomitant appearance of a vibration at ~558 cm^{-1} in both infrared spectra, assigned to the S-S vibrational stretching mode of **M^{II}_2SS** (Figure 17).

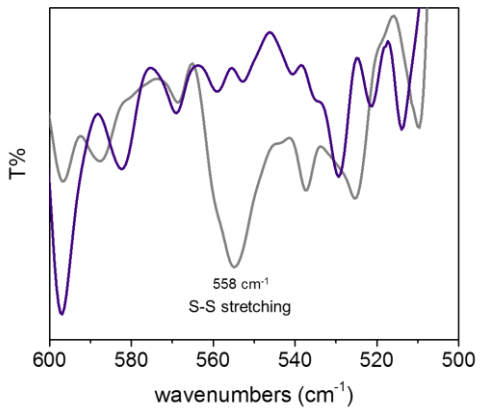

Figure 17. Infrared spectra of solid **Mn^{II}_2SS** (—) and **$Mn^{III}I$** (—) complexes (zoom in the 500-600 cm^{-1} spectral range).

The homologous process involving the isostructural **Co^{II}_2SS** complex (Figure 18) is much more efficient. Under comparable conditions (2.0 eq. of Bu_4NI in CH_2Cl_2 at 20 °C), the clear yellow solution of **Co^{II}_2SS** is converted immediately and quantitatively into a dark brown solution containing the Co^{III} iodide species, similarly to what happens to **Co^{II}_2SS** in the presence of chlorides.[6] However, with X = I, it should be noted that partial aggregation of **$Co^{III}I$** is observed in solution.

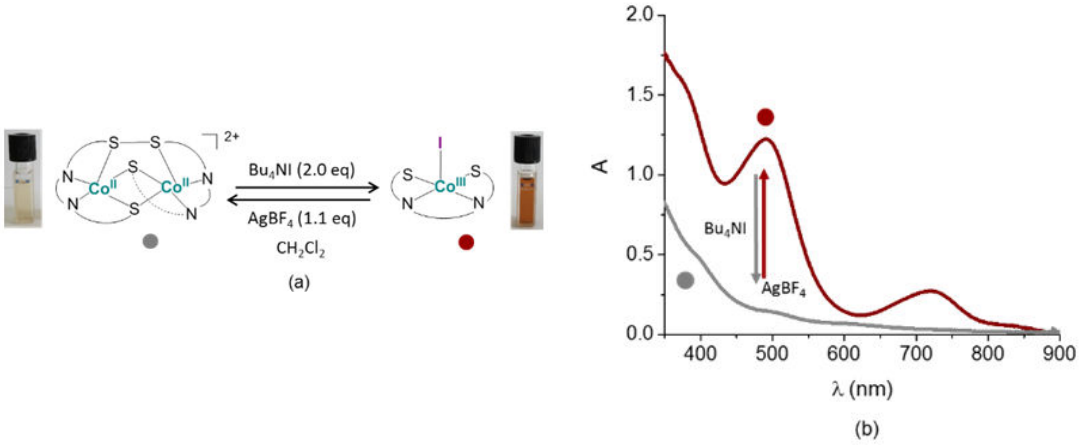

Figure 18. UV-visible absorption spectra (b) of **Co^{II}_2SS** (0.1 mM in CH_2Cl_2, 1.0 cm path length) recorded before (—) and (—) after the addition of Bu_4NI (2.0 eq), affording **Co^{III}I** immediately and quantitatively. The complete reversibility of the process is attested by the subsequent addition of $AgBF_4$ (1.1 equiv., 0.1 M in MeCN). The experimental data are rationalized in (a).

The formation of **Co^{III}I** is evidenced by the immediate increase in the absorbance of two visible bands at 495 nm and 718 nm and its formation is quantitative. Besides, the conversion of **Co^{III}I** into **Co^{II}_2SS** is direct and instantaneous in the presence of 1.1 eq of $AgBF_4$. This work has also been performed for the two others Co complexes **Co^{III}Br** and **Co^{III}Cl**[6]. The backward process with $AgBF_4$ is comparable for the three complexes, efficient and quantitative.

It is not the case for **Mn^{III}I**. In the conditions of Figure 16, the addition of $AgBF_4$ to a solution of **Mn^{III}I** leads to its conversion into a deep orange solution with a broad absorption band at ~475 nm in less than 5 seconds (step 2, Figure 16). This species corresponds to the previously described bis μ-thiolato dinuclear Mn^{III} complex with two terminal thiolate groups, **Mn^{III}_2** (Figure 6).[8] Then, **Mn^{III}_2** evolves in less than 6 minutes to its isoelectronic form, the dinuclear **Mn^{II}_2SS** complex (step 3, Figure 6), to fully complete the thiolate/disulphide cycle.

To understand the differences between both systems (Mn *vs* Co), further investigations have been carried out and especially electrochemistry studies.

3.5. Electrochemical properties.

The redox properties of the different complexes have been investigated by cyclic voltammetry (CV, Figure 19 and Table 5) in order to get insights on the feasibility of the M^{III}-thiolate/M^{II}-disulphide interconversion to occur for both the **Mn^{II}_2SS/Mn^{III}I** and **Co^{II}_2SS/Co^{III}I** systems. The CV of **Mn^{II}_2SS** displays an irreversible cathodic peak located at Ep_c = -1.17 V *vs* Fc^+/Fc. This redox signature can be attributed to the two-electron reduction of the disulphide bridge. Note that in the CV recorded immediately after addition of Bu_4NI (2.5 eq) to **Mn^{II}_2SS**, thus before its evolution into **Mn^{III}I**, the Ep_c

value remains unchanged suggesting that the possible coordination of iodide(s) to Mn^{II} has a negligible effect on the redox stability of the S-S bridge.

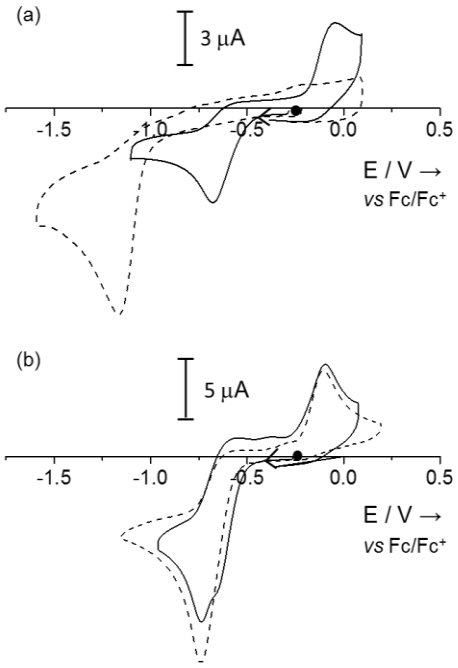

Figure 19. CVs of CH_2Cl_2 solutions (0.1 M Bu_4NPF_6) of (a) **Mn^{II}_2SS** (---, 0.5 mM) and **Mn^{III}I** (—, 0.4 mM), compared to (b) CVs of **Co^{II}_2SS** (---, 0.85 mM) and **Co^{III}I** (—, 1.4 mM).

Remarkably, the disulphide/thiolate redox system for the homologous **Co^{II}_2SS** complex is shifted 430 mV more positively (Ep_c = -0.74 V),[6] when compared to **Mn^{II}_2SS**. This implies a remarkable impact of the metal ion on the redox stability of the disulphide, the disulphide form being more stabilized when coordinated to Mn^{II} than to Co^{II}.

The CVs of both **M^{III}I** complexes display an irreversible metal-based reduction process. The CV of **Mn^{III}I** displays Ep_c = -0.68 V, promptly assigned to a one-electron Mn^{III}/Mn^{II} reduction. The anodic peak located at Ep_a = -0.04 V in the backward process is attributed to the oxidation of iodide released after the $Mn^{III} \rightarrow Mn^{II}$ reduction. The CV of **Co^{III}I** is more complicated. In this case, two reduction systems are observed, one at Ep_c = -0.66 V and one at Ep_c = -0.74 V. The ratio between the intensities of these two peaks varies with the concentration of complex, the first one slightly increasing under dilution. This is consistent with the presence of two species with different nuclearities in equilibrium, when **Co^{III}I** is dissolved in CH_2Cl_2. In this respect, two alternative equilibriums can be proposed:

$2[Co^{III}(LS)I] = [Co^{II}_2(LSSL)]^{2+} + 2I^-$ (Equation 1)

$2[Co^{III}(LS)I] = [Co^{III}_2(LS)_2I]^+ + I^- = [Co^{III}_2(LS)_2I_2]$ (Equation 2)

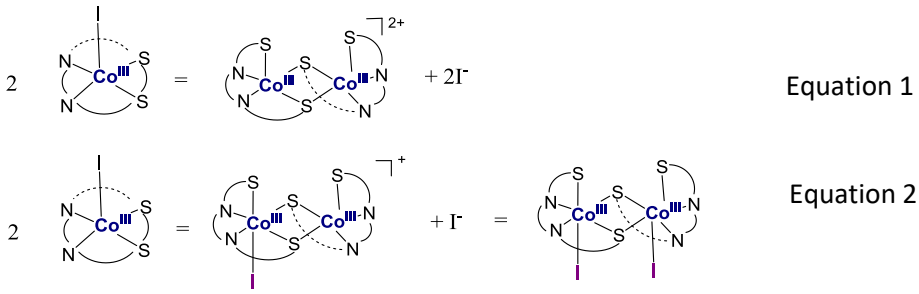

Figure 20. Illustration of equation 1 and equation 2.

The scenario illustrated in Equation 1 can be excluded as two equivalents of Bu_4NI are enough to fully convert $[Co^{II}_2(LSSL)]^{2+}$ into $[Co^{III}(LS)I]$. However, equilibrium described in Equation 2 is consistent with both the spectroscopic and redox properties of **Co^{III}I** complex. The peaks in the CV at Ep_c=-0.66 and -0.74 V can be assigned to the one-electron reduction process of $[Co^{III}(LS)]$ and the proposed $[Co^{III}_2(LS)_2I]^+$/$[Co^{III}(LS)_2I_2]$ species, respectively (Figure 20, Table 6).

Table 6. Cathodic peak potentials (Ep_c) for the **M^{II}_2SS** and **M^{III}I** complexes (M = Mn, Co), as determined from the corresponding CVs in CH_2Cl_2, 0.1 M Bu_4NPF_6. The anodic peak potentials (Ep_a) of the corresponding backward processes are also shown.

	Ep_c (Ep_a)
Mn^{II}_2SS	-1.17 (-)
Co^{II}_2SS	-0.74 (-0.10)[6]
Mn^{III}I	-0.68 (-0.04)
Co^{III}I	-0.66, -0.74 (-0.10)

3.6. Theoretical calculations.

DFT calculations were performed as a further contribution in the attempt to rationalize the different behaviour of the Co and Mn systems for the M^{II}_2-disulphide/M^{III}-thiolate conversion. Geometry optimizations were performed both on the $[M^{II}_2(LSSL)]^{2+}$ dinuclear complexes and on the corresponding monomers obtained by breaking the S-S bond, $[M^{III}(LS)]^+$ (Figure 21).

The resulting optimized geometries of $[Mn^{II}_2(LSSL)]^{2+}$ and $[Co^{II}_2(LSSL)]^{2+}$ compare well with the crystallographic data (maximum discrepancy of 0.12 Å and 0.16 Å[6] for coordination distances in the **Mn^{II}_2SS** and **Co^{II}_2SS** complexes, respectively,) thus validating our computational approach.

Regarding the optimized theoretical monomers, the Loedwin spin populations, which represent the charge distributions, are +1.82 and +4.05 for the Co and Mn centres, respectively. These results are consistent with M^{III}-thiolate complexes, theoretical values of 2 (Co^{III}, *S* = 1, two unpaired electrons) and 4 (Mn^{III}, *S* = 2, four unpaired electrons) being expected for isolated ions, respectively. On the other hand, the low Loedwin spin populations on the sulphur atoms (between -0.03and 0.09) are inconsistent with a thiolate radical character (Table 7).

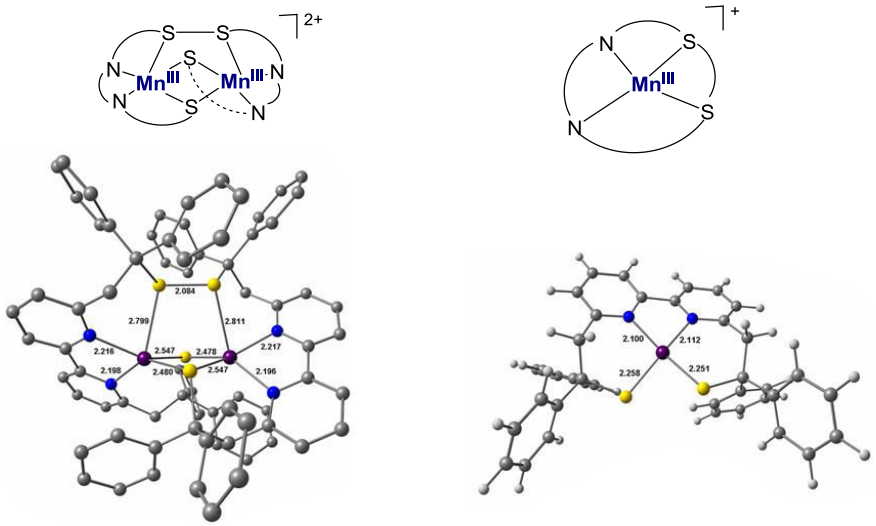

$[Mn^{II}_2(LSSL)]^{2+}$ (S=0) **$[Mn^{III}(LS)]^{+}$ (S=2)**

Figure 21. DFT-optimized structures of $[Mn^{II}_2(LSSL)]^{2+}$ (left) and $[Mn^{III}(LS)]^{+}$ (right).

Table 7. Loedwin spin population analysis for the DFT-optimized structures of $[M^{III}(LS)]^{+}$ and $[M^{II}_2(LSSL)]^{2+}$ (M = Mn, Co).[†]

Complex	M(1)	M(2)	S(1)	S(2)	S(3)	S(4)
$[Mn^{III}(LS)]^{+}$	4.05	-	-0.03	-0.03	-	-
$[Mn^{II}_2(LSSL)]^{2+}$	4.79	-4.78	0.01	0.01	-0.01	-0.01
$[Co^{III}(LS)]^{+}$	1.82	-	0.09	0.08	-	-
$[Co^{II}_2(LSSL)]^{2+}$	1.036	-1.030	0.16	0.01	-0.16	-0.01

[†]S(1) and S(3) are bridging sulphurs in the dinuclear complexes, while S(2) and S(4) are involved in the S-S bond.

These conclusions are confirmed by the analysis of the SOMOs of both complexes (Figure 22). The electronic spin density of the four SOMOs of $(Mn^{III}LS)^{+}$ is mainly localized on the metal from 87 % up to 95.6 %. In the same vein, the electronic spin density of the two SOMOs of $(Co^{III}LS)^{+}$ is also mainly localized on the metal, but in a much less manner (from 77 % to 84.4 %). Besides, the percentage of the SOMO of the sulphurs is about 10 times higher in the mononuclear Co unit, with respect to the Mn one. All these data suggest a stronger radical character of the sulphur in the Co complex why the Co complex is capable to form **Co^{II}_2SS** instantaneously in the presence of $AgBF_4$, while the reaction is much slower with the Mn complex.

The Gibbs free energy (ΔG^0 at 0 K) of the reaction in Equation 3 can be considered as a rough estimation of the driving force for M^{II}_2-disulphide/M^{III}-thiolate conversion.

$$[M^{II}_2(LSSL)]^{2+} = 2[M^{III}(LS)]^{+} \qquad \text{(Equation 3)}$$

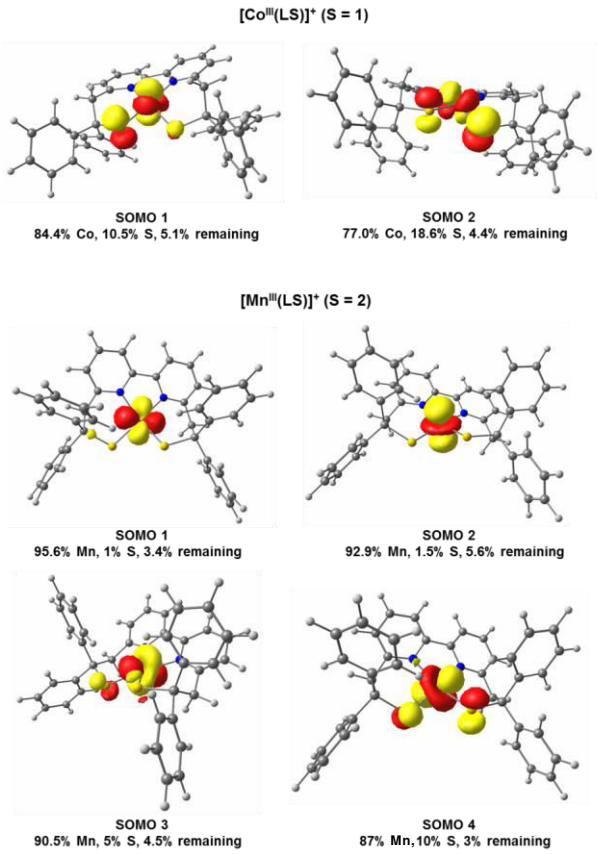

Figure 22. Localized SOMOs for $[Mn^{III}(LS)]^+$ (top) and $[Co^{III}(LS)]^+$ (bottom).

The computed values of ΔG^0 (0 K) are reported in Table 8, both in the gas-phase and in solution (CH_2Cl_2 medium) for M = Mn and Co. The dissociation of the Co^{II}_2-disulphide into two Co^{III}-thiolate units is highly exergonic (ΔG^0 = -15.1 kcal·mol^{-1} in CH_2Cl_2). The relative high stability of the monomeric $[Co^{III}(LS)]$ complex with respect to the corresponding dinuclear $[Co^{II}_2(LSSL)]^{2+}$ complex is in perfect agreement with the easy and efficient Co^{II}_2-disulphide to Co^{III}-thiolate conversion experimentally observed. In contrast, the computed ΔG^0 for the parent Mn system is positive (ΔG^0 = +7.9 kcal·mol^{-1} in CH_2Cl_2), in accordance with the low reactivity of the Mn-based system. Furthermore, the iodide coordination to the Mn^{III} ion quite stabilizes the mononuclear complex to allow the process to occur.

Table 8. Gibbs free energies (ΔG^0), computed at 0 K, for the reaction(s) in Equation 3, both in the gas-phase and in CH_2Cl_2 solution.

	ΔG^0 *in vacuum* (kcal·mol^{-1})	ΔG^0 *in* CH_2Cl_2 (kcal·mol^{-1})
$[Mn^{II}_2(LSSL)]^{2+} = 2[Mn^{III}(LS)]^+$	+3.6	+7.9
$[Co^{II}_2(LSSL)]^{2+} = 2[Co^{III}(LS)]^+$	-31.0	-15.1

Conclusion

In this Chapter, we report the first example of a reversible disulphide/thiolate interconversion, which involves manganese ions. As for the parent cobalt system, iodide coordination (or decoordination) to the metal ions induces disulphide to thiolate (thiolate to disulphide) conversion with concomitant metal oxidation (reduction). For both Mn and Co systems, the reversibility of the process seems to be favoured by the fact that the disulphide-bridge remains coordinated to the metal centres in **M^{II}_2SS**.

The conversion of **Mn^{II}_2SS** into **Mn^{III}I** is clearly less efficient (it occurs in a few minutes and partially) when compared with the corresponding evolution of **Co^{II}_2SS** into **Co^{III}I**, which is quantitative and instantaneous. The reverse reaction, initiated by removing the bound iodide, is also slower for the Mn complex. Indeed, the Mn^{II}_2-disulphide complex is not directly regenerated as in the case of **Co^{II}_2SS**, but it arises from evolution of its isoelectronic **Mn^{III}_2** form.

Due to the high structural similarity of the dinuclear Mn and Co complexes, the difference in reactivity (disulphide to thiolate conversion) between them should be related to their electronic and/or redox properties. With this respect, we have analysed and compared i) the electrochemical cathodic potential (Ep_c) values for **M^{II}_2SS** and **M^{III}I** species (Table 2) and ii) the calculated dissociation energies of the M^{II}_2-disulphide complexes into the corresponding M^{III}-thiolate monomers (Equation 3). The cathodic peak of **M^{II}_2SS** can be attributed to the reduction of the S-S bridge, while that of **M^{III}I** is assigned to the reduction of the metal ion (from M^{III} to M^{II}). Although the Ep_c values do not contain any direct thermodynamic information on the system (lack of redox reversibility), they give an indication on the feasibility of the internal redox process. In particular, in order to achieve disulphide/thiolate interconversion, the Ep_c values of the LSSL/2LS and M^{III}/M^{II} redox couples should be close enough to allow small structural modifications to address the direction of the internal electron transfer between the ligand and the metal ion. It is the case for the **Co^{II}_2SS/Co^{III}I** pair (see Table 2), which results of an efficient switchable system. The coordination of iodide decreases the redox potential of the Co^{III}/Co^{II} couple so that the Co^{II} ions can reduce the disulphide into thiolates groups. On the other hand, the redox potential of the LSSL/2LS couple for the Mn-based system is surprisingly much lower than for the Co-based one (-1.17 V and –0.74 V, respectively). Consequently, coordination of iodide might not sufficiently decrease the redox potential of the Mn^{III}/Mn^{II} couple: as a result, the disulphide/thiolate conversion cannot occur efficiently.

Dissociation energies of the M^{II}_2-disulphide complexes into the corresponding M^{III}-thiolate monomers calculated by DFT methods confirm the same trend. The process is exergonic for the Co system, whereas it becomes endergonic for the Mn system, confirming the higher stability of the disulphide bridge in **Mn^{II}_2SS** with respect to the Co analogue. The conversion of **Mn^{II}_2SS** to **Mn^{III}I** with such unfavourable thermodynamics can be explained by the fact that iodide coordination to the Mn^{III}-

thiolate fragment strongly stabilizes **Mn^{III}I** complex. In conclusion, this work represents an original contribution to improve the understanding of how the electronic and redox properties of the metal centres should be perfectly fine-tuned to allow a disulphide/thiolate (inter)conversion, mediated by metal ions, to occur efficiently.

References

1. a) C. E. Paulsen and K. S. Carroll, *Chem. Rev.* **2013**, *113*, 4633-4679; b) L. E. S. Netto, M. A. de Oliveira, G. Monteiro, A. P. D. Demasi, J. R. R. Cussiol, K. F. Discola, M. Demasi, G. M. Silva, S. V. Alves, V. G. Faria and B. B. Horta, *Comp. Biochem. Physiol. C Pharmacol. Toxicol. Endocrinol.* **2007**, *146*, 180-193; c) N. M. Giles, G. I. Giles and C. Jacob, *Biochem. Biophys. Res. Comm.* **2003**, *300*, 1-4.
2. a) L. Banci, I. Bertini, V. Calderone, S. Ciofi-Baffoni, S. Mangani, M. Martinelli, P. Palumaa and S. Wang, *Proc. Natl. Acad. Sci. USA* **2006**, *103*, 11814-11814; b) Y. C. Horng, S. C. Leary, P. A. Cobine, F. B. J. Young, G. N. George, E. A. Shoubridge and D. R. Winge, *J. Biol. Chem.* **2005**, *280*, 34113-34122; c) T. R. Cawthorn, B. E. Poulsen, D. E. Davidson, D. Andrews and B. C. Hill, *Biochemistry* **2009**, *48*, 4448-4454; d) B. C. Hill and D. Andrews, *Biochim. Biophys. Acta* **2012**, *1817*, 948-954.
3. a) K. Jomova and M. Valko, *Toxicology* **2011**, *283*, 65-87; b) J. T. Pedersen, C. Hureau, L. Hemmingsen, N. H. H. Heegaard, J. Ostergaard, M. Vasak and P. Faller, *Biochemistry* **2012**, *51*, 1697-1706; c) G. Meloni, P. Faller and M. Vasak, *J. Biol. Chem.* **2007**, *282*, 16068-16078; d) T. Finkel and N. J. Holbrook, *Nature* **2000**, *408*, 239-247; e) A. M. Thomas, B.-L. Lin, E. C. Wasinger, T. D. P. Stack, *J. Am. Chem. Soc.* **2013**, *135,* 18912 – 18919.
4. a) E. I. Stiefel in *Transition metal sulfur chemistry: Biological and industrial significance and key trends*, *Vol. 653* Eds.: E. I. Stiefel and K. Matsumoto), **1996**, pp. 2-38; b) S. C. Lee, W. Lo and R. H. Holm, *Chem. Rev.* **2014**, *114*, 3579-3600; c) R. H. Holm, P. Kennepohl and E. I. Solomon, *Chem. Rev.* **1996**, *96*, 2239-2314; d) C. G. Young, *J. Inorg. Biochem.* **2007**, *101*, 1562-1585.
5. a) Y. Ueno, Y. Tachi and S. Itoh, *J. Am. Chem. Soc.* **2002**, *124*, 12428-12429; b) A. Neuba, R. Haase, W. Meyer-Klaucke, U. Flörke and G. Henkel, *Angew. Chem. Int. Ed.* **2012**, *51*, 1714-1718; c) A. M. Thomas, B.-L. Lin, E. C. Wasinger and T. D. P. Stack, *J. Am. Chem. Soc.* **2013**, *135*, 18912-18919; d) E. C. M. Ording-Wenker, M. van der Plas, M. A. Siegler, S. Bonnet, F. M. Bickelhaupt, C. Fonseca Guerra and E. Bouwman, *Inorg. Chem.* **2014**, *53*, 8494-8504; e) E. C. M. Ording-Wenker, M. van der Plas, M. A. Siegler, C. Fonseca Guerra and E. Bouwman, *Chemistry – A European Journal* **2014**, *20*, 16913-16921.
6. M. Gennari, B. Gerey, N. Hall, J. Pécaut, M.-N. Collomb, M. Rouzières, R. Clérac, M. Orio and C. Duboc, *Angew. Chem. Int. Ed.* **2014**, *53*, 5318-5321.
7. W.-F. Liaw, C.-K. Hsieh, G.-Y. Lin and G.-H. Lee, *Inorg. Chem.* **2001**, *40*, 3468-3475.
8. M. Gennari, D. Brazzolotto, J. Pecaut, M. V. Cherrier, C. J. Pollock, S. DeBeer, M. Retegan, D. A. Pantazis, F. Neese, M. Rouzieres, R. Clerac and C. Duboc, *J. Am. Chem. Soc.* **2015**.
9. a) N. Begum, M. I. Hyder, S. E. Kabir, G. M. G. Hossain, E. Nordlander, D. Rokhsana and E. Rosenberg, *Inorg. Chem.* **2005**, *44*, 9887-9894; b) K. Hou and W. Y. Fan, *Dalton Trans.* **2014**, *43*, 16977-16980; c) H. Braunwarth, P. Lau, G. Huttner, M. Minelli, D. Günauer, L. Zsolnai, I. Jibril and K. Evertz, *J. Organomet. Chem.* **1991**, *411*, 383-394.
10. A. W. Addison, T. N. Rao, J. Reedijk, J. Vanrijn and G. C. Verschoor, *J. Chem. Soc., Dalton Trans.* **1984**, 1349-1356.
11. a) P. J. Pospisil, D. H. Carsten and E. N. Jacobsen, *Chem. Eur. J.* **1996**, *2*, 974-980; b) A. Berkessel, M. Frauenkron, T. Schwenkreis, A. Steinmetz, G. Baum and D. Fenske, *J. Mol. Catal. A: Chem.* **1996**, *113*, 321-342.

12. a) W. R. Scheidt, Y. J. Lee, W. Luangdilok, K. J. Haller, K. Anzai and K. Hatano, *Inorg. Chem.* **1983**, *22*, 1516-1522; b) M. M. Williamson and C. L. Hill, *Inorg. Chem.* **1986**, *25*, 4668-4671.
13. A. De, *J. Crystallogr. Spectrosc. Res.* **1990**, *20*, 279-284.
14. a) K. Wieghardt, *Angew. Chem. Int. Ed. Engl.* **1989**, *28*, 1153-1172; b) J. Wu, J. E. Penner-Hahn and V. L. Pecoraro, *Chem. Rev.* **2004**, *104*, 903-938; c) S. Blanchard, G. Blain, E. Riviere, M. Nierlich and G. Blondin, *Chem. Eur. J.* **2003**, *9*, 4260-4268.
15. M. Mikuriya, F. Adachi, H. Iwasawa, M. Handa, M. Koikawa and H. Okawa, *Bull. Chem. Soc. Jpn.* **1994**, *67*, 3263-3270.
16. O. V. Dolomanov, L. J. Bourhis, R. J. Gildea, J. A. K. Howard and H. Puschmann, *J. Appl. Crystallogr.* **2009**, *42*, 339-341.
17. L. Palatinus and G. Chapuis, *SUPERFLIP program*, J. Appl. Cryst., 40, 2007, 786-790, **2007**, p.
18. G. M. Sheldrick in *SHELXTL-Plus, Structure Determination Software Programs, (Version 6.14.) Bruker Analytical X-ray Instruments Inc.*, *Vol.* Madison, Wisconsin, USA, **1998**.
19. F. Neese, *Wiley Interdiscip. Rev. Comput. Mol. Sci.* **2012**, *2*, 73-78.
20. a) J. P. Perdew, *Phys. Rev. B* **1986**, *33*, 8822-8824; b) J. P. Perdew, *Phys. Rev. B* **1986**, *34*, 7406-7406; c) A. D. Becke, *Phys. Rev. A* **1988**, *38*, 3098-3100.
21. A. Schäfer, C. Huber and R. Ahlrichs, *J. Chem. Phys.* **1994**, *100*, 5829-5835.
22. F. Neese, *J. Comput. Chem.* **2003**, *24*, 1740-1747.
23. F. Weigend, *PhysChemChemPhys* **2006**, *8*, 1057-1065.
24. A. Klamt and G. Schürmann, *J. Chem. Soc., Perkin Trans. 2* **1993**, 799-805.
25. a) A. D. Becke, *J. Chem. Phys.* **1993**, *98*, 5648-5652; b) C. T. Lee, W. T. Yang and R. G. Parr, *Phys. Rev. B* **1988**, *37*, 785-789.
26. a) L. Noodleman, *J. Chem. Phys.* **1981**, *74*, 5737-5743; b) L. Noodleman and D. A. Case, *Adv. Inorg. Chem.* **1992**, *38*, 423-+; c) L. Noodleman and E. R. Davidson, *Chem. Phys.* **1986**, *109*, 131-143.
27. a) T. Soda, Y. Kitagawa, T. Onishi, Y. Takano, Y. Shigeta, H. Nagao, Y. Yoshioka and K. Yamaguchi, *Chem. Phys. Lett.* **2000**, *319*, 223-230; b) K. Yamaguchi, Y. Takahara and T. Fueno, *Applied Quantum Chemistry* **1986**, 155-184.
28. a) W. Heisenberg, *Z. Phys.* **1928**, *49*, 619-636; b) P. A. M. Dirac, *Proc. Roy. Soc.* **1929**, *A123*, 714; c) J. H. Van Vleck in Oxford University: London, **1932**, p. 384; d) W. Heisenberg, *Z. Physik* **1926**, *38*, 411-426.
29. a) P. S. Donnelly, , A. Caragounis, , T. Du, , K. M. Laughton, , I. Volitakis, , R. A. Cherny, , R. A. Sharples, , A. F. Hill, , Q. X. Li, and C. L. Masters,. **2008**, *J. Biol. Chem. 283*, 4568−4577. b) C. Opazo, X. Huang, R.A. Cherny, R. D. Moir, A. E. Roher, A. R. White, R. Cappai, C. L. Masters, R. E. Tanzi, N. C. Inestrosa, and A. I. Bush, *Journal of Biological Chemistry*, **2002**, *277*, 40302-40308.
30. R. Roychaudhuri, M. Yang, M. M Hoshi, and Teplow, D. B. **2009**, *J. Biol. Chem. 284,* 4749−4753.
31. a) H. N. Rabinowitz, K. D. Karlin, S. J. Lippard, *J. Am. Chem.Soc*. **1977**, *99*, 1420 – 1426; b) C. A. Ghilardi, C. Mealli, S. Midollini, V. I. Nefedov, A. Orlandini, L. Sacconi, *Inorg.Chem.* **1980**, *19*, 2454 – 2462; c) K. S. Hagen, R. H. Holm,*Inorg. Chem*. **1984**, *23*, 418 – 427; d) D. Bonnet, P. Leduc, E.Bill, G. Chottard, D. Mansuy, I. Artaud, Eur. J. *Inorg. Chem.* **2001**, 1449 – 1456; e) X. Xu, G. Jiao, H. Sun, X. Li, Z. *Anorg.Allg. Chem*. **2011**, *637*, 430 – 435.

Chapter IV

An Experimental and Theoretical Investigation on Penta-coordinated Cobalt (III) complexes with an Intermediate spin state *S* = 1, respectively: How Halide Ligands Affect their Magnetic Anisotropy.

Table of contents

Résumé 152

Introduction 156

Results 159

4.1. Synthesis, structures and characterizations. 159

4.2. Magnetic properties of **$M^{III}X$ (M=Mn** or **Co**, **X= Cl, Br, I)**. 159

4.2.1. Magnetic properties of **$Mn^{III}I$**. 159

4.2.2. Magnetic properties of **$Co^{III}X$** (X=Cl, Br, I). 160

4.3. Quantum chemical calculations. 162

4.3.1. Optimized structure of **$Co^{III}X$** (X = Cl, Br, I). 162

4.3.2. Prediction of the spin state of $Co^{III}X$ (X = Cl, Br, I). 162

4.3.3. Electronic structure of **$Co^{III}X$** (X = Cl, Br, I). 163

4.3.2. Prediction of the *zfs* of **$Co^{III}X$** (X = Cl, Br, I). 165

Discussion and conclusion 167

References 169

Résumé

Comprendre les facteurs qui contrôlent les ordres de grandeurs et la symétrie de l'anisotropie magnétique devrait faciliter la conception de complexes métalliques mononucléaires dans le but de synthétiser des aimants moléculaires (Single-Molecular Magnets, SMMs), à haute température de blocage et avec de grandes barrières énergétiques.[1] La température de blocage correspond à la température à laquelle le temps pris pour mesurer l'aimantation est égal au temps de relaxation. En dessous de cette température, l'aimantation est comme bloquée à l'échelle de la mesure.

Les SMMs peuvent être classés selon différents critères : (i) le bloc de la classification périodique du métal (bloc d ou f), (ii) le nombre d'ions métalliques et (iii), le type de ligand. Une des propriétés les plus importantes des SMMs est l'anisotropie magnétique. Elle se définit comme le moment magnétique d'une seule molécule orientée, ne dépendant pas d'un champ magnétique externe et conduisant à une magnétisation propre. Les propriétés magnétiques des SMMs peuvent disparaitre si l'orientation du moment magnétique est inversée. Pour empêcher ce phénomène, une barrière énergétique thermique doit être surmontée (U_{eff}). U_{eff} sert à comparer les différents SMMs : plus la barrière est grande, plus les propriétés magnétiques de ces molécules seront intéressantes pour des applications potentielles. Dans la plupart des cas, l'anisotropie est déterminée à partir de la mesure de la susceptibilité magnétique (χ) dans un champ magnétique.[57] Ainsi, en 1993, une toute nouvelle aire de recherche a émergé après la découverte des propriétés exceptionnelles du fameux cluster $[Mn_{12}O_{12}(CH_3CO_2)_{16}(H_2O)_4]$[1] qui se comporte comme une molécule aimant, premier SMM décrit dans la littérature.

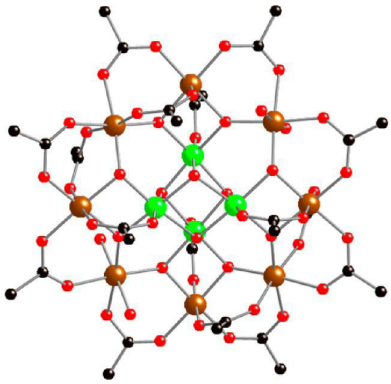

Figure 1. Structure moléculaire de $[Mn_{12}O_{12}(OAc)_{16}(H_2O)_4]$.[57]

Durant les premières décennies qui ont suivi cette découverte, le défi chimique était de concevoir et de synthétiser des SMMs avec les plus hautes températures de blocage possible (T_B). T_B est associée à la barrière énergétique (U_{eff}) qui doit être surmontée pour inverser le moment magnétique, avec

$U_{eff} = |D|S^2$ (*S* étant le spin de l'état fondamental et *D* l'écart en champ nul ou zero-field splitting (*zfs*) défini par l'Hamiltonien : $H = DS_z^2$).

D'importants efforts en chimie théorique ont également été entrepris pour développer des méthodologies permettant d'évaluer le paramètre *zfs* d'un système donné en déterminant les origines physiques de l'anisotropie magnétique. On peut ainsi comparer les prédictions théoriques aux résultats expérimentaux.[15] Pour de telles investigations, il est nécessaire de calculer précisément les deux contributions du *D* : (i) le couplage spin-spin (D_{SS}), ou l'interaction entre deux électrons non appariés, et (ii) le couplage spin-orbite (D_{SOC}) qui provient du mélange entre l'état fondamental et les états excités. Dans ce contexte, les calculs de la Théorie de la Fonctionnelle de la Densité (DFT : density functional theory) ont été utilisés pour prédire le signe et l'ordre de grandeur de *D*. Bien que les valeurs calculées soient généralement sous-estimés,[16-19] sauf dans le cas où des halogénures sont coordonnés au métal,[20,21] de tels calculs sont essentiels pour comprendre les résultats expérimentaux en définissant les différents facteurs qui contribuent à la valeur de *D*. D'autres approches, comme la méthode CASSCF (Complete Active Space Self-Consistent Field)[19,23-27] permet de calculer des valeurs de *D* cohérentes aux résultats expérimentaux mais cette approche est beaucoup plus couteuse en temps de calculs. En utilisant ces différentes approches théoriques, plusieurs travaux combinant des mesures expérimentales et des calculs théoriques ont été publiés utilisant différents métaux de transition tels que Mn^{II},[28,29] Mn^{III},[19] Ni^{II},[20,30-32] Fe^{II},[33] Co^{II},[34] ou V^{III}.[24] Toutes ces études nous montrent que chaque cas doit être traité indépendamment des autres et qu'aucune règle générale ne peut être appliquée pour définir la meilleure stratégie pour prédire *D*. Ainsi, pour chaque ion métallique, à différents degrés d'oxydation et d'états de spin, des études systématiques doivent être menées sur une série de complexes de référence.

Depuis qu'il a été démontré que D_{SOC} représente la contribution la plus importante à la valeur de *D* pour des métaux de transition, les chercheurs se sont intéressés à la nature du ligand ainsi qu'à des métaux qui présentent un large couplage spin-orbite (SOC). En ce qui concerne les ligands, l'effet du SOC des halogénures a été très fortement étudié. Il a été souvent observé que la valeur de *D* augmente des dérivés chlorés au dérivés iodés : séries de complexes bas-spin spin Cr^{II} et Cr^{III},[35] ou haut spin Mn^{II},[29,36] et Co^{II}.[37-40] Quant aux ions métalliques, les complexes de Co^{III}, majoritairement ceux en géométrie plan carré peuvent présenter un état de spin intermédiaire $S = 1$ particulièrement intéressants du à leur large *D* (jusqu'à 145 cm^{-1}).[41-43] Cependant, bien que les complexes penta-coordonnés de Co^{III} ont généralement un spin $S = 2$, il existe une seule exception d'un complexe haut spin à géométrie bipyramide trigonale distordue qui présente une valeur de *D* de +107 cm^{-1}.[44]

Dans le chapitre III, des complexes penta-coordonnés de Co^{III}, **$Co^{III}Cl$**, **$Co^{III}Br$**, **$Co^{III}I$** ont été décrits (Figure 2). Au sein de ce chapitre, nous allons nous concentrer sur leurs propriétés magnétiques et comment celles-ci peuvent être rationnalisées par des calculs théoriques.

Ces trois complexes, **$Co^{III}Cl$**, **$Co^{III}Br$**, **$Co^{III}I$**, ont été synthétisés et leurs structures ont été caractérisées par diffraction des rayons X. Ces trois composés sont isostructuraux. Leur sphère de coordination pentacoordonnée présente une géométrie de type pyramide à base carrée, où l'halogénure est localisé en position axiale sur le Co^{III}. (Figure 2)

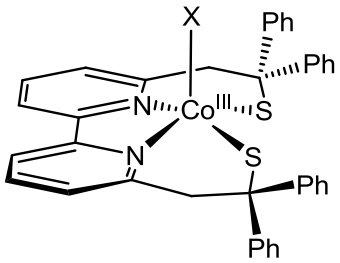

Figure 2. Complexes de **$Co^{III}X$** (X = Cl, Br, I)

La susceptibilité magnétique pour les trois complexes est constante vers environ 30-50 K, ce qui est cohérent avec des complexes de Co^{III} de spin S = 1. A basse température, les valeurs de χT affichent une nette diminution, expliquée par la présence d'un large *zfs*. Des valeurs du facteur g largement supérieur à 2 (2.27(5), 2.17(5) and 2.28(5)), et des valeurs de D positives de 35(1) cm^{-1}, 26(1) cm^{-1} et 18(1) cm^{-1} ont été obtenues respectivement, pour **$Co^{III}Cl$**, **$Co^{III}Br$** et **$Co^{III}I$**, ce qui est contraire à ce qui est attendu. Les larges valeurs de g mettent en évidence une importante contribution spin-orbite, en accord avec la présence d'une forte anisotropie magnétique. Les propriétés magnétiques ont également été étudiées en solution par la méthode Evans et sont cohérentes avec les mesures de susceptibilité magnétique réalisées sur poudre. (Figure 3)

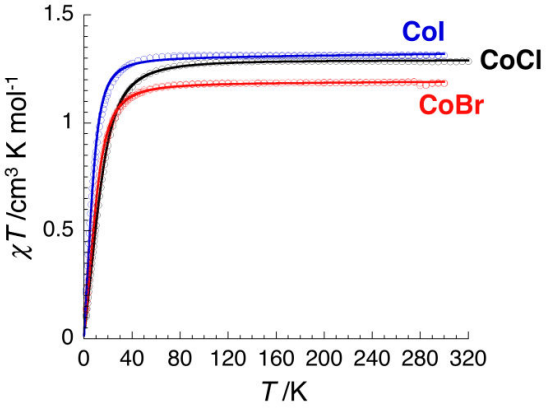

Figure 3. Dépendance de la température de χT (où χ est la susceptibilité magnétique molaire égale à M/H par complexe de cobalt) mesuré a 0.1 T pou **$Co^{III}Cl$** (O), **$Co^{III}Br$** (O) and **$Co^{III}I$** (O). Les lignes en trait plein représentent les meilleures simulations des mesures expérimentales.

Pour essayer de rationaliser cette tendance, des calculs théoriques basés des méthodes DFT et sur des méthodes CASSCF ont été utilisées avec succès. A un certain niveau d'analyse, nous avons été capables de mettre en évidence une corrélation magnéto-structurale. **$Co^{III}Cl$** présente une géométrie pyramidale à base carrée qui est la plus distordue de la série (τ_5 élevé et un déplacement du métal en dehors du plan équatorial plus grand). Ceci conduit à une déstabilisation de la SOMO (orbitale moléculaire simplement occupée) et une faible différence d'énergie avec la VMO (orbitale moléculaire virtuelle), expliquant l'accessibilité à un état quintuplet en tant que premier état excité. De manière cohérente, pour le complexe de **$Co^{III}Cl$**, la différence d'énergie entre la SOMO et la DOMO (orbitale moléculaire doublement occupée), devient plus petite, favorisant la transition vers un état excité de même état de spin (α→α et β→β) (Figure 4), contribution majoritaire à *D* pour **$Co^{III}Cl$**. Contrairement à **$Co^{III}Cl$**, le complexe de **$Co^{III}I$** présente la géométrie la moins distordue et la DOMO la plus stabilisée, de telle sorte que la principale contribution à D_{SOC} vient des contributions « spin-flip » (α→β) conduisant au spin *S*-1. De manière cohérente, le premier état excité calculé correspond à un singulet. **$Co^{III}Br$** représente un cas intermédiaire. (Figure 4)

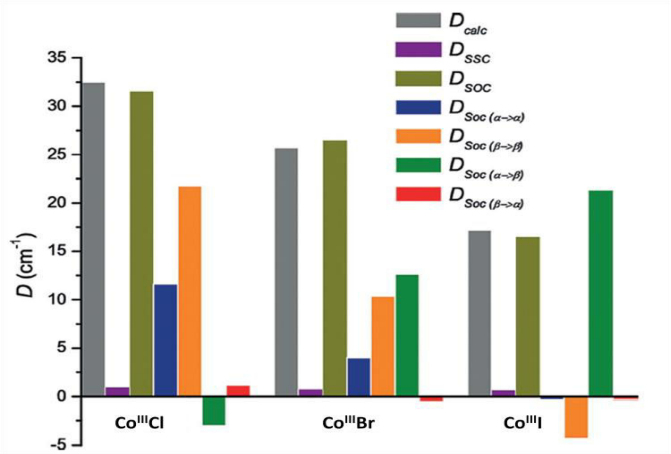

Figure 4. Contributions individuelles du *zfs* calculées par DFT pour les complexes **$Co^{III}X$** avec X=I, Br, Cl.

Finalement, cette étude montre que les méthodes de DFT et de CASSCF sont des outils puissants pour non seulement prédire le signe mais aussi les valeurs de *D* pour des complexes de Co^{III} avec un spin *S* = 1. Par ailleurs, DFT est la méthode la plus appropriée pour déterminer les différentes contributions à *D*, ce qui est particulièrement intéressant pour obtenir des relations structure-propriété. Il faut noter qu'il n'existe pas de règles générales à extrapoler de cette étude. Il est nécessaire d'effectuer des études systématiques pour chaque ion métallique, à chaque degré d'oxydation et d'état de spin pour établir l'approche théorique la plus appropriée pour prédire les paramètres *zfs* rendant la synthèse rationnelle de SMMs basés sur un seul métal difficile.

Introduction

Understanding the factors that control the magnitude and symmetry of the magnetic anisotropy should facilitate the rational design of mononuclear metal complexes in the quest of single molecule magnets (SMMs), based on a single metal ion with high blocking temperatures and large energy barriers.[1] The best strategy is to define magneto-structural correlations through investigation of series of metal complexes.

SMMs can be classified according divers criteria such as the block of the periodic table, in which the paramagnetic metal belongs to f-block or d-block, the number of metal centers and the type of ligand. One of the most important properties of SMMs is the magnetic anisotropy. It is defined as the magnetic moment of an individual molecule with a preferred orientation, which doesn't depend on the presence of an external magnetic field, leading to a net magnetization. The SMMs properties can be lost if the orientation of the magnetic moment is reversed. In order to prevent this phenomenon, a thermal energy barrier (U_{eff}) must be raised above. The value of U_{eff} is one way to compare different SMMs: bigger the barrier, more prominent the SMMs properties are. In most of the case, the anisotropy barrier is determined from the magnetic susceptibility (χ) in a magnetic field. Another relevant point of SMMs is whether or not the field dependence of the magnetization shows hysteresis.[57]In 1993, an entire new area of research emerged after the discovery of the exceptional properties of the famous $[Mn_{12}O_{12}(CH_3CO_2)_{16}(H_2O)_4]$ complex,[1] which displays single molecule magnet (SMM) behavior (Figure 1). [57]

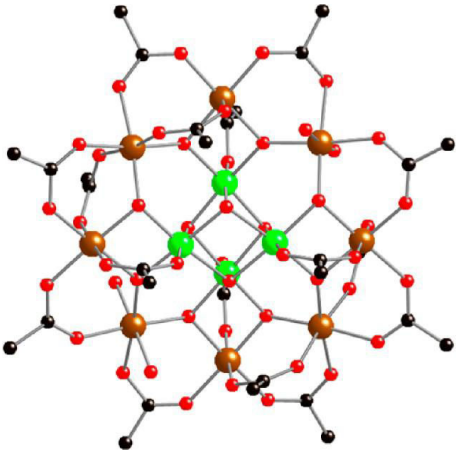

Figure 1. Molecular structure of $[Mn_{12}O_{12}(OAc)_{16}(H_2O)_4]$.[57]

During the first decade, the chemical challenge was to design and synthesize SMMs with the highest possible blocking temperature (T_B), T_B being related to the energy barrier (U_{eff}) that needs to be overcome for the reversal of the magnetic moment, with $U_{eff} = |D|S^2$ (S being the spin ground state of the complex and D the axial zero-field-splitting parameter (*zfs)* characterizing the magnetic

anisotropy measurement, defined by the following Hamiltonian: $\boldsymbol{H} = DS_z^2$). Consequently, complexes with large nuclearities have been designed with the aim of reaching large *S*, using mononuclear complexes characterized by significant *D* magnitude as building blocks. However, this strategy has proven to be unsuccessful, the highest reported blocking temperature of such type of SMMs does not exceed a few kelvins up to now. In fact, U_{eff} is independent from the total spin, because *D* is inversely proportional to S^2.[2,3]Alternative strategies have been developed, including the development of SMMs whose magnetic properties arise from a single metal ion in a ligand field. These mononuclear systems are mainly based on lanthanides that display the highest blocking temperatures and energy barriers.[4-7]

By contrast, the number of such systems based on transition metal ions is still much more limited but reasonable energy barriers have been observed especially for several mononuclear Co^{II} complexes and also for other 3d ions such as a few mononuclear Mn^{III}, Fe^{III}, Fe^{II}, Fe^{I} and Ni^{I} compounds.[8-10] This family of systems has been recently extended to the 5d metal ions in the special case of mononuclear Re^{IV} complexes.[11,12] On the other hand, a recent theoretical investigation has shown that Ni^{II} could be potentially attractive candidate. This was later confirmed by an experimental study, which reports a Ni^{II} complex displaying field-induced slow magnetic relaxation.[58, 59]

For a rational design of SMMs based on a single metal ion, an important aspect of the current research concerns the identification of the factors that govern the sign, symmetry and magnitude of the magnetic anisotropy in mononuclear complexes. Regarding the sign of *D*, the general belief was that it should be negative to observe SMM behavior. However, it has been recently shown that Kramers metal complexes (i.e. half integer spin systems) with positive *D* values can also present SMM properties.[8,13]

In order to establish correlation between the structure and the *zfs* parameters, series of complexes have been synthesized and characterized by magnetic susceptibility measurements and/or spectroscopic techniques, high-field EPR spectroscopy leading to the most accurate data regarding the determination of the *zfs* parameters.[14]

In parallel, important theoretical efforts have been undertaken to develop appropriate methodologies to evaluate the *zfs* parameters of a given system by determining the physical origin of the magnetic anisotropy and to compare these theoretical predictions with the experimental observations.[15] For such investigations, it is necessary to precisely calculate the two contributions to *D*, *i.e.* the electron-electron spin-spin interaction (D_{SS}) between unpaired electrons (to first order in perturbation theory) and the spin-orbit coupling (D_{SOC}) of electronically excited states into the ground state (to second order in perturbation theory). In line with this approach, DFT calculations have been applied to predict both sign and magnitude of *D*, but the magnitude is generally underestimated

when compared to the experimental data[16-19] with the exception of overestimated values in the case of complexes containing heavier halide ligand(s).[20,21] However, such DFT calculations are very useful to help in the rationalization of experimental trends by properly defining the different contributions to the total *D*-value.[22] Other methods including *ab initio* approaches, commonly give more satisfactory predictions of *D*. Several multi-determinantal methods especially the complete active space self-consistent field (CASSCF) approaches lead to calculated *D* values in perfect agreement with the experimental data,[19,23-27] but are much more expensive with respect to DFT. Using these different theoretical approaches, several combined experimental and theoretical investigations have been reported on various transition metal ions, such as Mn^{II},[28,29] Mn^{III},[19] Ni^{II},[20,30-32] Fe^{II},[33] low-spin Co^{II},[34] or V^{III}.[24] The main conclusion that can be drawn from these studies is that each case should be treated independently and no general rule can be applied to define the most adapted methodology to predict *D*. Therefore, for each metal ion, at the different oxidation and spin states, systematic studies should be carried out with series of benchmark complexes.

Since it has been also demonstrated that D_{SOC} is the main contribution to the final *D* value, particular focuses have been made both on ligands and metals characterized by large spin-orbit coupling (SOC). Concerning the ligands, the effect of the SOC contribution of halide on the magnetic anisotropy has been thoroughly investigated.

It has been commonly observed that the *D* magnitude increases from the chloride to the iodide derivatives, including series of low spin Cr^{II} and Cr^{III},[35] or high spin Mn^{II},[29,36] and Co^{II},[37-40] complexes. Regarding the metal ion, intermediate spin $S = 1$ Co^{III} complexes, mainly found in square planar geometry, are attractive because of their remarkable large *D* magnitudes up to 145 cm^{-1}.[41-43] However, although penta-coordinated Co^{III} complexes are usually $S = 2$, there is a unique exception of a distorted trigonal bipyramidal $S = 1$ system displaying a *D* value of +107 cm^{-1}.[44]

In chapter III, penta-coordinated Co^{III} complexes, **$Co^{III}Cl$**, **$Co^{III}Br$**, **$Co^{III}I$** have been described. In this chapter, we will focus on their magnetic properties and how calculations can explain their magnetic behaviors. Their magnetic properties have been determined and compared within the three complexes. Magnetic measurements have revealed that the three complexes are intermediate $S = 1$ spin systems. Theoretical calculations based on both DFT and CASSCF methods have been successfully carried out to rationalize the unexpected decrease of *D* from the chloride to the iodide derivatives. Besides, the magnetic properties of these three complexes is also compared with **$Mn^{III}I$**, which display an $S = 2$ ground spin state (Chapter III). Additional high field EPR experiments and calculations are in progress for this last complex and will not be discussed in this chapter.

This work has been recently published (*Chem. Eur. J.* **2016**, *22*, 925-933.)

Results

4.1. Synthesis, structures and characterizations.

The synthesis and the structure of these Co and Mn mononuclear complexes have been already described in chapter III. As a reminder, the **$M^{III}X$** complexes (M = Co or Mn) has been obtained from **M^{II}_2SS** in the presence of Et_4NX (X = Cl, Br, I) as illustrated in Figure 2.

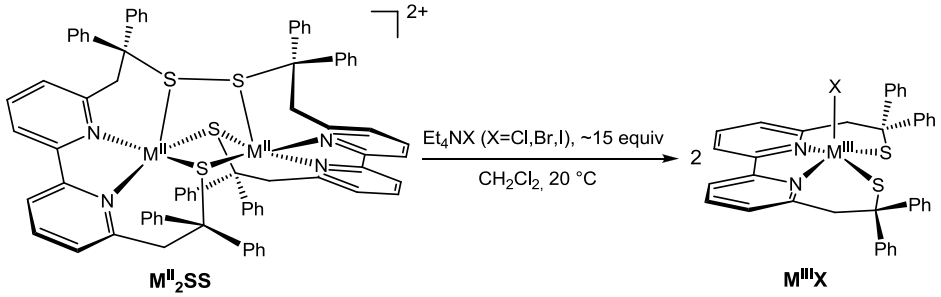

Figure 2. M^{II} disulphide/ M^{III} thiolate interconversion implicated the coordination/release of halide (Cl, Br, I) anions (M=Co, Mn).

These complexes have also been characterized by different techniques such as electronic absorption, infra-red spectroscopy and cyclic voltammetry. Chapter III also reports on their potential to act as molecular switch based on the interconversion thiolate/disulphur mediated by halide.

4.2. Magnetic properties of **$M^{III}X$ (M=Mn** or **Co**, **X= Cl, Br, I)**.

4.2.1. Magnetic properties of **$Mn^{III}I$**.

The magnetic susceptibility of a powdered sample of **$Mn^{III}I$** was measured between 1.8 and 300 K at 1000 Oe.

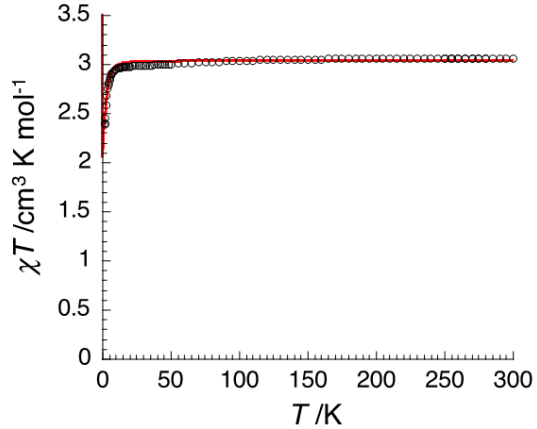

Figure 3. Temperature dependence of the χT product (where χ is the molar magnetic susceptibility equal to M/H per complex) measured at 1000 Oe for **$Mn^{III}I$**. The solid line is the best fit of the experimental data to the isotropic $S = 2$ spin.

High-spin Mn^{III} leads to an integer ground spin state, $S = 2$. Because of Jahn-Teller effect, this ion is characterized by larger magnetic anisotropy with respect to Mn^{II} and Mn^{IV}, ($|D|$ generally comprised in a small range 2.5 - 4.5 cm^{-1}. The temperature dependence of the χT product of the complex is

shown in Figure 3. The room temperature χT values of 3.01 $cm^3.K.mol^{-1}$ for the **$Mn^{III}I$** is consistent with the expected value for S=2. The magnetic susceptibility remains constant until 10 K, as expected with magnetically isolated Mn^{III} center. At lower temperature, the χT value decreases due to *zfs* estimated by fitting experimental data to D = -2.9(3) K, (D = -2.03 cm^{-1}) and g = 2.01(5) (with **H**= $DS_{T,z}^2$) consistent with high spin Mn^{III}. The negative D value is consistent with an elongation along the tetragonal axis as observed in the X-ray structure of **$Mn^{III}I$** (Mn-I; 2.7450(2) Å vs Mn-S; 2.2846(15)-2.2792(16) and Mn-N; 2.059(4)-2.091(4)). Despite structural and electronic (+3 oxidation state and three possible spin states 0, 1 or 2) similarities between **$Co^{III}I$** and **$Mn^{III}I$**, the fundamental spin state are different S = 2 for Mn vs S = 1 for Co (see below).

4.2.2. Magnetic properties of **$Co^{III}X$** (X=Cl, Br, I).

In this chapter, the magnetic properties of the three complexes, **$Co^{III}Cl$**[45], **$Co^{III}Br$**, **$Co^{III}I$** in solid state and in solution are compared (Figure 4 and Table 1). The magnetic susceptibility for the powdered samples was measured as a function of temperature (1.8-300 K).

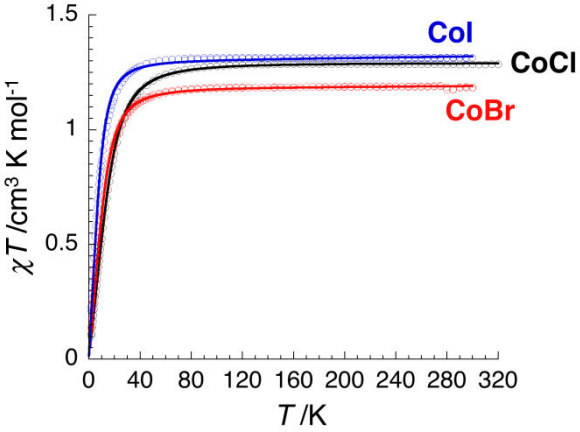

Figure 4. Temperature dependence of the χT product (where χ is the molar magnetic susceptibility equal to M/H per cobalt complex) measured at 0.1 T for **CoCl** (○), **CoBr** (○) and **CoI** (○). The solid lines are the best fits of the experimental data.

Table 1. Experimental determination of the spin states for **CoX** with X = I, Br, Cl.

	$Co^{III}Cl$[a]	**$Co^{III}Br$**	**$Co^{III}I$**
Powder			
χT (cm^3 K/mol)	1.35	1.18	1.31
S	1	1	1
Solution			
μ_{eff} (μ_B) at 20°C	2.44	2.63	2.94
χT (cm^3 K/mol)	0.74	0.86	1.07
S	1	1	1

[a] *data issued from* [45]

The magnetic susceptibility for all complexes remains constant down to approximately 30-50 K, consistent with magnetically isolated Co^{III} centers. The room temperature χT for the three complexes are consistent with the expected values 2.83 μ_B for S = 1. At lower temperatures, the χT values display a notable decrease, explained by the presence of large *zfs*. Considering the well separation of the Co^{III} complexes in the crystal structure and thus the absence of obvious inter-molecular magnetic interactions, a simple spin Hamiltonian including the D and the isotropic Zeeman interaction (g) have been considered to fit the experimental data with equation 1 (Table 1).

$$\mathbf{H} = DS_z^2 + g\mu_B\mu_0HS \qquad \text{(Equation 1)}$$

Together with g factors significantly larger than 2 (2.27(5), 2.17(5) and 2.28(5)), large positive D values of 35(1) cm^{-1}, 26(1) cm^{-1} and 18(1) cm^{-1} have been found for **Co^{III}Cl**, **Co^{III}Br** and **Co^{III}I** respectively. The large g-values found for **Co^{III}Cl**, **Co^{III}Br** and **Co^{III}I** evidence important spin-orbit contributions in consistent with notable magnetic anisotropy in the complexes.

In solution, the ^{1}H NMR spectra of the three compounds **Co^{III}Cl**[45] **Co^{III}Br** and **Co^{III}I** characterized by large signals and high chemical shifts are consistent with paramagnetic species (Figure 5, 6, respectively).

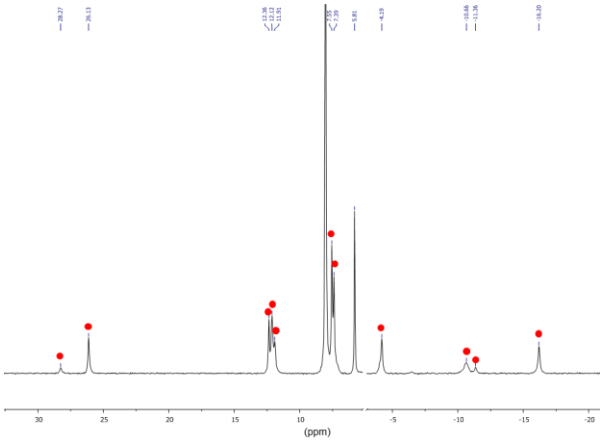

Figure 5. ^{1}H NMR spectrum of a d_7-DMF solution of **Co^{III}Br** (protons belonging to **Co^{III}Br** are evidenced by a ●).

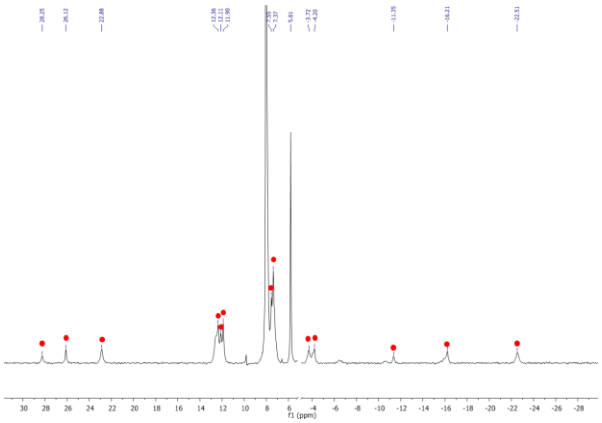

Figure 6. ^{1}H NMR spectrum of a d_7-DMF solution of **Co^{III}I** (protons belonging to **Co^{III}I** are evidenced by a ●).

The effective magnetic moments determined in DMF solutions by the Evans method[52,53] evidence that the triplet state is conserved in solution for both complexes (Table 1), as in the case of **Co^{III}Cl**. The Evans method is used for the determination of the spin state of paramagnetic compound in a diamagnetic solvent by measuring the magnetic susceptibility using precision-made coaxial tubes.

These measurements also confirm that the mononuclear structures of **Co^{III}Br** and **Co^{III}I** are retained in solution as for **Co^{III}Cl**.

In order to obtain further information about the contribution of the halides on the *zfs*, calculations have been performed to determine which factors are responsible for this unexpected trend for *D* observed in this series of Co complexes.

4.3. Quantum chemical calculations.

4.3.1. Optimized structure of **Co^{III}X** (X = Cl, Br, I).

Calculations have been performed on optimized structures initiated from the respective X-ray data of the three complexes. The optimized structures are very close to the experimental ones with less than 5 pm of difference in the metal-ligand bond distances.

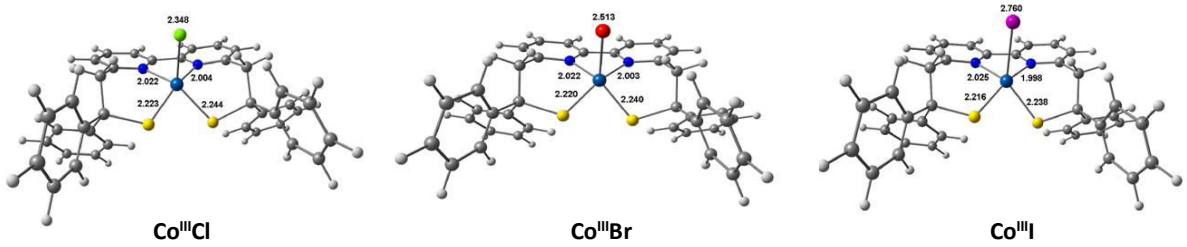

Co^{III}Cl **Co^{III}Br** **Co^{III}I**

Figure 7. Optimized structures of **CoI^{II}X** (X = Cl, Br, I).

4.3.2. Prediction of the spin state of Co^{III}X (X = Cl, Br, I).

DFT calculations have been carried out in order to determine the ground spin state of the complexes but also the stability of the first excited spin states with respect to the ground state (Table 2). In all complexes, a triplet ground spin state is predicted in agreement with the experimental data. In the cases of **Co^{III}Cl** and **Co^{III}Br**, the first excited spin state is *S* = 2 with an energy gap from the triplet state increasing from 8.5 kcal/mol to 10.3 kcal/mol, respectively. Conversely, for **Co^{III}I**, the first excited spin state is *S* = 0 with an energy gap of 8.5 kcal/mol with respect to the *S* = 1 ground state. The nature of the halide ligand, especially its SOC contribution notably affects the spin state energy spectrum with expected consequences on the *zfs* (*vide infra*).

Table 2. Calculated Gibbs free energies for the singlet, triplet and quintet states of **CoX** with X = I, Br, Cl at 0 K.

	Spin State	*E* (Eh)	Stability (kcal/mol)	Favored species
CoCl	$S = 0$	−4213.839378850	+13.7	$S = 1 > S = 2 > S = 0$
	$S = 1$	**−4213.861225540**	**0**	
	$S = 2$	−4213.847693219	+8.5	
CoBr	$S = 0$	−6328.885087986	+14.0	$S = 1 > S = 2 > S = 0$
	$S = 1$	**−6328.907428921**	**0**	
	$S = 2$	−6328.890987185	+10.3	
CoI	$S = 0$	−10675.294858226	+8.5	$S = 1 > S = 0 > S = 2$
	$S = 1$	**−10675.308410866**	**0**	
	$S = 2$	−10675.290704974	+11.1	

4.3.3. Electronic structure of $\mathbf{Co^{III}X}$ (X = Cl, Br, I).

Before calculating the *zfs* parameters, the electronic structures of the three complexes were investigated to help in the rationalization of the results. This study has been carried out based on the set of quasi-restricted orbitals (QROs), as this approach has been previously applied with success.[18,28,47] In particular, we have defined the energy diagram of the five 3d metal-based MOs of the three complexes (Figure 8).

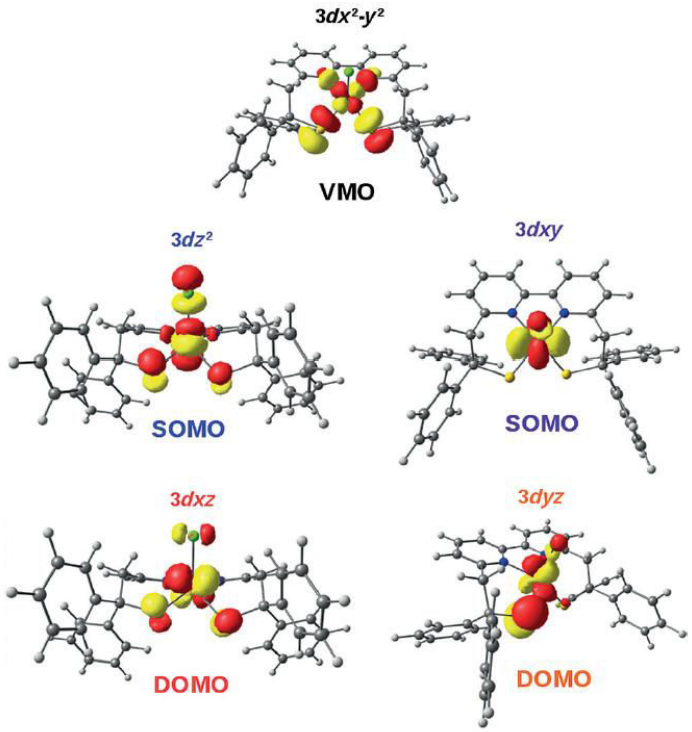

Figure 8. Graphical representation of the five 3d orbitals of $\mathbf{Co^{III}X}$ with X=Cl.

These square pyramidal complexes present the typical scheme of a pseudo C_{4V} symmetry with strong destabilization of the $d_{x^2-y^2}$ orbital, which corresponds to the unoccupied virtual molecular orbital (VMO). While the other four 3d metal ion-based orbitals are close in energy in **Co^{III}Cl**, in **Co^{III}I** the two singly occupied molecular orbitals (SOMOs), d_{z^2} and d_{xy}, are well separated from the two doubly occupied molecular orbitals (DOMOs), d_{xz} and d_{yz}. The much larger energy splitting between the DOMOs and the VMO in **Co^{III}I** than in **Co^{III}Cl** (4.222 eV *vs* 2.397 eV, Figure 9) disfavors transitions to *S* = 2 excited states. This is in coherence with a singlet as first excited spin state for **Co^{III}I** (large energy gap) and a quintet for **Co^{III}Cl** (smaller energy gap).

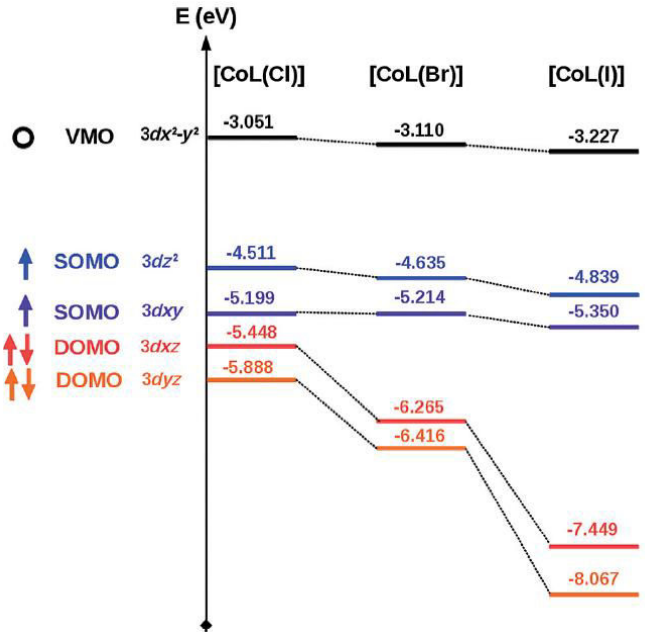

Figure 9. Energy diagram of the five 3d-orbitals of CoX with X=I, Br, Cl.

From Figure 9, it also clearly appears that the energy splitting between the SOMOs and the DOMOs is mainly dictated by the varying degrees of stabilization of the DOMOs. Consistently with the structural properties of the complexes, the more distorted the square pyramidal geometry is, the less the d_{xz} and d_{yz} orbitals are stabilized (τ_5 = 0.360, 0.353 and 0.332 and metal shift out of the mean equatorial plane of 0.485 Å, 0.464 Å and 0.435 Å for **Co^{III}Cl**, **Co^{III}Br** and **Co^{III}I**, respectively). Besides, it can be observed that both DOMOs have a main metal character in **Co^{III}I**, whereas they become notably delocalized over the halide ligand in **Co^{III}Br** and to more extent in **Co^{III}Cl** (Figure 10). The larger delocalization of the electronic density on the chloride observed for the DOMOs in **Co^{III}Cl** with respect to that on the iodide in **Co^{III}I** suggests that the covalency of the Co-halide bond depends on the nature of the halide with Co-Cl being more covalent than Co-I. This is fully supported by the Mülliken analysis that shows an increase of the spin population found at the metal ion going from the chloride (1.89) to the iodide derivative (1.93) meaning that the radical character of the iodide is less strong than the other halide.

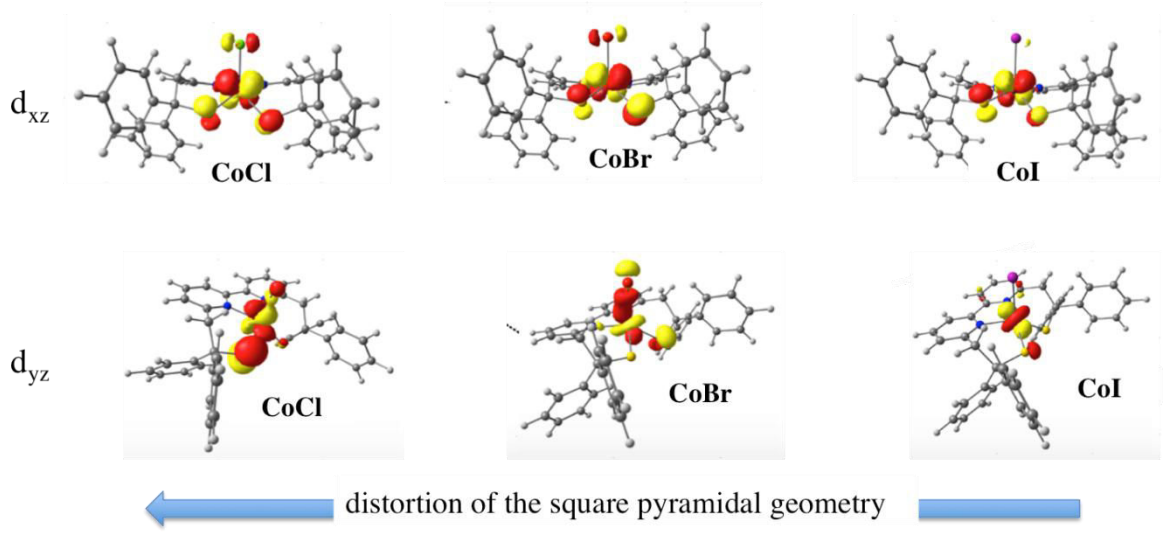

Figure 10. Representation of the two DOMOs of **$Co^{III}X$** with X = Cl, Br and I.

Concerning Co^{III} complexes, only one Co^{III}, containing two aromatic dithiolates complex, with S = 1 as spin ground state has been described so far reported by the group of Wieghardt.[48] However, in this case, the authors cannot discriminate between a Co^{III} and Co^{II}-radical species. In our case, the oxidation state of the three Co complexes can be unambiguously described as a Co^{III}. This is evidenced by the Mülliken analysis displaying values close to 2 (as expected for a species with two unpaired electrons). The difference between these two families of compounds (**$Co^{III}X$** and Wieghardt's complex) comes from the nature of the thiolate ligands: alkyl *vs* aromatic, respectively. Indeed, radical-based species can be strongly stabilized in the case of aromatic thiolates, while this is not the case for alkyl thiolates. A recent investigation on a series of Ni^{II} complexes containing one aromatic and one alkyl thiolate ligand has been reported. It has been shown that the one-electron reduction and oxidation processes mainly occur on the aromatic thiolate ligand, highlighting the difference of reactivity between these types of ligands.[55] Furthermore, it has been previously demonstrated that the dialkylthiolate ligand LS can stabilize Ni-based complexes in a large range of oxidation states, i.e. (+III) to (+I).[54]

4.3.2. Prediction of the *zfs* of **$Co^{III}X$** (X = Cl, Br, I).

The *zfs* parameters of the present Co^{III} complexes have been predicted with the DFT and the CASSCF method. The results are reported in Table 3.

Interestingly, the experimental and the theoretical data are in very good agreement for the DFT in both the sign and the magnitude of D for all the compounds (Figure 11). The contribution of the spin-spin dipolar interaction (D_{SS}) is quite small, below 5% of the total contribution, and the magnitude is between 0.64 and 0.94 cm^{-1}.

Table 3. Experimental *vs*. DFT- and CASSCF- calculated *D*-values and their individual contributions for **$Co^{III}X$** with X = I, Br, Cl.

	$Co^{III}Cl$	**$Co^{III}Br$**	**$Co^{III}I$**	**$Co^{III}Cl(I)^{b}$**
Experimental				
g	2.27(5)[a]	2.17(5)	2.28(5)	
D_{exp} (cm^{-1})	+35(1)[a]	+26(1)	+18(1)	
DFT-calculated				
D_{calc} (cm^{-1})	+32.49	+25.72	+17.17	+24.62
D_{SS} (cm^{-1})	+0.94	-0.75	+0.63	+0.91
D_{SOC} (cm^{-1})	+31.56	+26.48	+16.50	+23.79
D_{SOC} ($\alpha\rightarrow\alpha$) (cm^{-1})	+11.63	+4.01	-0.30	+ 3.69
D_{SOC} ($\beta\rightarrow\beta$) (cm^{-1})	+21.80	+10.38	-4.29	+ 10.86
D_{SOC} ($\alpha\rightarrow\beta$) (cm^{-1})	-3.01	+12.63	+21.37	+ 9.04
D_{SOC} ($\beta\rightarrow\alpha$) (cm^{-1})	+1.15	-0.53	-0.27	+ 0.17
CASSCF-calculated				
D_{calc} (cm^{-1})	+31.64	+21.98	+16.27	
D_{SS} (cm^{-1})	+0.59	-0.72	+2.21	
D_{SOC} (cm^{-1})	+31.37	+21.98	+13.93	
$D_{S=1}$ (cm^{-1})	+33.94	+13.70	-2.49	
$D_{S=0}$ (cm^{-1})	-2.57	+8.28	+16.42	

[a]*data issued from [45]; [b]**$Co^{III}Cl(I)$** is a theoretical complex corresponding to the optimized structure of **$Co^{III}I$**, in which the iodide ligand has been replaced by a chloride ligand.*

Regarding the different contributions to the spin-orbit coupling (D_{SOC}), three main types of transitions are involved which are the two types of spin-conserving excitation from i) the DOMOs to the SOMOs ($\beta\rightarrow\beta$) , ii) the SOMOs to the VMO ($\alpha\rightarrow\alpha$) and spin-flip excitations between the two SOMOs ($\alpha\rightarrow\beta$). The values of each contribution to D_{SOC} evolve steadily as a function of the nature of the halide from the chloride to the iodide. Concerning the spin-flip $\alpha\rightarrow\beta$ contribution, the trend is different from the spin-conserving $\alpha\rightarrow\alpha$ and $\beta\rightarrow\beta$ for the three complexes. Indeed, the $\alpha\rightarrow\beta$ transitions represent the main contribution to D_{SOC} in **$Co^{III}I$**, whereas they become negligible for **$Co^{III}Cl$**, for which the main contribution to D_{SOC} comes from both spin-conserving excitations. The **$Co^{III}Br$** complex represents an intermediate case.

To check the reliability of these results, *ab initio* calculations using CASSCF approach, which corresponds to a higher level of theory compared to DFT were performed. The CASSCF-computed parameters compare well with those obtained by DFT. Indeed, both the CASSCF-calculated triplet ($D_{S=1}$) and singlet ($D_{S=0}$) contributions, which are related to the spin-conserving and the spin-flip excitations, respectively, are consistent with DFT calculations. In the case of **$Co^{III}Cl$** the main contribution to D_{SOC} arises from the triplet states, whereas for **$Co^{III}I$** it originates from the singlet states. Consequently, it can be concluded that both CASSCF and DFT methods are appropriate to predict the *zfs* parameters of these intermediate spin Co^{III} halide complexes (Table 3).

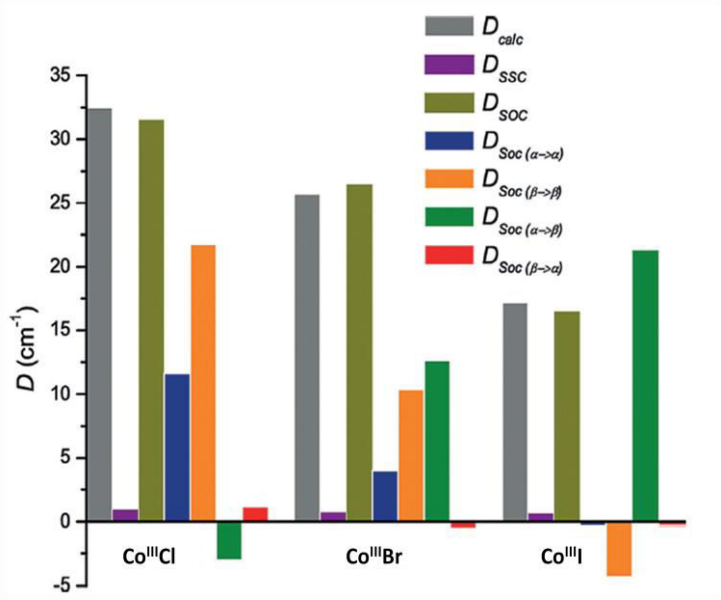

Figure 11. Individual contributions to the DFT-calculated *zfs* parameters of **Co^{III}X** with X=I, Br, Cl.

In an attempt to further rationalize the origin of the discrepancy in *D* between the three complexes, especially the impact of structural effects on D_{SOC} with respect to the nature of the halide, DFT calculations have been performed on a theoretical complex, corresponding to the optimized structure of **Co^{III}I**, in which the iodide ligand has been replaced by a chloride without any further optimization procedure. The resulting *D*-value ($D_{calc}^{(I)Cl}$) of +24.63 cm^{-1} is in between D_{calc}^{Cl} and D_{calc}^{I} (+32.49 cm^{-1} and +17.17 cm^{-1}, respectively), with all contributions to *D* following the same tendency (Table 3). The increase from $D_{calc}^{(I)Cl}$ to D_{calc}^{Cl} implies the intrinsic effect of the structure on the D_{SOC} contribution, whereas the increase from D_{calc}^{I} to $D_{calc}^{(I)Cl}$ shows that of the nature of the halide.

Discussion and conclusion

A series of mononuclear penta-coordinated halide Co^{III} complexes displaying an intermediate *S* = 1 spin state has been investigated. It has been experimentally evidenced that the magnetic anisotropy of these complexes is sensitive to the nature of the halide, but in an unexpected way: the largest *D*-value has been measured for the chloride compound and the smallest for the iodide one. In the literature, examples of such reported behavior are still very limited to: (i) two *S* = 2 pseudo-tetrahedral Co^{I} complexes, in which the *D* value decreases from +6.00 cm^{-1} to +3.89 cm^{-1} from the chloride to the bromide derivative;[21] (ii) an *S* = 2 Mn^{III} iodide complex that displays an unexpected small positive *D* values of +0.604 cm^{-1} in an elongated octahedral environment;[49] and (iii) a series of *S* = 1 pseudo-tetrahedral Ni^{II} complexes, in which *D* fluctuates from +3.9 cm^{-1}to -22.8 cm^{-1} from the chloride to the iodide derivative.[20,31] Conversely, in most of previous studies, it has been observed that the *D* magnitude increases from the chloride to the iodide metal complexes.[29,35-40] This previously reported trend was tentatively correlated to the magnitude of the SOC contribution of the

halide that can override the SOC contribution of the metal ion center. However, using theoretical Mn^{II},[29] and Fe^{III},[50] models, it was also demonstrated that the main contribution to the final *D* values results from a balance between the metal ion and halide SOC contributions, which are proportional to the $\xi_{Mn}\xi_X$ product, ($\xi_{Mn/X}$ being the metal ion/ligand SOC constant). Therefore, depending on the metal ion and the halide, the SOC contribution of the heavier ligand and the metal ion can compensate each other leading to an inverse tendency, as in the present case.

At a further level of analysis, we have been able to define magneto-structural correlation. **Co^{III}Cl** displays the more distorted square pyramidal geometry within the series (the higher τ_5 parameter and larger metal displacement out of the equatorial plane), leading to a destabilization of the DOMOs and to a smaller energy gap with the VMOs explaining the accessibility of a quintet as first excited state. Coherently, in the more distorted **Co^{III}Cl** complex, the SOMOs - DOMOs energy gap becomes smaller which favor the spin-conserving excitations that mainly contribute to the *zfs* parameters of **Co^{III}Cl**. In contrast, **Co^{III}I** presents the less distorted geometry and the most energetically stabilized DOMOs such as the main contribution to D_{SOC} arises from spin-flip excitations ($\alpha \rightarrow \beta$) and the first excited spin state is a singlet. In any case, other contributing factors to *D* should be taken into account including the SOC contribution of the ligands and the covalency of the Co-halide bond. However, it is difficult to identify the weight of each of these factors; the overall data demonstrates that all of them affect the final *D*-values in a balanced manner.

Finally, this investigation evidences that both DFT and CASSCF are powerful tools to predict both the sign and magnitude of *D* for *S* = 1 Co^{III} complexes. However, it should be noted that DFT is the most appropriate method to determine the different contributions to *D*, which is particularly useful to obtain structure-property relationship. It also remains clear that no general rule can be extrapolated from the present case: for each metal ion, at each oxidation and spin state, benchmark investigations are required to define magneto-structural correlations and to establish the most appropriate theoretical method to predict the *zfs* parameters, rendering rational synthesis of SMMs based on a single metal ion still very challenging.

Concerning Mn complexes, the investigation is still in progress. Currently, only the iodide derivate is available. Synthetic effort will be carried out to isolate the bromide and chloride derivates. It will be interesting to see how the halides will affect the spin state and the magnetic anisotropy of these compounds.

References

1. Sessoli, R.; Gatteschi, D.; Caneschi, A.; Novak, M. A. *Nature* **1993**, 365, 141-143.
2. Waldmann, O. *Inorg. Chem.* **2007**, 46, 10035-10037.
3. Neese, F.; Pantazis, D. A. *Faraday Discussions* **2011**, 148, 229-238.
4. Blagg, R. J.; Muryn, C. A.; McInnes, E. J. L.; Tuna, F.; Winpenny, R. E. P. *Angew. Chem. Int. Ed.* **2011**, 50, 6530-6533.
5. Meihaus, K. R.; Long, J. R. *J. Am. Chem. Soc.* **2013**, 135, 17952-17957.
6. Ungur, L.; Le Roy, J. J.; Korobkov, I.; Murugesu, M.; Chibotaru, L. F. *Angew. Chem. Int. Ed.* **2014**, 53, 4413-4417.
7. Le Roy, J. J.; Ungur, L.; Korobkov, I.; Chibotaru, L. F.; Murugesu, M. *J. Am. Chem. Soc.* **2014**, 136, 8003-8010.
8. Craig, G. A.; Murrie, M. *Chem. Soc. Rev.* **2015**.
9. Atanasov, M.; Aravena, D.; Suturina, E.; Bill, E.; Maganas, D.; Neese, F. *Coord. Chem. Rev.* **2015**, 289–290, 177-214.
10. Gomez-Coca, S.; Aravena, D.; Morales, R.; Ruiz, E. *Coord. Chem. Rev.* **2015**, 289, 379-392.
11. Pedersen, K. S.; Sigrist, M.; Sorensen, M. A.; Barra, A. L.; Weyhermuller, T.; Piligkos, S.; Thuesen, C. A.; Vinum, M. G.; Mutka, H.; Weihe, H.; Clerac, R.; Bendix, J. *Angew. Chem. Int. Ed.* **2014**, 53, 1351-1354.
12. Martínez-Lillo, J.; Faus, J.; Lloret, F.; Julve, M. *Coord. Chem. Rev.* **2015**, 289–290, 215-237.
13. Vallejo, J.; Castro, I.; Ruiz-García, R.; Cano, J.; Julve, M.; Lloret, F.; De Munno, G.; Wernsdorfer, W.; Pardo, E. *J. Am. Chem. Soc.* **2012**, 134, 15704-15707.
14. Krzystek, J.; Ozarowski, A.; Telser, J. *Coord. Chem. Rev.* **2006**, 250, 2308-2324.
15. Boca, R. *Coord. Chem. Rev.* **2004**, 248, 757-815.
16. Reviakine, R.; Arbuznikov, A. V.; Tremblay, J.-C.; Remenyi, C.; Malkina, O. L.; Malkin, V. G.; Kaupp, M. *J. Chem. Phys.* **2006**, 125, 054110.
17. Zein, S.; Duboc, C.; Lubitz, W.; Neese, F. *Inorg. Chem.* **2008**, 47, 134-142.
18. Duboc, C.; Collomb, M. N.; Neese, F. *Appl. Magn. Reson.* **2010**, 37, 229-245.
19. Duboc, C.; Ganyushin, D.; Sivalingam, K.; Collomb, M.-N.; Neese, F. *J. Phys. Chem. A* **2010**, 114, 10750-10758.
20. Ye, S.; Neese, F. *J. Chem. Theory Comput.* **2012**, 8, 2344-2351.
21. Krzystek, J.; Ozarowski, A.; Zvyagin, S. A.; Telser, J. *Inorg. Chem.* **2012**, 51, 4954-4964.
22. Neese, F. In *Calculation of NMR and EPR Parameters*; M. Kaupp, M. B., V. G. Malkin, Ed.; Wiley-VCH: Heidelberg, **2004**.
23. Singh, S. K.; Gupta, T.; Badkur, P.; Rajaraman, G. *Chem. Eur. J.* **2014**, 20, 10305-10313.
24. Ye, S.; Neese, F.; Ozarowski, A.; Smirnov, D.; Krzystek, J.; Telser, J.; Liao, J.-H.; Hung, C.-H.; Chu, W.-C.; Tsai, Y.-F.; Wang, R.-C.; Chen, K.-Y.; Hsu, H.-F. *Inorg. Chem.* **2010**, 49, 977-988.
25. Martinez-Lillo, J.; Mastropietro, T. F.; Lhotel, E.; Paulsen, C.; Cano, J.; De Munno, G.; Faus, J.; Lloret, F.; Julve, M.; Nellutla, S.; Krzystek, J. *J. Am. Chem. Soc.* **2013**, 135, 13737-13748.
26. Kubica, A.; Kowalewski, J.; Kruk, D.; Odelius, M. *J. Chem. Phys.* **2013**, 138.
27. Maurice, R.; de Graaf, C.; Guihery, N. *PhysChemChemPhys* **2013**, 15, 18784-18804.
28. Duboc, C.; Collomb, M. N.; Pécaut, J.; Deronzier, A.; Neese, F. *Chem. Eur. J.* **2008**, 14, 6498-6509.
29. Duboc, C.; Phoeung, T.; Zein, S.; Pécaut, J.; Collomb, M. N.; Neese, F. *Inorg. Chem.* **2007**, 46, 4905-4916.
30. Schweinfurth, D.; Krzystek, J.; Schapiro, I.; Demeshko, S.; Klein, J.; Telser, J.; Ozarowski, A.; Su, C.-Y.; Meyer, F.; Atanasov, M.; Neese, F.; Sarkar, B. *Inorg. Chem.* **2013**, 52, 6880-6892.
31. Desrochers, P. J.; Telser, J.; Zvyagin, S. A.; Ozarowski, A.; Krzystek, J.; Vicic, D. A. *Inorg. Chem.* **2006**, 45, 8930-8941.
32. Maurice, R.; Bastardis, R.; de Graaf, C.; Suaud, N.; Mallah, T.; Guihery, N. *J. Chem. Theory Comput.* **2009**, 5, 2977-2984.

33. Atanasov, M.; Ganyushin, D.; Pantazis, D. A.; Sivalingam, K.; Neese, F. *Inorg. Chem.* **2011**, 50, 7460-7477.
34. Vaidya, S.; Upadhyay, A.; Singh, S. K.; Gupta, T.; Tewary, S.; Langley, S. K.; Walsh, J. P. S.; Murray, K. S.; Rajaraman, G.; Shanmugam, M. *Chem. Commun.* **2015**, 51, 3739-3742.
35. Karunadasa, H. I.; Arquero, K. D.; Berben, L. A.; Long, J. R. *Inorg. Chem.* **2010**, 49, 4738-4740.
36. Mantel, C.; Baffert, C.; Romero, I.; Deronzier, A.; Pécaut, J.; Collomb, M. N.; Duboc, C. *Inorg. Chem.* **2004**, 43, 6455-6463.
37. Saber, M. R.; Dunbar, K. R. *Chem. Commun.* **2014**, 50, 12266-12269.
38. Krzystek, J.; Zvyagin, S. A.; Ozarowski, A.; Fiedler, A. T.; Brunold, T. C.; Telser, J. *J. Am. Chem. Soc.* **2004**, 126, 2148-2155.
39. Yang, F.; Zhou, Q.; Zhang, Y.; Zeng, G.; Li, G.; Shi, Z.; Wang, B.; Feng, S. *Chem. Commun.* **2013**, 49, 5289-5291.
40. Boča, R.; Miklovič, J.; Titiš, J. *Inorg. Chem.* **2014**, 53, 2367-2369.
41. García-Monforte, M. A.; Ara, I.; Martín, A.; Menjón, B.; Tomás, M.; Alonso, P. J.; Arauzo, A. B.; Martínez, J. I.; Rillo, C. *Inorg. Chem.* **2014**, 53, 12384-12395.
42. Van der Put, P. J.; Schilperoord, A. A. *Inorg. Chem.* **1974**, 13, 2476-2481.
43. Birker, P. J. M. W. L.; Bour, J. J.; Steggerda, J. J. *Inorg. Chem.* **1973**, 12, 1254-1259.
44. Cho, C. H.; Chien, T. Y.; Chen, J. H.; Wang, S. S.; Tung, J. Y. *Dalton Trans.* **2010**, 39, 2609-2614.
45. Gennari, M.; Gerey, B.; Hall, N.; Pécaut, J.; Collomb, M.-N.; Rouzières, M.; Clérac, R.; Orio, M.; Duboc, C. *Angew. Chem. Int. Ed.* **2014**, 53, 5318-5321.
46. Addison, A. W.; Rao, T. N.; Reedijk, J.; Vanrijn, J.; Verschoor, G. C. *J. Chem. Soc., Dalton Trans.* **1984**, 1349-1356.
47. Schöneboom, J. C.; Neese, F.; Thiel, W. *J. Am. Chem. Soc.* **2005**, 127, 5840-5853.
48. Ray, K.; Begum, A.; Weyhermuller, T.; Piligkos, S.; van Slageren, J.; Neese, F.; Wieghardt, K. *J. Am. Chem. Soc.* **2005**, 127, 4403-4415.
49. Mossin, S.; Weihe, H.; Barra, A. L. *J. Am. Chem. Soc.* **2002**, 124, 8764-8765.
50. Neese, F.; Solomon, E. I. *Inorg. Chem.* **1998**, 37, 6568-6582.
52. Evans, D. F. *J. Chem. Soc.* **1959**, 2003-2005.
53. Sur, S. K. *J. Magn. Reson.* **1989**, 82, 169-173.
54. a) Gennari, M.; Orio, M.; Pécaut, J.; Bothe, E. Neese, F. M-N Collomb and C. Duboc, *Inorg. Chem*, **2011**, *50*, 3707-3716. b)M. Gennari, M. Orio, J. ; F. Neese; Collomb, M-N.; and Duboc, C. *Inorg. Chem*. **2010**, *49*, 6399-6401.
55. Broering, E. P.; Dillon, S.; Gale, E. M.; Steiner, R. A.; Telser, J.; Brunold, T. C.; Harrop, T. C. *Inorg. Chem*. **2015**, *54*, 3815–3828.
56. Mantel, C.; Hassan, A. K.; Pécaut, J.; Deronzier, A.; Collomb, M.-N. and Duboc-Toia, C. *J. Am. Chem. Soc.* **2003**, *125*, 12337-12344
57. Layfield, R.A. *Organometallics*. **2014**, *33*, 1084–1099.

Conclusion

Résumé

L'objectif de ma thèse était d'améliorer les connaissances sur le rôle des liaisons métal-thiolates au sein des métalloenzymes en utilisant une approche bio-inspirée par l'étude des propriétés structurales, électroniques et/ou magnétiques de modèles chimiques ainsi que de leur réactivité. Dans une approche bio-inspirée, les projets développés au cours de ma thèse ont traité de complexes modèles de l'hydrogénase [NiFe], de catalyseurs à base de Mn pour la réduction d'O_2 et de systèmes à base de Mn et de Co impliqués dans la conversion disulfure/thiolate.

Dans le cadre de l'hydrogénase [NiFe], deux modèles structuraux et fonctionnels de $Ni^{II}Fe^{II}$ ont été étudiés. Ces complexes présentent les meilleures performances pour la production électrocatalytique d'H_2, par rapport aux autres modèles déjà décrits dans la littérature. Ils représentent également les premiers modèles hétérodinucléaires de NiFe pour lesquels la réactivité est localisée sur le centre Ni. Comme dans l'enzyme, le centre Fe des complexes **$Ni^{II}Fe^{II}Cp$** et **$Ni^{II}Fe^{II}Cp^*$** est impliqué dans la modulation des propriétés électroniques et redox du cœur $\{N_2S_2\}$ et de sa réactivité. Un des points forts de notre étude a été la caractérisation de deux intermédiaires dont un complexe $Ni^{II}Fe^{II}$ hydrure, tous deux mimant ceux proposés dans le cycle catalytique de l'enzyme. Cependant, contrairement à l'hydrogénase [NiFe], les complexes de NiFe doivent subir deux réductions successives avant de pouvoir réagir avec les protons. En présence de CO, l'activité catalytique est partiellement inhibée pour le complexe **$Ni^{II}Fe^{II}Cp$**. Ce phénomène est réversible lorsque le CO est remplacé par de l'argon. En revanche, l'activité catalytique du complexe **$Ni^{II}Fe^{II}Cp^*$** est complètement inhibée en présence de CO, et également de manière réversible. **$Ni^{II}Fe^{II}Cp^*$** représente donc un bon modèle de l'hydrogénase [NiFe] pour la réduction des protons et son inhibition en présence de CO (intermédiaire Ni-CO de l'enzyme). Les perspectives de ce travail sont multiples. A court et moyen termes, des efforts vont être poursuivis pour caractériser un complexe de $Ni^{III}Fe^{II}$ hydrure, intermédiaire clé de l'enzyme encore jamais observé avec des modèles. Basées sur le fait que **$Ni^{I}Fe^{II}Cp$** puisse produire H_2 en présence d'un acide fort, des expériences d'électrocatalyse en présence d'acide fort (HBF_4) sont en cours d'étude. Les résultats préliminaires montrent une activité catalytique sur le premier système redox suggérant la formation d'un nouvel intermédiaire réactionnel, soit **$Ni^{III}Fe^{II}Cp(H)$**.

Dans le chapitre II, un nouveau complexe dinucléaire de Mn^{II}, **Mn^{II}_2SH**, où un thiol protoné est coordonné à l'un des deux Mn^{II} est décrit Ce complexe est capable d'activer l'oxygène. En particulier, en conditions stœchiométriques **Mn^{II}_2SH** réagit avec O_2 pour générer un complexe μ-hydroxo, **Mn^{III}_2OH**. Dans ce cas, on observe une coupure réductrice de la liaison O-O, conduisant à une réduction de O_2 à quatre électrons. Inversement, en présence d'une source de protons et d'un agent

réducteur à un électron, **Mn^{II}_2SH** catalyse sélectivement la réduction de O_2 en peroxyde d'hydrogène. Dans ce cas, la coupure de la liaison M-O de l'intermédiaire manganèse-peroxo présumé est favorisée en milieu acide, conduisant à une réduction à deux électrons. **Mn^{II}_2SH** représente un rare exemple de catalyseur moléculaire à base de manganèse, sélectif pour une réduction de O_2 à deux électrons en milieu homogène. En fonction des conditions expérimentales (état de protonation du complexe de Mn^{II} initial, température ou concentration), un complexe à hauts degrés d'oxydation, un dinucléaire de Mn^{IV} bis-μ-oxo, a pu être généré et caractérisé. L'étude de ses propriétés acido-basiques nous a permis d'isoler et de caractériser un rare dinucléaire de Mn^{IV} μ-oxo-μ-hydroxo. Un mécanisme expliquant la compétition entre la formation d'un dinucléaire de Mn^{III} et de Mn^{IV} lors de l'activation d'O_2 en rationnalisant l'ensemble des données expérimentales a été proposé. Actuellement, des calculs théoriques sont en cours d'analyse en collaboration avec le groupe de De Visser pour comprendre les différents mécanismes impliqués dans l'activation de O_2 avec les complexes de Mn^{II}, et plus particulièrement, le rôle de la liaison Mn-SH. Par ailleurs, nous avons montré que seul le complexe de Mn^{IV} bis-μ-oxo était capable de transférer des atomes d'hydrogène en présence de dérivés phénoliques. Des études cinétiques sont envisagées pour mieux comprendre le mécanisme impliqué. A plus long terme, il serait intéressant de comprendre le rôle du métal dans les processus d'activation et de réduction d'O_2 avec des complexes thiol/thiolate similaires. Dans ce cadre un complexe de Fe^{II} isostructural au complexe de Mn^{II}, possédant une liaison métal-SH a déjà été isolé. L'étude de ses propriétés et de sa réactivité est en cours.

Le chapitre III a présenté le premier exemple d'un système réversible impliqué dans la conversion disulfure/thiolate à base de manganèse. Comme le complexe parent à base de cobalt, la coordination d'un iodure (ou la décoordination) au métal induit la conversion du pont disulfure en thiolate (thiolate en pont disulfure) avec l'oxydation (réduction) concomitante du métal. Pour les systèmes à base de Mn et de Co, la réversibilité du processus semble être favorisée par le fait que le pont disulfure reste coordonné au centre métallique. La conversion de **Mn^{II}_2SS** en **Mn^{III}I** est beaucoup moins efficace (réaction en quelques minutes et réactivité partielle) en comparaison avec l'évolution de **Co^{II}_2SS** en **Co^{III}I**, qui est quantitative et instantanée. La réaction inverse, initiée par l'élimination de l'iodure lié au métal, est aussi plus lente pour le complexe de Mn. En effet, **Mn^{II}_2SS** n'est pas directement généré comme dans le cas de **Co^{II}_2SS**, mais provient de l'évolution de sa forme iso-électronique, **Mn^{III}_2**. Ce travail représente une contribution originale permettant de mieux comprendre comment les propriétés électronique et redox d'un centre métallique peuvent finement moduler une conversion disulfure/thiolate, régulée par des ions métalliques et de manière plus ou moins efficace.

Dans le chapitre IV, les propriétés magnétiques d'une série de complexes mononucléaires de Co^{III} penta-coordonnés avec un halogénure, ont été étudiées. Tous les complexes présentent un rare spin intermédiaire S = 1, et leur anisotropie magnétique est sensible à la nature de l'halogénure, mais de manière inattendue : une plus grande valeur de D a été mesurée pour le composé chloré et une plus petite valeur pour le complexe iodé. Basé sur des calculs de chimie quantique, il a été montré que les valeurs de D provenaient d'une balance entre différentes contributions, et que de nombreux facteurs dont des différences de structure et des contributions variables de l'halogénure devaient être pris en compte pour expliquer la tendance observée. De cette étude, il apparaît aussi qu'il n'est pas possible d'extrapoler de règles générales de cette étude : pour chaque ion métallique, pour chaque degré d'oxydation et état de spin, des études de référence sont nécessaires pour définir des corrélations magnéto-structurales et pour établir la méthode théorique la plus appropriée pour prédire les paramètres de zfs, rendant ainsi la synthèse rationnelle de SMM sur la base d'un seul ion métallique difficile. En ce qui concerne les complexes de Mn, l'étude de leurs propriétés magnétiques est particulièrement intéressante et toujours en cours. En effet, l'ion Mn^{III} est généralement trouvé dans un environnement octaédrique combiné à état de spin S= 2. Actuellement, seul le dérivé iodure a put être étudié. Même si ce composé présente un état de spin S = 2, des calculs théorique prédisent un état excité S = 1 très proche en énergie. Ainsi, des efforts vont été menés pour isoler les dérivés bromé et chloré. Il serait également intéressant de voir si les différents halogénures ont un effet sur l'état de spin et l'anisotropie magnétique de ces composés.

Conclusion

The aim of my thesis was to improve the knowledge on the role of metal-thiolate bonds in metalloenzymes using a bio-inspired approach by investigating the structural, electronic and/or magnetic properties of chemical models as well as their reactivity. In this context, the projects developed during my PhD focused on models of [NiFe] hydrogenase, Mn-thiolate catalysts for O_2 reduction and Mn/Co–based molecular switches involving disulfide/thiolate interconversion.

Chapter I described the synthesis and characterization of two $Ni^{II}Fe^{II}$ complexes. These complexes display the best performance of any reported [NiFe] hydrogenase mimics to date with regards to electrocatalytic H_2 production. They are also the first heterodinuclear mimics, whose reactivity occurs on the Ni site. As in the enzyme, the Fe site of **$Ni^{II}Fe^{II}$Cp and $Ni^{II}Fe^{II}$Cp*** is involved in the modulation of the electronic and redox properties of the Ni site as well as its reactivity. An important aspect of this work was the characterization of two intermediates including a $Ni^{II}Fe^{II}$ hydride species, both mimicking those present during the catalytic cycle of the enzyme. However, unlike the [NiFe] hydrogenase, must undergo two successive reductions (and not only one) before reacting with protons. In the presence of CO, the catalytic activity is partially inhibited for **$Ni^{II}Fe^{II}$Cp** and its reactivity is recovered when CO is removed. Interestingly, the catalytic activity of **$Ni^{II}Fe^{II}$Cp*** is fully inhibited in the presence of CO and recovered when CO is removed. **$Ni^{II}Fe^{II}$Cp*** thus represents a good model of the [NiFe] hydrogenase as it shows proton reduction activity that is inhibited in the presence of CO in analogy to the Ni-CO state of the enzyme. There are many perspectives of this work. In the short to medium term, synthetic efforts will be pursued to characterize a $Ni^{III}Fe^{II}$ hydride species, a key intermediate of the enzyme, never isolated with models. Based on the fact the **$Ni^{I}Fe^{II}$Cp** could produce H_2 in the presence of a strong acid, electrocatalytic experiments using HBF_4 and **$Ni^{II}Fe^{II}$Cp** are currently under investigation. The preliminary results are promising since the electrocatalytic activity occurs on the first reduction system suggesting that the mechanism may go through the formation of a **$Ni^{III}Fe^{II}$(H)** species, thus perfectly mimicking the mechanism of [NiFe] hydrogenase.

Chapter II described a new thiolate-bridged dimanganese(II) complex, which represents an unusual system with a metal-bound pendant thiol (M-SH). This complex is capable of binding and activating dioxygen. In particular, under stoichiometric conditions and in the absence of an external proton source, it reacts with dioxygen to generate a μ-hydroxo Mn^{III} dinuclear complex. In this case, the reductive cleavage of the O-O bond is achieved, leading to a 4-electron O_2 reduction process. Conversely, in the presence of a proton source and of a one-electron reducing agent, the dinuclear Mn^{II} complex selectively catalyzes the reduction of dioxygen to hydrogen peroxide. In this case, the

rupture of the M-O bond in the putative manganese-peroxo intermediate is favored by the acidic medium, leading to 2-electron O_2 reduction. This Mn^{II} complex represents a rare example of manganese-based molecular catalysts for selective 2-electron O_2 reduction in homogeneous solution. As a function of the experimental conditions (protonation state of the initial dinuclear Mn^{II} complex, temperature and concentration), a high valent bis- μ-oxo Mn^{IV} complex could be generated and characterized. The investigation of its acid/base properties allowed us to isolate and characterize a rare dinuclear μ-hydroxo μ-oxo Mn^{IV} complex. A mechanism explaining the competition between the formation of a dinuclear Mn^{III} and Mn^{IV} complex and rationalizing all experimental data has been proposed. Currently, theoretical calculations are performed in collaboration with the group of De Visser to fully understand the different mechanisms involved in O_2 activation with this Mn^{II} complex, especially the role of the Mn-bound SH. We have also shown that only the bis-μ-oxo complex displays hydrogen atom transfer reactivity in the presence of phenol substrates. Kinetic studies are envisaged to better understand the involved mechanism.

In a long term, it would be interesting to understand the role of the metal in the O_2 activation and reduction processes with similar thiol/thiolate complexes. In this context, a dinuclear Fe^{II} complex, isostructural to the Mn^{II} one, containing a Fe-bound SH has been isolated. The investigation of its physical-chemical properties and reactivity is in progress.

Chapter III reported the first example of a reversible disulphide/thiolate interconversion involving manganese ions. As for the parent cobalt system, iodide coordination (or decoordination) to the metal ion induces disulphide to thiolate (thiolate to disulphide) conversion with concomitant metal oxidation (reduction). For both Mn and Co systems, the reversibility of the process seems to be favored by the fact that the disulphide-bridge remains coordinated to the metal centers.The conversion of **Mn^{II}_2SS** into **Mn^{III}I** is clearly less efficient (it occurs in a few minutes and partially) when compared with the corresponding evolution of **Co^{II}_2SS** into **Co^{III}I**, which is quantitative and instantaneous. The reverse reaction, initiated by removing the bound iodide, is also slower for the Mn complex. Indeed, the Mn^{II}_2-disulphide complex is not directly regenerated as in the case of **Co^{II}_2SS**, but it arises from evolution of its isoelectronic **Mn^{III}_2** form. This work represents an original contribution to improve the understanding of how the electronic and redox properties of the metal centers should be fine-tuned to allow a disulphide/thiolate (inter)conversion, mediated by metal ions, to occur efficiently.

In chapter IV, the magnetic properties of the series of mononuclear penta-coordinated halide-Co^{III} complexes have been investigated. They all display a rare intermediate S = 1 spin state and their magnetic anisotropy is sensitive to the nature of the halide in an unexpected way: the largest D-value has been measured for the chloride compound and the smallest for the iodide one. Based on

theoretical calculations, it has been shown that the resulting *D* values originate from a balance of several contributions, and that many factors, including differences in their structural properties and in the contribution of the halide, should be taken into account to explain the trend of *D* in this series of complexes. From this study, it also remains clear that no general rule can be extrapolated from the present case: for each metal ion, at each oxidation and spin state, benchmark investigations are required to define magneto-structural correlations and to establish the most appropriate theoretical method to predict the *zfs* parameters. Concerning the Mn^{III} complexes, the investigation of their magnetic properties is of great interest and still under progress. Indeed, Mn^{III} is generally found in an octahedral environment combined with an $S = 2$ spin state. Currently, only the iodide derivate is available. Even if this compound displays an $S = 2$ spin state, theoretical calculations predict a first $S = 1$ excited state very close. Therefore synthetic efforts will be carried out to isolate the bromide and chloride derivates. It would be interesting to see how the halides will affect the spin state and the magnetic anisotropy of these compounds.

Experimental section

Table of contents

I. Chapter I 183
Material and methods. 183
Physical methods. 183
Electrochemical measurements. 183
Mössbauer spectroscopy. 184
X-ray Crystallography 184
DFT calculations 184
Synthesis. 185
Synthesis of Diphenylmethanethiol 185
Synthesis of 2-[(Diphenylmethyl)thiol]tetrahydro-2H-pyrane 185
Synthesis of 6,6'-Dibromo-2,2'-bipyridine 185
[2,2'-bipyridine)]-6,6'-dicarbaldehyde 186
Synthesis of [2,2'-bipyridine)]-6,6'-diyldimethanol 186
Synthesis of 6,6'-Bis-(bromomethyl)- 2,2'-bipyridine 186
Synthesis of 6,6'-Bis[2,2-diphenyl-2-(tetrahydropyran-2-ylsulfanyl)ethyl]-2,2'-bipyridine 187
Synthesis of 2,2′-(2,2′-bipyridine-6,6′-diyl) bis -(1,1-diphenylethanethiol) 187
Synthesis of $[Cp(*)Fe(CO)(MeCN)_2]BF_4$ 187
Synthesis of $[(LS)Ni^{II}Fe^{II}(Cp(*))(CO)]BF_4$ ($Ni^{II}Fe^{II}Cp(*)$ 188
Synthesis of $[(LS).Ni^{I}Fe^{II}(Cp)(CO)]$ ($Ni^{I}Fe^{II}Cp$) 188
Reaction of $Ni^{II}Fe^{II}Cp$ with $NaBH_4$ 189
References 189
II. Chapter II 191
Material and Methods 191
X-ray Crystallography. 191
Magnetic measurements. 191
XAS spectroscopy. 192
Electrochemistry. 192
Synthesis 192
Synthesis of $[Mn^{II}_2(LS)(LSH)]ClO_4$ (Mn^{II}_2SH) 193
Synthesis of $[Mn^{III}_2(LS)_2(OH)]ClO_4$ (Mn^{III}_2OH). 193
Synthesis of $[Mn^{IV}_2(LS)_2(O)_2]$ ($Mn^{IV}_2(O)_2$). 194
Catalytic experiments. 194
Detection of H_2O_2 by the Ti-TPyP reagent. 195
Computational details. 196
References 196
III. Chapter III 197
Material and Methods 197
Electrochemical measurements. 197
X-ray Crystallography. 197
Magnetic measurements. 198

Computational details. 198
Synthesis 199
Electrosynthesis of $[Mn^{II}_2(LSSL)](PF_6)_2$ (Mn^{II}_2SS). 199
Synthesis/electrosynthesis of $[Mn^{III}(LS)I]$ 199
Synthesis of $[Co^{III}L(X)]$ (CoX, X=Cl, Br or I) 200
References 201
IV. Chapitre IV 202
Material and Methods 202
Magnetic Measurements 202
Computational details. 202
References 204

I. Chapter I

Material and methods.

Physical methods. The infrared spectra were recorded on a Thermo Scientific Nicolet iS10 FT-IR spectrometer (equipped with ATR accessory) as neat solids. ^{1}H NMR spectra were recorded on Bruker Avance III 400 and 500 MHz spectrometers. The elemental analyses were carried out with a C, H, N analyzer (SCA, CNRS). The ESI-MS spectra were registered on a Bruker Esquire 3000 Plus ion trap spectrometer equipped with an electrospray ion source (ESI). The samples were analyzed in positive ionization mode by direct perfusion in the ESI-MS interface (ESI capillary voltage= 2kV, sampling cone voltage= 40 V). The electronic absorption spectra were recorded on a Varian Cary 300 absorption spectrophotometer in quartz cells (optical path length: 2 mm). X-band EPR spectra were recorded on a Bruker EMX, equipped with the ER-4192 ST Bruker cavity and an ER-4131 VT at 100 K.

Electrochemical measurements. Electrochemical measurements were carried out in MeCN solution, 0.1 M Bu_4NClO_4, under argon (cyclic voltammetry) or nitrogen (bulk electrolysis) atmosphere at 20 °C using a SP300 Bio-Logic potentiostat/galvanostat. A standard three-electrode electrochemical cell was used for cyclic voltammetry experiments. Potentials were referred to an Ag/0.01 M $AgNO_3$ reference electrode in MeCN + 0.1 M Bu_4NClO_4 and measured potentials were calibrated through the use of an internal Fc/Fc^+ standard. The working electrode was a vitreous carbon disk (3 mm in diameter) polished with 2 μm diamond paste (Mecaprex Presi; Ep_a, anodic peak potential; Ep_c, cathodic peak potential; $E_{1/2} = (Ep_a + Ep_c)/2$; $\Delta Ep = Ep_a - Ep_c$). The auxiliary electrode was a Pt wire in MeCN + 0.1 M Bu_4NClO_4 solution. Bulk electrolyses and coulometry were carried out in a three-electrode electrochemical cell using a mercury pool cathode. An Ag/0.01 M $AgNO_3$ reference electrode closed by a Vycor frit was dipped directly into the solution. A titanium wire counter electrode was placed in a separate compartment connected by a glass-frit and filled with 0.1 M solution of Bu_4NClO_4 in degassed CH_3CN. The compartment of the working electrode is continuously flushed by N_2 as a carrier gas, where the rate is fixed through a Bronkhorst mass flow at 5 $mL.min^{-1}$. The output gas is analyzed with a Perkin-Elmer Clarus 500 gas chromatograph equipped with a porapack Q 80/100 column (6' 1/8") thermostated at 40 °C and a TCD detector thermostated at 100 °C. The GC is mounted in a "continuous flow" mode in which the carrier gas stream fills an injection loop of 100 µL in the GC. The contents of the injection loop have fed every 2.01 minutes into the GC, where gases (H_2 and O_2) are separated and areas under peaks computed. A control calibration was performed *via* a chronopotentiometric experiment at a cathodic current of –1 mA, in which a platinum mesh was used as the working electrode to evolve hydrogen from a 0.1 M sulfuric acid solution at pH 0.94.

Mössbauer spectroscopy. Mössbauer spectra were recorded with a ^{57}Co source in a Rh matrix using an alternating constant acceleration *Wissel* Mössbauer spectrometer operated in the transmission mode and equipped with a *Janis* closed-cycle helium cryostat. The isomer shift is given relative to iron metal at ambient temperature. Simulation of the experimental data was performed with the *Mfit* program using *Lorentzian* line doublets (E. Bill, Max-Planck Institute for Chemical Energy Conversion, Mülheim/Ruhr, Germany. E-mail: eckhard.bill@cec.mpg.de; webpage: http://www.cec.mpg.de/research/molecular-theory-and-spectroscopy/moessbauer-mcd.html?L=1).

X-ray Crystallography. Single-crystal diffraction data were collected on an Oxford-Diffraction XCalibur S Kappa geometry diffractometer (Mo-Kα radiation, graphite monochromator, λ 0.71073Å). The CrysAlisPro program package (Agilent Technologies) was used for cell refinements and data reductions. An absorption correction (CrysAlisPro) was applied to the data. The molecular structures were solved by charge flipping method (Superflip)[4] and refined on F2 by full matrix least-squares techniques using SHELXLT[5] in OLEX 2.1.65 software environment.[6] All non-hydrogen atoms were refined anisotropically. All hydrogens were placed at their calculated positions and refined with a riding model. Two crystallographically independent molecules are present in the asymmetric unit containing one ordered and one disordered BF_4^- anions, as well as two ordered and one disordered solvent molecules (Et_2O).

DFT calculations. All theoretical calculations were performed with the ORCA program package.[7] Structure optimizations (Supplementary Table 3) were performed using the resolution of the identity (RI)[8] approximation. The GGA functional BP86[9-11] was employed in combination with the def2-TZV/P[12,13] basis set, and the corresponding def2-TZVP/J auxiliary basis set. Increased integration grids and tight SCF convergence criteria were used. To ensure that the resulting structures converged to a local minimum on the potential energy surface, numerical frequency calculations were performed and resulted in only positive normal vibrations. Electronic structures and spectroscopic parameters (Supplementary Table 4) were calculated with the hybrid functional B3LYP[14,15] in conjunction with the RIJCOSX[16] approximation, the def2-TZVP basis set, and the def2-TZV/J auxiliary basis set. The magnetic properties were evaluated from single point calculations based on the Broken Symmetry (BS) approach using the B3LYP functional and the TZV/P basis set.[17-19] NBO analysis was performed with inclusion of the 3-center bond option in the search algorithm.[20,21] Mossbauer parameters were obtained using an expanded CP(PPP) basis set for iron.[22] Isomer shifts were evaluated using the calibration curve for the B3LYP functional.[23] For g-tensor calculations the triply polarized core property basis set CP(PPP) was applied for the metal center while the EPR-II[24] basis set was used for all remaining atoms. Special care was also taken to ensure accurate results by increasing the size of the integration grid.[25] Chemical shift tensors were obtained using the IGLO-II[26,27] basis set. The

calculated shielding tensors were transformed to relative chemical shifts by subtracting the calculated chemical shift of TMS. Geometries, molecular orbitals and electronic densities were visualized with the Chemcraft program.[28]

Synthesis.

$Ni^{II}L$ was prepared according to a previously reported procedure.[29] $[CpFe(CO)(MeCN)_2]BF_4$ was prepared from $[CpFe(CO)_2(thf)]BF_4$,[2] as reported in the Supplementary Information. All other reagents were used as received. All solvents were dried and distilled prior to use according to conventional methods. All reactions and manipulations were performed under inert atmosphere (argon, in a glove box or in Schlenk tubes).

Synthesis of Diphenylmethanethiol *(a)*.[30] Diphenylmethylchloride (13.0 g, 64.14 mmol) and thiourea (4.5 g, 58.69 mmol) was refluxed in ethanol (30 mL) for 2 h. After which the solution was cooled to room temperature. Upon the addition of NaOH (4 g, 3 M aq.) a precipitate forms and refluxing is continued for a further 2 h. The reaction mixture was then cooled to ambient temperature and the oil was separated. To the aqueous phase H_2SO_4 (1 mL in 10 mL of water) was added, the aqueous phase was then extracted with EtO_2. After reducing the volume under vacuum to 10 mL, the mixture was stored at-18°C overnight. The resulting mixture was filtered to remove impurities, and the filtrate was reduced to the product as an oil (10.0 g, 79 %). ^{1}H NMR (400 nm, $CDCl_3$): δ 7.736 (1H, t, *J* = 8 Hz, H-bipy) δ 7.405 (2H, d, *J* = 8 Hz, H-bipy) δ 4.568 (4H, s, CH_2)

Synthesis of 2-[(Diphenylmethyl)thiol]tetrahydro-2H-pyrane *(b)*.[31] HCl (1 mL, 37%) was added dropwise to a stirring solution of **a** (10.0 g, 50 mM) and 2,3-dihydropyrane, giving a colour change from light yellow to dark brown. After 3 h of stirring, Et_2O (200 mL) was added and the mixture was then washed wit Na_2CO_3 (sat. aq. 2 x 100 mL). The organic phase was extracted and washed with NaCl (sat. aq. 2 x 50 mL). Organic phases were then combined and dried over Na_2SO_4, filtered and reduced to give an orange oil. The orange oil was was purified by column chromatography (SiO_2, AcOEt:Pentane; 1:9). ^{1}H NMR (400 MHz, $CDCl_3$): δ 7.71 (1H,d, Ph), 7.41-7.20 (8H, m, Ph), 5.36 (1H, s, Ph_2CH), 4.63 (1H, m, H-THP), 3.53-3.46 (1, m, H-THP), 1.92 (2H, m, H-THP), 1.53 (6H, m, H-THP).

Synthesis of 6,6'-Dibromo-2,2'-bipyridine *(1)*.[32] This procedure was modified from the reported procedure of Artaud *et. al.* A solution of 44.43 ml of 2M of *n*-BuLi (88.83 mmol, 1.05 eq) was dropped slowly to a solution of 2,6-dibromo-pyridine (84,43 mmol, 20 g, 1 eq) in dry Et_2O (300 mL) over 30 min at -78˚C. After 45 min of stirring, anhydrous $CuCl_2$ (42.32 mmol, 5.69 g, 0.527 eq) was added with keeping the temperature at -78˚C. By warming from -78°C to -50°C dioxygen was

gently bubbled through the solution for 1 h with vigorous stirring. Then, the mixture was hydrolyzed with 210 ml of 1.2N HCl under -50˚C. The crude product was recrystallized in EtOH (300 mL).The residue was filtered, dried in vacuous with P_2O_5 and collected as a white powder (7.3 g, 55%). ^{1}H NMR (δ, $CDCl_3$): 7.50 (d, 2H *J* = 7.9 Hz,), 7.67 (t, 2H *J* = 7.8 Hz), 8.37 (d, 2H *J* = 7.8 Hz). Anal. Calcd. for $C_{10}H_6Br_2N_2$: C, 38.25; H, 1.93; N, 8.92. Found: C, 38.43; H, 2.08; N, 8.88.

[2,2'-bipyridine)]-6,6'-dicarbaldehyde *(2).* [33] This procedure was modified from the reported procedure of Parks *et. al*. **1** (7.3 g, 22.93 mmol) was dissolved in THF (180 mL) and slowly added to a solution of *n*-BuLi (2.5 M in hexane, 10.5 mL, 26.74 mmol) in THF (80 mL) at -78 °C. After 45 min at -78 °C, DMF (6.3 mL, 80.3 mmol) was added dropwise to the mixture. After 1 h at-78 °C the dark violet mixture was warmed to -30 °C and quenched with HCl 4 M (90 mL). It was basified with Na_2CO_3 (aq, sat) and concentrated under vacuum to remove the organic solvent. The aqueous suspension was extracted with $CHCl_3$ (5 × 100 mL). The organic layers were mixed and dried with Na_2SO_4. After removing the solvents under vacuum, the residual solid was washed with methanol (45 mL) and diethyl ether and dried in vacuo, yielding **b2** as a pale yellow powder (3.147 g, 14.83 mmol, 65 %). ^{1}H NMR (400 MHz, $CDCl_3$): δ 8.05 (m, 4H, CH) δ 8.83 (dd, J_{orto} = 7.2 Hz, J_{meta} = 2.0 Hz, 2H, CH *para*-CHO) δ 10.19 (2H, s, CHO).

Synthesis of [2,2'-bipyridine)]-6,6'-diyldimethanol *(3)*. [33] This procedure was modified from the reported procedure of Parks *et. al.* **2** (3.2 g, 14.83 mmol) and $NaBH_4$ (1.40 g, 37.1 mmol) in methanol (165 mL) were stirred at ambient temperature for 2 h. HCl 1.2 M (52 mL) was added to the solution and stirring was continued, after 10 min the mixture was basified with Na_2CO_3 (aq, sat) and concentrated under vacuum to remove the organic solvent. The aqueous suspension was extracted with $CHCl_3$ (5 × 100 mL). The organic layers were mixed and dried with Na_2SO_4. After removing the solvents under vacuum, the residual solid was washed with methanol (45 mL) and diethyl ether and dried in vacuo, yielding **3** as a pale cream powder (3.15 g, 14.2 mmol, 95 %). ^{1}H NMR (400 MHz, $CDCl_3$): δ 3.97 (t, J = 4.3 Hz, 2H, OH), 4.84 (d, J = 4.3 Hz, 4H, CH_2), 7.27 (d, 2H, CH), 7.84 (d, J = 7.8 Hz, 2H, CH *para*-N), 8.36 (d, J = 4.3 Hz, 2H, CH *para*-CH_2OH).

Synthesis of 6,6'-Bis-(bromomethyl)- 2,2'-bipyridine *(4).* [32] HBr (33 % in acetic acid, 90 mLl) was added to **3** (3.15 g, 14.1 mmol). The mixture was refluxed for 3 h. After cooling to room temperature and stirring at room temperature for 14 hours, it was basified with K_2CO_3 (aq, sat, excess). The precipitate was filtered, and washed with water (6 x 100 mL) and EtOH (2 x 20 mL). The crude product was recrystallized in EtOH (100 mL). the powder was filtered, dried collected and

sonicated during 15 minyielding a pale white powder **4** (2.84 g, 8.34 mmol, 63 %).[1]H NMR (300 MHz, $CDCl_3$): 4.62 (s, 4H, CH_2), 7.47 (d, J = 7.8 Hz, 2H, $CH_{meta\text{-}N}$ py), 7.82 (t, J = 7.8 Hz, 2H, $CH_{para\text{-}N}$ py), 8.38 (d, J = 8.1 Hz, $CH_{meta\text{-}N}$ py).

Synthesis of 6,6'-Bis[2,2-diphenyl-2-(tetrahydropyran-2-ylsulfanyl)ethyl]-2,2'-bipyridine *(5)*.[31] A solution of **b** (4.94 g, 18.48 mmol) in distilled diethyl ether (80 mL) was cooled to -80 ˚C, and *n*-BuLi (6.9 mL, 2.5 % in hexanes) was added dropwise. The solution was then allowed to warm to ambient temperature over 1 h. This solution was then cooled again to -80 ˚C and a solution of **4** (2.84 g, 8.34 mmol) and HMPA (17.5 mL) in distilled THF (180 mL) was added. This solution was then allowed to warm to ambient temperature over 4 h, after which the reaction solution was quenched with water (200 mL) and the organic phase was separated. The aqueous phase was then extracted with EtOAc (3 × 100 mL). The organic fractions were then combined and dried over Na_2SO_4, filtered and reduced to an orange oil. The resulting oil was then dissolved in minimal amount of acetone and left in the fridge overnight. The insoluble fraction was filtered and washed with acetone (3 × 20 mL) and Et_2O (3 × 20 mL) yielding a white solid (4.1 g, 5.56 mmol, 67 %).[1]H NMR (400 MHz, $CDCl_3$): δ 4.62 (s, 4H, CH_2), 7.47 (d, J = 7.8 Hz, 2H, CH *meta*-N), 7.82 (d, J = 7.8 Hz, 2H, CH *para*-N), 8.38 (d, J = 8.1 Hz, 2H, CH *meta*-N).

Synthesis of 2,2′-(2,2′-bipyridine-6,6′-diyl) bis -(1,1-diphenylethanethiol) *LS (6).*[31] To a suspension of compound **5** (4.1 g, 5.56 mmol) in ethyl acetate (125 mL) and methanol (95 mL) was added a solution of $AgNO_3$ (2.35 g, 2.5 eq) in pyridine (1.4 mL) and methanol (160 ml). The solid material dissolved immediately and the solution became yellow. After 5 h at room temperature the solvent was removed under vacuum yielding a yellow powder. The material was dissolved in deaerated dichloromethane (70 mL) and H_2S bubbled through the solution until the solution became colorless. The black precipitate was filtered off and washed thoroughly with dichloromethane (500 mL). The combined filtrates were washed with $NaHCO_3$ (aq, sat) and the aqueous layer extracted with CH_2Cl_2. The combined organic layers were dried over Na_2SO_4, the solvent was removed under vacuum and the residual solid was washed with MeOH (3x15 mL) to yield 2.83 g (90%) of the product as a white powder **6**. **[1]**H NMR, (400 MHz, $(CD_3)_2SO$): δ 7.72 (2H, d, *J* = 7.5, H bipy, H), 7.55 (2H, t, *J* = 7.5 Hz, Hbipy), 7.45–7.3 (8H, m, *o*-H of Ph), 7.3–7.15 (12 H, m, *m*- and *p*-H of Ph), 6.79 (2H, d, H bipy), 4.1 (2H, br s, 2 SH) and 4.05 (4H, s, CH_2^7, $CH_2^{7'}$). The resonance at δ 4.1 disappeared upon addition of D_2O.

Synthesis of $[Cp(*)Fe(CO)(MeCN)_2]BF_4$. $[CpFe(CO)(MeCN)_2]BF_4$[1,2] was prepared according to

the following new method. [Cp(*)Fe(CO)$_2$(thf)]BF$_4$[3] (1.01 g, 3.0 mmol) was placed in an oven-dried photolysis flask and dissolved in MeCN (15 mL) to give a red solution. The flask was carefully placed under a partial vacuum and exposed to a UV filtered Hg/Xe lamp, resulting in the evolution of gas bubbles. The reaction was monitored by FTIR (before exposure for [CpFe(CO)$_2$(thf)]BF$_4$: 2073 cm^{-1}, 2026 cm^{-1}, 2253 cm^{-1}; after exposure: 2008 cm^{-1}; before exposure for [Cp*Fe(CO)$_2$(thf)]BF$_4$: 2054 cm^{-1}, 2006 cm^{-1}; after exposure: 1976 cm^{-1}) and UV-Vis spectroscopy, and after 10 days the mixture was filtered via celite loaded cannula, layered with Et$_2$O (40 ml) and cooled overnight (-26 ºC) to give [CpFe(CO)(MeCN)$_2$]BF$_4$ as a light brown powder (0.84 g, 87%). IR (cm^{-1}, MeCN): 2008 (CO). NMR and microanalytical data correspond to those previously reported for [CpFe(CO)(MeCN)$_2$]BF$_4$.[1]

Synthesis of [(LS)Ni^{II}Fe^{II}(Cp(*))(CO)]BF$_4$ (Ni^{II}Fe^{II}Cp(*)). Solid **Ni^{II}L** (0.157 mmol) was added to a solution of [Cp(*)Fe(CO)(MeCN)$_2$]BF$_4$ (0.157 mmol) in CH$_2$Cl$_2$ (10 mL) under stirring at 20 °C. The color of the resulting solution slowly turned to dark brown. After 48 hours, diethyl ether was allowed to slowly diffuse into the reaction solution. After few days, X-ray suitable dark brown crystals, corresponding to **Ni^{II}Fe^{II}Cp(*)**BF$_4$ were obtained.

Ni^{II}Fe^{II}Cp. Crystals were filtered, washed with diethyl ether and dried (0.130 mmol, 83%). IR (cm^{-1}): 3055w, 3027w, 2350w, 1929vs (CO stretching), 1604m, 1488m, 1442m, 1425w, 1265w, 1053s, 1030s, 810m, 803w, 753m, 695s. ^{1}H NMR (400 MHz, CD$_3$CN): δ 7.87 (d, J = 7.4 Hz, 2H, CH bpy), 7.67 (t, J = 7.9 Hz, 2H, CH bpy), 7.56 (s br, 4H), 7.38 (m, 10H), 7.20 (m, 6H), 6.70 (d, J = 7.4 Hz, 2H, CH bpy), 4.11 (d, J = 13.4 Hz, 2H, CH of diastereotopic CH$_2$), 3.86 (d, J = 13.4 Hz, 2H, CH of diast. CH$_2$), 3.52 (s, 5H, CH Cp). ESI-MS (5·10^{-5} M, MeCN, m/z, I%): 785.2 100 [M]$^+$. Anal. Calcd. for C$_{44}$H$_{35}$FeN$_2$NiOS$_2$BF$_4$·0.5Et$_2$O·0.9H$_2$O (926.51): C, 59.63; H, 4.55; N, 3.02; Found: C, 59.69; H, 4.38; N, 3.19.

Ni^{II}Fe^{II}Cp*; Crystals were filtered, washed with diethyl ether and dried (0.130 mmol, 83%). IR (cm^{-1}): 3055w, 3027w, 2350w, 1926vs (CO stretching), 1604m, 1488m, 1442m, 1425w, 1265w, 1053s, 1030s, 810m, 803w, 753m, 695s. ^{1}H NMR (500 MHz, CD$_3$CN): δ 8.20 (s, br, 2H, H$_{arom}$), 7.49 (m, 10H, H$_{arom}$), 7.28 (t, J =7.23 Hz, 4H, H$_{arom}$), 7.11 (q, 6H, H$_{arom}$), 7.03 (t, J =7.04 Hz, 2H, H$_{arom}$), 6.93 (m, 2H, H$_{arom}$), 4.14 (d, br, 4H, CH of diastereotopic CH$_2$), 0.71 (s, 15H, CH$_3$, pentamethylcyclopendienyl). ESI-MS (5·10^{-5} M, MeCN, m/z, I%): 855.0 100 [M]$^+$. Anal. Calcd. for C$_{49}$H$_{45}$FeN$_2$NiOS$_2$BF$_4$·0.2Et$_2$O·0.1H$_2$O (959.99): C, 62.31; H, 4.96; N, 2.92; Found: C, 62.54; H, 4.96; N, 3.10.

Synthesis of [(LS).Ni^{I}Fe^{II}(Cp)(CO)] (Ni^{I}Fe^{II}Cp). A solution of bis(cyclopentadienyl)cobalt(II) (7.2 mg, 0.038 mmol) in MeCN (2 mL) was added to a solution of **Ni^{II}Fe^{II}Cp** (30.0 mg, 0.034 mmol) in MeCN (2 mL) at 20 °C, yielding a black precipitate. After 15 min, it was filtered, washed with MeCN (1 mL), dried and collected as a black powder (18.0 mg, 67%). IR (cm^{-1}): 3056w, 1889w (minor species,

assigned to [(LS)$Ni^{I}(OH_2)Fe^{II}$(Cp)(CO)], 1770vs (CO stretching), 1593w, 1487m, 1440m, 1418w, 1390m, 1080w, 1032w, 804w, 786w, 751m, 701s, 670m.

Reaction of $Ni^{II}Fe^{II}$Cp with $NaBH_4$. When a solution of $NaBH_4$ in EtOH (freshly distilled over CaH_2, 5-20 equiv.) was added to one of **$Ni^{II}Fe^{II}$Cp** (10 mM) in MeCN, a black precipitate was formed. After 3 min, it is filtered, dried and analysed by IR spectroscopy. The infrared spectrum showed a mixture of three products: **$Ni^{I}Fe^{II}$Cp** (main product, CO peak at 1770 cm^{-1}), [(LS)$Ni^{I}(OH_2)Fe^{II}$(Cp)(CO)] (CO peak at 1888 cm^{-1}), and [(LS)Ni^{II}(H)Fe^{II}(Cp)(CO)] (**$Ni^{II}Fe^{II}$(H)**, CO peak at 1838 cm^{-1}). **$Ni^{II}Fe^{II}$(H)** can be identified (and quantified) also by the presence of a singlet at -6.81 ppm (H-Ni) in the ^{1}H NMR spectrum in d^{8}-thf. up to a ~15% of **$Ni^{II}Fe^{II}$(H)** could be detected under the present conditions.

References

1. Cutler, A. R. & Todaro, A. B. *Organometallics* **1988**, *7*, 1782-1787.
2. Lai, C.-H. *et al. J. Am. Chem. Soc.* ***1998***, *120*, 10103-10114.
3. Reger, D. L. & Coleman, C. *J. Organomet. Chem.* **1977**, *131*, 153-162.
4. Palatinus, L. & Chapuis, G. *J. Appl. Cryst.* **2007**, *40*, 786-790.
5. Sheldrick, G. M. *Acta Cryst. C.* **2015**, *71*, 3-8.
6. Dolomanov, O. V., Bourhis, L. J., Gildea, R. J., Howard, J. A. K. & Puschmann, H. Olex II: *J. Appl. Crystallogr.* **2009**, *42*, 339-341.
7. Neese, F. The ORCA program system. *Wiley Interdiscip. Rev. Comput. Mol. Sci.* **2012**, *2*, 73-78.
8. Vahtras, O., Almlöf, J. & Feyereisen, M. W. *Chem. Phys. Lett.* 1993, *213*, 514-518.
9. Becke, A. D. *Phys. Rev. A.* 1988, *38*, 3098-3100.
10. Perdew, J. P. *Phys. Rev. B.* **1986**, *33*, 8822-8824.
11. Perdew, J. P. *Phys. Rev. B.* **1986**, *34*, 7406-7406 .
12. Schäfer, A., Horn, H. & Ahlrichs, R. J. *Chem. Phys.*, **1992**, 2571-2577.
13. Weigend, F. & Ahlrichs, R. *Phys. Chem. Chem. Phys.* **2005**, *7*, 3297-3305.
14. Becke, A. D*J. Chem. Phys.* **1993**, *98*, 1372-1377.
15. Lee, C. T., Yang, W. T. & Parr, R. G. *Phys. Rev. B*. **1988**, *37*, 785-789.
16. Neese, F., Wennmohs, F., Hansen, A. & Becker, U. *Chem. Phys.* **2009**, *356*, 98-109.
17. Noodleman, L. *J. Chem. Phys.* **1981**, *74*, 5737-5743.
18. Noodleman, L. & Case, D. A. *Adv. Inorg. Chem.* **1992**, *38*, 423-458.
19. Noodleman, L. & Davidson, E. R. *Chem. Phys.* **1986**, *109*, 131-143.
20. Reed, A. E., Curtiss, L. A. & Weinhold, F. *Chem. Rev.* **1988**, *88*, 899-926.
21. Wiberg, K. B. *Tetrahedron*. **1968**, *24*, 1083-1096.
22. Neese, F. *Inorg. Chim. Acta*. **2002**, *337*, 181-192.
23. Römelt, M., Ye, S. & Neese, F. *Inorg. Chem.* **2009**, *48*, 784-785.
24. Barone, V. in *Recent advances in density functional methods* Vol. Part I., D. P. Chong (World Scientific, **1996**).
25. Neese, F. *J. Chem. Phys. 118*, 3939-3948 **2003**.
26 Kutzelnigg, W., Fleischer, U. & Schindler, M. Vol. 23 (Springer-Verlag, **1990**).
27. Huzinaga, S. *J. Chem. Phys. 42*, 1293-1302 **1965**.
28. Chemcraft. (http://chemcraftprog.com).
29. Gennari, M. *et al. Inorg. Chem.* **2010**, *49*, 6399-6401.
30. Klenk, M., M. Suter, C. M., Archer, S. *J. Am. Chem. Soc.*, **1948**, *70*, 3846–3850.
31. Berg, J. M., Holm, R. H., *J. Am. Chem. Soc.*, **1985**, *107*, 917–925.

32. Artaud, I., Chatel, S., Chauvin, A. S., Bonnet, D., Kopf, M. A., Leduc, P. Coord. Chem. Rev, **1999**, *190-192*, 577-586.
33. Parks, J. E.; Wagner, B. E.; Holm, R. H., Journal of Organometallic Chemistry, **1973**, *56*, 53-66.

II. Chapter II

Material and Methods.

X-ray Crystallography. Single-crystal diffraction data of **Mn^{II}_2SH**·1.55CH_3CN·0.45CH_3OH were measured on an Oxford-Diffraction XCalibur diffractometer with a Sapphire 3 CCD detector (MoKα radiation, graphite monochromator, λ 0.71073Å) at 150(2) K. The CrysAlisPro program package (Agilent Technologies) was used for cell refinements and data reductions. For both complexes an absorption correction (CrysAlisPro) was applied to the data. Single-crystal diffraction data of **$Mn^{III}_2OH^{\#}$**·7.16CH_3CN were collected at beamline proxima1 of the Soleil synchrotron (Saint-Aubin, France) using a Dectris Pilatus 6M detector (λ = 0.8856 Å) at 100 K. Indexation, absorption correction and scaling of the data were performed using XDS Package.[1] The molecular structures of all the complexes were solved by direct methods and refined on F^2 by full matrix least-squares techniques using SHELXTL package.[2] All non-hydrogen atoms were refined anisotropically for both complexes. In the case of **Mn^{II}_2SH**·1.55CH_3CN·0.45CH_3OH, all hydrogen atoms were found by Fourier transformation and refined with individual isotropic displacement parameters, except those on solvent molecules. For the **$Mn^{III}_2OH^{\#}$**·7.16CH_3CN, hydrogen atoms were placed at their calculated positions. The structure of **Mn^{II}_2SH**·1.55CH_3CN·0.45CH_3OH contains partially occupied solvent molecules (CH_3CN, CH_3OH), whereas the structure of **$Mn^{III}_2OH^{\#}$**·7.16CH_3CN contains partially occupied anions (PF_6^-, ClO_4^-) and solvent molecules (CH_3CN). T*wo crystallographically independent* molecules are present in the asymmetric *unit of* **$Mn^{III}_2OH^{\#}$**·7.16CH_3CN. The structure of the **$Mn^{IV}_2(O)_2$**·0.64CH_2Cl_2·2.71H_2O.complex contains molecule of solvents (CH_2Cl_2 and H_2O).

Magnetic measurements. Magnetic measurements were performed on polycrystalline samples of **Mn^{II}_2SH**·1.55CH_3CN·0.45CH_3OH and **$Mn^{III}_2OH^{\#}$**·7.16CH_3CN with mass of 14.2 and 16.75 mg respectively. Magnetic measurement for $Mn^{IV}_2(O)_2$ are still under investigation. Samples were sealed in polyethylene bags (3 × 0.5 × 0.02 cm; 21.90 and 23.23 mg) in order to collect data in the temperature range of 1.8 to 300 K at 1000 Oe. Magnetic measurements were obtained with the use of a Quantum Design SQUID magnetometer MPMS-XL functioning between 1.8 and 400 K for direct-current (dc) applied fields ranging from -7 to +7 T. Prior to the experiments, the field-dependent magnetization was measured at 100 K on each sample in order to prove the absence of any bulk ferromagnetic impurities. On the other hand, when fitting the magnetic data, it was necessary to introduce in the magnetic model a paramagnetic Curie impurity that was assumed to be a mononuclear Mn^{II} species (S = 5/2) for **Mn^{II}_2SH**·1.55CH_3CN·0.45CH_3OH and a mononuclear Mn^{III} species (S = 2) for **$Mn^{III}_2OH^{\#}$**·7.16CH_3CN. Their amount was estimated at 0.5(2) and 3.0(5) % respectively. All magnetic data were corrected for the sample holder and diamagnetic contributions.

XAS spectroscopy. Manganese K-edge X-ray absorption spectra were recorded in transmission mode at beamline 7-3 of the Stanford Synchrotron Radiation Lightsource (SSRL) with ring conditions of 3 GeV and 350 mA. Energy selection was achieved using a double crystal Si(220) monochromator and an upstream Rh-coated mirror provided harmonic rejection (together with 25% detuning) and an energy cutoff of 9 keV. Samples were prepared in an argon atmosphere glovebox by diluting the solid compounds with boron nitride, grinding to a fine powder, and packing into a 1 mm think aluminum sample cell sealed with 38 µm Kapton tape. During measurement, samples were maintained at 10 K in an Oxford CFI208 liquid helium flow cryostat. Data were normalized with respect to the incident beam using an upstream N_2-filled ion chamber and the energy was calibrated using the first inflection point of a Mn foil (6539.0 eV). Sulfur K-edge XAS experiments were performed at SSRL beamline 4-3 under identical ring conditions. Samples were prepared in an argon atmosphere glovebox by grinding the compounds together with boron nitride and then dispersing as thinly as possible on 38 µm Kapton tape. A window of 5 µm polypropylene was applied over the samples to prevent exposure to air during sample changes. All samples were measured at room temperature in a He atmosphere in fluorescence mode using a Lytle detector. The incident energy was selected with a Si(111) double crystal monochromator and calibrated using the pre-edge of $Na_2S_2O_3 \bullet 5\ H_2O$ (2472.02 eV). All data were calibrated and averaged using EXAFSPAK[3] (3-5 scans for each spectrum) and normalized to an edge jump of one using Blueprint XAS.[4]

Electrochemistry. Electrochemical experiments were performed in acetonitrile solution under an argon-saturated (in a glove box or by argon purging) atmosphere. Tetrabutylammonium hexafluorophosphate (NBu_4PF_6) was used as received and stored in glove box. Cyclic voltammetry and controlled potential electrolysis experiments were carried out by using a SP300 Bio-Logic potentiostat/galvanostat. A standard three-electrode electrochemical cell was used. Potentials were referred to an Ag/0.01 M $AgNO_3$ reference electrode in CH_3CN + 0.1 M Bu_4NClO_4 and measured potentials were calibrated through the use of an internal Fc/Fc^+ standard. The working electrode was a vitreous carbon disk (3 mm in diameter) polished with 2 µm diamond paste (Mecaprex Presi) for cyclic voltammetry (Ep_a, anodic peak potential; Ep_c, cathodic peak potential; $E_{1/2} = (Ep_a + Ep_c)/2$; $\Delta Ep = Ep_a - Ep_c$). Exhaustive electrolyses were carried out on reticulated vitreous carbon electrode 45 PPI (the electrosynthesis Co. Inc.; 1 cm^3). The auxiliary electrode was a Pt wire in CH_3CN + 0.1 M Bu_4NClO_4.

Synthesis

LS was prepared according to a reported procedure as described in experimental section, chapter I.[22] All other reagents and solvents were used as received. THF was distilled over Na/benzophenone prior to use. Acetonitrile (99.9+ %, extra dry) was distilled over CaH_2 prior to use. The synthesis of the complexes was performed under argon (in a glove box with less than 5 ppm of O_2 for **Mn^{II}_2SH**, and in

a Schlenk tube for **Mn^{III}_2OH**). *Caution! Perchlorate salts of metal complexes are potentially explosive. Only small quantities of material should be prepared and the samples should be handled with care.* The elemental analyses were carried out with a C, H, N analyzer (SCA, CNRS). The ESI-MS spectra were registered on a Bruker Esquire 3000 Plus ion trap spectrometer equipped with an electrospray ion source (ESI). The samples were analyzed in positive ionization mode by direct perfusion in the ESI-MS interface (ESI capillary voltage= 2kV, sampling cone voltage= 40 V). The electronic absorption spectra were recorded on a Varian Cary 300 absorption spectrophotometer in quartz cells (optical path length: 1 cm).

Synthesis of $[Mn^{II}_2(LS)(LSH)]ClO_4$ (Mn^{II}_2SH). Solid KH (30% in mineral oil, 150 mg, 1.122 mmol) was added to a solution of H_2L (200 mg, 0.344 mmol) in THF (10 mL). After 20 min, the excess of KH was filtered off and a solution of $Mn(ClO_4)_2{\cdot}6H_2O$ (310 mg, 0.856 mmol) in THF (5 mL) was slowly added to the yellow solution under stirring. During the addition, the color of the solution turned to dark brown, and subsequently to orange. After few minutes, a pale orange precipitate was formed. After 1 hour, this solid was separated from the mother liquid by filtration and extracted with dichloromethane (3 × 5 mL). The solvent was removed in vacuo, and the residual solid was washed with THF (3 mL), dried and collected as a pale orange powder (**Mn^{II}_2SH**, 182 mg, 0.133 mmol, 77%). ESI-MS ($5{\cdot}10^{-4}$ M, CH_3CN, *m/z*, I%): 633.2, 100 $[MnL]^+$ + $[Mn_2L(LH)]^{2+}$; 1267.2, 95 $[Mn_2L_2]^+$. Anal. Calcd. for $C_{76}H_{61}N_4S_4Mn_2ClO_4{\cdot}0.5KClO_4$ (1437.19): C, 63.51; H, 4.28; N, 3.90; Found: C, 63.40; H, 4.36; N, 3.79. Absorption spectrum in CH_3CN (λ_{max}, nm (ε, M^{-1} cm^{-1})): 309 (~25000). X-ray suitable orange-brown single crystals corresponding to **Mn^{II}_2SH**$\cdot 1.55CH_3CN \cdot 0.45CH_3OH$ were obtained by slow diffusion of diethyl ether onto a solution of the product in acetonitrile at 293 K.

Synthesis of $[Mn^{III}_2(LS)_2(OH)]ClO_4$ (Mn^{III}_2OH). A suspension of **Mn^{II}_2SH** (30 mg, 0.021 mmol) in acetonitrile (10 mL) in presence of 0.2 M Bu_4NClO_4 was cooled to 0 ºC. Dry air (10 mL, 293 K, 0.086 mmol O_2) was added, yielding a dark red-violet solution. *Note that,* w*hen vigorous bubbling of O_2 is carried out on a **Mn^{II}_2SH** solution, **Mn^{III}_2OH** is not the main product of the reaction but $Mn^{IV}_2(O)_2$ (see below).* After few minutes, a dark red-purple precipitate was formed. After stirring for 1 h at 0 ºC, this solid was filtered, washed with acetonitrile (2 × 2 mL), dried and collected as a dark red-purple powder (**Mn^{III}_2OH**, 18 mg, 0.013 mmol, 62%). ESI-MS ($6.5{\cdot}10^{-5}$ M, CH_3CN, *m/z*, I%): 633.3, 16 $[MnL]^+$ + $[Mn_2L(LH)]^{2+}$; 1283.5, 100 $[(MnL)_2OH]^+$. Anal. Calcd. for $C_{76}H_{61}N_4S_4Mn_2OClO_4$ (1383.92): C, 65.95; H, 4.44; N, 4.05; Found: C, 66.06; H, 4.57; N, 3.91. Absorption spectrum in CH_3CN (λ_{max}, nm (ε, M^{-1} cm^{-1})): 311 (~27500), 530 (~4300). **Mn^{III}_2OH** crystallizes from the following procedure: 1.5 equiv of dioxygen were added into a 0.9 mM solution of **Mn^{II}_2SH** in acetonitrile at -18 ºC, in presence of 0.02 M Bu_4PF_6,

without stirring. After few days, X-ray suitable dark red single crystals of the product were obtained, corresponding to $[(Mn^{III}L)_2(OH)](PF_6)_{0.81}(ClO_4)_{0.19})$ (**$Mn^{III}_2OH^{\#}$**)·7.16CH_3CN.

Synthesis of $[Mn^{IV}_2(LS)_2(O)_2]$ ($Mn^{IV}_2(O)_2$). Solid NaH (10 mg, 0.25 mmol, excess) was added to a suspension of **Mn^{II}_2SH** (30 mg, 0.021 mmol) in acetonitrile (4 mL). The suspension was stirred for 30 min under argon. After removing the solvent under vacuum the residual brown solid was extracted with dichloromethane (10 mL) giving a brown solution. $CH_2Cl_2$was removed under vacuum and then acetonitrile was added to give a brown suspension. Dry dioxygen was bubbled vigorously for 2 min into this suspension to give a dark brown mixture. The obtained suspension was sonicated for 10 min in order to complete the precipitation of the dark brown solid. The solid was filtered, washed with acetonitrile (2 X 2 mL), dried and collected as a dark black powder (**$Mn^{IV}2(O)_2$**, 16mg, 0.012 mmol, 60%). Anal. Calcd. for $C_{76}H_{61}N_4S_4Mn_2O_2.3CH_2Cl_2$. 2.1MeCN.2$H_2O$. (1632.86): C, 59.6; H, 4.67; N, 4.2; Found: C, 59.53; H, 4.57; N, 4.2. $Mn^{IV}_2(O)_2$ crystallizes from the following procedure: after layering MeOH on a solution of CH_2Cl_2 containing $Mn^{IV}_2(O)_2$ at -40°C, X-ray suitable crystal were obtained.

Catalytic experiments. The oxidation of Me_nFc (n = 8,10) by O_2 in the presence of a catalytic amount of **Mn^{II}_2SH** and an excess of 2,6-lutidinium tetrafluoroborate (LutHBF_4) was monitored by visible absorption spectroscopy in CH_3CN at 293 K for both Me_8Fc and $Me_{10}Fc$, and in propionitrile and acetone at 233 K for $Me_{10}Fc$. In a typical experiment, an air-saturated solution of LutHBF_4 (25 µL, 2.0 M) was added to an air-saturated solution of Me_nFc (2.225 mL, 2.24 mM), in presence of air (1 atm, 0.21 atm O_2), in a septum-sealed 1 cm quartz cuvette kept at 293 K, or at 233 K by a cryostat. After stirring for 5 s, an Ar-saturated solution of **Mn^{II}_2SH** (250 µL, 1.0 mM) was added to the sample under stirring (air-saturated, 2.0 mM Fc*, 15.0 mM LutHBF_4, 100 µM **Mn^{II}_2SH**). The increase in the absorbance of a band at 750 or 778 nm (corresponding to the formation of the Me_nFc^+ ion for Me_8Fc and $Me_{10}Fc$, respectively) was monitored with time, by using a MCS 501 UV-NIR (Carl Zeiss) photodiode-array spectrophotometer (Δt = 1 s). The corresponding blank experiment was performed in the same conditions, by adding degassed solvent (250 µL) instead of the **Mn^{II}_2SH** solution. The ε values for the absorption maxima of Me_nFc^+, required to determine the concentration of formed Me_nFc^+ in the samples, were estimated by the electron-transfer oxidation of Me_nFc with $AgBF_4$ (ε_{750} Me_8Fc^+ = 383 M^{-1} cm^{-1}, ε_{778} $Me_{10}Fc^+$ = 495 M^{-1} cm^{-1}). All the experiments were repeated 3 times, obtaining highly reproducible data (in the 5% range).

Detection of H_2O_2 by the Ti-TPyP reagent.

a) Stoichiometric conditions. A series of sample solutions was prepared, containing **Mn^{II}_2SH** (0.8 mM) in CH_3CN, in presence of different equivalents (0, 5, 10, 20, 30, 40, 50) of $LutHBF_4$, prepared under argon (glove box) and stirred to air for 3 min before analysis.

b) Catalytic conditions. Samples were prepared as described above (air-saturated solution, 2.0 mM Me_nFc, 15.0 mM $LutHBF_4$, 100 μM **Mn^{II}_2SH**), at 293 K in CH_3CN (Me_8Fc and $Me_{10}Fc$) and at 233 K in propionitrile or acetone ($Me_{10}Fc$), and analyzed after reaction completion.

c) Method. The amount of produced hydrogen peroxide in the samples was determined by spectroscopic titration with an acidic solution of $[TiO(tpypH_4)]^{4+}$ complex (Ti-TPyP reagent).[23]

Detailed procedure for the detection of H2O2 by the Ti-TPyP reagent. The Ti-TPyP reagent (~$4.5 \cdot 10^{-5}$ M) was prepared by dissolving 3.44 mg of the [TiO(tpyp)] complex (≥90%, from TCI) in 100 mL of 0.05 M HCl(aq) and stored at 277 K. A small portion (15 μL) of each sample solution was added to a mixture of Ti-TPyP reagent (250 μL), 4.8 M perchloric acid (250 μL) and water (235 μL). The resulting solution was then allowed to stand for 5 min at 293 K. After dilution to 2.5 mL with water in a 1 cm pathlength UV-vis cuvette, the absorbance at λ = 433 nm was measured. A blank solution was prepared in a similar manner by adding the corresponding solvent (15 μL) instead of sample solutions. All the experiments were repeated 3 times, obtaining highly reproducible data (in the 2% range). A decrease in the absorbance from the blank value is expected if the sample contains H_2O_2. In particular, H_2O_2 concentration in the sample is related to $\Delta A_{sample(i)} = A_{blank} - A_{sample(i)}$. The method was calibrated by replicating the same procedure using aqueous solutions of H_2O_2 (in the 0-5 μM range, prepared by dilution of a 0.105 M standard solution), instead of the sample solutions. The obtained ΔA values ($\Delta A_{cal(i)}$) were plotted against H_2O_2 concentration in the *final sample*, $[H_2O_2]_{\text{final sample}}$ (μM), giving the following calibration equation (Equation 1):

$$[H_2O_2]_{\text{final sample}} = (\Delta A + 0.0035) / 0.1488 \qquad (1)$$

Based on this equation, the amount of hydrogen peroxide in the different *final samples* ($A_{sample(i)}$) was determined. The concentration of H_2O_2 in the *original samples* (*i.e.* before addition to the Ti-TPyP reagent solution) is determined by taking into account the dilution factor (Equation 2):

$$[H_2O_2]_{\text{original sample}}\ (\mu M) = [H_2O_2]_{\text{final sample}} \cdot 2500/15 \qquad (2)$$

Note. The amount of H_2O_2 lost by decomposition during catalytic oxidation of Me8Fc in CH_3CN at 293 K was roughly estimated by performing the Ti-TPyP test, both at t = "0 s" and at t = 600 s, on a stirred 1 mM solution of H_2O_2 (corresponding to the maximum expected amount of H_2O_2) in the presence of 2.0 mM Me_nFc, 15.0 mM $LutHBF_4$, 100 μM **Mn^{II}_2SH** under Ar atmosphere.

Computational details. Density functional theory calculations employed the crystallographic structures of **Mn^{II}_2SH** and **Mn^{III}_2OH** and were carried out with ORCA.[11] Broken-symmetry geometry optimizations on the antiferromagnetic potential energy surface used the hybrid B3LYP functional,[12] D3 dispersion correction with the Becke-Johnson damping,[13] and the zero-order regular approximation (ZORA) Hamiltonian.[14, 15] The ZORA recontracted version of the def2-TZVP basis set was used for all atoms, except hydrogen and carbon for which it was reduced to the ZORA version of the def2-SVP.[16, 17] The RIJCOSX approximation to Coulomb and exact exchange used increased integration grids, "Grid6" and "GridX6" in ORCA convention, to accurately describe the metal centers.[18] The conductor-like screening model (COSMO) with appropriate parameters described the acetonitrile solvent.[19] Absorption spectra calculation used the range-separated CAM-B3LYP functional,[20] and was similar for the additional computational details with the geometry optimizations. Natural transition orbitals (NTOs) simplified the analysis of the individual electronic transitions.[21]

References

1. Kabsch, W., *Acta Crystallogr. Sect. D-Biol. Crystallogr.* **2010,** *66*, 125-132.
2. Sheldrick, G. M. *SHELXTL-Plus, Structure Determination Software Programs, (Version 6.14.) Bruker Analytical X-ray Instruments Inc.*, Madison, Wisconsin, USA, 1998.
3. George, G. N., *EXAFSPAK, EXAFSPAK, SSRL, SLAC*.
4. Delgado-Jaime, M. U.; Mewis, C. P.; Kennepohl, P., *J. Synchrotron Radiat.* **2010,** *17*, 132-137.
5. Addison, A. W.; Rao, T. N.; Reedijk, J.; Vanrijn, J.; Verschoor, G. C., *J. Chem. Soc., Dalton Trans.* **1984**, 1349-1356.
6. Schneider, J.; Schnautz, B.; Hauptman, R.; Henkel, G., *Acta Crystallogr. Sect. C-Cryst. Struct. Commun.* **1999,** *55*, 489-491.
7. Costa, T.; Dorfman, J. R.; Hagen, K. S.; Holm, R. H., *Inorg. Chem.* **1983,** *22*, 4091-4099.
8. Brines, L. M.; Shearer, J.; Fender, J. K.; Schweitzer, D.; Shoner, S. C.; Barnhart, D.; Kaminsky, W.; Lovell, S.; Kovacs, J. A., *Inorg. Chem.* **2007,** *46*, 9267-9277.
9. Coggins, M. K.; Toledo, S.; Shaffer, E.; Kaminsky, W.; Shearer, J.; Kovacs, J. A., *Inorg. Chem.* **2012,** *51*, 6633-6644.
10. Seela, J. L.; Knapp, M. J.; Kolack, K. S.; Chang, H.-R.; Huffman, J. C.; Hendrickson, D. N.; Christou, G., *Inorg. Chem.* **1998,** *37*, 516-525.
11. Neese, F., *WIREs Comput. Mol. Sci.* **2012,** *2*, 73-78.
12. Becke, A. D., *J. Chem. Phys.* **1993,** *98*, 1372.
13. Grimme, S.; Antony, J.; Ehrlich, S.; Krieg, H., *J. Chem. Phys.* **2010,** *132*, 154104.
14. van Lenthe, E.; Baerends, E. J.; Snijders, J. G., *J. Chem. Phys.* **1993,** *99*, 4597.
15. van Lenthe, E.; Baerends, E. J.; Snijders, J. G., *J. Chem. Phys.* **1994,** *101*, 9783.
16. Weigend, F., *Phys. Chem. Chem. Phys.* **2006,** *8*, 1057.
17. Pantazis, D. A.; Chen, X.-Y.; Landis, C. R.; Neese, F., *J. Chem. Theory Comput.* **2008,** *4*, 908-919.
18. Izsák, R.; Neese, F., *J. Chem. Phys.* **2011,** *135*, 144105.
19. Klamt, A.; Schüürmann, G., *J. Chem. Soc. Perk. Trans. 2* **1993**, 799.
20. Yanai, T.; Tew, D. P.; Handy, N. C., *Chem. Phys. Lett.* **2004,** *393*, 51-57.
21. Martin, R. L., *J. Chem. Phys.* **2003,** *118*, 4775.
22. Kopf, M. A.; Varech, D.; Tuchagues, J. P.; Mansuy, D.; Artaud, I. *J. Chem. Soc., Dalton Trans.* **1998**, 991.
23. Matsubara, C.; Kawamoto, N.; Takamura, K. *Analyst* **1992**, *117*, 1781.

III. Chapter III

Material and Methods

$[Mn^{II}_2(LS)(LSH)]ClO_4$ (**Mn^{II}_2SH**)[1] (described in chapter II) and $[Co^{II}_2(LSSL)](PF_6)_2$ (**Co^{II}_2SS**)[2] were prepared according to reported procedures. The syntheses/electrosynthesis of $[Mn^{II}_2(LSSL)](PF_6)_2$ (**Mn^{II}_2SS**) and $[Mn^{III}(LS)I]$ (**$Mn^{III}I$**) were performed under argon, while the corresponding work-up was carried out under air atmosphere. The infrared spectra were recorded on a Magna-IR TM 550 Nicolet spectrometer as KBr pellets. The elemental analyses were carried out with a C, H, N analyser (SCA, CNRS). The ESI-MS spectra were registered on a Bruker Esquire 3000 Plus ion trap spectrometer equipped with an electrospray ion source (ESI). The samples were analysed in positive and negative ionization mode by direct perfusion in the ESI-MS interface (ESI capillary voltage= 2kV, sampling cone voltage= 40 V). The electronic absorption spectra were recorded on a Varian Cary 300 absorption spectrophotometer or on a MCS 501 UV-NIR (Carl Zeiss) photodiode-array spectrophotometer in quartz cells (optical path length: 0.5-1.0 cm).

Electrochemical measurements. Tetrabutylammonium hexafluorophosphate (NBu_4PF_6) was used as received and stored in glove box. Acetonitrile (99.9+ %, extra dry) and dichloromethane (99.99%) were degassed with argon prior to use. Electrochemical experiments were performed under argon, in a glove box with less than 5 ppm of O_2, by using a SP300 Bio-Logic potentiostat/galvanostat. A standard three-electrode electrochemical cell was used. Potentials were referred to an Ag/0.01 M $AgNO_3$ reference electrode in CH_3CN + 0.1 M Bu_4NClO_4 and measured potentials were calibrated through the use of an internal Fc/Fc^+ standard. The working electrode was a vitreous carbon disk (3 mm in diameter) polished with 2 µm diamond paste (Mecaprex Presi) for cyclic voltammetry (Ep_a, anodic peak potential; Ep_c, cathodic peak potential). Exhaustive electrolysis was carried out on reticulated vitreous carbon electrode 45 PPI (the electrosynthesis Co. Inc.; 1 cm^3). The auxiliary electrode was a Pt wire in CH_3CN + 0.1 M Bu_4NPF_6.

X-ray Crystallography. A summary of data collection and structure refinement for **Mn^{II}_2SS**·$2CH_3CN$ and **$Mn^{III}I$** is reported in chapter III. Selected bond distances and angles are provided in chapter III. CCDC 1412558 and CCDC 1412559 contain the supplementary crystallographic data for **$Mn^{III}I$** and **Mn^{II}_2SS**·$2CH_3CN$, respectively. Single-crystal diffraction data for **Mn^{II}_2SS**·$2CH_3CN$ were measured on an Oxford-Diffraction XCalibur diffractometer with a Sapphire 3 CCD detector (MoK radiation, graphite monochromator, λ = 0.71073Å) at 150(2) K. The CrysAlisPro program package (Agilent Technologies, Version 1.171.37.35) was used for cell refinements and data reductions. An empirical absorption correction (CrysAlisPro) was applied to the data. Single-crystal diffraction data for **$Mn^{III}I$** were measured on a Bruker-AXS-Enraf-Nonius KappaCCD diffractometer with a CCD area

detector and an Incoatec high brilliance microfocus source (MoKα radiation, Multilayers mirrors monochromator, λ 0.71073Å) at 200 K. The OLEX2 program package was used for cell refinements and data reductions.[3] An absorption correction (SADABS) was applied to the data. For both complexes, the molecular structure was solved by charge flipping or direct methods and refined on F^2 by full matrix least-squares techniques, using the SUPERFLIP[4] and SHELXTL packages[5] for $\mathbf{Mn^{II}_2SS}\cdot 2CH_3CN$ and $\mathbf{Mn^{III}I}$, respectively. In both cases, all non-hydrogen atoms were refined anisotropically and all hydrogen atoms were placed at their calculated positions.

Magnetic measurements. Magnetic measurements were performed on a polycrystalline sample of $\mathbf{Mn^{II}_2SS}\cdot 2CH_3CN$ (14.9 mg). The sample was sealed in a polyethylene bag (3 □ 0.5 □ 0.02 cm; 21.9 mg) in order to collect data in the temperature range of 1.8 to 300 K at 1000 Oe. Magnetic measurements were obtained with the use of a Quantum Design SQUID magnetometer MPMS-XL functioning between 1.8 and 400 K for direct-current (dc) applied fields ranging from -7 to +7 T. Prior to the experiment, the field-dependent magnetization was measured at 100 K on the sample in order to prove the absence of any bulk ferromagnetic impurities. On the other hand, when fitting the magnetic data, it was necessary to introduce in the magnetic model a paramagnetic Curie impurity that was assumed to be a mononuclear Mn^{II} species (S = 5/2). Its amount was estimated at 0.5(1)%. The magnetic data were corrected for the sample holder and diamagnetic contributions.

Computational details. All theoretical calculations were based on the Density Functional Theory (DFT) and were performed with the ORCA program package.[6] Full geometry optimizations were carried out for all complexes using the hybrid functional B3LYP[7-9] in combination with the TZV/P[10] basis set for all atoms and by taking advantage of the resolution of the identity (RI) approximation in the Split-RI-J variant[11] with the appropriate Coulomb fitting sets.[12] Increased integration grids (Grid4 in ORCA convention) and tight SCF convergence criteria were used. Vibrational frequency calculations were performed to ensure that each geometry optimization converged to a real minimum. Solvent effects were accounted for according to the experimental conditions. For that purpose, we used the acetonitrile solvent (ε = 9.08) within the framework of the conductor like screening (COSMO) dielectric continuum approach.[13] The relative energies were obtained from single-point calculations using the B3LYP[14, 15] functional together with the TZV/P basis set. They were computed from the gas-phase optimized structures as a sum of electronic energy, thermal corrections to free energy, and free energy of solvation. The Heisenberg isotropic exchange coupling constants J were evaluated from single point calculations based on the Broken Symmetry (BS) approach[16-18] using the B3LYP functional and the TZV/P basis set. The Yamaguchi formula[19, 20] was used to estimate the

exchange coupling constants J based on the Heisenberg–Dirac–van Vleck Hamiltonian: $H = -2JS_1S_2$.[21-24]

Synthesis

Electrosynthesis of $[Mn^{II}_2(LSSL)](PF_6)_2$ (Mn^{II}_2SS). In a standard three-electrode electrochemical cell, an exhaustive electrolysis was carried out at controlled potential (+0.05 V *vs* Fc/Fc^+) on a pale orange suspension of **Mn^{II}_2SH**·0.5$KClO_4$ (53.0 mg, 0.037 mmol) in CH_3CN 0.1 M Bu_4NPF_6 (6 ml). During the electrolysis the mixture turned deep orange, and the formation of a yellow precipitate was successively observed. The experiment was stopped when the current was seen to decay to about 5% of its initial value. Under these conditions, the passed charge reached 6.3 C (corresponding to 1.76 electrons for **Mn^{II}_2SH**). The resulting mixture was left to stand overnight and then stored at -18 °C for 8 hours. The obtained solid was filtered and extracted with CH_2Cl_2 (a big excess). The volume was then reduced to ~20 ml, and few drops of CH_3CN were added. After slow diffusion of diethyl ether, X-ray suitable orange-yellow single crystals were obtained (28 mg, 0.017 mmol, 46%), corresponding to **Mn^{II}_2SS**·2CH_3CN. IR (cm^{-1}): 3058 (w), 1598 (s), 1570 (m), 1491 (m), 1480 (m), 1465 (m), 1443 (s), 1287 (w), 1210 (w), 1187 (w), 1155 (w), 1087 (s br), 1022 (w), 1016 (w), 847 (vs), 754 (s), 743 (s), 697 (s), 558 (s, S-S stretching). ESI-MS ($5\cdot10^{-5}$ M, CH_2Cl_2, m/z, I%, M = $[Mn^{II}_2(LSSL)]$ unit): 633.2, 55 $[M]^{2+}$; 1311.3, 100 $[M(HCOO)]^+$ (positive ion mode); 1557.2, 25 $[M(PF_6)_2(H)]^-$; 1601.4, 80 $[M(PF_6)_2(HCOO)]^-$; 1655.2, 65 $[M(PF_6)_2(ClO_4)]^-$; 1701.2, 100 $[M(PF_6)_3]^-$ (negative ion mode). Anal. Calcd. for $C_{76}H_{60}F_{12}Mn_2N_4P_2S_4$.0.5$CH_3CN$.4$H_2O$ (1650.05): C, 56.05; H, 4.25; N, 3.82; Found: C, 56.20; H, 4.12; N, 3.73.

Synthesis/electrosynthesis of $[Mn^{III}(LS)I]$ ($Mn^{III}I$). (A) Bu_4NI (260 ml, 0.1 M solution in CH_2Cl_2, 0.026 mmol) was added to a yellow suspension of **Mn^{II}_2SS**·2CH_3CN (19.0 mg, 0.012 mmol) in CH_2Cl_2 (5 ml) under stirring. After 40 hours, the resulting dark violet mixture was filtered to remove traces of unreacted **Mn^{II}_2SS**. After removing under vacuum the solvent from the filtrate, the resulting dark violet solid was washed with CH_3CN (3 ml) and dried. X-ray suitable dark violet crystals, corresponding to **$Mn^{III}I$**, were obtained by slow diffusion of diisopropyl ether onto a CH_2Cl_2 solution of the product (6.1 mg, 0.008 mmol, 33%). (B) Alternatively, **$Mn^{III}I$** was obtained in higher yields by carrying out the following procedure. In a standard three-electrode electrochemical cell, an exhaustive electrolysis was carried out at controlled potential (-0.15 V *vs* Fc/Fc^+) on a pale orange suspension of **Mn^{II}_2SH**·0.5$KClO_4$ (60.0 mg, 0.045 mmol) in CH_3CN 0.1 M Bu_4NPF_6 (7 ml), in the presence of Bu_4NI (188.1 mg, 0.509 mmol). During the electrolysis the mixture turned dark brown-violet, and the formation of a violet precipitate was successively observed. The experiment was stopped when the passed charge reached 9.5 C (corresponding to ~2.2 electrons for **Mn^{II}_2SH**). The obtained solid was filtered and extracted with CH_2Cl_2 (in a big excess). The solvent was removed

under vacuum and the resulting solid was washed with CH_3CN (2 × 5 ml), filtered, dried and collected as a dark violet powder (36.0 mg, 0.047 mmol, 52%), corresponding to **Mn^{III}I**. IR (cm^{-1}): 3046w, 2922m, 2852.70w, 2363w, 1598s, 1568m, 1484s, 1484m, 1466m, 1441s, 1421w, 1260m, 1183w, 1154w, 1080s br, 1017m, 743m, 693m, 597m. ESI-MS ($5\cdot10^{-5}$ M, CH_2Cl_2, m/z, I%, M = [Mn^{III}(LS)] unit): 633.2, 100 $[M]^+$; 1002.3, 60 $[(Bu_4N)MI]^+$; 1393.2, 50 $[M_2I]^+$ (positive ion mode); 887.0, 100 $[MI_2]^-$; 1647.0, 50 $[M_2I_3]^-$ (negative ion mode). Anal. Calcd. for $C_{38}H_{30}MnN_2S_2I\cdot0.1CH_2Cl_2$ (769.17): C, 59.49; H, 3.96; N, 3.64; Found: C, 59.39; H, 3.99; N, 3.82.

Synthesis of [Co^{III}L(X)] (CoX, X=Cl, Br or I). Solid tetrabutylammonium halide (0.940 mmol) was added to a solution of **Co_2SS**$(PF_6)_2$ (96 mg, 0.060 mmol) in CH_2Cl_2 (10 mL). After stirring for 15 min, the solvent was removed under vacuum. The dark brown residue was washed with acetonitrile (3 x 10 ml), dried and collected.

Co^{III}Cl (87 mg, 0.129 mmol, 72%). IR (cm^{-1}): 3052m, 3027w, 1958w, 1890w, 1809w, 1602s, 1570m, 1488s, 1469m, 1443s, 1266w, 1184w, 1157w, 1126m, 1084m, 1060m, 1034m, 793m, 754m, 747m, 697vs. ^{1}H NMR (400 MHz, CD_2Cl_2): δ -12.41 (s, 2H), -6.30 (br, 2H), -4.15 (s, 2H), 2.37 (s, 2H), 3.26 (s, 4H), 7.25 (s, 4H), 7.45 (s, 2H), 8.43 (s, 4H), 11.95 (s, 4H), 12.30 (s, 2H), 27.46 (s, 2H). ESI-MS (0.15 mM, CH_2Cl_2, *m/z*, I%): 637.2, 95 $[CoL]^+$; 774.2, 100 $[CoLCl]^+\cdot H_2O\cdot CH_2Cl_2$; 1310.2, 20 $[CoLCl][CoLH]^+$. Anal. Calcd. for $C_{38}H_{30}N_2S_2CoCl$ (673.14): C, 67.80; H, 4.49; N, 4.16 Found: C, 67.44; H, 4.71; N, 4.32. Absorption spectrum in CH_2Cl_2 (λ_{max}, nm (ε, M^{-1} cm^{-1})): ~795 (~700), 675 (~1100), 477 (~6200), 373 (~6600).

Co^{III}Br (60 mg, 0.084 mmol, 70% yield). IR (cm^{-1}): 3052m, 3027w, 1958w, 1890w, 1809w, 1602s, 1570m, 1488s, 1469m, 1443s, 1266w, 1184w, 1157w, 1126m, 1084m, 1060m, 1034m, 793m, 754m, 747m, 697vs, 534m, 522m. ^{1}H NMR (400 MHz, CD_2Cl_2): δ -16.20, -11.36, -10.66, -4.19, 7.39, 7.55, 11.91, 12.12, 12.36, 26.13, 28.27. ESI-MS ($5\cdot10^{-5}$ M, CH_3CN, *m/z*, I%): 637.2, 77 $[CoL]^+$; 757.1, 56 $[CoLBr\cdot MeCN]^+$; 1355.2, 100 $[Co_2L_2Br]^+$ 1473.1, 90 $[Co_2L_2Br_2\cdot MeCN]^+$ (positive ion mode); 797.1, 37 $[CoLBr_2]^-$; 1513.4, 100 $[Co_2L_2Br_3]^-$ (negative ion mode). Absorption spectrum in CH_2Cl_2 (λ_{max}, nm (ε, M^{-1} cm^{-1})): 822 (~1100), 683 (~1900), 475 (~6400), 380 (~6900).

Co^{III}I (77 mg, 0.101 mmol, 84%). IR (cm^{-1}): 3052m, 3027w, 1958w, 1890w, 1809w, 1602s, 1570m, 1488s, 1469m, 1443s, 1266w, 1184w, 1157w, 1126m, 1084m, 1060m, 1034vs, 793m, 754m, 747m, 697vs. ^{1}H NMR (400 MHz, CD_2Cl_2): δ -22.51, -16.21, -11.35, -4.20, -3.72, 7.37, 7.55, 11.90, 12.11, 12.36, 22.88, 26.12, 28.25. ESI-MS ($5\cdot10^{-5}$ M, CH_3CN, *m/z*, I%): 637.2, 100 $[CoL]^+$; 1401.2, 50 $[Co_2L_2I]^+$ (positive ion mode); 891.0, 16 $[CoLI_2]^-$; 1655.2, 100 $[Co_2L_2I_3]^-$ (negative ion mode). Absorption spectrum in CH_2Cl_2 (λ_{max}, nm (ε, M^{-1} cm^{-1})): 859 (~1200), 726 (~2200), 490 (~6800), 377 (~8200).

X-ray suitable dark brown single crystals of **CoX** (X = Cl Br, I) were obtained by slow evaporation of a solution of the corresponding complex in toluene: CH_2Cl_2 1:1.

References

1. M. Gennari, D. Brazzolotto, J. Pecaut, M. V. Cherrier, C. J. Pollock, S. DeBeer, M. Retegan, D. A. Pantazis, F. Neese, M. Rouzieres, R. Clerac and C. Duboc, *J. Am. Chem. Soc.*, 2015.
2. M. Gennari, B. Gerey, N. Hall, J. Pécaut, M.-N. Collomb, M. Rouzières, R. Clérac, M. Orio and C. Duboc, *Angew. Chem. Int. Ed.*, 2014, 53, 5318-5321.
3. O. V. Dolomanov, L. J. Bourhis, R. J. Gildea, J. A. K. Howard and H. Puschmann, *J. Appl. Crystallogr.*, 2009, 42, 339-341.
4. L. Palatinus and G. Chapuis, *SUPERFLIP program*, J. Appl. Cryst., 40, 2007, 786-790, 2007.
5. G. M. Sheldrick, Madison, Wisconsin, USA, 1998.
6. F. Neese, *Wiley Interdiscip. Rev. Comput. Mol. Sci.*, 2012, 2, 73-78.
7. J. P. Perdew, *Phys. Rev. B*, 1986, 33, 8822-8824.
8. J. P. Perdew, *Phys. Rev. B*, 1986, 34, 7406-7406.
9. A. D. Becke, *Phys. Rev. A*, 1988, 38, 3098-3100.
10. A. Schäfer, C. Huber and R. Ahlrichs, *J. Chem. Phys.*, 1994, 100, 5829-5835.
11. F. Neese, *J. Comput. Chem.*, 2003, 24, 1740-1747.
12. F. Weigend, *Phys. Chem. Chem. Phys.*, 2006, 8, 1057-1065.
13. A. Klamt and G. Schürmann, *J. Chem. Soc., Perkin Trans. 2*, **1993**, 799-805.
14. A. D. Becke, *J. Chem. Phys.*, 1993, 98, 5648-5652.
15. C. T. Lee, W. T. Yang and R. G. Parr, *Phys. Rev. B*, 1988, 37, 785-789.
16. L. Noodleman, *J. Chem. Phys.*, 1981, 74, 5737-5743.
17. L. Noodleman and D. A. Case, *Adv. Inorg. Chem.*, 1992, 38, 423-+.
18. L. Noodleman and E. R. Davidson, *Chem. Phys.*, 1986, 109, 131-143.
19. T. Soda, Y. Kitagawa, T. Onishi, Y. Takano, Y. Shigeta, H. Nagao, Y. Yoshioka and K. Yamaguchi, *Chem. Phys. Lett.*, 2000, 319, 223-230.
20. K. Yamaguchi, Y. Takahara and T. Fueno, *Applied Quantum Chemistry* 1986, 155-184.
21. W. Heisenberg, *Z. Phys.*, 1928, 49, 619-636.
22. P. A. M. Dirac, *Proc. Roy. Soc.*, **1929**, *A123*, 714.
23. J. H. Van Vleck, in *The Theory of Electronic and Magnetic Susceptibilies*, Oxford University: London, 1932, p. 384.
24. W. Heisenberg, *Z. Physik*, 1926, 38, 411-426.

IV. Chapitre IV

Material and Methods.

All reagents and solvents were used as received. **Co^{II}_2SS** has been synthesized according to a reported procedure.[1] ^{1}H NMR spectra were recorded on a Bruker Avance III 400 MHz spectrometer using standard Bruker pulse sequences. Chemical shifts are reported in ppm referenced to residual solvent protons (d_7-DMF). UV-Vis experiments were performed on a Perkin-Elmer Lambda 650 using quartz cells. The cell dimension (i.e. optical path length) has been chosen to obtain an absorption in the linear region of Beer-Lambert plot.

Magnetic Measurements. The magnetic susceptibility measurements performed on powdered samples were obtained with the use of MPMS-XL Quantum Design SQUID magnetometer. This magnetometer works between 1.8 and 400 K for dc applied fields ranging from 7 to 7 T. Measurements were performed on polycrystalline samples of de **Mn^{III}X** (10.2, 8.40, 10.8 and 15.6 mg for **Mn^{III}I**, **Co^{III}Cl**, **Co^{III}Br** and **Co^{III}I** respectively, introduced in a polyethylene bag (3 × 0.5 × 0.02 cm; of about 30 mg) and covered with mineral oil (typical 8-10 mg). The ac susceptibility measurements were measured with an oscillating ac field of 3 Oe with frequency between 1 to 1500 Hz. It is worth noting that no out-of-phase ac susceptibility signal has been detected above 1.8 K in zero dc field. The magnetic data were corrected for the sample holder (plastic bag) and the diamagnetic contribution.

Magnetic susceptibility measurements on solution samples were performed following Evans' method[2,3] using precision-made coaxial tubes. Cyclohexane (5% by volume) was used as internal standard in CD_2Cl_2. Molar susceptibilities were calculated according to:

$$\chi \approx M\,(\chi_0 + 3000\Delta\nu/4\pi\nu_0 cM)$$

where χ_0 is the mass susceptibility of the pure solvent (cgs units), $\Delta\nu$ is the paramagnetic shift (Hz), ν_0 is the operating RF frequency of the spectrometer (Hz), c is the concentration (mol·l^{-1}) of the paramagnetic molecule and M is its molecular weight. The values were corrected for the ligand diamagnetic susceptibility derived from Pascal's constants, giving χ^{corr}. The magnetic moments (μ_{eff}) have been then calculated from:

$$\mu_{eff} = (8\times\chi T)^{1/2}$$

where T = 293 K.

Computational details. All theoretical calculations were performed with the ORCA program package.[4] Full geometry optimizations were carried out for all complexes using the GGA functional

BP86[5-7] in combination with the TZV/P[8] basis set for all atoms and by taking advantage of the resolution of the identity (RI) approximation in the Split-RI-J variant[9] with the appropriate Coulomb fitting sets.[10] Increased integration grids (Grid4 in ORCA convention) and tight SCF convergence criteria were used. Solvent effects were accounted for according to the experimental conditions. For that purpose, we used the CH_2Cl_2 (ε = 9.08) solvent within the framework of the conductor like screening (COSMO) dielectric continuum approach.[11] The relative energies were obtained from single-point calculations using the B3LYP[12,13] functional together with the TZV/P basis set. They were computed from the gas-phase optimized structures as a sum of electronic energy, thermal corrections to free energy, and free energy of solvation. Optical properties were predicted from additional single-point calculations using the same functional/basis set as employed before. Electronic transition energies and dipole moments for all models were calculated using time-dependent DFT (TD-DFT)[14-16] within the Tamm-Dancoff approximation.[17,18] To increase computational efficiency, the RI approximation[19] was used in calculating the Coulomb term and at least 30 excited states were calculated in each case. For each transition difference density plots were generated using the orca_plot utiliy program and were visualized with the Chemcraft program.[20]

Zero Field Splitting (ZFS) parameters were obtained from single-point calculations using the B3LYP functional. Direct spin−spin (SS) and spin−orbit couplings (SOC) were taken into account. For the estimation of the SOC effects, the mean-field approximation (SOMF), including both the spin-own-orbit and spin-other-orbit interactions in the exchange term as well as coupled-perturbed approach (CP), was carried out. The spin-spin contribution to the ZFS was calculated from the equation of McWeeny and Mizuno[21] in which the spin density matrix is obtained on the basis of the spin-unrestricted natural orbital (UNO) determinant.[22,23] Scalar relativistic effects were included using the scalar relativisitc zero-order regular approximation (ZORA)[24] and the scalar relativistically recontracted (SARC)[25,26] version of the def2-TZVP(-f) basis set[27] together with the decontracted def2-TZVP/J Coulomb fitting basis sets for all atoms. Increased integration grids (Grid4 and GridX4 in ORCA convention) and tight SCF convergence criteria were used in the calculation. ZFS parameters were alternatively obtained from *ab initio* calculations based on the complete active space self-consistent field (CASSCF) approach. The spin-orbit coupling was calculated within a quasi-degenerate perturbation theory formalism where the SOC operator is diagonalized in a basis of multiconfigurational wave functions obtained from a full configuration interaction (CI) calculation in a limited set of active electrons and orbitals that were obtained from a preceding CASSCF calculation.[25] The active space was chosen to consist of 6 active electrons occupying the five 3d-based molecular orbitals CAS(6,5). The SOC matrix was diagonalized on the basis of all possible triplet (35) and singlet (45) states. The spin-spin (SS) contribution to the ZFS was calculated on the basis of single root CASSCF (12,7) wave function.[28]

References

1. Gennari, M.; Gerey, B.; Hall, N.; Pécaut, J.; Collomb, M.-N.; Rouzières, M.; Clérac, R.; Orio, M.; Duboc, C. *Angew. Chem. Int. Ed.* **2014**, 53, 5318-5321.
2. Evans, D. F. *J. Chem. Soc.* **1959**, 2003-2005.
3. Sur, S. K. *J. Magn. Reson.* **1989**, 82, 169-173.
4. Neese, F. *Wiley Interdiscip. Rev. Comput. Mol. Sci.* **2012**, 2, 73-78.
5 Perdew, J. P. *Phys. Rev. B* **1986**, 33, 8822-8824.
6. Perdew, J. P. *Phys. Rev. B* **1986**, 34, 7406-7406.
7. Becke, A. D. *Phys. Rev. A* **1988**, 38, 3098-3100.
8. Schäfer, A.; Huber, C.; Ahlrichs, R. *J. Chem. Phys.* **1994**, 100, 5829-5835.
9. Neese, F. *J. Comput. Chem.* **2003**, 24, 1740-1747.
10. Weigend, F. *PhysChemChemPhys* **2006**, 8, 1057-1065.
11. Klamt, A.; Schürmann, G. *J. Chem. Soc., Perkin Trans. 2* **1993**, 799-805.
12. Becke, A. D. *J. Chem. Phys.* **1993**, 98, 1372-1377.
13. Lee, C. T.; Yang, W. T.; Parr, R. G. *Phys. Rev. B* **1988**, 37, 785-789.
14. Casida, M. E. In *Recent Advances in Density Functional Methods*; Chong, D. P. Ed. World Scientific: Singapore, **1995**.
15. Stratmann, R. E.; Scuseria, G. E.; Frisch, M. J. *J. Chem. Phys.* **1998**, 109, 8218-8224.
16. Bauernschmitt, R.; Ahlrichs, R. *Chem. Phys. Lett.* **1996**, 454-464.
17. Hirata, S.; Head-Gordon, M. *Chem. Phys. Lett.* **1999**, 314, 291-299.
18. Hirata, S.; Head-Gordon, M. *Chem. Phys. Lett.* **1999**, 302, 375-382.
19. Neese, F. *J. Chem. Phys.* **2001**, 115, 11080-11080.
20. Chemcraft http://chemcraftprog.com.
21. McWeeny, R.; Mizuno, Y. *Proceedings of the Royal Society A: Mathematical, Physical and Engineering Sciences* **1961**, 259, 554-577.
22. Sinnecker, S.; Neese, F. *J. Phys. Chem. A* **2006**, 110, 12267-12275.
23. Neese, F. *J. Chem. Phys.* **2007**, 127, 164112.
24. van Wüllen, C. *J. Chem. Phys.* **1998**, 109, 392-399.
25. Pantazis, D. A.; Chen, X. Y.; Landis, C. R.; Neese, F. *J. Chem. Theory Comput.* **2008**, 4, 908-919.
26. Pantazis, D. A.; Neese, F. *J. Chem. Theory Comput.* **2009**, 5, 2229-2238.
27. Weigend, F.; Ahlrichs, R. *PhysChemChemPhys* **2005**, 7, 3297-3305.
28. Ganyushin, D.; Neese, F. *J. Chem. Phys.* **2006**, 125, 024103.

Appendix

Summary of X-ray crystallographic data for **$Ni^{II}Fe^{II}Cp$**$BF_4 \cdot 1.5Et_2O$
and **$Ni^{II}Fe^{II}Cp^*$**$BF_4 \cdot 0.7CH_2Cl_2 \cdot 0.15Et_2O \cdot 0.15H_2O$

Empirical formula	$C_{50}H_{50}BF_4FeN_2NiO_{2.50}S_2$	$C_{50}H_{48}BF_4FeN_2NiO_{1.30}S_2Cl_{1.39}$
Formula weight	984.52	1016.44
Colour, habit	Dark brown, irregular	Black,needle
Crystal size, mm	0.56 × 0.35 × 0.16	0.5 × 0.44 × 0.1
Crystal system	Triclinic	Monoclinic
Space group	P -1	c-2yc
a, Å	14.2066(7)	25.286(5)
b, Å	17.4343(11)	23.295(5)
c, Å	22.2493(12)	20.693(4)
α deg.	67.734(5)	90.00
β, deg.	71.474(5)	127.48(3)
γ, deg.	71.906(5)	90.00
V, Å^3	4720.6(5)	9673(3)
Z	4	8
T, K	150(2)	200
ρ (calc), Mg/m^3	1.385	1.396
μ, mm^{-1}	0.853	0.907
θ range, deg.	2.92 to 30.51	2.21to 27.54
No.of rflcn/obsv	55577 / 28388	63313 / 11047
GooF	1.031	1.260
*R*1	0.0671	0.0698
*wR*2	0.1491	0.1692

Summary of X-ray crystallographic data for **$Ni^{II}Fe^{II}Cp$** *(CCDC 1438146)*

Summary of X-ray crystallographic data for $\mathbf{Mn^{II}_2SH}\cdot 1.55CH_3CN\cdot 0.45CH_3OH$ and $\mathbf{Mn^{III}_2OH^{\#}}\cdot 7.16CH_3CN$.

	$\mathbf{Mn^{II}_2SH}$	$\mathbf{Mn^{III}_2OH^{\#}}$
Empirical formula	$C_{79.55}H_{67.45}ClMn_2N_{5.55}O_{4.45}S_4$	$C_{90.33}H_{82.50}Cl_{0.19}F_{4.86}Mn_2N_{11.16}O_{1.76}P_{0.81}S_4$
Formula weight	1445.93	1714.86
Colour, habit	Orange-brown, plate	Dark red, plate
Crystal size, mm	0.44 × 0.23 × 0.03	not measured
Crystal system	Monoclinic	Monoclinic
Space group	P 21/c	P 21/c
a, Å	15.9886(3)	31.840(4)
b, Å	17.4199(4)	33.121(8)
c, Å	25.8842(6)	17.559(9)
α deg.	90	90
β, deg.	107.741(2)	91.04(4)
γ, deg.	90	90
V, Å^3	6866.4(3)	18514(11)
Z	4	8
T, K	150(2)	293(2)
ρ (calc), Mg/m^3	1.399	1.230
μ, mm^{-1}	0.586	0.443
θ range, deg.	3.37 to 24.71	0.71 to 24.39
No.of rflcn/obsv	39673 / 11662	161400 / 22621
GooF	0.801	1.530
*R*1	0.0399	0.0922
*wR*2	0.0753	0.3107

Summary of X-ray crystallographic data for $\mathbf{Mn^{II}_2SH}$ *(CCDC 1417371)* and $\mathbf{Mn^{III}_2OH}$ *(CCDC 1417372).*

Summary of X-ray crystallographic data for **$Co^{II}Br$** and **$Co^{III}I$**.

	$Co^{III}Br$	**$Co^{III}I$**
Empirical formula	$C_{38}H_{30}CoN_2S_2Br$	$C_{38}H_{30}CoN_2S_2I$
Formula weight	717.60	764.59
Color, habit	Dark brown, plate	Dark brown, plate
Crystal size, mm	0.62x0.26x0.01	0.27x0.22x0.01
Crystal system	Monoclinic	Monoclinic
Space group	*P* $2_1/c$	*P* $2_1/c$
a, Å	14.5871(8)	14.783(2)
b, Å	14.9087(5)	14.9433(7)
c, Å	15.9418(8)	16.0542(14)
α deg.	90	90
β, deg.	113.697(6)	113.108(4)
γ, deg.	90	90
V, $Å^3$	3174.6(3)	3261.9(7)
Z	4	4
T, K	150(2)	150(2)
ρ (calc), Mg/m^3	1.501	1.557
μ, mm^{-1}	1.962	1.631
θ range, deg.	3.07 to 30.51	2.91 to 26.37
No.of rflcn/obsv (R_{int})	33301 / 9677 (0.1000)	27360 / 6665 (0.1822)
GooF	1.000	1.024
*R*1	0.0604	0.0985
*wR*2	0.0970	0.1871

Summary of X-ray crystallographic data for **$Co^{III}I$** *(CCDC 1471930),* **$Co^{III}Br$** (*CCDC 1471931*)

Summary of X-ray crystallographic data for $\mathbf{Mn^{II}_2SS}\cdot 2CH_3CN$ and $\mathbf{Mn^{III}I}$.

	$\mathbf{Mn^{II}_2SS}\cdot 2CH_3CN$	$\mathbf{Mn^{III}I}$
Empirical formula	$C_{80}H_{66}F_{12}Mn_2N_6P_2S_4$	$C_{38}H_{30}IMnN_2S_2$
Formula weight	1639.44	760.60
Colour, habit	Orange, triangle prism	Violet, plate
Crystal size, mm	0.44 × 0.22 × 0.20	0.74 × 0.43 × 0.38
Crystal system	Monoclinic	Monoclinic
Space group	C 2/c	P 2_1/c
a, Å	19.9121(15)	14.460(3)
b, Å	17.3032(8)	15.448(3)
c, Å	22.1976(17)	16.028(3)
α, deg.	90	90
β, deg.	111.524(9)	112.40(3)
γ, deg.	90	90
V, Å^3	7114.7(9)	3310.5(11)
Z	8	4
T, K	150	200
ρ (calc), Mg/m^3	1.531	1.526
μ, mm^{-1}	0.601	1.487
θ range, deg.	3.375 to 26.372	2.09 to 26.00
No.of rflcn/obsv	31113 / 7266	36752 / 6418
GooF	0.887	1.188
*R*1	0.0523	0.0427
*wR*2	0.1053	0.0931

Summary of X-ray crystallographic data for $\mathbf{Mn^{II}_2SS}$ *(CCDC 1412559)* and $\mathbf{Mn^{III}I}$ *(CCDC 1412558).*

Summary of X-ray crystallographic data for $\mathbf{Mn^{IV}_2(O)(OH)}\cdot ClO_4.5.68CH_3CN.1.5H_2O$ X-ray crystallographic data for $\mathbf{Mn^{IV}_2(O)_2}\cdot 0.64CH_2Cl_2\cdot 2.71H_2O$.

	$\mathbf{Mn^{IV}_2(O)(OH)}$	$\mathbf{Mn^{IV}_2(O)_2}$
Empirical formula	$C_{76}H_{61}Mn_2N_4S_4O_2.ClO_4$	$C_{76}H_{60}Mn_2N_4S_4O_2$
Formula weight	1399.5	1299.40
Colour, habit	Black, Block	Black, Block
Crystal size, mm	0.42 × 0.32 × 0.24	0.25 × 0.22 × 0.22
Crystal system	Triclinic	Monoclinic
Space group	2-P1	C 2/y
a, Å	13.706(3)	22.009(4)
b, Å	17.254(4)	14.268(3)
c, Å	19.02(4)	15.679(3)
α, deg.	107.57(3)	90
β, deg.	90.10(3)	130.38(3)
γ, deg.	95.85(3)	90
V, Å^3	3750.5(13)	3750.5(13)
Z	2	4
T, K	200	200
ρ (calc), Mg/m^3	1.334	1.334
μ, mm^{-1}	0.485	0.596
θ range, deg.	2.12 to 25.00	2.86 to 27.50
No.of rflcn/obsv	65705 / 7584	28113 / 7439
GooF	1.045	1.100
*R*1	0.1175	0.0415
*wR*2	0.2900	0.1112

Abstract.

The aim of my thesis was to improve the knowledge on the role of metal-thiolate bonds in metalloenzymes using a bio-inspired approach by investigating the structural, electronic and/or magnetic properties of chemical models as well as their reactivity.

In this context, we report the synthesis and analysis of two heterodinuclear NiFe complexes, structural and functional models of the active site of [NiFe] hydrogenase, which produce H_2 electrocatalytically at high rates. Intermediate species have been generated and characterized by different spectroscopic techniques. The reversible inhibition of the catalytic activity by CO has been also investigated and discussed.

We also describe the synthesis and characterization of a new manganese-thiolate complex, bearing a pendant thiol group bound (in its -SH form) to one Mn^{II} ion. This complex is capable of activating dioxygen, and is an active catalyst for selective 2-electron O_2 reduction in the presence of a one-electron reducing agent and a proton source. The O_2 activation and reduction pathways have been studied under both stoichiometric and catalytic conditions. Several high valent Mn complexes resulting from O_2 activation have been isolated and characterized and their reactivity toward hydrogen or oxygen atom transfer (HAT or OAT, respectively) has been evaluated.

A series of pentacoordinated metal-halide complexes $M^{III}X$ (M = Co and Mn ; X = Cl, Br, I) has been investigated with the aim of understanding the role of the metal ion in disulphide/thiolate interconversion. While such conversion is reversible in the presence of both Co and Mn, the process becomes much faster and quantitative for the Co–based system with respect to the Mn one. Besides, this work has allowed improving the understanding of how the electronic and redox properties of the metal centers should be fine-tuned to permit a disulphide/thiolate (inter)conversion, mediated by metal ions, to occur efficiently.

Finally, the magnetic properties of the series of mononuclear $Co^{III}X$ complexes have been investigated. They display a rare intermediate *S* = 1 spin state and their magnetic anisotropy is sensitive to the nature of the halide in an unexpected way: the largest *D*-value has been measured for the chloride compound and the smallest for the iodide one. This behavior has been rationalized through a theoretical study.

Résumé

L'objectif de ma thèse était d'améliorer les connaissances sur le rôle des liaisons métal-thiolates au sein des métalloenzymes en utilisant une approche bio-inspirée par l'étude des propriétés structurales, électroniques et/ou magnétiques de modèles chimiques ainsi que de leur réactivité.

Dans ce contexte, nous avons synthétisé deux complexes de NiFe, modèle structuraux et fonctionnels de l'hydrogénase [NiFe], capables de produire H_2 efficacement de manière électrocatalytique de H_2. Des espèces intermédiaires ont été synthétisées et caractérisées par différentes techniques spectroscopiques. L'inhibition réversible de l'activité catalytique de ces catalyseurs en présence de CO a été étudiée et discutée.

Nous décrivons également un nouvel exemple de complexe de Mn-thiolate, dont l'un des thiolates coordonné à un Mn est protoné. Ce complexe est capable d'activer l'oxygène moléculaire (O_2) et de le réduire de manière catalytique par un processus à deux électrons en présence d'une source de protons et d'un agent de réduction. L'activation et la réduction de l'oxygène ont été étudiées en conditions stœchiométriques et catalytiques. Des complexes de Mn à hauts degrés d'oxydation résultant de l'activation d'O_2 ont été isolés et caractérisés. Leur réactivité vis-à-vis de l'hydrogène (HAT) et de l'oxygène (OAT) a été évaluée.

Une série de complexes métal-halogénure pentacoordinés, $M^{III}X$ (M = Mn ou Co ; X = Cl, Br, I) a été étudiée pour comprendre le rôle du métal dans la conversion disulfure/thiolate. Il a été montré que cette conversion est réversible pour les deux ions métalliques mais que le processus est plus rapide et quantitatif dans le cas du système à base de Co par rapport à celui du Mn. Ce travail nous a permis de comprendre comment les propriétés redox et électroniques du métal peuvent intervenir sur l'efficacité de cette interconversion.

Enfin les propriétés magnétiques de la série des complexes de Co^{III} contenant un halogénure ont été étudiées. Ces complexes présentent un spin *S* = 1 intermédiaire et leur anisotropie magnétique est sensible à la nature de l'halogénure de manière inattendue : la plus grande valeur de D a été mesurée pour le complexe chloré et la plus petite pour le composé iodé. Ce comportement a été rationalisé au travers d'une étude théorique.

Abstract.

The aim of my thesis was to improve the knowledge on the role of metal-thiolate bonds in metalloenzymes using a bio-inspired approach by investigating the structural, electronic and/or magnetic properties of chemical models as well as their reactivity.

In this context, we report the synthesis and analysis of two heterodinuclear NiFe complexes, structural and functional models of the active site of [NiFe] hydrogenase, which produce H_2 electrocatalytically at high rates. Intermediate species have been generated and characterized by different spectroscopic techniques. The reversible inhibition of the catalytic activity by CO has been also investigated and discussed.

We also describe the synthesis and characterization of a new manganese-thiolate complex, bearing a pendant thiol group bound (in its -SH form) to one Mn^{II} ion. This complex is capable of activating dioxygen, and is an active catalyst for selective 2-electron O_2 reduction in the presence of a one-electron reducing agent and a proton source. The O_2 activation and reduction pathways have been studied under both stoichiometric and catalytic conditions. Several high valent Mn complexes resulting from O_2 activation have been isolated and characterized and their reactivity toward hydrogen or oxygen atom transfer (HAT or OAT, respectively) has been evaluated.

A series of pentacoordinated metal-halide complexes $M^{III}X$ (M = Co and Mn ; X = Cl, Br, I) has been investigated with the aim of understanding the role of the metal ion in disulphide/thiolate interconversion. While such conversion is reversible in the presence of both Co and Mn, the process becomes much faster and quantitative for the Co–based system with respect to the Mn one. Besides, this work has allowed improving the understanding of how the electronic and redox properties of the metal centers should be fine-tuned to permit a disulphide/thiolate (inter)conversion, mediated by metal ions, to occur efficiently.

Finally, the magnetic properties of the series of mononuclear $Co^{III}X$ complexes have been investigated. They display a rare intermediate *S* = 1 spin state and their magnetic anisotropy is sensitive to the nature of the halide in an unexpected way: the largest *D*-value has been measured for the chloride compound and the smallest for the iodide one. This behavior has been rationalized through a theoretical study.

Résumé

L'objectif de ma thèse était d'améliorer les connaissances sur le rôle des liaisons métal-thiolates au sein des métalloenzymes en utilisant une approche bio-inspirée par l'étude des propriétés structurales, électroniques et/ou magnétiques de modèles chimiques ainsi que de leur réactivité.

Dans ce contexte, nous avons synthétisé deux complexes de NiFe, modèle structuraux et fonctionnels de l'hydrogénase [NiFe], capables de produire H_2 efficacement de manière électrocatalytique de H_2. Des espèces intermédiaires ont été synthétisées et caractérisées par différentes techniques spectroscopiques. L'inhibition réversible de l'activité catalytique de ces catalyseurs en présence de CO a été étudiée et discutée.

Nous décrivons également un nouvel exemple de complexe de Mn-thiolate, dont l'un des thiolates coordonné à un Mn est protoné. Ce complexe est capable d'activer l'oxygène moléculaire (O_2) et de le réduire de manière catalytique par un processus à deux électrons en présence d'une source de protons et d'un agent de réduction. L'activation et la réduction de l'oxygène ont été étudiées en conditions stœchiométriques et catalytiques. Des complexes de Mn à hauts degrés d'oxydation résultant de l'activation d'O_2 ont été isolés et caractérisés. Leur réactivité vis-à-vis de l'hydrogène (HAT) et de l'oxygène (OAT) a été évaluée.

Une série de complexes métal-halogénure pentacoordinés, $M^{III}X$ (M = Mn ou Co ; X = Cl, Br, I) a été étudiée pour comprendre le rôle du métal dans la conversion disulfure/thiolate. Il a été montré que cette conversion est réversible pour les deux ions métalliques mais que le processus est plus rapide et quantitatif dans le cas du système à base de Co par rapport à celui du Mn. Ce travail nous a permis de comprendre comment les propriétés redox et électroniques du métal peuvent intervenir sur l'efficacité de cette interconversion.

Enfin les propriétés magnétiques de la série des complexes de Co^{III} contenant un halogénure ont été étudiées. Ces complexes présentent un spin *S* = 1 intermédiaire et leur anisotropie magnétique est sensible à la nature de l'halogénure de manière inattendue : la plus grande valeur de D a été mesurée pour le complexe chloré et la plus petite pour le composé iodé. Ce comportement a été rationalisé au travers d'une étude théorique.